JPL D–26280

Earth Observing System (EOS)

Microwave Limb Sounder (MLS)

EOS MLS
Instrument Calibration Report
Volume 1

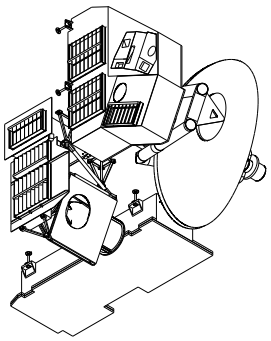

$$\dot{\mathbf{P}}_{\mathbf{i}}^{\mathbf{L}} = \frac{\mathbf{1}}{\eta_{\mathbf{r}}^{\mathbf{ML}}}\left(\frac{\mathbf{C}_{\mathbf{i}}^{\mathbf{L}} - \widehat{\mathbf{C}}_{\mathbf{i}}^{\mathbf{S}}(\mathbf{L})}{\hat{\mathbf{g}}_{\mathbf{i}}(\mathbf{L})} + \eta_{\mathbf{r}}^{\mathbf{MS}}\dot{\mathbf{P}}_{\mathbf{r}}^{\mathbf{S}} - (\mathbf{1} - \eta_{\mathbf{r}}^{\mathbf{ML}})\dot{\mathbf{P}}_{\mathbf{r}}^{\mathbf{BL}} + (\mathbf{1} - \eta_{\mathbf{r}}^{\mathbf{MS}})\dot{\mathbf{P}}_{\mathbf{r}}^{\mathbf{BS}}\right)$$

Robert F. Jarnot, Richard E. Cofield, Herbert M. Pickett, Paul C. Stek

Version: 6 November 2019

Jet Propulsion Laboratory
California Institute of Technology
Pasadena, CA 91109-8099

The research was carried out at the Jet Propulsion Laboratory, California Institute of Technology, under a contract with the National Aeronautics and Space Administration (80NM0018D004).

Release Record

Version	Date	Comments
draft	12 Feb 2003	Start of working/draft version
	30 Mar 2004	Initial release for review
Public	11 Feb 2025	URS wording added to cover

As a side effect of adding the URS wording to the cover it was no longer possible to use the selected default font (Optima) for this document, and no THz FOV-related figures could be included due to font-related issues when converted from Postscript to PDF. This means that the references to the figure in the body of the document are unresolved.

Note that this document was never fully completed before one of the authors (Herb Pickett) became deceased. The other three volume are complete however.

Primary contact for further information on material related to this document:
Robert Jarnot, Robert.F.Jarnot@jpl.nasa.gov

Additional contacts:
Richard Cofield, Richard.E.Cofield-IV@jpl.nasa.gov for GHz FOV-related questions.
Herbert Pickett, Herbert.M.Pickett@jpl.nasa.gov for all THz-related questions.
Paul Stek, Paul.C.Stek@jpl.nasa.gov for GHz Near-Field Range-related questions.

/users/jarnot/texinput/calrep/EOS/CalRep.TEX

Contents

Chapter 1

Introduction

The Microwave Limb Sounder experiment (MLS) on the Earth Observing System (EOS) Aura spacecraft measures thermal limb emission from molecules and radicals of special interest in the stratosphere and upper troposphere, with some measurements extending into the mesosphere. By measuring emission spectra as a function of limb altitude it is possible during ground processing to infer concentration profiles of various species including ClO, BrO, HNO_3, N_2O, CO, H_2O, H_2O_2, HO_2, O_3, OH, HCl, HCN and SO_2. Measurement of O_2 emission provides pressure and temperature data necessary for accurate constituent retrievals, and the spacecraft inertial reference unit (IRU) provides the pointing reference necessary for measurement of geopotential height. An overview of the EOS MLS experiment is given in [1].

This document assumes a reasonable degree of familiarity with the EOS MLS instrument, its operation and internal timing, and with the terminology used to describe both the instrument and its operation. It is not the intention of this document to serve as an MLS tutorial. A detailed description of instrument operation and timing is provided in the EOS MLS Level 1 Data Processing Algorithm Theoretical Basis document [2].

This report is divided into four volumes. Volume 1 describes the calibrations, the calibration data analyses, and the measured instrument performance. For those desiring a deeper view into EOS MLS calibration data, Volume 2 provides a comprehensive presentation of the data, with the voluminous high-resolution spectral sweep data presented in Volume 3. All post-launch updates are presented in Volume 4 in order to allow the majority of this report (i.e., the first 3 volumes) to remain stable. Volume 4 of this report must be referenced by those wishing to fully understand the in-orbit refinements to calibration of EOS MLS, as well as its observed performance in its intended operating environment. For an instrument which operates exclusively in a total-power observing mode (like this one) it is extremely difficult to accurately predict in-orbit sensitivity, since environmental conditions have a strong impact on the behavior of time-series data from the individual measurement channels.

1.1 Objectives

The primary objectives of this report are to document calibration methods and results, and compliance with calibration requirements. The large volume of calibration data for this instrument means that it is impossible to reproduce it in its entirety as part of this report. We have chosen instead to provide comprehensive coverage of these data by emphasizing

graphical representations of much of these data, and presenting the end results of higher level analyses performed on the data sets.

A secondary objective of this report is to document measured instrument performance to show compliance with performance requirements. This document has been chosen as the appropriate place for such data since performance verifications were a prerequisite to definitive calibrations, and often the calibration data sets were the ones which demonstrated that performance requirements were met.

A final objective of this report is to document some of the non-idealities in instrument behavior that were noted during radiometric and spectral calibrations. We consider these observations to be of most importance to follow-on instruments derived from EOS MLS, particularly ones which exercise greater dynamic range of their signal chains (e.g., SIS receivers), and which are targeted towards far more demanding measurements (e.g., small spectral features riding on top of significant radiance offsets).

1.2 Calibration Efficiency

The tight schedule of the EOS calibrations necessitated implementation of calibration setups requiring only trivial reconfiguration to support switching between spectral, radiometric and Field-of-View (FOV) calibration activities. This was achieved with a configuration that directly supported the Near-field Range (NFR) FOV measurements, and with a simple 180° rotation of the GHz switching mirror (by software command to the instrument) reconfigured into a radiometric/spectral calibration setup. The large number of instrument channels and calibration measurements necessitated a high degree of automation for the measurements. High measurement efficiency was obtained by tightly synchronizing the calibration equipment to internal instrument operation, and by using fast acting calibration mechanisms. This is described further in the body of this document.

Experience gained from calibration of the Upper Atmosphere Limb Sounder (UARS) MLS instrument was invaluable in developing the improved calibration methods for EOS MLS. The number of channels calibrated on EOS MLS was approximately an order of magnitude larger than on UARS MLS, but the improvements in equipment and techniques allowed EOS MLS calibrations to be performed in less time than those on the earlier instrument, and to higher precision and accuracy. UARS MLS calibrations are described in [3].

1.3 Verification and non-idealities

Most of the radiometric data presented in this document are related to performance verification rather than calibration, but are included because this document is the appropriate place to record such information. These data were taken to verify adequate instrument performance prior to making definitive calibration measurements.

It is of interest to note that the performance data sets, as well as some of the calibration data sets, were of vital importance to the detection (and ultimate resolution) of some subtle, but potentially devastating, instrumental problems. Important examples include:

- ❑ Radiometric noise characterization data showed systematic offsets between alternate science data measurements.

- ⇨ These arose from small changes in power consumption of the Filterbank subassemblies between odd and even minor frames (MIFs) as a consequence of the way in which engineering data are acquired.
  - ➳ For the Wide Filters in the GHz Radiometer Module, the solution to this problem was to change the design of the Field Programmable Gate Array (FPGA) controlling the engineering data measurement electronics to eliminate the odd/even power consumption differences.
  - ➳ For the filter spectrometers and digital autocorrelators (DACS) in the Spectrometer Module the solution was to modify the Spectrometer Assembly power distribution, discussed further below. The modified FPGA solution implemented for the Wide Filters would have corrected this problem for these spectrometers too, but would not have addressed some of the other issues described below.

- ❑ GHz relative sideband spectra displayed large, and completely unexpected, channel-to-channel differences when measured on the Flight hardware. This problem was not evident with the Engineering Model hardware.
  - ⇨ These artifacts were traced to inadequate power supply stability at the spectrometer shear-plates, the result of an early design decision to have a centralized power supply feed all spectrometers via a lengthy wiring harness.
    - ➳ The chosen solution to this problem was to add local regulation (6 low dropout regulators on each of the 14 spectrometer shearplates), and raise the output voltages of the supplies feeding the shearplates. This modification also eliminated the odd/even problem discussed in the previous bullet.

- ❑ The 'Blue Sky' test during which the instrument observed the atmosphere at similar high elevation angles via the GHz Antenna and Space port revealed a most unexpected result in the 640 GHz radiometer spectra: the very high atmospheric absorption (due to water vapor) in these bands should have resulted in nearly flat spectral differences between the Limb and Space port data, instead of which we observed that the center 11 channels of each band were offset by ∼0.5 K in calibrated radiance from the surrounding 14 channels of each 25 channel filterbank spectrometer.
  - ⇨ This effect arose because of the changing radiance differences between signals from the Limb and Space ports of many of the other bands in the instrument, and the effect that these signal differences had on power consumption of the spectrometer electronics.
    - ➳ It was these data that conclusively indicated the source of the problem with the relative sideband measurements (previous bullet), and led to the power supply/regulation changes described above.

- ❑ Measurements of T_{sys} varied relatively smoothly from channel to channel in each 25-channel filterbank, except for the center 11 channels which were noticeably offset in value.
  - ⇨ This effect was caused by spectrometer/power supply interactions described in the previous bullet, and eliminated by the power supply modifications.

- ❏ Measured time-series *rms* noise levels for some of the Wide Filter channels in the GHz module were much higher than theory would predict, with abnormally strong $\frac{1}{f}$ artifacts, and not consistent with T_{sys} for these channels.

  - ⇨ This was caused by excess low frequency noise from the subminiature surface mount collector load resistors of the discrete post-detector amplifiers for these channels.

    - ➳ These components were replaced with equivalent, but physically larger components, correcting this performance problem.

- ❏ Initial Flight Model THz sideband measurements displayed large, and unexpected, coupling between the orthogonally polarized receivers, manifesting as large standing waves.

  - ⇨ After some study this was determined to have a clear cause, and could be eliminated by addition of a quarter wave plate at the appropriate point in the optical paths. Herb should rewrite this bullet, and the next.

    - ➳ The quarter wave plate was installed, and the standing waves eliminated.

- ❏ Unexpectedly elevated values of T_{sys} in R1A and R2 measured during radiometric performance verifications were traced to an Engineering Model (EM) dichroic plate being used in the quasi-optical diplexer of the Flight Model instrument.

  - ⇨ This was corrected by removing the EM dichroic and replacing it with the correct unit.

- ❏ Initial FOV patterns measured in R1A indicated an internal alignment problem in the GHz Module.

  - ⇨ The FM dichroic was found to have been installed with one bolt that was too long. This was corrected using the correct length bolt.

- ❏ Measurements of radiances of similar LN_2–cooled targets through the GHz Limb and Space ports indicated small, but unexpected radiance differences for the R1B radiometer.

  - ⇨ These could arise from missalignment (or other problems) in the optics feeding the Switching Mirror, or in the alignment of the Switching Mirror itself.

    - ➳ This effect was traced to an unusually large (and somewhat unexpected) frequency dependence with FOV direction at the receiver horn, documented in the paperwork supplied with the horn. This was determined not to be a performance issue that needed corrective action.

Some of the effects described above were readily observed, while others could easily have been overlooked if extremely thorough analyses of both characterization and calibration data had not been performed. Some of these analyses required intimate knowledge of how the instrument data was going to be used, and past experience with UARS MLS characterization and calibration proved invaluable in this regard.

An important point to note is that complete and thorough performance verifications and calibrations, combined with appropriate in-depth analyses and close scrutiny of the results are vital if subtle, but potentially devastating, performance problems are not to be overlooked. Measurements of parameters such as Y-factor T_{sys} are not a reliable measure of instrument noise, and are merely necessary (but not sufficient) performance indicators. The nature of some of the problems encountered (e.g., spectrometer power supply, and hence signal level, dependencies) would not have been correctable by enhancements to the data processing software if they had been correctly identified after launch. It is also interesting to note that Functional Verification tests (run independently of the calibration activities) were unable to detect any of the subtle instrument performance problems uncovered by analyses of calibration data. We thus propose that future activities of this type forgo independent functional verification activities, and instead make such measurements a component of the calibration task. This should not present much of a burden to the calibration team, and it also affords the opportunity for early testing of key pieces of calibration equipment.

1.4 Requirements

The requirements on instrument performance and calibration are given in [4], and appropriate extracts from this document are presented at the start of the chapters describing Radiometric, Spectral and Field-of-View calibrations.

1.5 Summary of Calibration Accuracy

The large bulk of this 4 volume report makes it difficult to ascertain pre-launch estimates of calibration accuracy. These estimates are provided in Table 1.1 below. The body of this report should be referenced for further information on how these estimates were obtained.

1.6 Calibration Parameters required in Data Processing

Tables 1.2 and 1.3 summarize the calibration data required by Level 1 and 2 data processing software.

1.7 Acknowledgments

The material presented in this report is not the work of the authors alone. Many other people made valuable contributions to the calibration efforts, and we wish to extend special thanks to Vince Perun, Kumar Chandra, Tim Crawford, Karen Lee, Ray Swindlehurst, Chris Tippit and Pim Vosse. We also wish to acknowledge the instrument operations staff who patiently tolerated the many hours of instrument calibration activities, setting instrument operating parameters endlessly without complaint. Many others contributed to the success of this instrument, repairing faulty subsystems, correcting performance problems and stepping in to help when needed. We hesitate to try to list all of their names lest we inadvertantly omit someone. Without the combined efforts of everyone involved we would not have achieved our performance and calibration goals, and we wish to extend our gratitude to all who assisted in this significant undertaking.

Table 1.1: Summary of systematic calibration uncertainties. See the body of this report for further details.

GHz		THz	
Radiometric		*Radiometric*	
Calibration target temperature	0.1%	Calibration target temperature	0.1%
Standing waves	0.1%	Standing waves	0.1%
Switching mirror baffles	0.15%	Switching mirror baffles	N/A
End-to-end linearity	0.1%	End-to-end linearity	0.1%
Total	0.45%	Total	0.35%
Spectral		*Spectral*	
Channel shape and location:	0.3%	Channel shape and location:	0.3%
Relative sideband response		Relative sideband response	
R1 (single sideband system)	N/A		
R2	1%	B15, B18	0.1%
R3	0.5%	B16, B19	0.1%
R4 (see Volume 4 for update)	0.25%	B17, B20	0.1%
Total	0.55 – 1.3%	Total	0.4%
FOV		*FOV*	
To be added by Rick/Paul		To be added by Herb	

Table 1.2: Summary of parameters required by Level 1 software. IRU is the abbreviation for Inertial Reference Unit, a component of the spacecraft attitude determination system.

Symbol	Units	Description	Purpose
B_i	Hz	Noise bandwidth of each filter channel	Radiometric noise determination
τ	s	Integration time	Radiometric noise determination
$S_g(f)$	$\mathrm{W\,Hz^{-\frac{1}{2}}}$	Post detector noise power spectral density for each radiometer	Absolute radiance uncertainties
r'_l, r'_u	–	Relative sideband responses from mixer to switching mirror	Radiometric calibration
ρ_r^k	–	Reflectivity of antenna element k	Antenna emission (radiance) determination
$\eta_{i,s}^{AA}$	–	Antenna beam efficiencies	Limb port to limb radiance conversion
$\eta_{i,s}^{MX}$	–	Baffle transmissions	Radiometric calibration
$\eta_{i,s}^{k}$	–	Optical transmission of antenna reflector k	Radiometric calibration
ϵ_r	–	Calibration target emissivities	Target radiance determination
$\mathrm{d}\alpha$	$\mathrm{K^{-1}}$	Pointing thermal coefficients	Absolute pointing. These coefficients are combined with measured MLS structural temperatures to determine thermal distortions
α, ϵ	$^\circ\,\mathrm{Count^{-1}}$	Encoder coefficients	Conversion of encoder counts to pointing angles
$\mathbf{E}$	–	Rotation matrices from instrument to spacecraft reference cubes	Absolute pointing determination
$\mathbf{D}$	–	Rotation matrix from spacecraft reference cube to IRU reference frame	Absolute pointing determination
$\mathbf{E}^T$, $\mathbf{D}^T$	$\mathrm{K^{-1}}$	Thermal coefficients of $\mathbf{E}$ and $\mathbf{D}$	Absolute pointing. These coefficients are combined with spacecraft thermal data to correct for thermal distortions in spacecraft structure between MLS and the IRU.
$\mathrm{R_0}$	Ω	0 C resistances of individual PRD temperature sensors	Determination of cal target temperatures
$\mathrm{C_l}, \mathrm{C_h}$	Ω, V	Engineering Data Hybrid internal calibration values	Conversion of engineering data 'counts' to engineering units
a, b	–	PRD conversion coefficients	Conversion of PRD resistance into inferred temperature
c, d, e, f	–	Thermistor conversion coefficients	Conversion of thermistor resistance into inferred temperature

Table 1.3: Summary of parameters required by Forward Model (Level 2) software.

Symbol	Units	Description	Purpose
r_l, r_u	–	Relative sideband responses from mixer through entire optical system. See Level 1 ATBD for additional details	Forward Model radiance computations
$F_i(\nu)$	–	Filter channel shapes	Forward Model radiance computations
$G^M_{b,s}$	–	Collapsed (into vertical) FOV shapes	Forward Model radiance computations
ξ_0	$^\circ$	FOV polarization angles	Forward Model radiance computations

Chapter 2

Radiometric Calibration

Requirements:

Radiometric calibration shall be performed and provide the means to convert the output of each instrument channel to the total amount of power received by that channel through the MLS antenna.

The systematic uncertainty (i.e., not including the estimated contributions of random noise) in the absolute value of the atmospheric/Earth radiances measured through each spectral channel shall be less than 3 K (at the 90% confidence level).

The systematic uncertainty (i.e., not including the estimated contributions of random noise) in the spectrally-varying component of the atmospheric/Earth radiances, measured from one channel or filter to another throughout a given radiometer, shall be less than 1% or $\Delta I_{min}/3$, where ΔI_{min} for each spectral region is given in Table 3.2-2.

An extract from Table 3.2-2 of the instrument Science Requirements document [4] is provided in Table 2.1 to indicate the magnitude of ΔI_{min}, and of the maximum allowable noise, ΔI, on a single data integration. These levels are for spectrally-varying noise component of calibrated limb radiances. The total power calibration process, with additional contributions from low frequency noise arising from thermal drifts, and $\frac{1}{f}$ noise arising from gain variations, provide additional spectrally-averaged noise components, budgeted as no more than $4 \times 10^{-4} \times \mathrm{T_{sys}}$ ($2 \times 10^{-3} \times \mathrm{T_{sys}}$ for the THz channels) in each 0.17 s data integration.

2.1 Introduction

The major items in the radiometric calibration error budget are uncertainties in the differences in transmissions through the different ports of the GHz switching mirror enclosure (baffle transmissions), uncertainties in knowledge of internal calibration target temperature, standing waves in the various Switching Mirror views, and overall linearity. Baffle transmissions are discussed in Chapter 4, and engineering data in Chapter 6. The remaining topics are discussed later in this chapter.

The bulk of this chapter is devoted to *characterization* rather than *calibration* simply because this document is the appropriate place to document such measurements and results

Table 2.1: Extract from Table 3.2–2 of Requirements Document summarizing allowable spectrally-varying noise. See text for further details.

radiometer frequency	expected signal intensity (K, SSB)	allowable noise				
		T_{sys} (K, SSB)	spectrally-varying component (K, SSB)			
			ΔI for 0.17 s			
			6 MHz	96 MHz	500 MHz	ΔI_{min}
118 GHz	1–300	1,500	1.5	0.4	0.2	0.1
190 GHz	0.5–300	4,000	4	1		0.1
(B5)	0.4		4	1		0.03
240 GHz	0.2–300	4,000	4	1	0.4	0.1
640 GHz	0.1–200	12,000	12	3		0.1
2.5 THz	0.2–300	30,000	30	8		0.2
(B17, B20)	1–300	90,000	90	25		1

for future reference, and satisfactory instrument radiometric performance is a prerequisite for successful pre-launch and in-flight radiometric calibration. For in-depth descriptions of instrument operation and radiometric calibration, the EOS MLS Level 1 Data Processing Algorithm Theoretical Basis document [2] should be consulted. A brief description of nominal instrument timing is given in the following paragraphs. Tables 1.2 and 1.3 at the end of Chapter 1 list the calibration parameters required by Level 1 and 2 processing. Most of the radiometric calibration parameters in Table 1.2 are FOV-related, and discussed in Chapter 4.

For the remainder of this chapter we discuss the results of end-to-end sensitivity and linearity measurements, as well as some special tests designed to verify radiometric performance. Additional details are provided in Appendix B of Volume 2, together with a discussion of instrument sensitivity.

2.2 Sensitivity and Noise

An important metric for MLS receiver noise is T_{sys}, plotted in Figures 2.1 and 2.2 for all GHz filter channels. The GHz performance data were taken on 3 November 2002, except for Band 12 data which was taken on 2 December 2002 (because the Band 12 filterbank was measuring R1B data on the previous occasion). All performance data in this chapter are double sideband, except those from the 118 GHz radiometers (R1A and R1B), unless explicitly stated otherwise. The whisker-contacted R4 tripler was changed out for a planar one after the data presented here was taken, with significant improvements to T_{sys} and minor changes to relative sideband response. These performance changes are described in Volume 4.

T_{sys} in conjunction with the Radiometer Equation provides an indication of the lower limit of noise achievable from a given measurement channel, but does not account for the effects of gain variations, noise added by the total-power radiometric calibration process, or such potentially performance-degrading characteristics as $\frac{1}{f}$ noise. Actual sensitivity depends upon measurement 'mode,' and is dependent on radiometric calibration timing details as described in [2]. In order for the data presented here to provide a good indication of the

expected in-flight performance we chose to operate the GHz portion instrument with a flight-like switching sequence (i.e., standard MAF duration of 24.7 s), viewing an LN_2-cooled target through the Space port for ∼3 s every MAF, the rest of the time being spent viewing the internal ambient target. Level 1 processing was then instructed to treat the LN_2 views as Target data with 80 K scene temperature, and 74 of the internal ambient target views in each MAF as 'Limb' data. The remaining ambient target views (∼50 per MAF) were treated as 'Space Reference' views by Level 1 processing, but with a fixed temperature corresponding to the actual target temperature at the beginning of the data acquisition period. This method of data processing provides noise levels representative of what we expect to see in flight for ambient calibration target data, with slightly lower noise levels expected for in-flight limb data due to the lower scene temperature (compared to the one being observed in this test). The HVAC system operation during instrument calibrations induced temperature cycling in the instrument electronics similar in magnitude to that predicted in orbit, and with similar derivatives. By forcing the reference views to be to a fixed temperature during data processing, the limb radiances are constrained to be at the equivalent Planck temperature, but exhibit realistic noise behavior.

Figures 2.3 to 2.6 show the results of noise measurements for R1A (the primary 118 GHz receiver) determined as described above. The upper panel of Figure 2.3 shows the measured *rms* noise from an ∼12 hour data set for each channel of Band 1 for the MIFs processed as 'Limb' data. These data are presented by MIF in order to reveal any MIF–dependent systematics that can arise for such reasons as systematic variations in RIU software activities throughout the MAF[1].

In the upper panel of Figure 2.4 the data for each channel have been processed to indicate the measured *rms* noise for each spectrometer channel. Departures from the Radiometer Equation noise predictions are clearly visible in the outermost channels, which exhibit time-series noise levels greater than one quarter of the observed value in the centermost channel. Note that the noise levels of the outer three 96 MHz channels of the filterbank group together, as do the levels of the next three 64 MHz wide channels, an indicator of stable, consistent and predictable performance. The lower panel of this figure shows the mean values of the measured 'limb minus space' radiances, the vertical bars indicating the measured *rms* divided by the square root of the number of 'limb' measurements in the data set, indicating how the random noise can be expected to integrate down. Each data point in this panel contains 263.5 s of 'limb' data, and the indicated noise levels are consistent with expectations.

Figure 2.5 contains 3 panels showing the measured *rms* noise on the *difference* between individual MIF calibrated radiances for different channels in the same radiometer. The upper two panels are for differences between the outermost channels, and between an outer and center channel in a spectrometer. The third panel indicates the same data for the difference between two 96 MHz wide filter channels in filterbank spectrometers of the R1A and R1B (i.e., different radiometers). For all other radiometers this panel shows the noise for the difference between two channels in different bands of the same radiometer. These data are intended to show that low-frequency noise and drift effects are sufficiently small that channel difference data are not compromised by unexpected systematic effects, and that a high degree of correlation exists in the spectrally-averaged noise across the IF passband of any given radiometer. The plot in Figure 2.5 clearly shows that the low frequency noise

[1]Each RIU processor executes a relatively fixed set of actions that are triggered on a MIF-by-MIF basis, this cycle repeating in every MAF.

in R1A and R1B are **not** well correlated between receivers, making this plot unique among those presented for the remaining bands (shown in Appendix B).

Figure 2.6 shows the mean values of the radiance differences for the channel selections in the previous plot, the vertical bars indicating the observed *rms* noise divided by the square root of the number of measurements. These data showed strong odd/even difference artifacts prior to the spectrometer power supply modifications mentioned in the first chapter of this document, and were instrumental in identifying the source of this particular problem. The final panel of this figure is a histogram derived from the data in the upper left panel, and prior to the spectrometer power supply modifications showed a strong bimodal distribution, rather than the approximately Gaussian one displayed here.

Similar plots are presented for all GHz filter channels in Appendix B (Volume 2). The plots for the 11 channel mid-band filterbanks and individual Wide Filters do not include the histogram panel described in the previous paragraph.

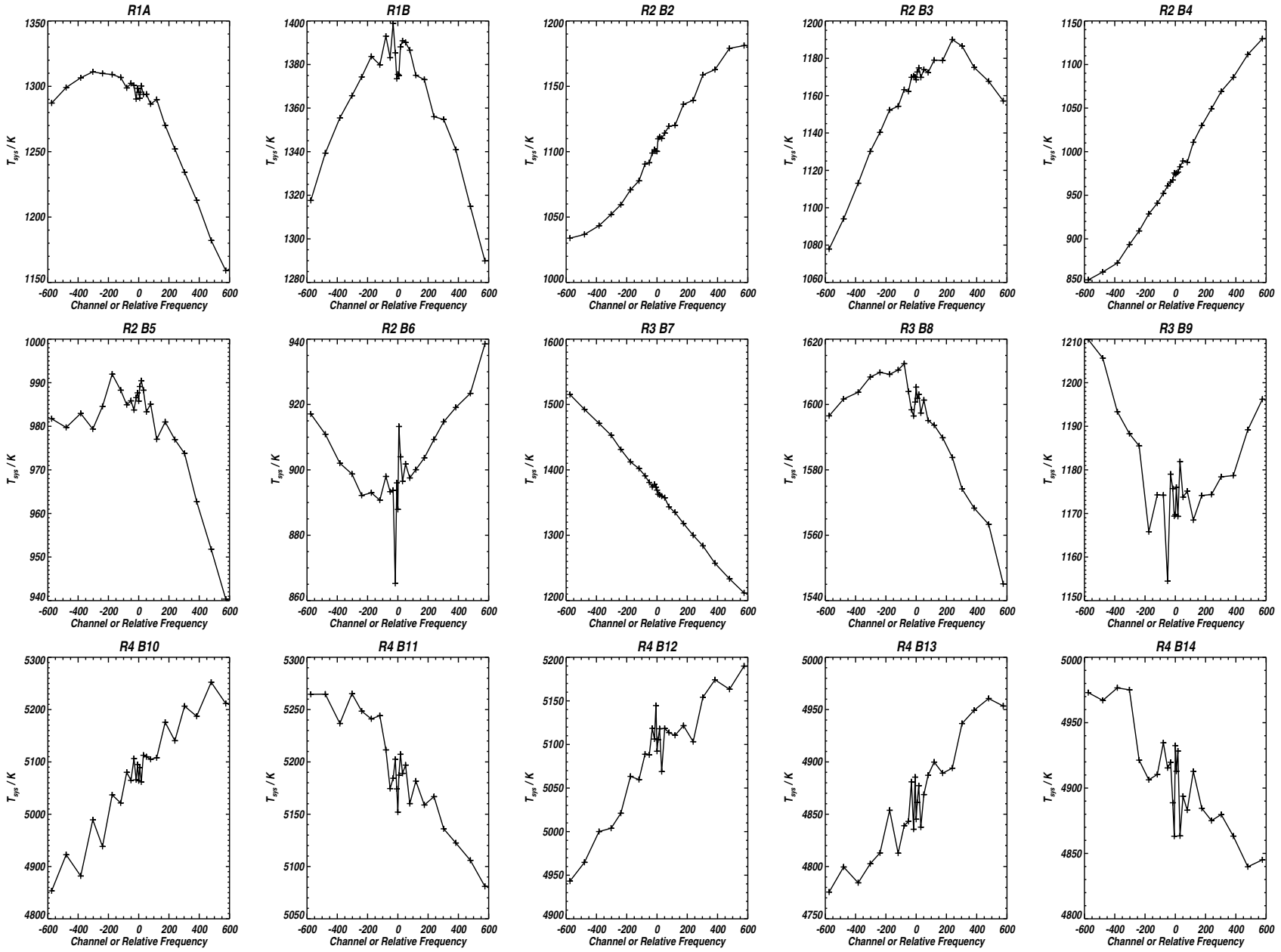

Figure 2.1: Plots of T_{sys} for all GHz 25-channel filterbank bands. X-axes indicate channel position *wrt* band center in MHz. All data are double sideband, except for R1A and R1B. Data for R4 (bands 10 to 14) are for the whisker-contacted tripler configuration, not the flight planar tripler.

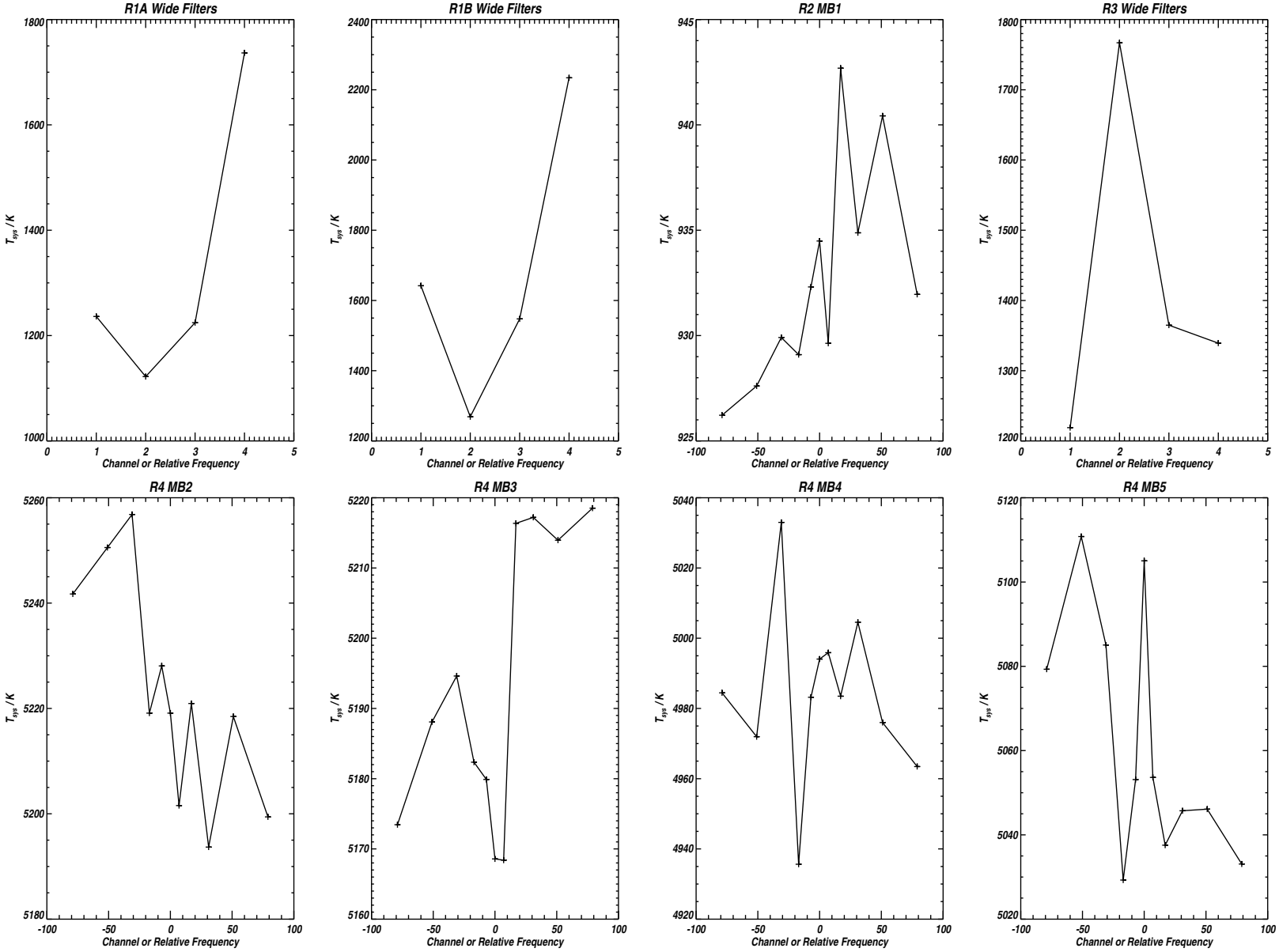

Figure 2.2: Plots of T_{sys} for all GHz Wide Filter and 11-channel filterbank bands. X-axes indicate channel number for Wide Filters, and position *wrt* band center in MHz for 11-channel filterbanks. All data are double sideband, except for R1A and R1B Wide Filters. Data for the R4 bands are for the whisker-contacted tripler configuration, not the flight planar tripler.

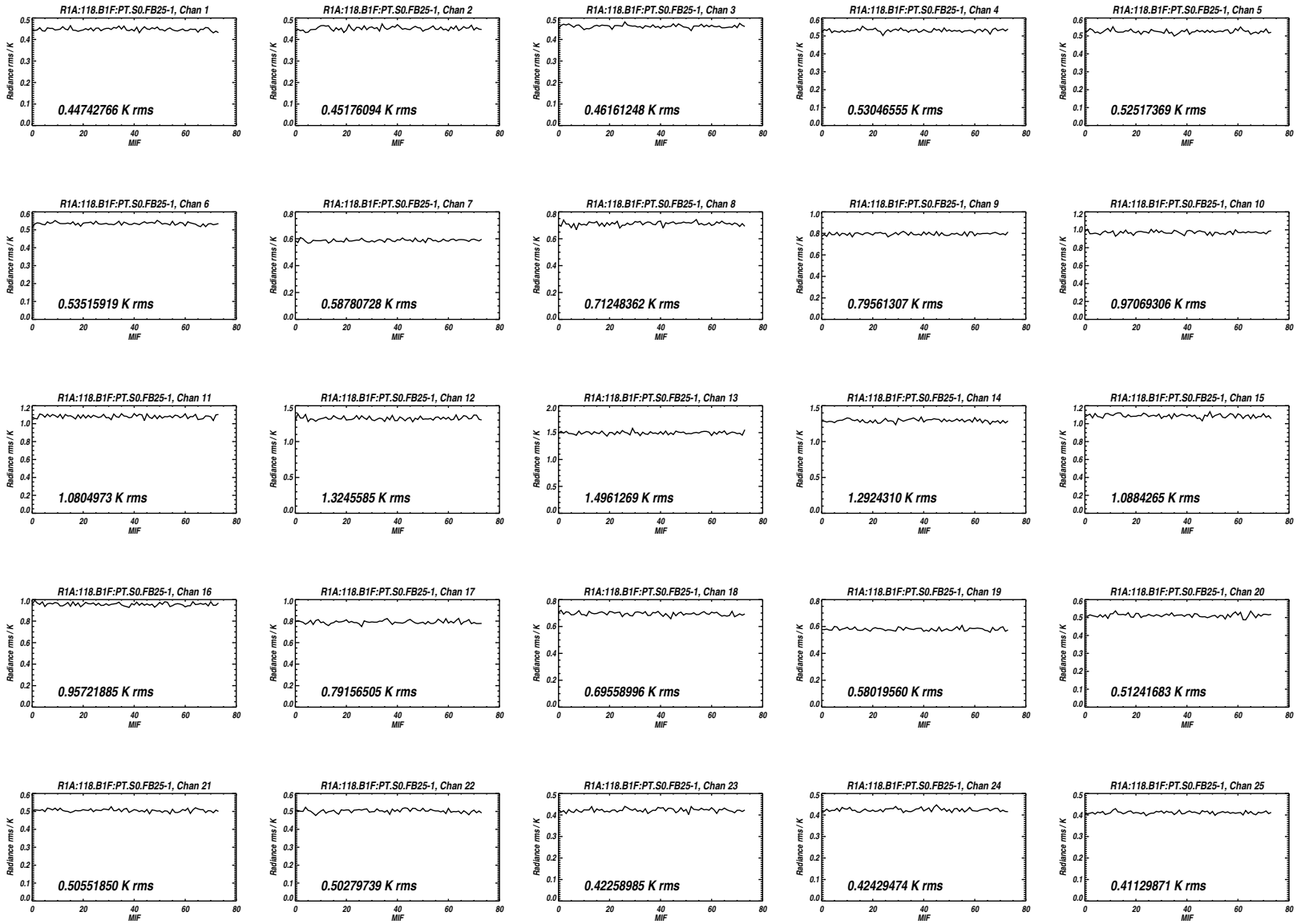

Figure 2.3: Measured *rms* noise for all 25 channels of Band 1 for the MIFs treated as Limb views in Level 1 processing.

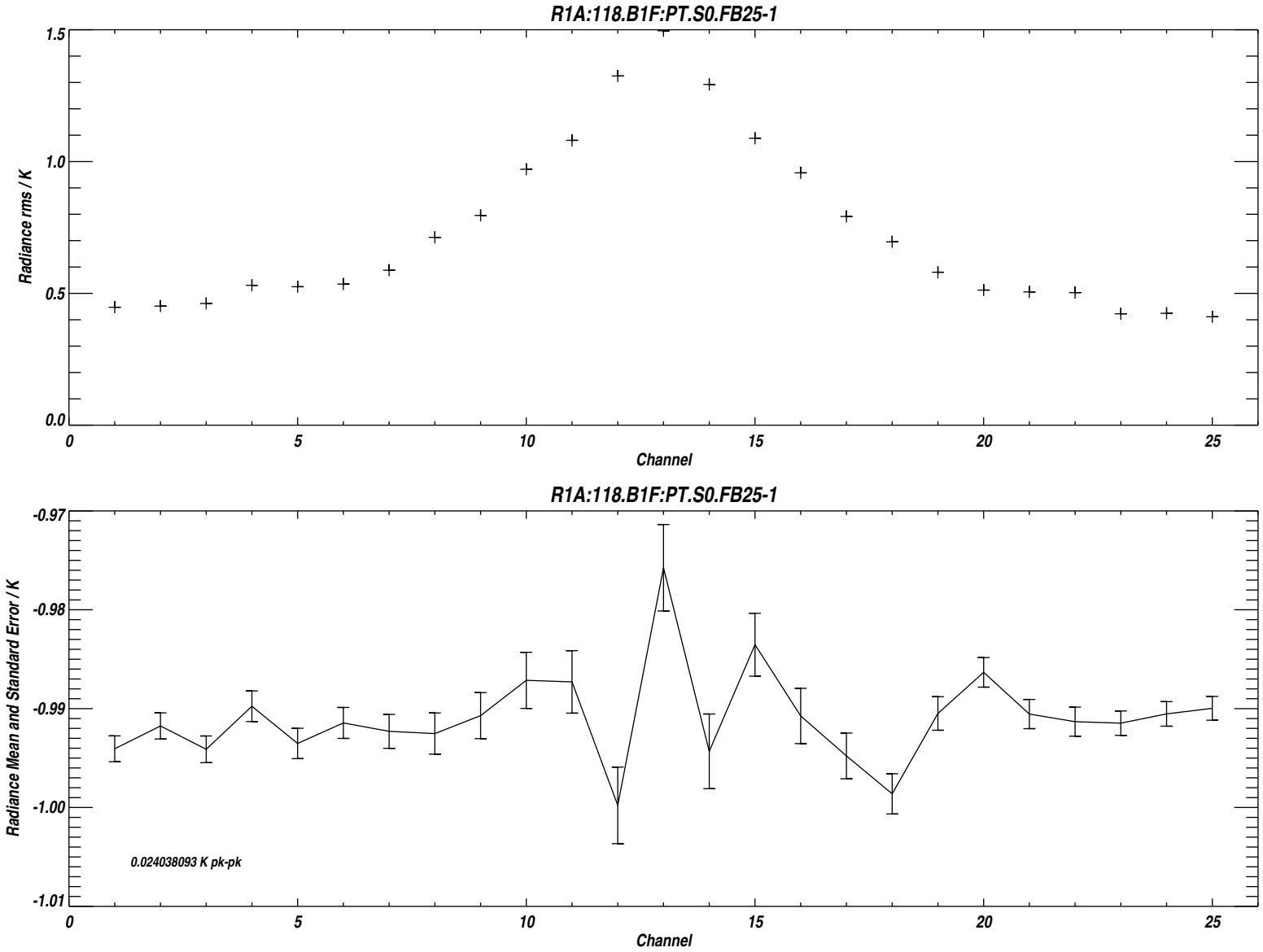

Figure 2.4: Measured *rms* noise for each channel of Band 1 (upper panel). The lower panel plots the difference between the mean 'Limb' and reference radiances, the vertical bars indicating the *rms* uncertainty due to noise.

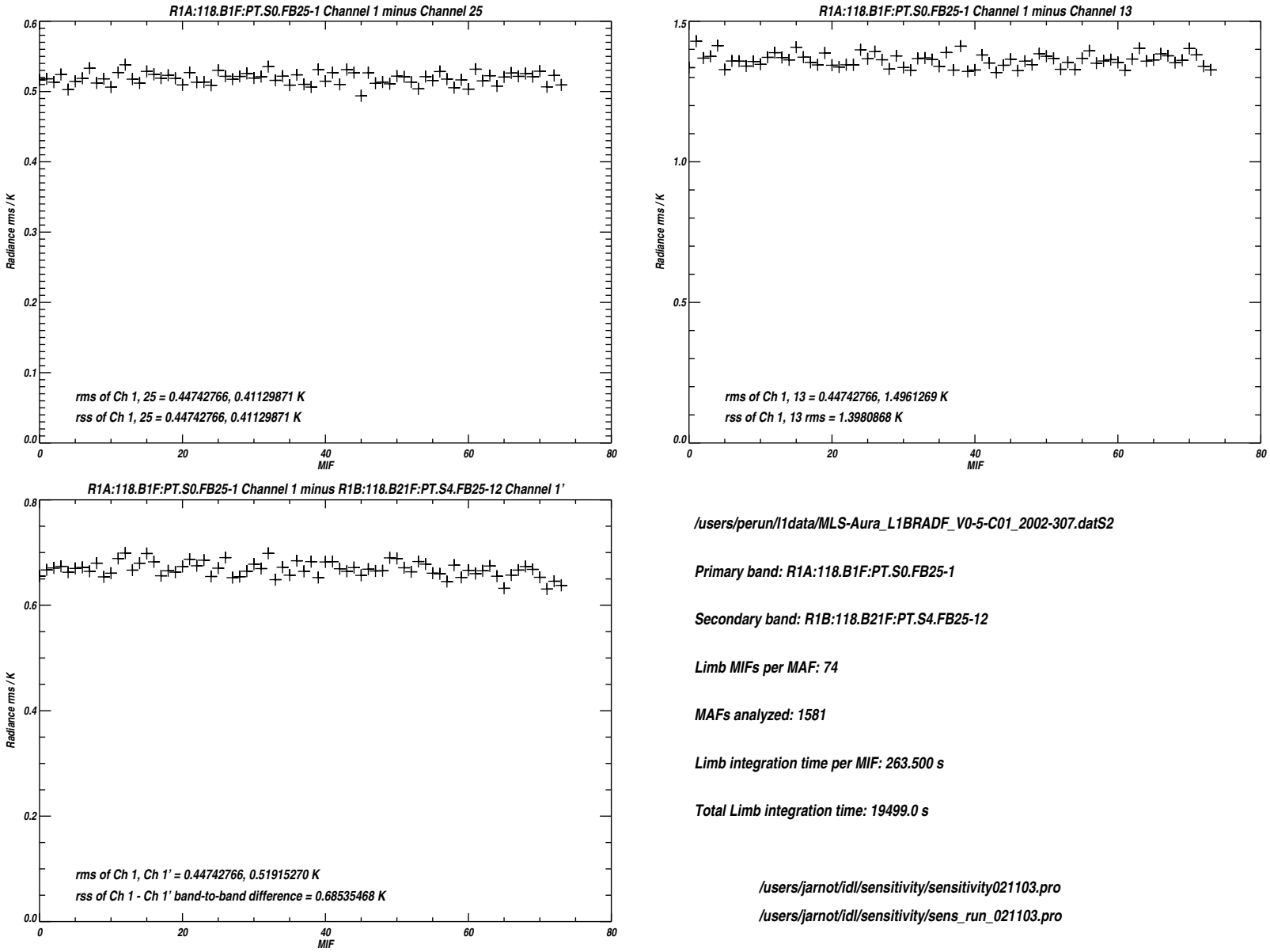

Figure 2.5: Measured *rms* noise on the radiance differences between Channels 1 and 25 of B1, Channels 1 and 13 of B1 (upper right panel), and between Channel 1 of B1 and Channel 1 of Band 21 (R1B).

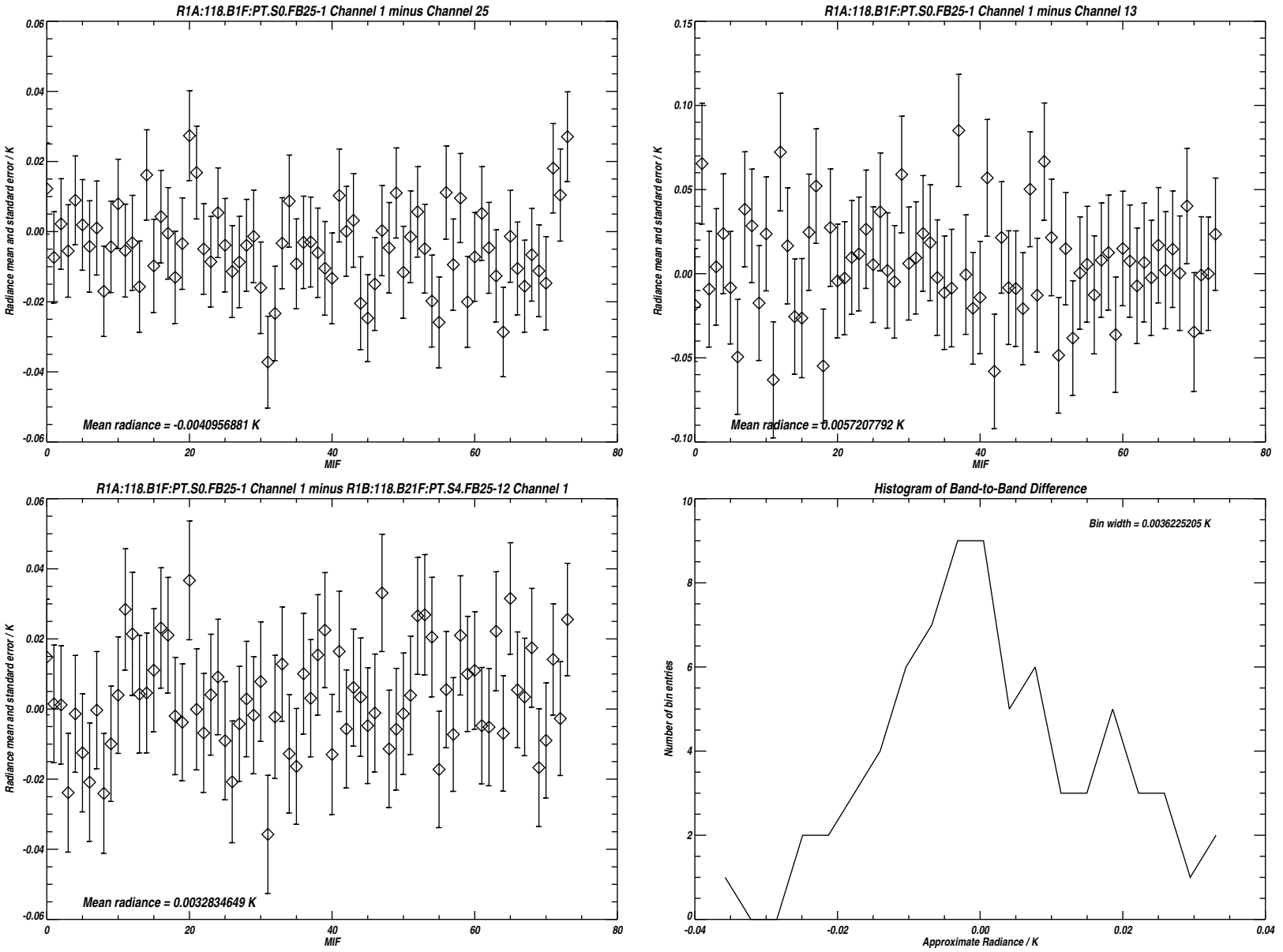

Figure 2.6: Radiance differences between the 3 channel pairs plotted in Figure 2.5. The vertical bars indicating the *rms* uncertainty due to noise. The lower right hand panel is a histogram of the data in the panel to its left. See text for additional details.

2.2.1 GHz Sensitivity Data

Several sensitivity data sets were taken during the course of instrument Integration and Test, with similar results. There are however certain features common to all of these data sets:

(1) Sensitivity requirements (based on noise levels measured during these characterizations) are met in all channels, with the sole exception of spectrally-varying noise in the difference between the outer 2 Wide Filter channels in R3 (Band 34), which exceeds requirements by a factor of two. The observed noise level is still less than that in the 96 MHz channels of other spectrometers in this radiometers, and this minor performance deficiency has been waived[2].

(2) The MMIC R1A and R1B radiometers exhibit substantially higher levels of $\frac{1}{f}$ noise than the receivers implemented with Schottky diode mixers. R1B, which is a reworked Engineering Model unit, is noticeably worse than R1A in this regard. This effect is easily observed by computing the noise level on the difference between 2 channels in the same radiometer, and comparing this to the noise level predicted by computing the *rss* of the noise levels measured on the individual channel time series data[3]. Measurements which contain significant $\frac{1}{f}$ noise have a substantial component of noise in each channel which is correlated to that in the other channels of the same radiometer, and the observed noise on a channel-to-channel difference is significantly lower than that predicted from the *rss* of the individual noise on each channel. It should be noted that even for the Bands with the largest $\frac{1}{f}$ noise (R1A and R1B), the noise levels observed in the center channels of the 25-channel filterbanks are consistent with simple predictions from the radiometer equation.

(3) MIF-dependent offsets are evident in the channel difference data for the R1B Wide Filters (Band 34). The magnitude of these systematic errors is substantially less than the noise on an individual measurement, and not considered to be either a problem or a performance limitation. The effect of these residual patterns can be eliminated by running some simple in-orbit tests to characterize them in their true operating environment, and applying the appropriate corrections at Level 1. Because of their small magnitude, no such corrections are currently planned[4].

Even though it is not clear why the R1B Wide Filters exhibit this phenomenon to a larger degree than any other set of channels, the source of the offsets is understood. RIU power consumption varies with MIF due to software driven activities (such as engineering data collection) that vary from MIF to MIF. For a given operating mode of the RIU, these activities repeat consistently from MIF to MIF during consecutive MAFs. The small changes in power consumption that arise are sufficient to vary the power supply voltages for the Wide Filter electronics enough to give rise to the observed small systematic offsets.

(4) The measured *rms* noise in Channel 22 of some 25-channel filterbank bands (especially noticeable in Band 4) is slightly higher than that of the neighboring channels

[2]Band 34 spectrally-varying noise requirements met with the instrument in orbit – see Vol 4 of this report.

[3]In other words, by separating the spectrally-varying and spectrally-averaged noise components.

[4]After instrument delivery to NGST, the FPGA design for the RIUs in question was changed, and rework performed, to eliminate this problem.

with similar bandwidth, but performance still meets requirements. This slightly elevated noise arises from interference generated by an internal instrument oscillator, and should have no significant impact on overall instrument performance in the affected bands.

(5) The measured noise levels on differences between the outputs of 2 filter channels in a given radiometer (even from bands at opposite extremes of the IF range of a given radiometer) are at the expected levels, indicating a high degree of correlation for spectrally-averaged noise across the entire frequency spans of all IF bands.

The spectrally-varying and spectrally-averaged noise performance for all GHz bands are summarized in Tables 2.2 and 2.3 below. All requirements that are met are presented in green, and the sole requirement not met, as previously discussed, is presented in red. The following points should be kept in mind when reviewing the radiometric performance data presented in this report:

- ❏ The noise levels indicated above are dependent upon the Instrument Calibration sequence and Calibration Algorithms.
- ❏ These results were derived using nominal switching sequences and algorithms with a Calibration Window of 6 MAFs. Increasing the Calibration Window size beyond this value will have negligible impact on measured noise.

2.3 GHz Linearity Measurements

Linearity measurements performed on the MLS GHz radiometers were intended to verify that performance requirements were being met, not to determine any calibration parameters to be used in data processing. It is possible that in-orbit data may be used to provide additional data in this area, resulting in future modifications to Level 1 algorithms. There are three aspects to linearity:

(1) *Integral linearity:* This is sometimes called *low-order linearity*, and is the 'curvature' in the variation of calibrated radiance with signal power in a channel.

Table 2.2: Summary of Spectrally-Varying Noise performance for the GHz radiometers.

Spectrally-Varying Allowable Noise Requirements:					Results:			
	T_{sys}	$\Delta I_{6\,MHz}$	$\Delta I_{96\,MHz}$	ΔI_{min}	T_{sys}	$\Delta I_{6\,MHz}$	$\Delta I_{96\,MHz}$	ΔI_{min}
R1A	1500 K	1.5 K	0.4 K	0.1 K	<1400 K	1.5 K	0.38 K	0.1 K
R2	4000 K	4 K	1 K	0.1 K	<3000 K	3.2 K	0.9 K	0.015 K
R2B5	4000 K	4 K	1 K	0.03 K	<2500 K	3 K	0.8 K	0.015 K
R3	4000 K	4 K	1 K	0.1 K	<3900 K	4 K	1 K	0.05 K
R3WF	4000 K	ΔI_{500} = 0.4 K		0.1 K	<4000 K	ΔI_{500} = 0.8 K		0.03 K
R4	12000 K	12 K	3 K	0.1 K	<11000 K	10 K	3 K	0.05 K

Table 2.3: Summary of Spectrally-Averaged Noise performance for the GHz radiometers.

Requirements for Spectrally-Averaged Noise:	Results:
The allowable 1σ noise in the spectrally-averaged component of the radiance from each radiometer (ssb, after calibration, average value over all channels of the radiometer) measured in an individual 0.17 s integration period is $4\times10^{-4}\times T_{sys}$ *for all GHz radiometers.*	R1A: 1.9E-4 $\times T_{sys}$ R1B: similar to R1A R2:1.2 – 1.6E-4$\times T_{sys}$ R3: 0.9 – 2.4E-4 $\times T_{sys}$ R4: 2.2E-4 $\times T_{sys}$

Ideally the relationship between signal power into a spectrometer channel, and its digitized output, should be completely linear.

(2) *Mid-order linearity:* This effect describes the channel-to-channel differences in calibrated radiance as a spectrally flat scene signal 'brightness' traverses between radiometric calibration points. Differences in the detailed form of integral linearity between channels give rise to such effects, as do systematic variations in overall integral linearity as a function of the scene being observed.

(3) *Differential linearity:* This is sometimes called *high-order linearity.* Whereas integral linearity is concerned with the overall shape of a channel transfer function, differential linearity describes the systematic variations in input signal spans of the digitizer output codes.

Differential linearity is purely a function of the properties of the filterbank digitizers, and for EOS MLS the digitizers were implemented so that the input signal spans of the digitizer output codes smoothly varied from code-to-code, changing only by the order of the channel integral linearity over the full input signal range. Because of the sizable T_{sys} of all EOS MLS receivers compared to the range of observed scene radiances, only restricted portions of the dynamic range of the signal chains and digitizers are exercised, and differential linearity may be safely ignored for this instrument.

Integral linearity, and to a lesser extent mid-order linearity, were measured using the test setup shown in Figure 2.7. This figure emphasizes the high resolution front-end sweeper setup, but also shows the UARS external Hot Target which was used as the temperature-varying scene. This target consists of a flight-like corrugated wedge absorber with aluminum backing, distributed heater resistors, and embedded PRD temperature monitors. An external controller allowed precise remote control of the temperature of the target from room temperature to beyond 100 C, with temperature monitoring provided on the controller front panel. Small temperature gradients across the surface of the target (when heated) were observed with an infra-red camera, and reduced to acceptable levels by placing additional thermal insulating material between the absorber backing plates and the exterior housing. The observed gradients in this configuration were small, and mainly isolated to the edges of

the absorber plates. For these measurements care was taken with alignment to ensure that the radiometer beams intercepted the heated target centrally, in the region with negligible temperature gradients (estimated to be substantially less than 1 K). Mirrors LSC1 and LSC2 focused the radiometer beams to small diameters compared to the elliptical entrance aperture of the target. Although this target was intended for test the UARS instrument over a ∼60 – 210 GHz range, it was found to perform very well up to the ∼660 GHz upper limit of the EOS GHz receivers.

For these measurements mirror SW1 moved the GHz Space Port view between the heated UARS and LN_2-cooled targets, and the internal GHz Switching Mirror provided switching between an internal GHz ambient target and mirror SW1. The GHz ambient target provided a reference view (corresponding to Space in normal instrument operation), and the view to the LN_2-cooled target provided the periodic radiometric gain reference. A time series of data for 1 MAF using this setup is shown in Figure 2.8 for a 96 MHz wide channel from each of the GHz radiometers. The first segment of the MAF is spent observing the internal ambient target, serving as the radiance reference for Level 1 processing. The next segment is spent observing the external UARS Hot Target (Level 1 Limb view), and the final segment observes the LN_2-cooled target (nominal Level 1 target reference view). After processing by Level 1 software, the Hot Target views are converted into radiances for further analysis. The entire measurement sequence consisted of repeats of that shown in Figure 2.8 with the UARS external Hot Target set to plateaus at ambient, 40, 55, 70, 85 and 100 C for approximately 20 minutes each. Synchronization of SW1 movements with internal instrument operation was accomplished using the control units described in Appendix F.

The raw data from an entire linearity measurement run is shown in Figure 2.9. Note the large temperature dependence of the 118 GHz MMIC receiver data compared to that from Bands 2 and 7. The data from Band 14 also shows substantial temperature dependence compared to Bands 2 and 7, but that is because of the relatively low radiometric gain (Counts per Kelvin) for the R4 radiometers compared to the others. This also results in the larger noise levels clearly evident in the data for Band 14.

Figure 2.10 presents the same data after processing by Level 1 software to convert the heated target views into calibrated radiances. Note the complete removal of artifacts due to signal chain temperature dependencies. Also of interest are the small 'wiggles' in Band 1 radiances, particularly at the higher target temperatures. These arise from small ringing in the target temperature controller electronics, and are most evident in the Band 1 data because of increased the skin depth at the lowest measurement frequencies. A similar effect was noted when this target was used for UARS MLS characterizations.

Several linearity data sets were taken during fabrication of the MLS instrument, using various external hot targets, in both cart and NFR configurations. The data presented here were taken on 21 November 2002, with Band 12 data taken on 2 December 2002 (since the IF Switch Network was configured to support THz activities via filterbank 12 on the first occasion). All of the GHz linearity data presented in this document were taken in the NFR configuration using the UARS hot target.

2.4 Data Analysis

The initial step in analyzing the data consisted of using Level 1 software to convert the UARS Hot Target view data into radiances as discussed above. This processing step converted all

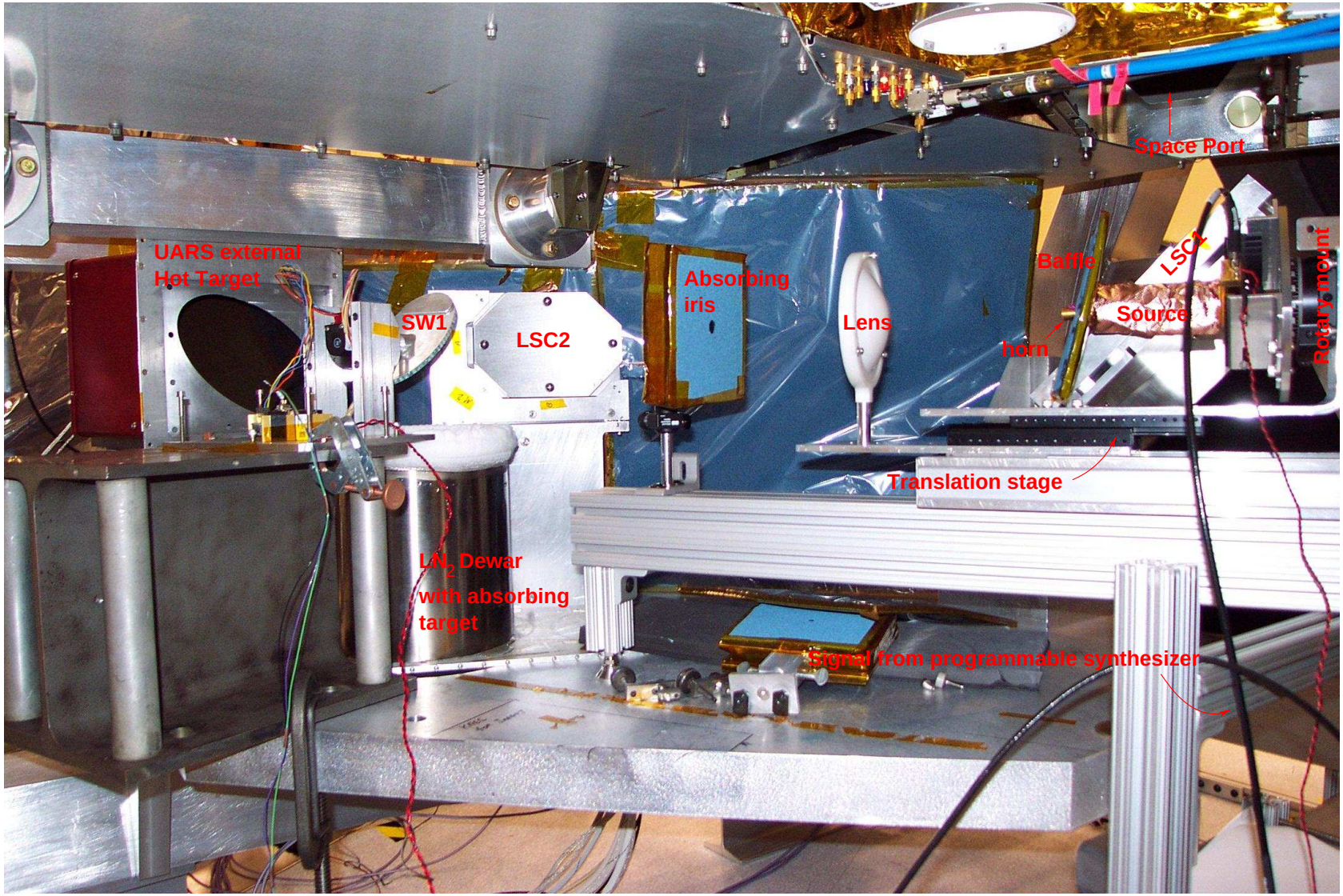

Figure 2.7: Linearity measurement apparatus in the NFR configuration. See text for additional details.

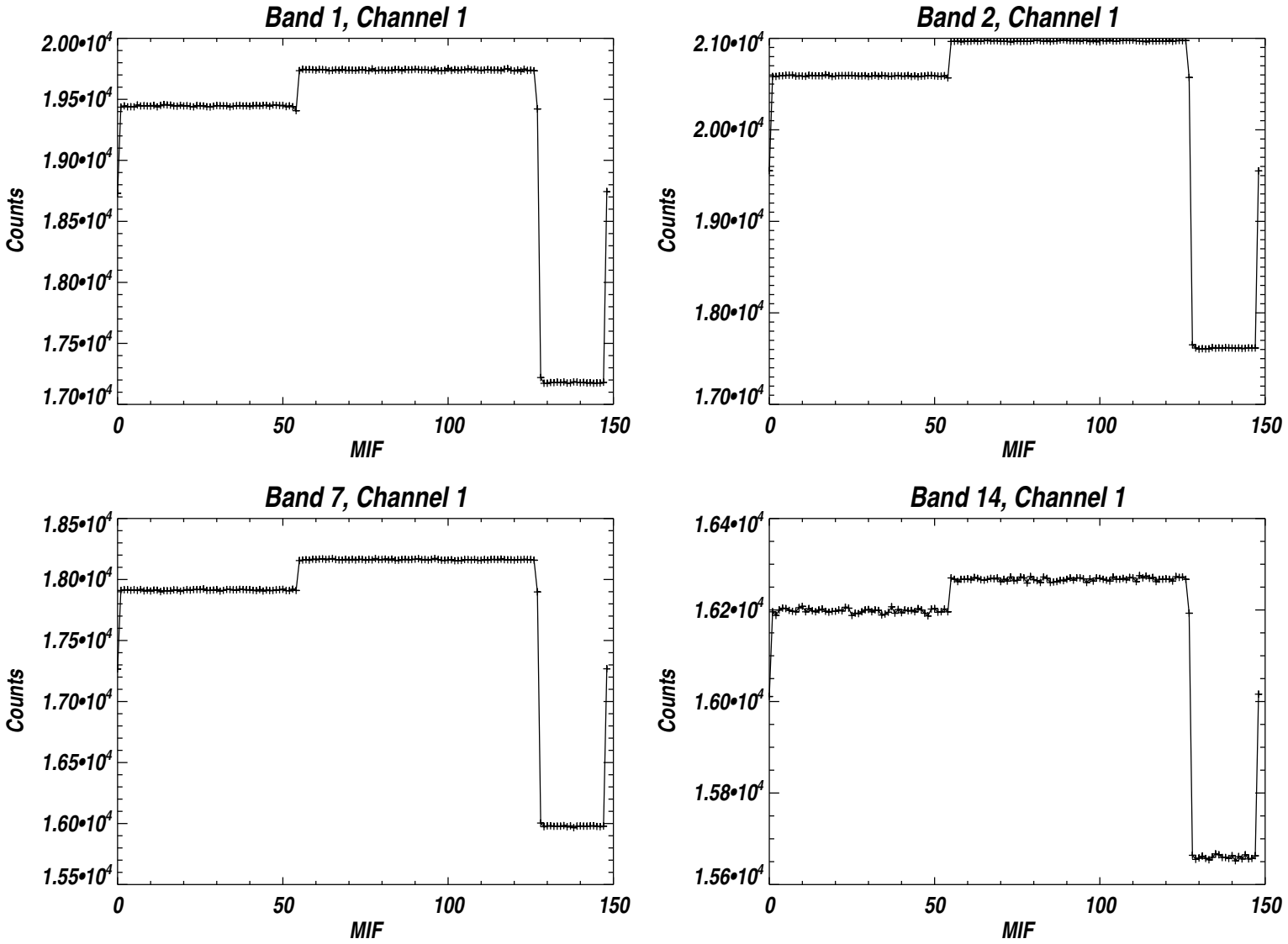

Figure 2.8: Linearity data taken with the setup shown in Figure 2.7. These raw data are time series from a single MAF for 96 MHz filter channels from each of the GHz radiometers. The three views to internal ambient, external heated, and external LN_2 targets are clearly visible.

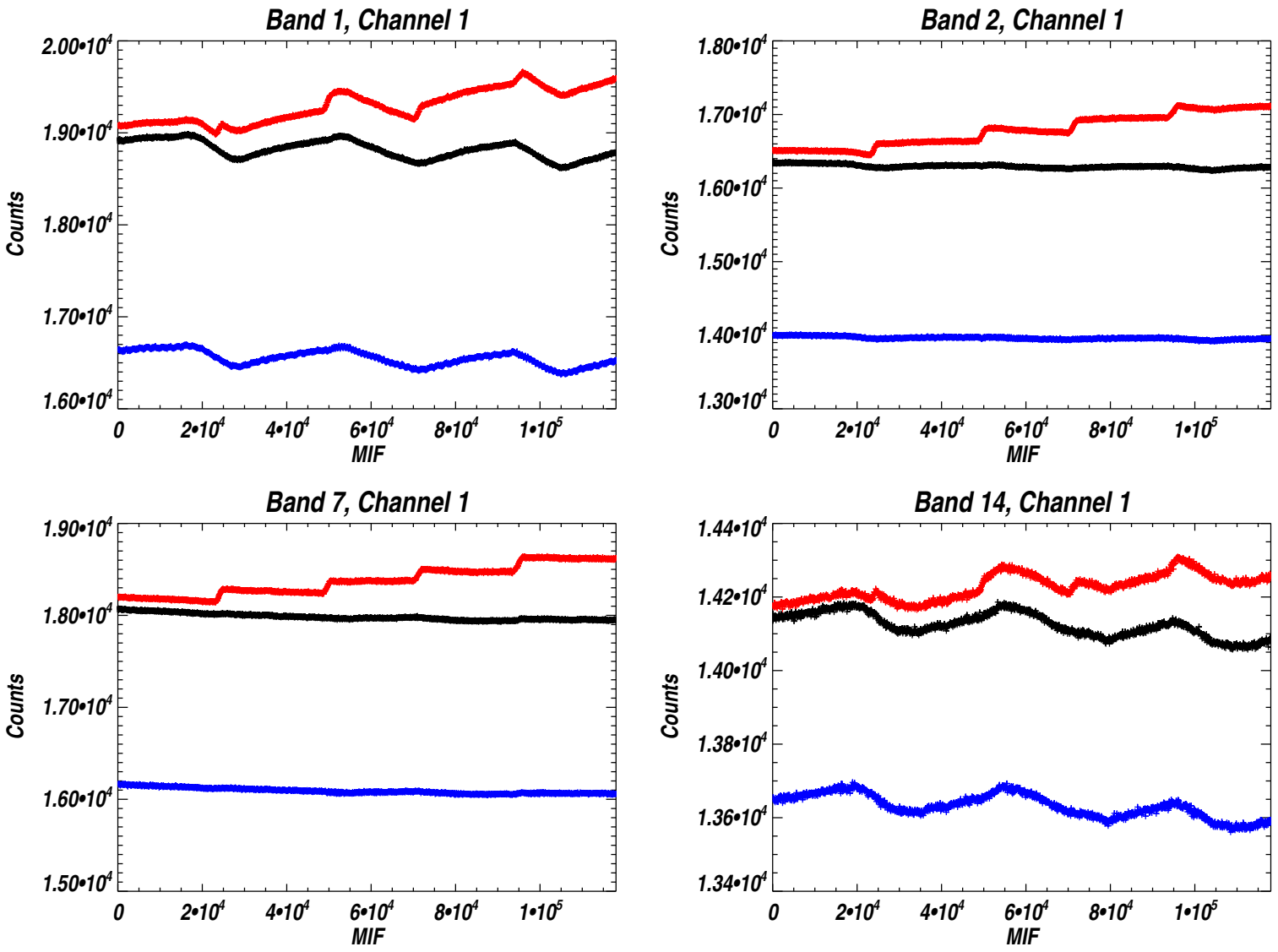

Figure 2.9: Raw data for the entire linearity measurement sequence. The black measurements are views to the internal GHz ambient target, the red measurements are of the external heated target, and the blue measurements are views to the external LN_2 target. The effects of variations in room temperature are clearly visible in the data for Bands 1 and 14.

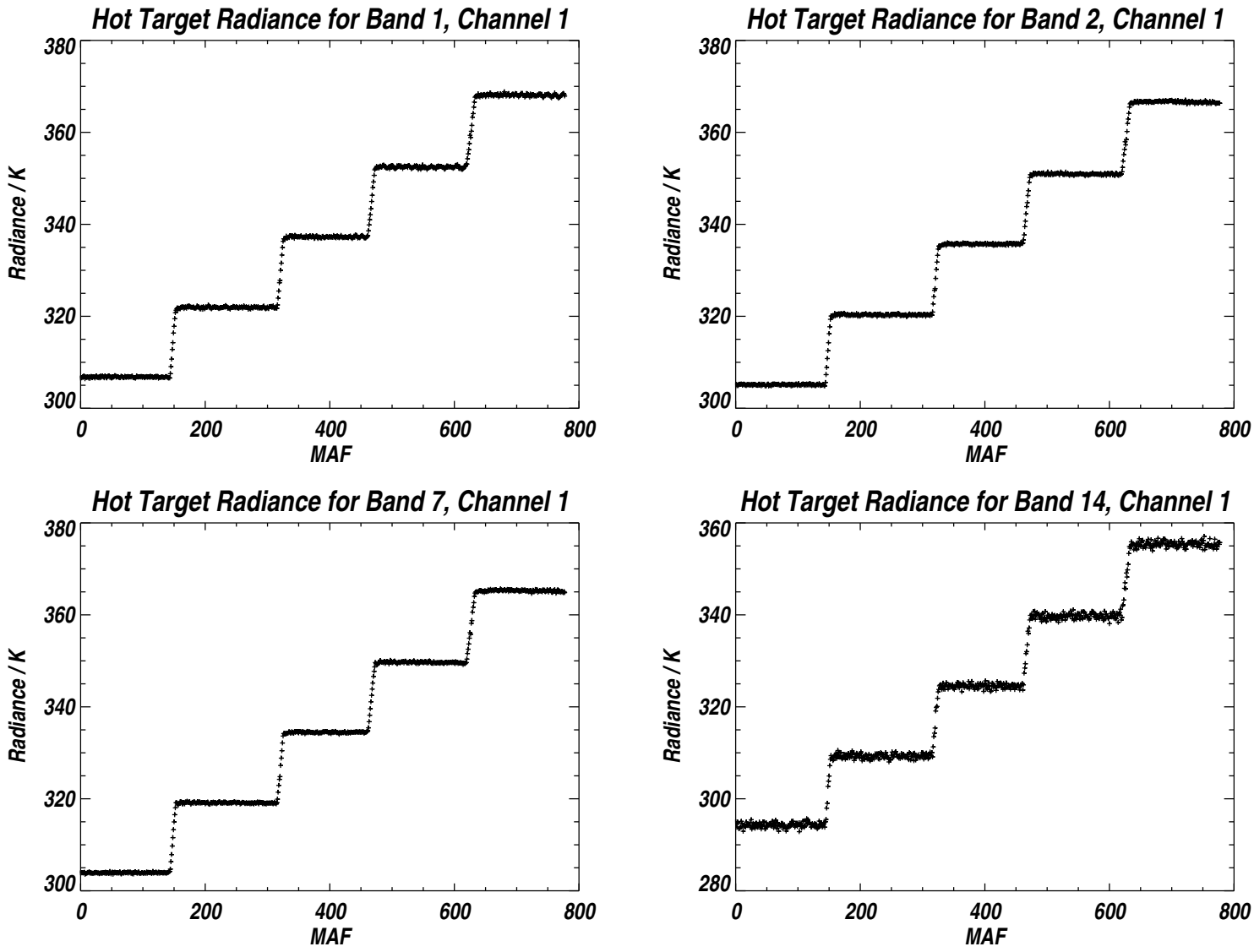

Figure 2.10: Level 1 radiances for the Hot Target viewing periods of the data in the previous figure. Notice the complete removal of artifacts due to variations in room temperature.

scene views to 'brightness temperatures' for easy interpretation, while accounting for gain and reference drifts during the course of the measurements.

The Level 1 radiances were analyzed further to verify adequate mid-order and integral linearity performance, and the results from R1A are discussed below. The data from all bands were analyzed in the same way, and the full linearity data set is presented in Appendix B of Volume 2. The standard linearity analysis produces three plots, described below.

2.4.1 Discussion of Linearity Data

The range of external radiances measured during the tests just discussed (∼70 K) is substantially lower than the ∼300 K range expected from atmospheric signals, but nonetheless sufficient to provide a useful indication of both integral and mid-order nonlinearity[5]. Linearity data sets were taken on several occasions, with consistent results. There are several points of note in the full data set that is presented in Appendix B:

(1) All bands/channels have the same slope for measured radiance plotted against target temperature, but the measured radiances are different for each radiometer, as expected, since they correspond to the brightness temperature of the target as determined by the Planck function.

(2) Overall integral linearity (the variation of signal DN with scene radiance) is excellent for all channels and bands.

(3) All bands exhibit measurable standing waves in this test setup which are largest for the band with highest beam truncation (R1B, Band 21). The standing waves reduce in magnitude as frequency increases, then increase again for the highest frequency GHz radiometers (in R4). This is not unexpected, since the external heated target was originally designed for use to frequencies up to ∼200 GHz. Other measurements (e.g., the Dual Cold-Load test) indicate that the artifacts observed here arise predominantly from the test setup, not the instrument.

(4) All three sets of Wide Filter channels exhibit measurable mid-order nonlinearity. The R1A Wide Filter (Band 32) data contain one measurement set (40 C target temperature, plotted in blue) that are clearly erroneous, for unknown reasons. Other Band 32 linearity data sets did not exhibit this behavior. R1B Wide Filter data (Band 34) shows a distinct band shape change of ∼0.8 K over the scene temperature range of ∼75 C, with most of the nonlinearity in Channel 1. Other data sets for Band 32 indicate very similar behavior to that shown for Band 34.

The Wide Filters in R3 (Band 33) show a distinct band shape change of ∼0.1 K over the scene temperature range of ∼75 C, but with more complex behavior that that exhibited in the R1 Wide Filters – channels 1 and 3 being grouped together, as are channels 2 and 4.

Extrapolating these observations to cover the full range of observed atmospheric brightnesses, we should not be surprised to observe systematic errors of ∼1.5 K in R1 Wide Filters and ∼0.2 K in R3 Wide Filters at mid-range atmospheric brightness temperatures around 150 K.

[5]In-orbit tests extend this range to cover ∼50% of the measurement dynamic range with no additional indications of non-linearity.

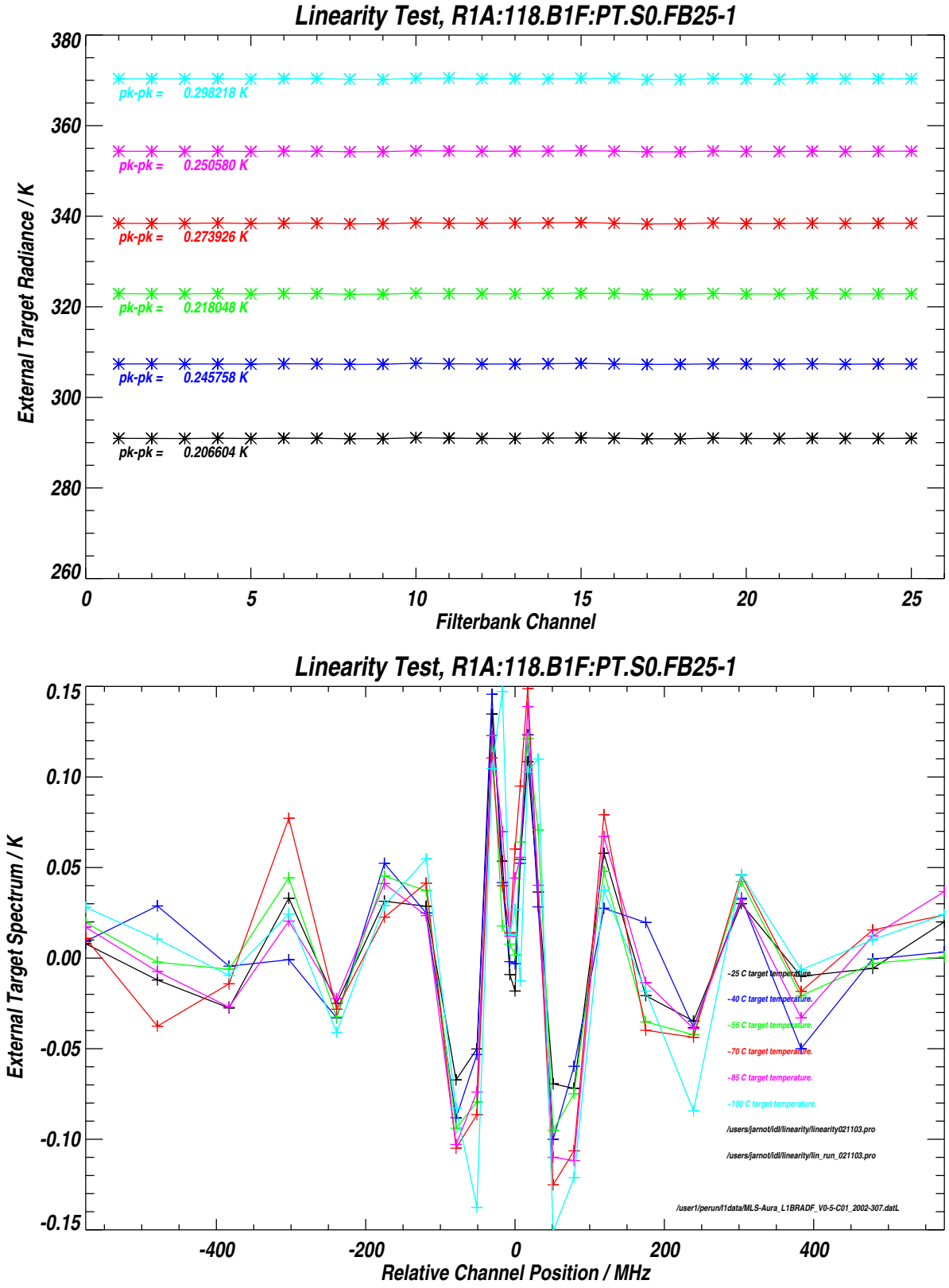

Figure 2.11: Hot Target Radiances for all 25 channels of Band 1 for 6 different target temperatures. The lower panel shows the data from the upper panel with the weighted mean radiance subtracted from each measurement group. See text for additional details.

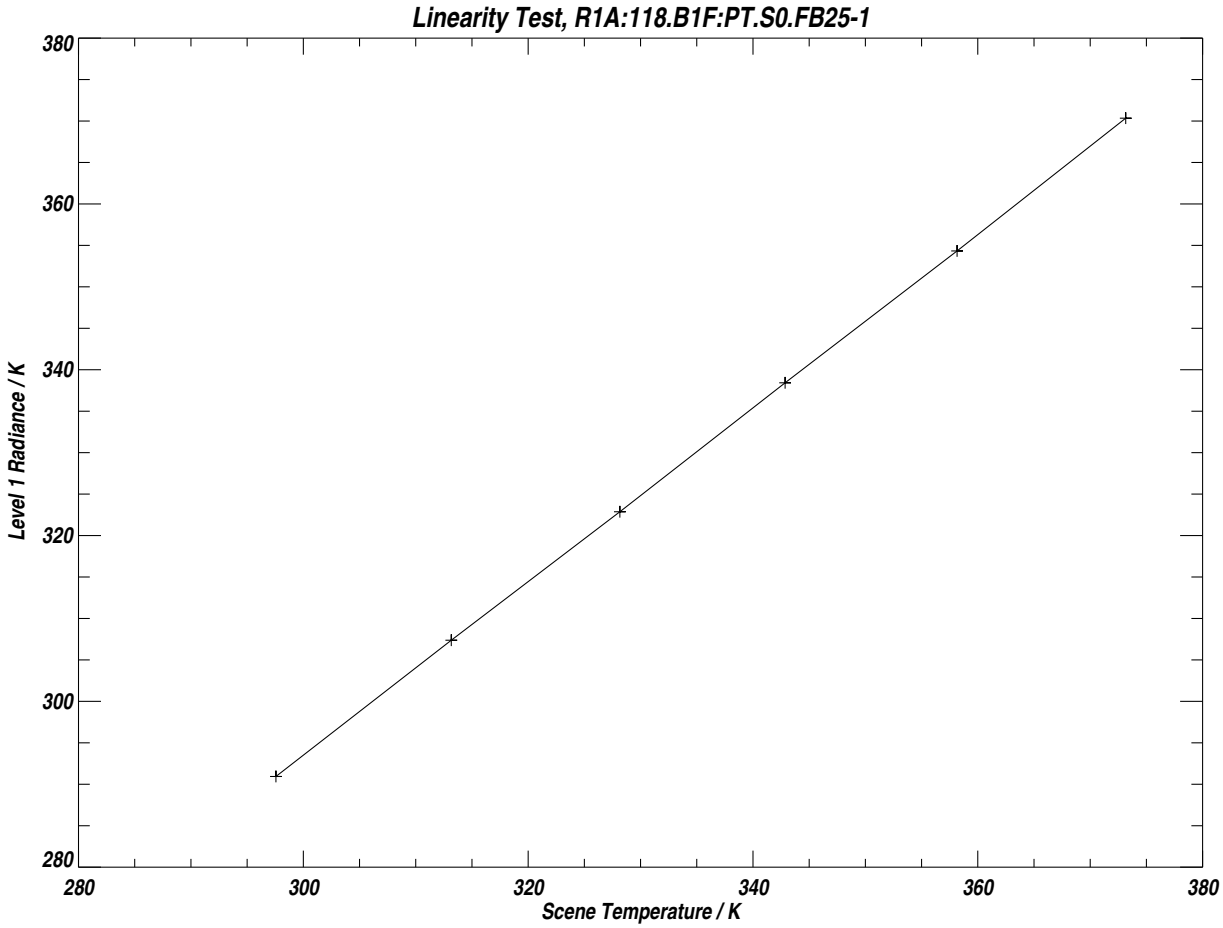

Figure 2.12: Data from Figure 2.11 with the weighted mean radiance for each measurement group plotted against target temperature. See text for additional details.

(5) There are hints of mid-order nonlinearity in several other 25-channel filterbank bands, but at levels less than the noise on individual radiance measurements, even when extrapolated to the wider range of scene temperatures that will be observed in the atmosphere.

The observed 'band shape changes' with overall signal level can arise from many sources, including:

- ❏ Detector diode nonlinearity that differs from diode to diode in the filter spectrometers.
- ❏ RF amplifier and filter bandpass shape changes with signal amplitude. RF ceramic capacitors are notorious for their voltage dependences, and the junction capacitances of the transistors and FETs used in the amplifiers have unavoidable voltage dependences.
- ❏ Changes in RF signal levels alter the power consumption of both pre- and post-detector electronics, which in turn alter the supply voltages to the active electronics. RF amplifiers typically operate without the benefits of sufficient feedback to define their closed-loop characteristics, and so even small supply voltage changes can appreciably alter the characteristics of these signal paths.

Although the effects noted on EOS MLS are not at a particularly worrisome level, they will have to be kept in mind (particularly in the R1 Wide Filters) should unexpected radiance residuals be seen in flight data.

The most important observation is that future instrument of this type are likely to have far higher dynamic range signal paths due to the use of SIS (or similar) low-noise front-end receivers. This has the potential to raise the mid-order nonlinearity of these systems to unprecedentedly high levels, necessitating operation 'in balance,' or close to balance for certain critical measurements. There are also possible ramifications for the spectrometer implementation, and wide bandwidth digital spectrometer will likely have to be developed to support the most challenging measurements in such future systems.

2.5 Dual Cold Load Test

A test was run to verify that the small differences in truncation of the GHz beams between the Switching Mirror Limb and Space ports did not introduce unacceptable spectral artifacts. Radiance differences (with spectral content) will arise if the two signal paths truncate the beams differently, as could happen if there was a significant misalignment within the GHz Radiometer assembly. This test was run with the GHz Radiometer Module in the cart configuration (i.e., with no antenna). In this configuration the Limb and Space port beams emerge horizontally from opposite sides of the module, and 45° plane reflectors were used to direct the FOVs from both ports into separate LN_2 dewars with nominally-identical submerged absorbing targets. These cooled targets provided views at temperatures considerably different from the radiometers and the targets within the GHz module, thus providing the necessary temperature contrast to identify differences in beam truncation between the two ports.

2.5.1 Measurement Timing and Processing

The measurement sequence in each MAF consisted of 71 MIFs viewing to the Limb port followed by 8 MIFs viewing the internal 'controlled' target, and finally 57 MIFs viewing to the Space port. The remaining MIFs were discarded because the the Switching Mirror was moving. This measurement cycle was repeated to provide 1,800 MAFs of Level 1 radiance data, sufficient to allow observation of any artifacts at levels consistent with instrument performance requirements.

Level 1 processing software was instructed to use the last 14 Limb port views in each MAF as Target views at 80 K, and to use the 8 internal target views as references at the telemetered temperature of the target. The first 57 Limb port views, and all 57 Space port views, were then processed as scene radiances. The two groups of scene radiances for each channel were then averaged and differenced for the entire data set, and these data are plotted in Figures 2.13 and 2.14.

2.5.2 Results

Figure 2.13 shows the processed data from all GHz 25-channel filterbank bands except for Band 12, since Filterbank 12 was used to analyze data from R1B during this test. The data from the 11-channel filterbanks and individual Wide Filter channels are shown in Figure 2.14.

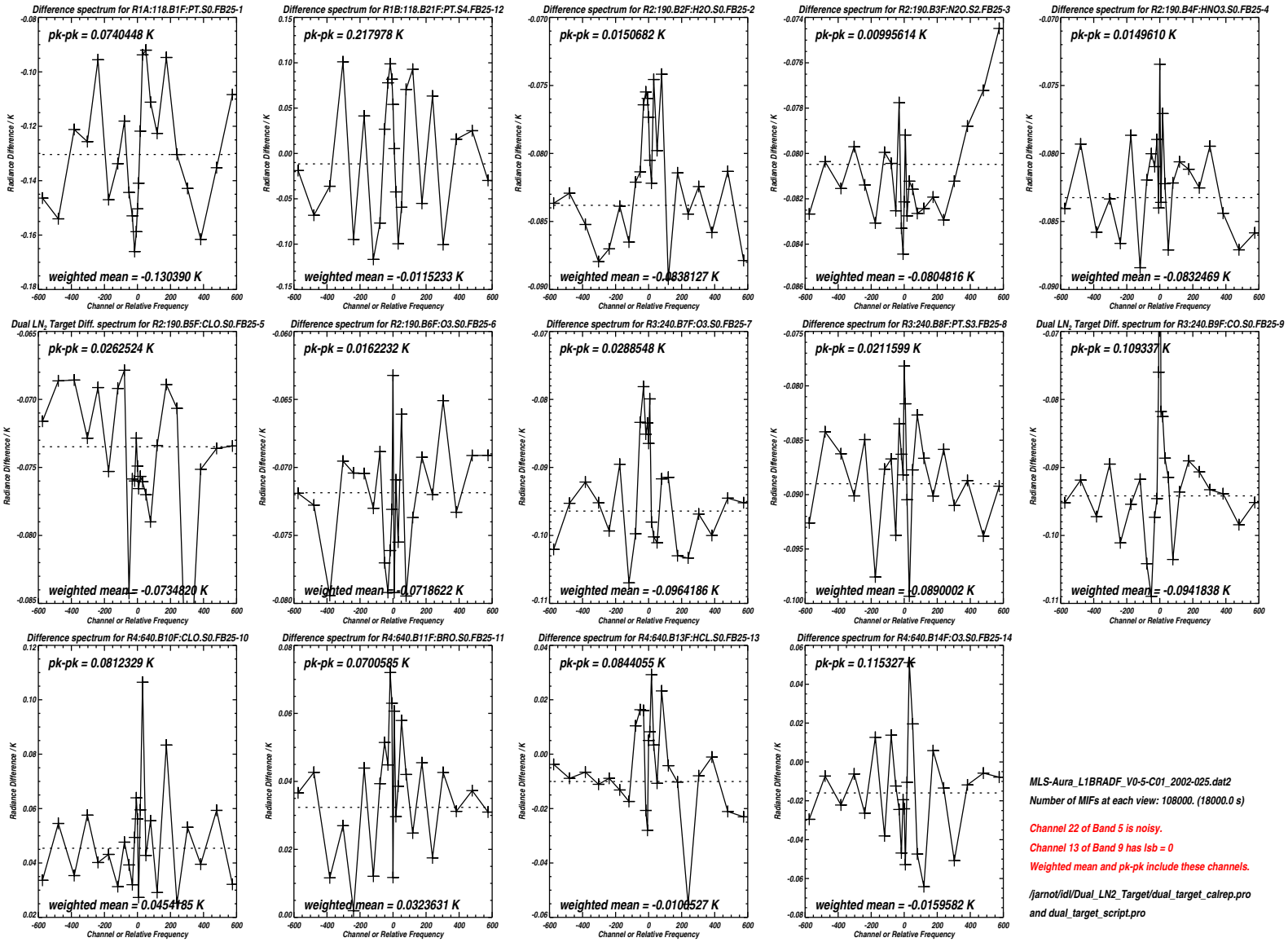

Figure 2.13: Differences between Limb and Space port views to similar LN_2-cooled targets for the GHz 25-channel filterbanks. See text for additional details.

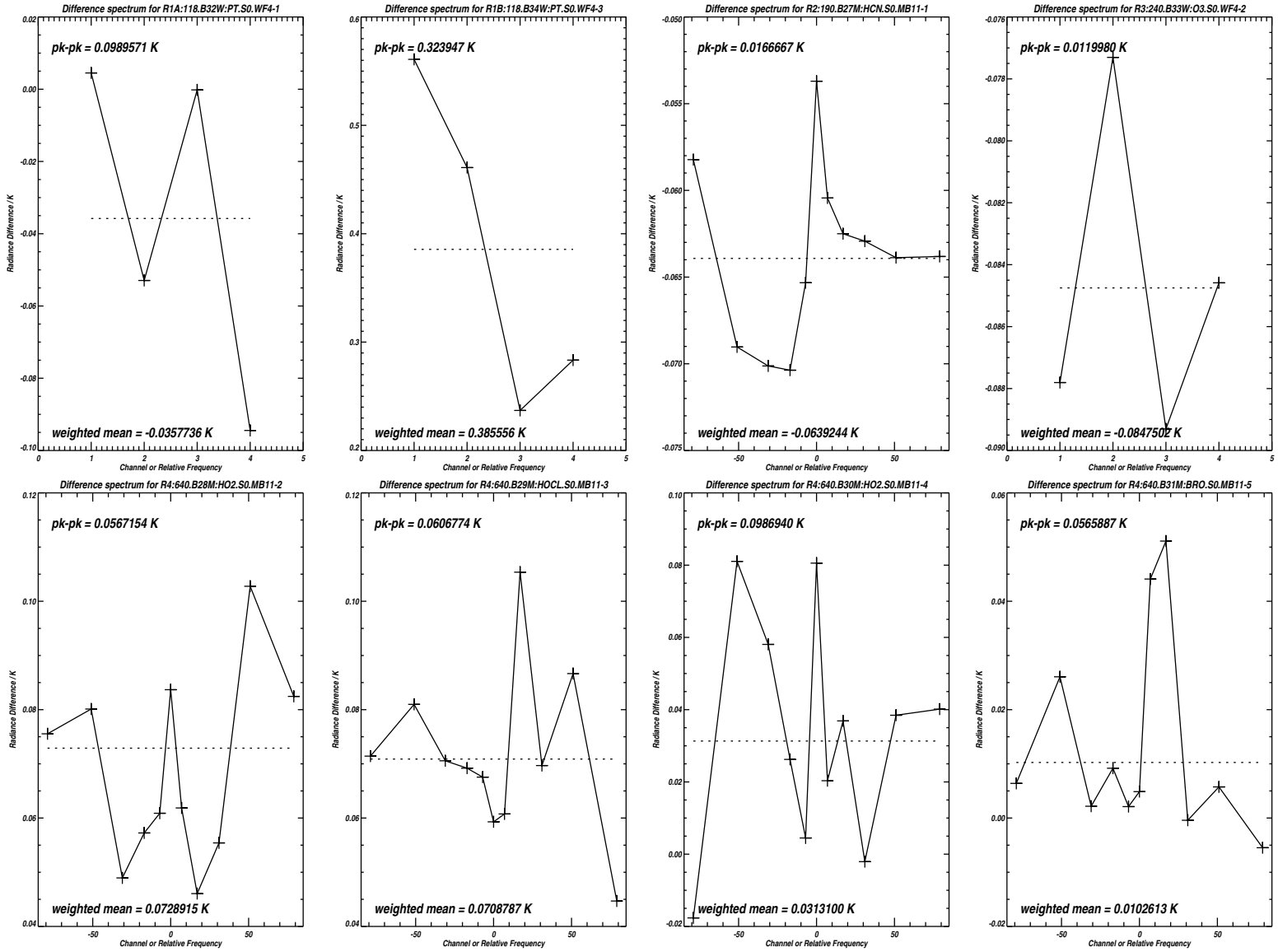

Figure 2.14: Differences between Limb and Space port views to similar LN_2-cooled targets for the GHz 11-channel filterbanks and Wide Filter channels. See text for additional details.

Note that channel 22 of Band 5 is off scale because of low-level intrument-generated noise in this particular channel. Channel 13 of Band 9 is also artificially noisy because of a GSE configuration oversight that forced the least significant byte of the 16-bit data from this channel to be incorrect in the instrument telemetry stream at the time of this test. Each panel of these plots includes a printout of the weighted mean (weighting by nominal channel noise bandwidth) of the difference radiances, and the *pk–pk* radiance difference in the band. The weighted mean and *pk–pk* data printed in the panels for Bands 5 and 13 include the data from the noisy and truncated channels.

There are several items of note in these plots:

(1) The long data set (over 8 hours of total measurement time) results in very low *rms* noise levels on the processed data, consistent with expectations from the radiometer equation.

(2) Even though R1A and R1B are simultaneously viewing the same targets, the 25-channel filterbank data from R1B exhibit noticeably larger standing waves. This difference in performance arises because of the higher truncation levels for the R1B beam in the GHz module, and also because of a small but unusual frequency dependence in the direction of the FOV pattern from the R1B receiver feedhorn. This is particularly noticeable in the Wide Filter Data for R1B (B34W) in Figure 2.14. The offset between the Limb and Space port data for R1B is also clearly evident in time series plots of calibrated radiance for this data set, confirming that this effect is real, and not the consequence of a bad data point or a data processing error.

(3) There appears to be a small but systematic offset in the data for the upper 3 channels of the FB25 data for Band 3, but this frequency range is overlapped by the highest frequency channel in Band 4 which shows no similar offset. Since the observed offset is statistically insignificant, and not present in an overlapping channel of another band, we choose to ignore it at this time.

(4) Perhaps the most important result from this data set is the clear indication that Limb and Space port difference data can be integrated down to levels well below those specified in the instrument requirements document.

2.6 Blue Sky Test

The Dual Cold Load test described earlier provides a very useful indication of correct alignment within the GHz module, but does not answer any questions regarding the GHz antenna alignment, or any potential antenna scan-dependent artifacts. A more cumbersome test was devised to help answer such questions, the test setup being shown in Figure 2.15. The MLS instrument is located in the outer airlock of the High Bay of Building 306 at JPL, and positioned with the GHz antenna viewing horizontally, the Space port viewing vertically downwards. A 45° aluminum reflector plate redirects the Space port beam to be parallel to the ground, and approximately parallel to the antenna beam. The 2 large plates into which the instrument beams face are adjustable plane aluminum reflectors large enough to fully capture both antenna (upper reflector) and Space port beams. They are positioned so as to

ensure that both beams miss the upper portion of the building, and the antenna reflector is further fine-tuned to obtain approximate radiometric balance when viewing the sky near zenith. Since this test was performed several times over the course of several days, periodic adjustments were necessary to maintain balance.

The switching sequence implemented for this test required views to both GHz internal calibration targets in order to provide periodic radiometric gain measurements. The 'Controlled' target was operated in its heated mode, providing a temperature difference of ∼20 C between the two internal reference views. The ambient target was viewed for 14 MIFs per MAF, and the heated target for 12 MIFs. The Limb and Space ports were each viewed for 50 MIFs during every MAF.

In order to check for scan dependencies, measurements were taken with the antenna in its nominal (near center) position, and at both scan extremes. To provide a robust data set for interpretation, sufficient data were taken at each scan position to allow two analysis data sets to be produced, typically one for nighttime observations, and one for daytime. The raw data were carefully examined to ensure that any regions of obvious instability, such as due to strong winds[6], were omitted from the final analyses. Examples of these data taken with the antenna in its nominal start-of-scan position are shown in Figures 2.16 and Figures 2.17. These data are for all GHz filter channels except for Band 12 (FB12 was being used to take R1B data during this sequence of tests).

See Appendix B for the full set of analysis results taken with the antenna in its nominal start-of-scan position, and at both scan extremes. This range of angles, ∼12°, is substantially larger than the ∼2.5° scan we expect to perform routinely in flight[7]. The importance of these data lies in the structure on the *differences* between the measured Limb-Space port radiance differences for the suite of data sets plotted in Appendix B. Close examination of these data indicate no obvious scan-dependent features in the radiance double-differences, giving us confidence that in-orbit spectral baseline performance will be satisfactory.

The Limb-Space port radiance difference plots provide no indication of the actual sky radiances being observed. Figures 2.18 and 2.19 show the data set taken with the antenna at its nominal scan position (corresponding to the data in Figures 2.16 and 2.17) reprocessed to indicate the Limb (black) and Space port (green) radiances. The differences between Limb and Space port radiances are plotted in blue. It is interesting to note the large atmospheric spectral features readily visible in the Wide Filter data of the 118 GHz radiometers, and the substantial thermal contrast between instrument and sky for all bands except those in the 640 GHz radiometer. Atmospheric simulation calculations were performed to verify that the atmospheric spectra presented here were reasonable for the atmospheric conditions (very dry) under which this test was run.

Given the lack of thermal contrast between instrument and sky for the 640 GHz bands, the ∼0.5 K offset readily apparent between the center 11 and outer 14 channels of each 25-channel filterbank is surprising, and is an indicator of a significant problem. The most likely candidate to be causing this effect was that the changing IF signal levels in the other bands, and resulting power consumption changes in the IF chains and spectrometers, were modulating the power supply voltages for these components sufficiently to cause the observed effects. A simple set of tests was run to confirm this theory:

[6]The Blue Sky data were taken during a period of strong Santa Ana winds.

[7]The ∼2.5° scan range includes the additional scan range required to compensate for the Earth's oblateness.

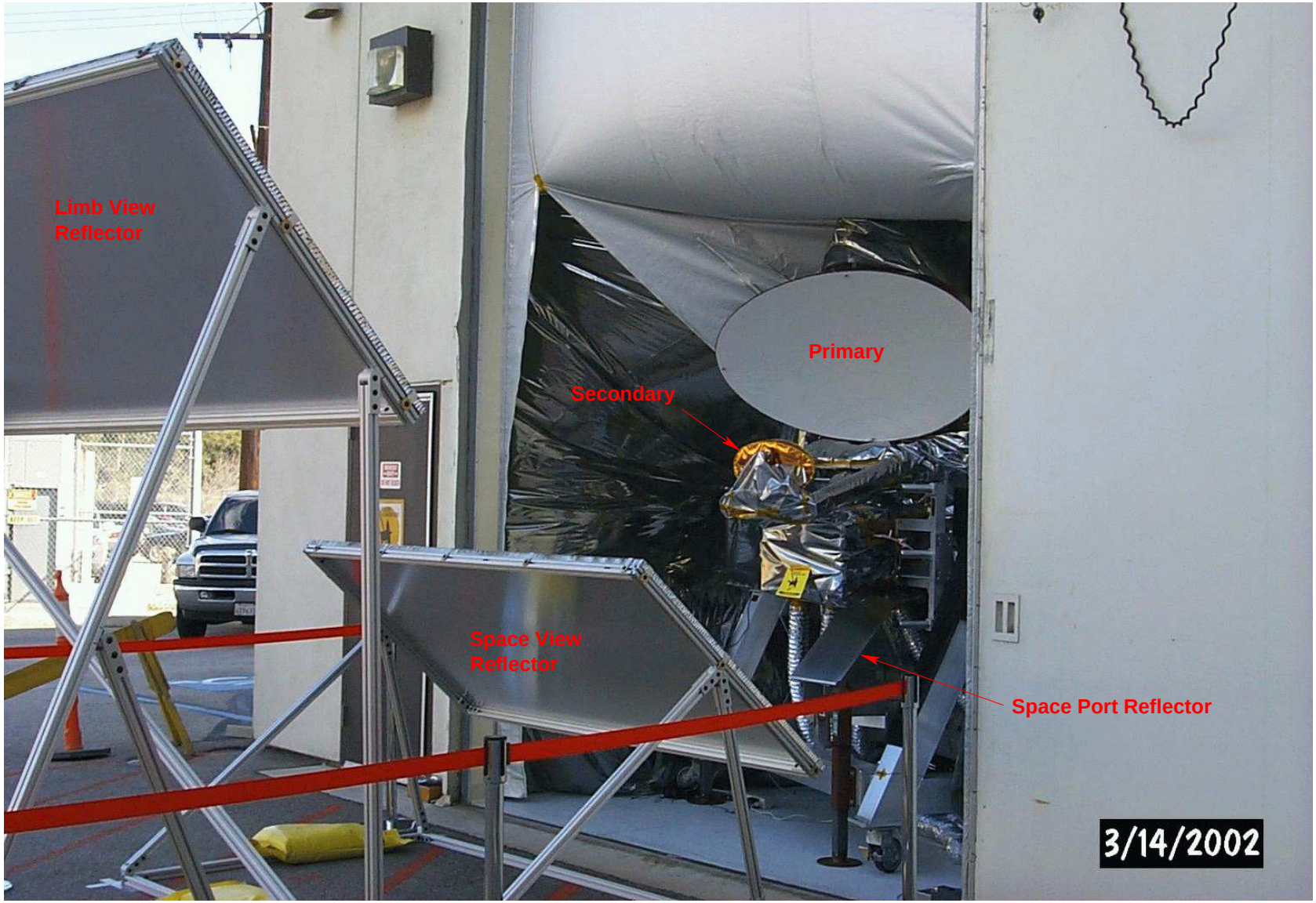

Figure 2.15: 'Blue Sky' measurement setup. See text for additional details.

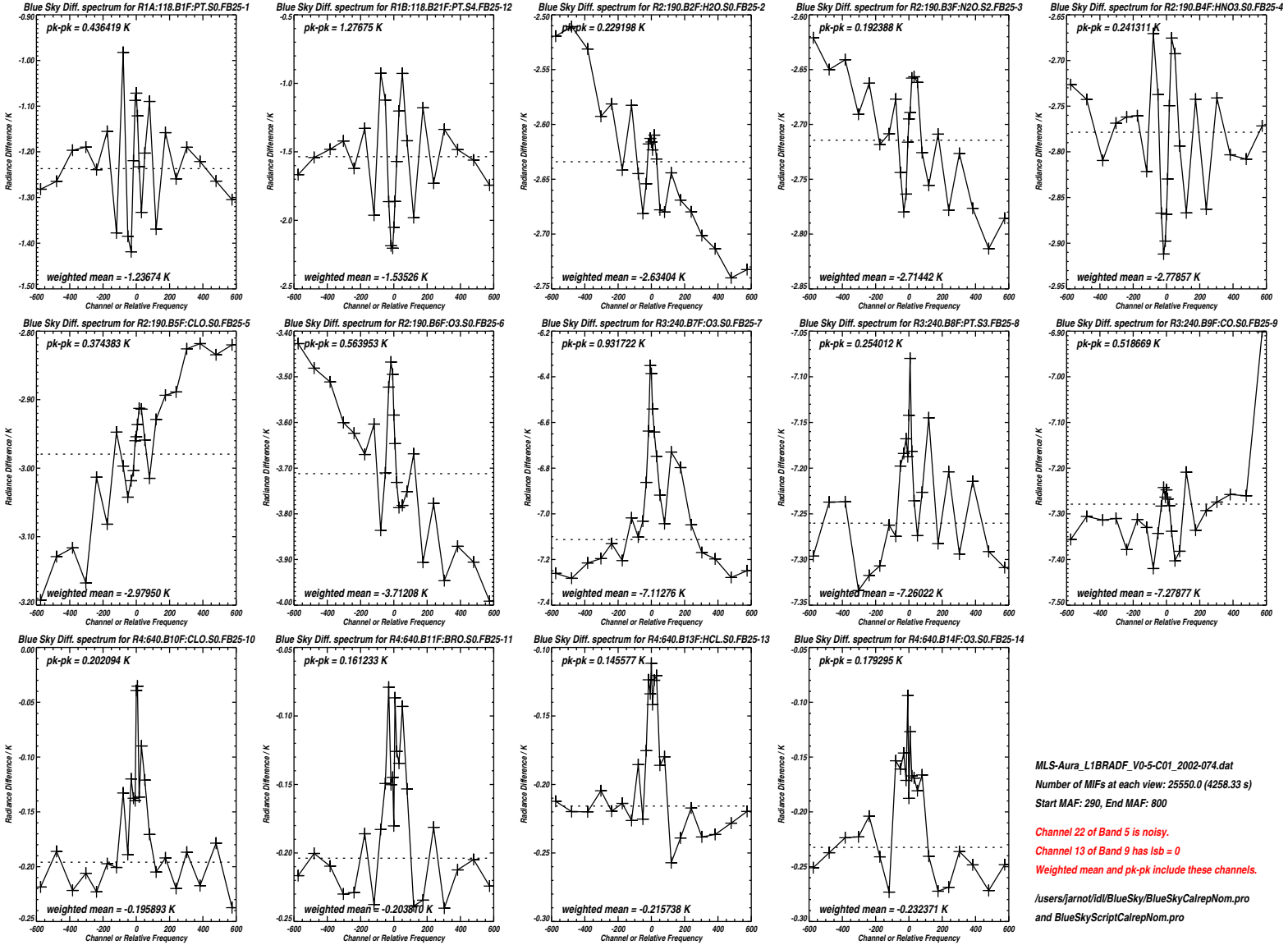

Figure 2.16: Blue Sky test Limb port minus Space port radiance differences for the GHz 25-channel filterbank bands. These data were taken with the antenna in its nominal start-of-scan position. See text for further details.

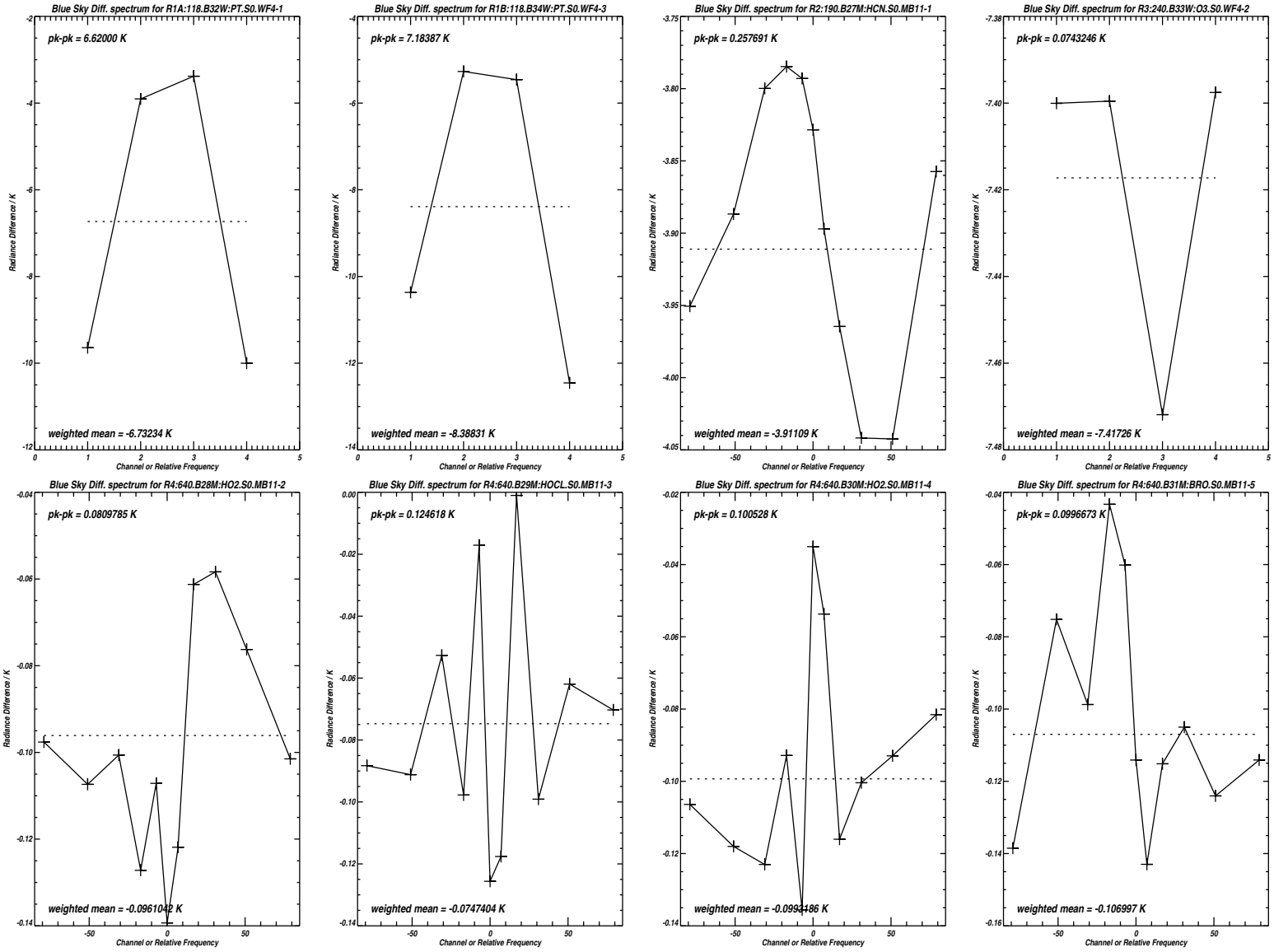

Figure 2.17: Plots of Blue Sky test Limb port minus Space port radiance differences for the GHz filter spectrometer bands not included in Figure 2.16.

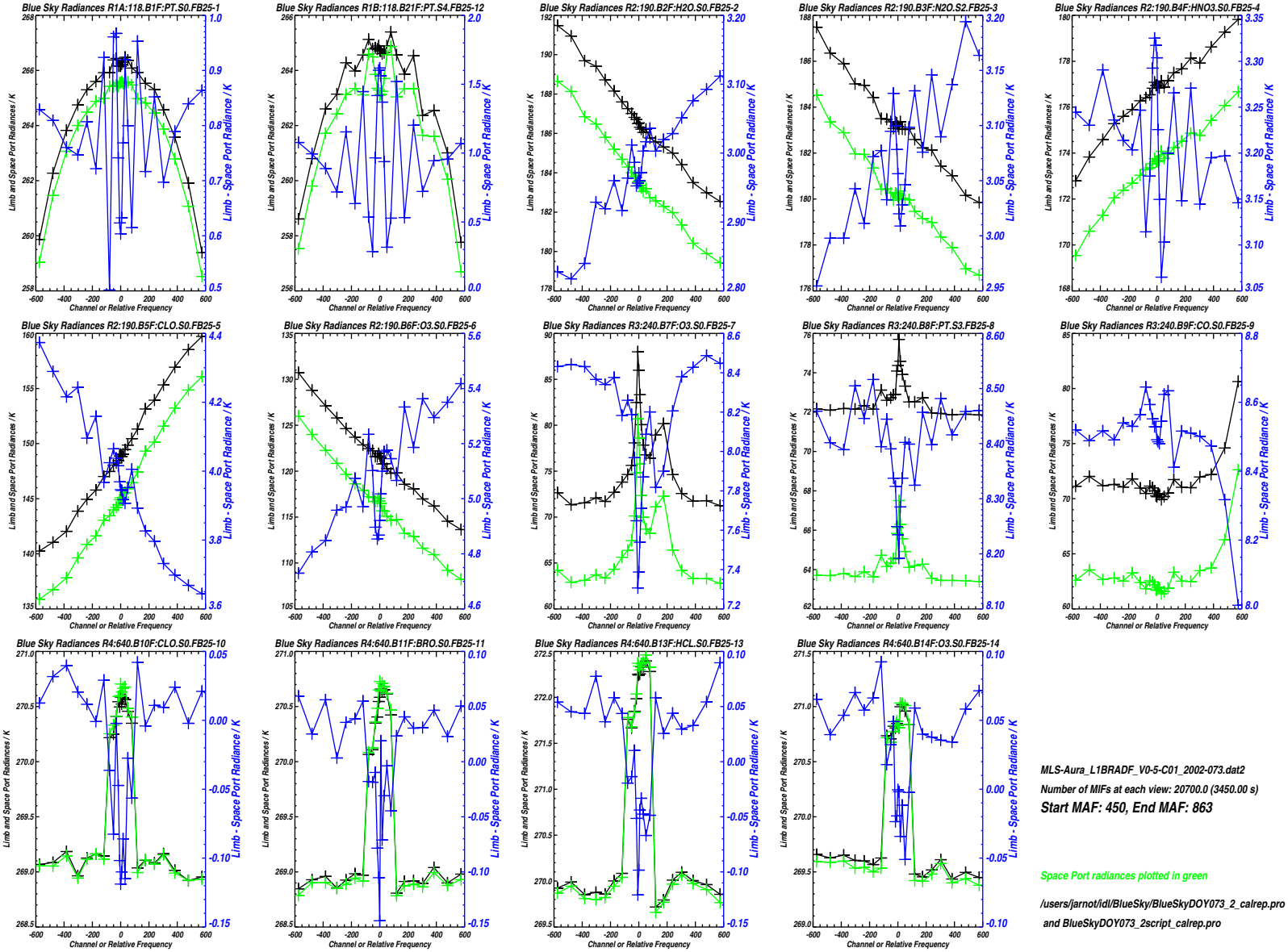

Figure 2.18: Data of Figure 2.16 processed to show sky radiances measured through the Limb (black) and Space (green) ports. The blue line indicates the difference between Limb and Space port radiances.

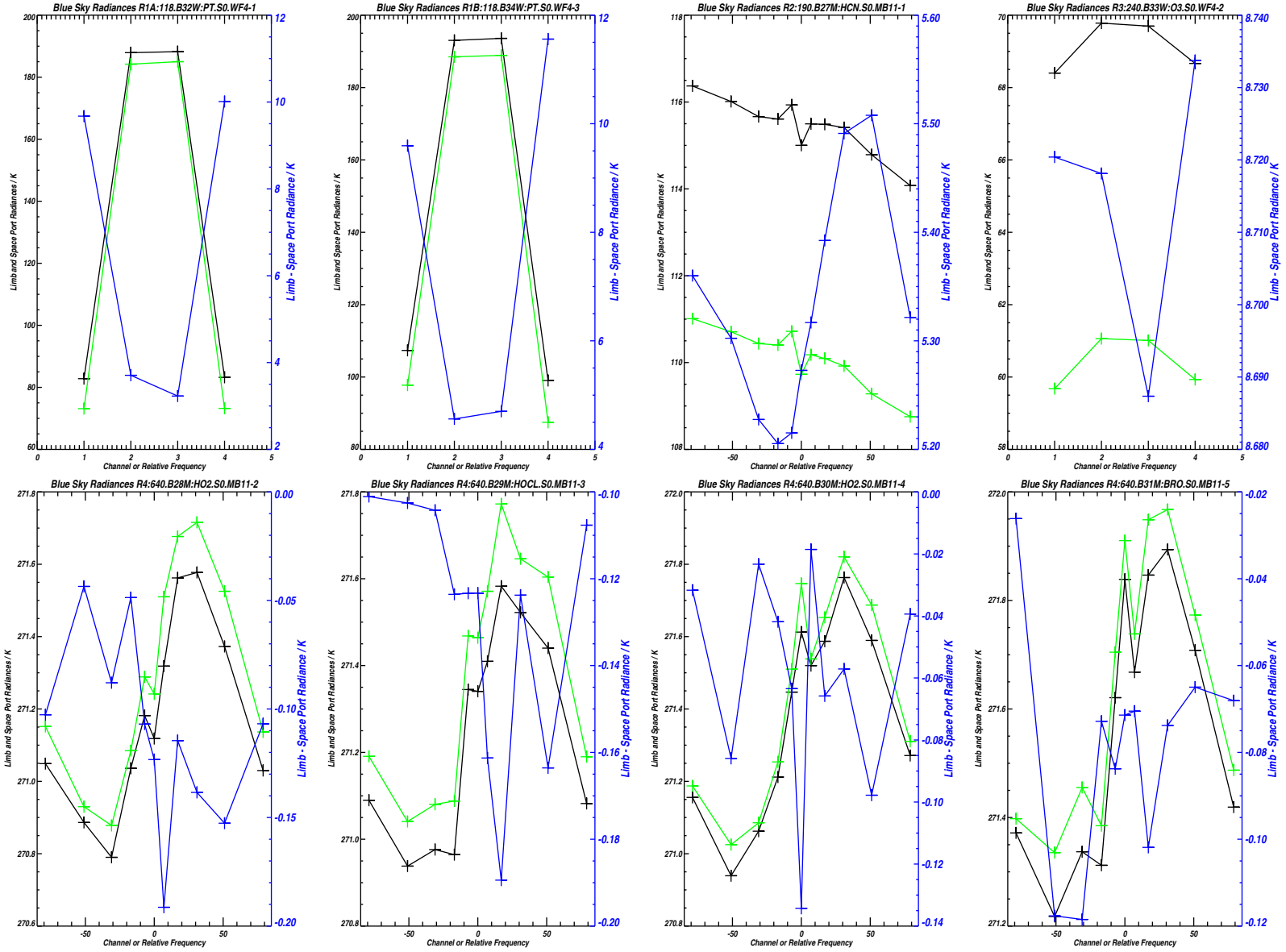

Figure 2.19: The 11-channel filterbank and Wide Filter data for the data set shown in Figure 2.18. Note the remarkably low atmospheric opacities in these data for the bands in R1 through R3, due to a prevailing Santa Ana condition.

- ❑ Each spectrometer shearplate houses 2 filter bank spectrometers which share a common set of supply lines from the central Spectrometer Power Supply Unit (SPCU).
  - ⇨ With the radiometer FOVs directed to an internal target, the IF attenuator to one spectrometer was moved between its nominal and maximum attenuation setting, and the data from the other spectrometer on the same shearplate examined for unwanted interactions.
    - ➳ This test revealed that the common wiring (with series FET power on/off switches) from the SPCU to each shearplate had sufficient resistance to cause substantial interactions between the 2 spectrometers.
  - ⇨ With the radiometer FOVs directed to an internal target, the IF attenuators to several sets of spectrometers were moved between their nominal and maximum attenuation settings, and the data from the spectrometers on different shearplates examined for unwanted interactions.
    - ➳ This test revealed that the SPCU regulation alone was insufficient to avoid substantial interactions between all of the spectrometers.
- ❑ It is clear from these data that the mid-band filters (center 11 channels of each 25-channel filterbank, and the independent 11-channel filterbanks) had considerably more power supply sensitivity than the outer 14 channels of each 25-channel filterbank. This can be attributed to the use of an active mixer (Gilbert cell) to downconvert the 11-channel data bands prior to analysis.

As a consequence of these observations, the SPCU ±5 V supplies were boosted to about ±5.8 V, and low dropout regulators installed on each spectrometer shearplate, with independent regulators for each filterbank spectrometer. This eliminated all spectrometer interactions observed in the tests outlined above, and furthermore eliminated the odd/even MIF differences described earlier. It also eliminated a very puzzling result evident in the relative sideband data (see Chapter 3), in which the data in the outer 14 channels of each 25-channel filterbank appeared to be quite well behaved, but the Fabry-Pérot radiances in the center 11 channels (and in all channels of each 11-channel filterbank) showed mysterious channel-to-channel peak radiance differences of up to ∼20 K for any given grid spacing.

2.7 GHz IF Attenuator Tests

This section should really be in Volume 4 of this report since the data was taken in orbit during the early instrument activation period. The results of these test fit better into this portion of the Calibration Report however. For this test the radiometric gain of each GHz band was determine with nominal attenuator settings, and for settings 1 dB above, and 1 dB, 2.5 dB and 4.5 dB below the nominal setting. The gain results were then normalized for each band so that they could be over-plotted to show the changes in bandpass shapes. The results for Bands 1, 2, 7 and 10 are shown on the following pages.

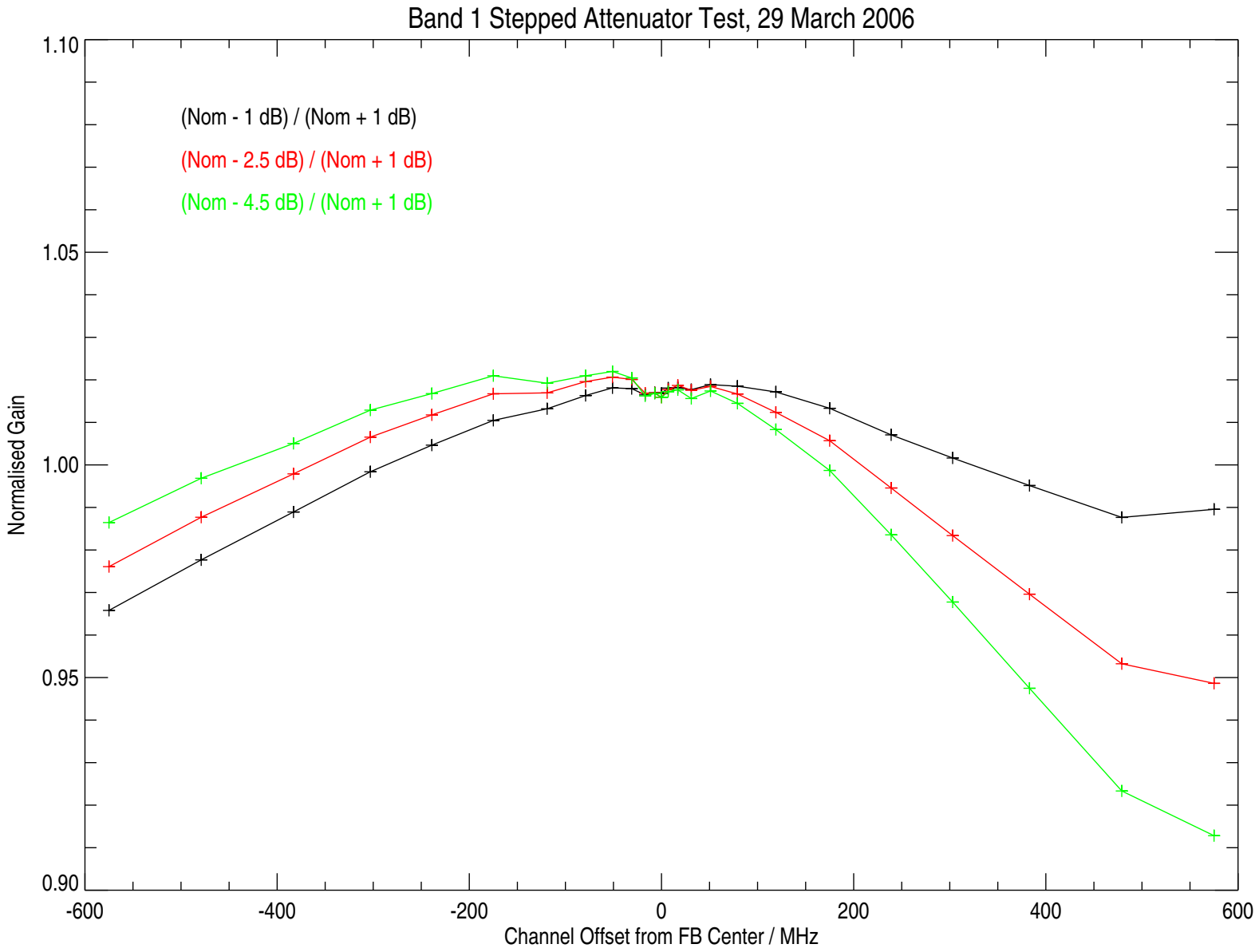

Figure 2.20: Relative band gains as a function of attenuator setting for Band 1. See text for additional information.

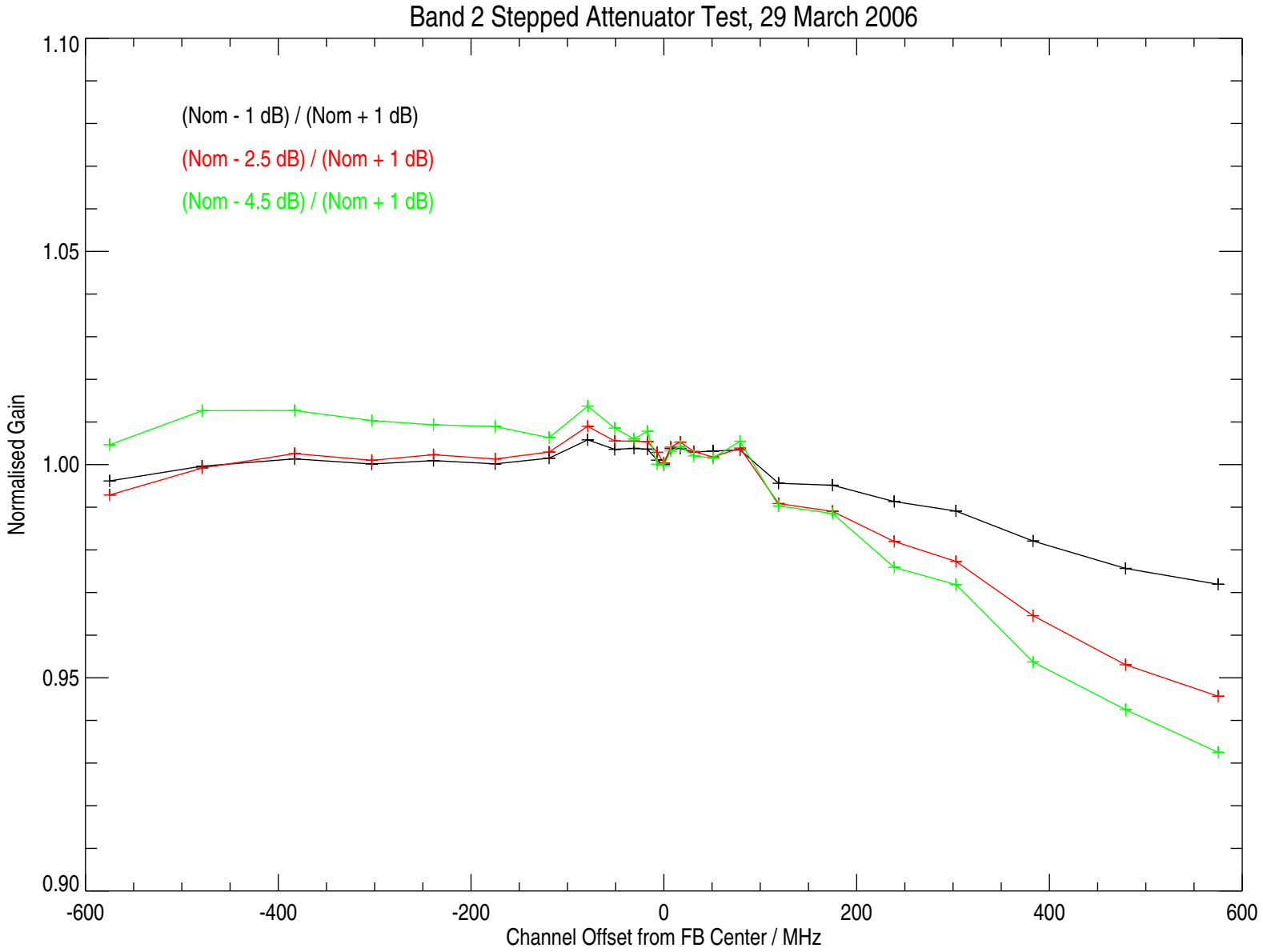

Figure 2.21: Relative band gains as a function of attenuator setting for Band 2. See text for additional information.

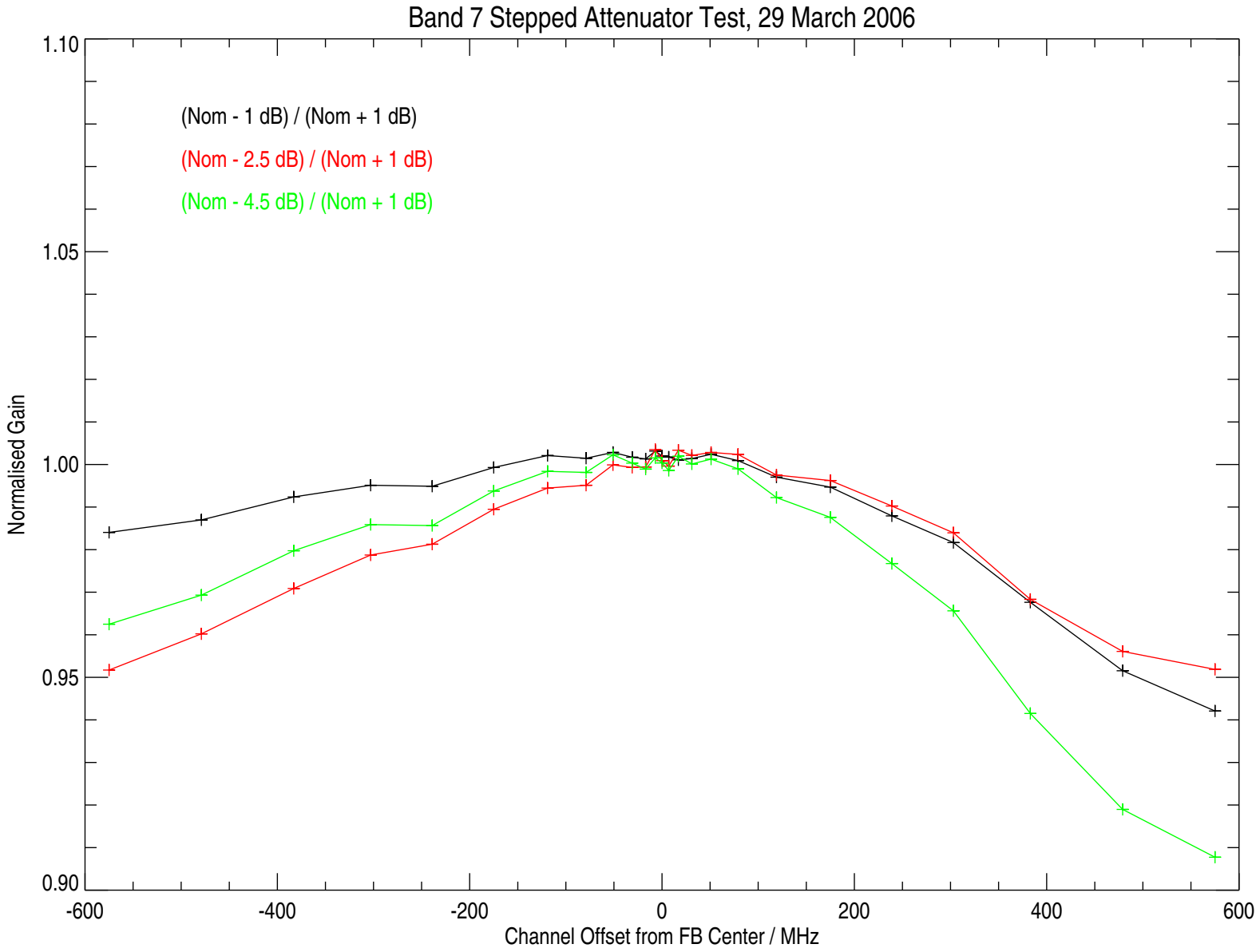

Figure 2.22: Relative band gains as a function of attenuator setting for Band 7. See text for additional information.

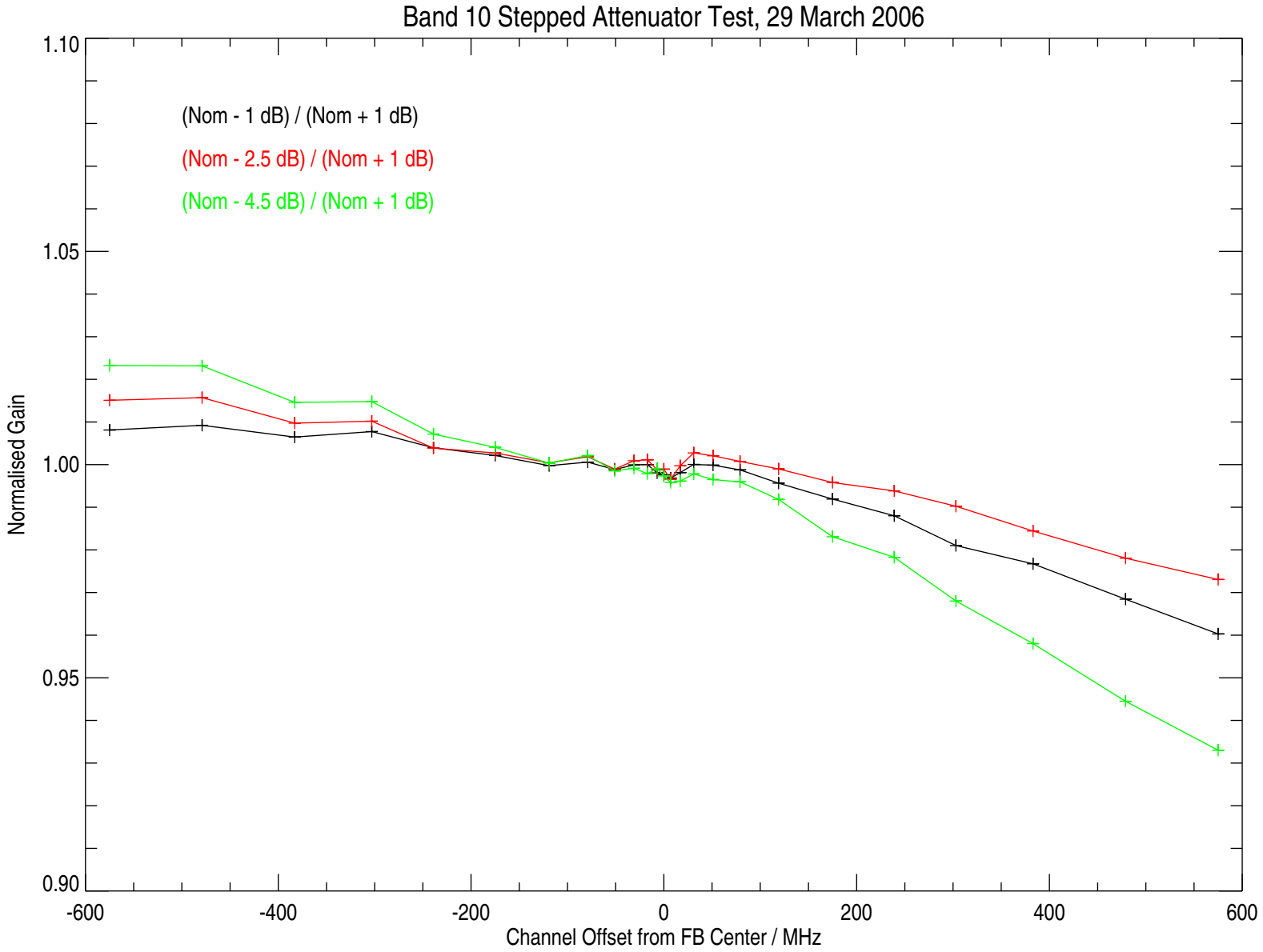

Figure 2.23: Relative band gains as a function of attenuator setting for Band 10. See text for additional information.

2.8 THz Sensitivity Measurements

Several sensitivity data sets were taken during the course of instrument Integration and Test, with similar results. However, a standing wave with the LLO port was found at the end of November, 2002. This problem was corrected by inclusion of a quarter wave plate in the LLO arm of the THz diplexer in the first week of December, 2002. Before this time the system temperature and sideband fraction was extremely variable over the IF channels within a band. Figure 2.24 shows the sensitivity performance after addition of the quarter wave plate. These THz data were taken on 8 December 2002. Sensitivity requirements (based on noise levels measured during these characterizations) are met in all THz channels. Measurements during spacecraft thermal vacuum tests are essentially identical. Performance is degraded during atmospheric tests because of attenuation (and fluctuations in attenuation) due to humidity. To meet these sensitivity performance requirements it is essential to apply special calibration processing that accounts for variation in LO power during the data and calibration signal integrations. This special processing is described in [2]. The margins in meeting the sensitivity requirements are such that it is unnecessary to distinguish between spectrally-varying and non spectrally-varying parts of the radiance sensitivity.

2.9 THz Linearity

The THz IF and spectrometer electronics are very similar, often essentially identical, to the correponding GHz signal chain subsystems. The relatively large T_{sys} of the THz receivers compared to their GHz counterparts means that the dynamic range of THz signals chains is substantially reduced. No explicit end-to-end linearity measurements were performed on the THz signal chains, but since we observed no significant linearity problems with the GHz chains, we can safely make the same assumption for the THz ones. In addition, some of the other THz calibrations (e.g., relative sideband) used large signals compared to those expected from atmospheric signatures, and analysis of these data did not indicate any linearity issues. The considerably larger source brightness temperatures in the corresponding THz relative sideband calibrations would have made any significant linearity issues readily apparent.

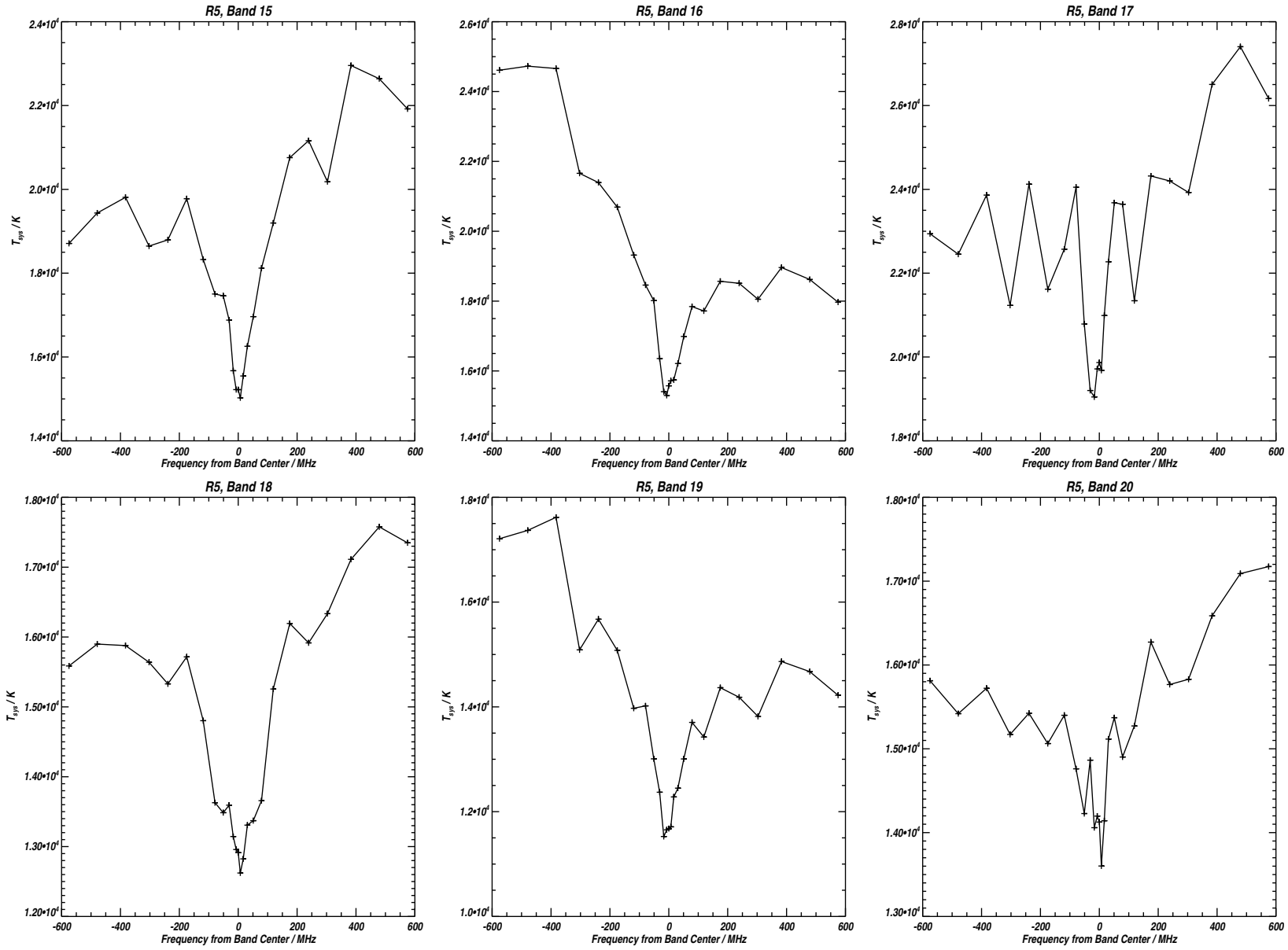

Figure 2.24: Plots of T_{sys} for all THz bands. X-axes indicate channel position *wrt* band center in MHz. All data are double sideband.

2.10 Radiometric Calibration Targets

The GHz and THz module implement separate ambient radiometric calibration targets, observed in tandem with views to cold space in order to provide the necessary radiometric gain calibration measurements for each channel. The two target designs are discussed below.

2.10.1 GHz Calibration Targets

The GHz module implements two internal black-body calibration targets located to face one another in the switching mirror enclosure. The two targets are nominally identical, but one is thermally tied to the local structure (GHz Ambient Target, GAT), the other somewhat thermally isolated and connected to a 'cold patch' (GHz Controlled Target, GCT) so that in the flight environment we expect them to maintain a temperature difference of ∼30 K. During ground testing we were able to take advantage of the thermal isolation of the GCT by heating it (to ∼40°C) using built-in resistive heating elements powered by the instrument main input power buses. This heating capability is disabled for flight, but provided an extremely convenient mechanism for periodic verification of radiometric performance under test conditions that would otherwise have precluded obtaining such data.

The design of these targets borrows heavily from the UARS MLS internal ambient target design[8], including choice of temperature sensing elements. Their basic design consists of two aluminum plates coated with microwave absorber. The plates are arranged in a wedge so that at least three reflections of any incident beams take place before the beams exit the target. As with their UARS predecessors, the targets were subject to extensive pre-delivery characterizations to verify adequate return loss (better than 30 dB at all GHz receiver frequencies), and lack of any harmful diffraction sidelobes from their ridged and pyramidal cone surfaces. Additional confidence in the adequacy of their performance comes from the detailed analyses of many 10's of hours of radiometric performance and calibration data which used one (or both) of these targets as reference views. During the course of these measurements the radiometers also viewed an original UARS target (see description of linearity measurements later in this chapter). The Dual Cold Load Test discussed earlier in this chapter essentially compared the signals seen from internal targets and external LN_2-cooled rubberized absorber targets. Many of the other measurements used an external LN_2-cooled target as a radiometric reference, and tests were routinely run which compared the radiances from the two internal targets. In these extensive data sets there is no evidence of any significant issue related to performance of the internal calibration targets, which would have manifested as standing waves. Photographs of the GAT and GCT are given in Figure 2.25 and 2.26.

Design Principles

A sketch of the construction of the GHz targets is given in Figure 2.27. Aluminum plates with attached PRD temperature sensors are coated with CRS-117 microwave absorber as shown. A ridge/pyramid spacing of 0.085" was chosen so that the diffraction from the surface of each plate was captured by the other plate at all operating frequencies.[9]

[8]The UARS internal calibration target, and its performance, is described in [3].

[9]Note that as operating frequency increases, the cross-section of the beams incident upon the target entrance decreases.

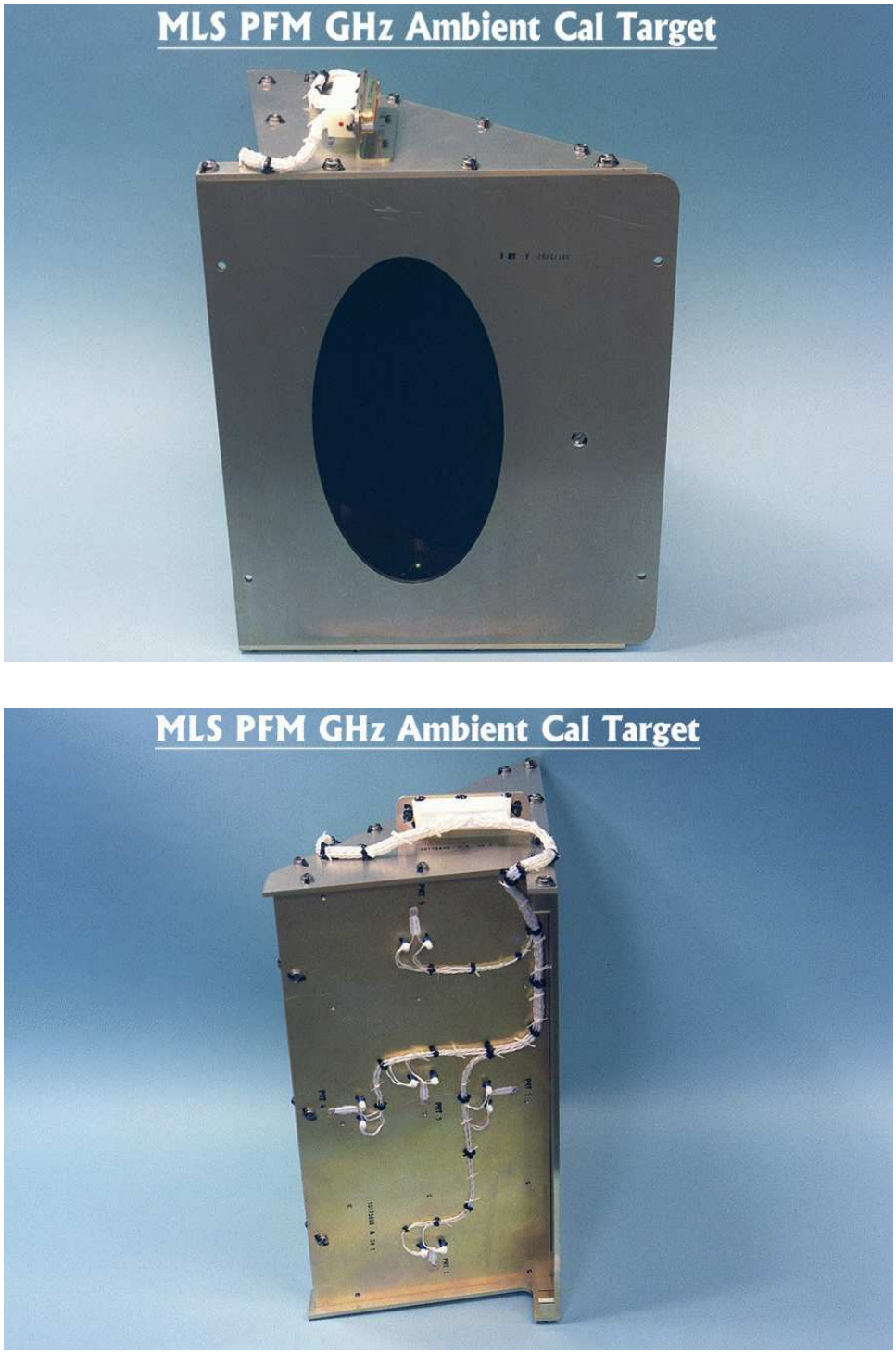

Figure 2.25: Front and side views of the GHz Module Ambient Calibration Target. Five PRD temperature sensors are visible in the lower picture. Five additional PRD sensors are mounted on the backing plate of the other absorbing panel.

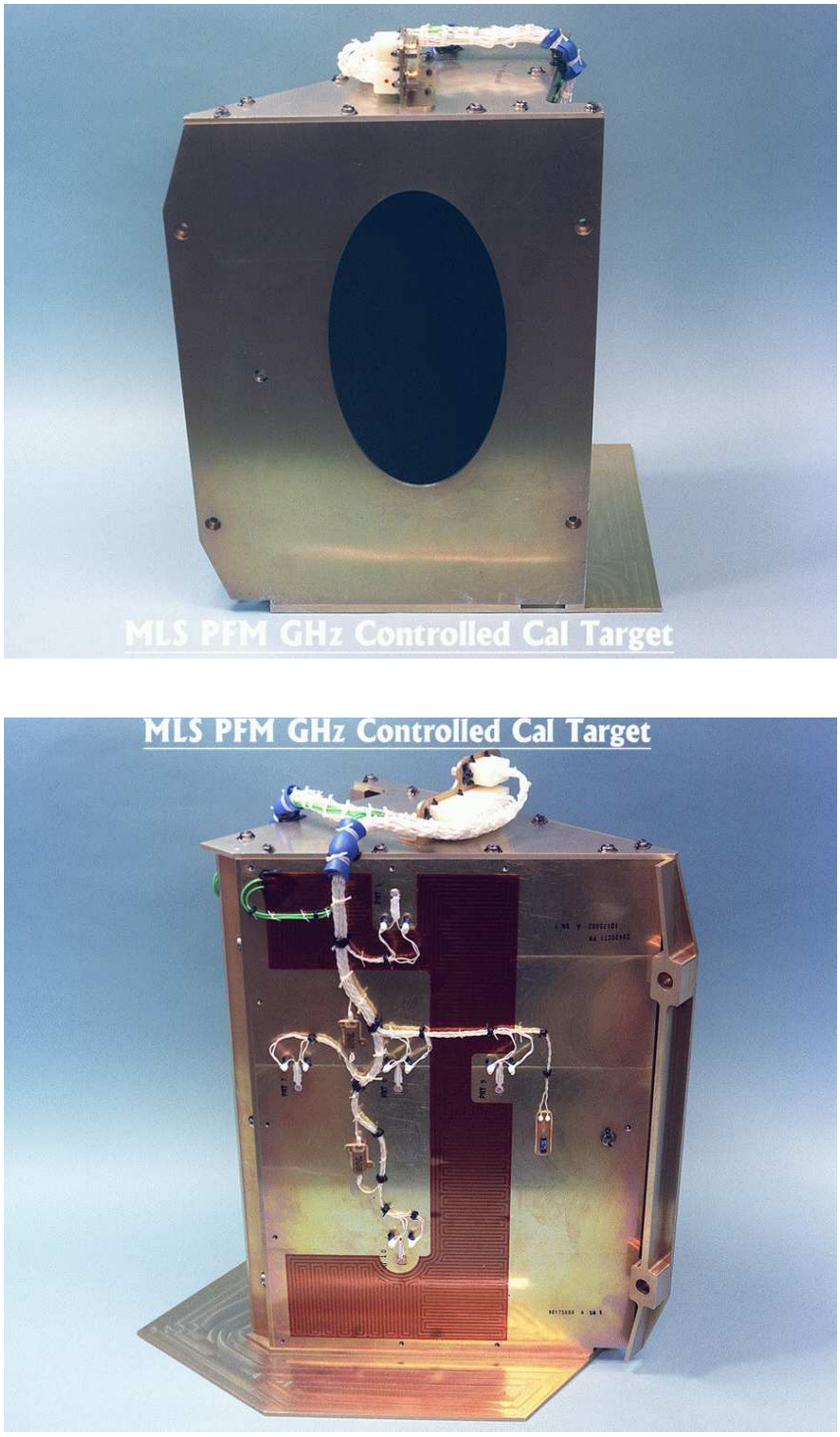

Figure 2.26: Front and rear views of the GHz Module Controlled Calibration Target. The surface-mount film heater on the side panel is clearly visible, as are the five PRD temperature sensors. Note also the radiator thermal interface at the bottom of these pictures.

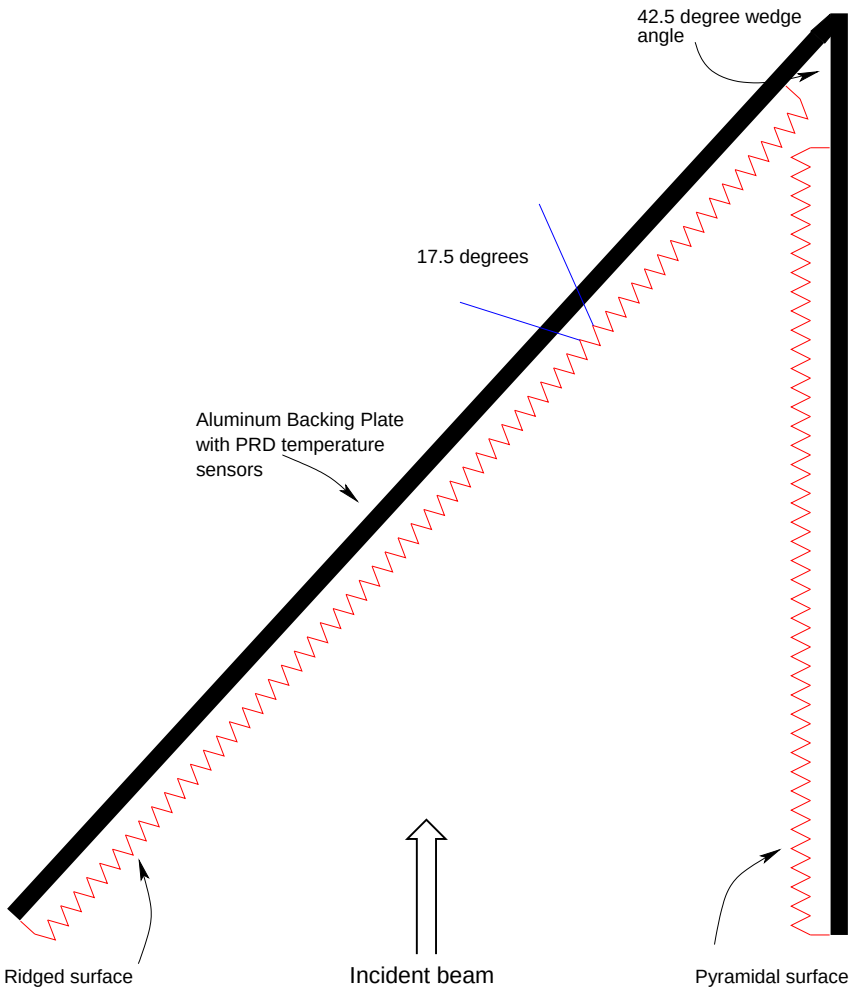

Figure 2.27: Sketch of GHz internal ambient calibration target design. See text for additional details.

The shape of the pyramids was chosen so that the reflection from the ridged surface impinged upon the flat sides of the pyramids at approximately the Brewster angle, and the thickness of the absorbing material (0.46 cm, 180 mil) on both surfaces was sufficient to ensure adequate absorption at all frequencies of operation.

Calibration target reflectivity was measured using the arrangement illustrated in Figure 2.28. A microwave source/receiver pair tunable over the full MLS GHz module measurement range was used to compare the reflection from the targets with that from a plane silver reference plate. The orientation of the target was manipulated during the course of the measurements to verify the absence of any unexpected diffractive features.

Further information on the construction of the targets, and their measured performance, is available on request from the authors.

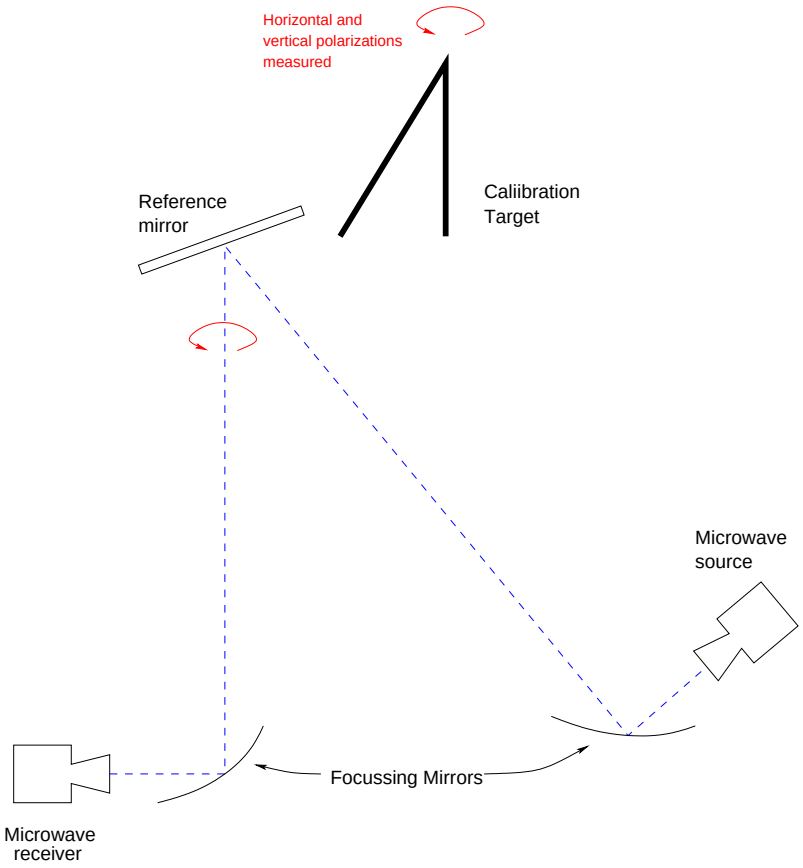

Figure 2.28: Simplified illustration of the test setup used to characterize the GHz calibration targets. Target performance is determined by comparing the reflected signals from the reference mirror and target. See text for additional details.

2.10.2 THz Ambient Calibration Target

Figure 2.29 shows the THz calibration target. It is located so that it can be viewed by the scan mirror when the scan angle is ∼180° from the nominal limb position. The surface of the target is a cylinder with radial 60° groves, and is machined from aluminum. The radius of the cylinder is 135 mm, and the groove pitch is 5 mm. However, the radiation pattern accepted by the THz receiver is a flat phase front with an approximately Gaussian profile (with -40 dB power at the edge of the target). The plane of the phase front is parallel to the cylindrical axis. Grooves were not needed in the direction of the cylindrical axis because of the curvature of the surface. The reflectivity of the target can be estimated by considering ray optics in groove cross-section. The 60° angle of the grooves assures that at least 3 reflections are required for a normal incident incoming ray to leave the surface. The reflectivity for such a ray will be equal to the cube of the reflectivity for a single reflection, i.e., $1 - \epsilon = (1 - \epsilon_1)^3$.

The surface of the calibration target is painted with Hincom paint that has a measured diffuse $\epsilon_1 = 95\%$ near 2,522 GHz. Therefore, $\epsilon = 99.988\%$. This paint looks white to the eye, i.e., the visible absorptivity is low, but is black in the infrared and far infrared. In fact, Hincom paint is the JPL-preferred thermal paint for radiators in flight applications.

The temperature of the target is measured with 5 PRD sensors mounted on the back of the target. During the 23 s of each MAF that are allocated to limb scanning or space view, the target is shielded from the limb-viewing aperture by the scan mirror. Similarly, when the scan mirror is pointing at the target for 1.3 s, the target is also shielded from this aperture. The only time that the target sees space is for a period of less than 0.35 s during the period of motor motion to and from the target. During this short period of time, the target can also be exposed to sunlight once an orbit. The high thermal mass of the target, its low visible absorptivity, and the short time period of exposure minimizes the temperature transients and assures that the PRD temperature is representative of the emitting surface.

The overall cylindrical shape of the target means that the fraction of the light returning into the instrument Gaussian beam is further attenuated by -38 dB due to the curvature of the surface. On the other hand, a portion of the black body radiation from the instrument can still be reflected without regard to the curvature of the surface. In other words, the curvature helps to inhibit standing waves, but does not affect the non-specular reflectivity. We can expect that the effective black body temperature of the reflected radiation will be within a few degrees of the target temperature since the aperture to space is blocked by the scan mirror. The power seen by the receiver during calibration is

$$P_{cal} = \epsilon\ B(T_c) + (1-\epsilon)B(T_0), \tag{2.1}$$

where $B(T)$ is the black body power at temperature T, T_c is the temperature of the target, and T_0 is the effective temperature of the surrounding instrument. If $T_c - T_0 = 10\,\mathrm{K}$, the effective emissivity is $\epsilon' = 1 - 0.03(1-\epsilon)$. However, even with the unrealistic assumption that $T_0 = 0\,\mathrm{K}$, ϵ is negligibly different from unity compared to the 99.9% requirement.

2.11 Accuracy

The systematic error sources in radiometric calibration are listed in Table 2.4. The total error indicated in the table is the straightforward linear sum of all of the listed components. In practise this worst-case error stackup is unlikely, and we can consider the the 0.45% error in calibrated radiance from the sources discussed in this chapter to be an upper limit.

Table 2.4: Systematic error contributions for GHz limb port radiances arising from radiometric calibration uncertainties, expressed as a percentage of reported limb radiance.

Calibration Target temperature uncertainty	0.1%
Standing Waves	0.1%
Switching Mirror Baffle uncertainty	0.15%
End-to-end linearity	0.1%
Total	0.45%

For the THz system ...

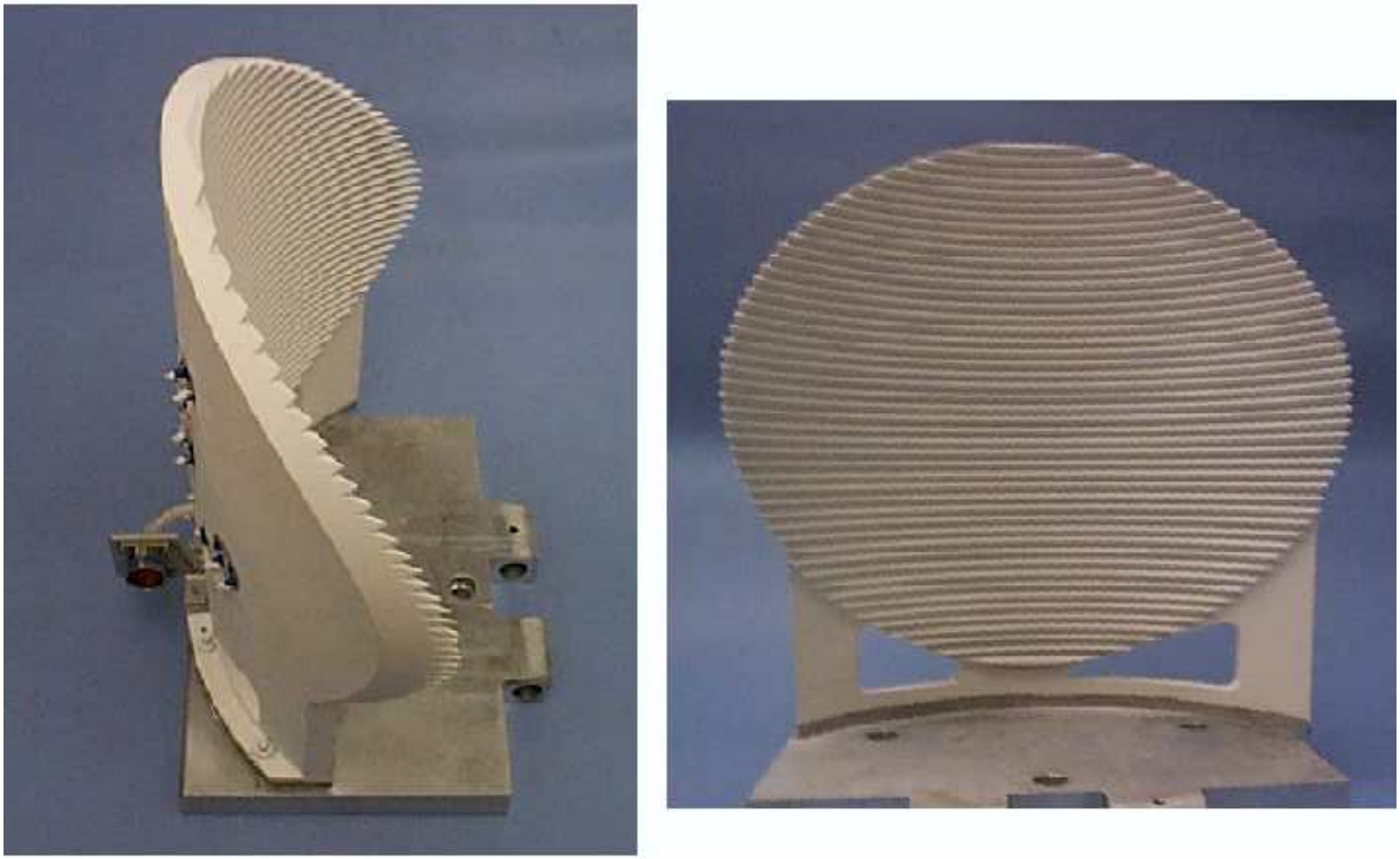

Figure 2.29: THz Module ambient radiometric calibration reference target. See text for additional details.

Chapter 3

Spectral Calibration

Spectral and FOV calibration shall be performed and provide the instrument relative response as a function of frequency and angle for each spectral channel.

The spectral and FOV responses of the instrument shall be characterized sufficiently that their separate uncertainties do not introduce uncertaincies in the MLS 'forward model' calculations of the atmospheric/Earth radiances of more than (at the 90% confidence level):

(1) *3 K in the absolute value of the atmospheric/Earth radiances measured through each spectral channel, and*

(2) *1% or $\Delta I_{min}/3$, where ΔI_{min} for each spectral channel is given in Table 3.2-2, in the spectrally-varying component of the atmospheric/Earth radiances measured from one channel or filter to another throughout a given radiometer.*

A portion of Table 3.2-2 is reproduced in Table 2.1 of this document. There are two major aspects to spectral calibration of EOS MLS:

(1) Measuring the precise location and shape of each channel response, and

(2) measuring the *relative* response of each channel in both sidebands (except for the single sideband R1A and R1B radiometer channels).

We accomplish this with two distinct measurement schemes: the channel shapes are measured end-to-end with a high-resolution fundamental sweeper, except for the THz channels for which no suitable sweeper currently exists; relative sideband responses are measured by observing thermal sources through scanning Fabry-Pérot interferometers. These two aspects of spectral calibration are the major subjects of the rest of this chapter.

3.1 High-Resolution Spectral Sweeps

The high-resolution spectral sweeps were based on the equivalent UARS MLS measurements, but with some implementation differences mainly directed towards improving the 'efficiency' of the measurement system. We discuss the setup used for GHz sweeps initially, then the

one used for THz sweeps. The GHz DACS were not swept using this system since (1) their channel shapes are readily determined analytically, and (2) they are designed to operate with 'noise' signals, not coherent ones, making it difficult to interpret the results of sweeps with a coherent signal source.

3.2 Description

The basic calibration setup is illustrated in schematic form in Figure 3.1, with a picture of the setup in the 'near-field' configuration used for the majority of the definitive calibrations in Figure 3.2. With the GHz module Switching Mirror directed at the Space Port, focussing mirrors LSC1 and LSC2 direct the receiver FOVs to the fundamental signal source (horn) via external switching mirror SW1. This external switching mirror is also able to direct the receivers FOVs towards an LN_2-cooled target for periodic radiometric gain determination.

The second (ambient) radiometric calibration point is provided by directing the receiver FOVs towards the source, with the source frequency set 'out of band.' The timing of the cold and ambient calibration views is described further in Section 3.6. It should be noted that the option existed with this setup to provide views to either of the internal GHz module ambient calibration targets, or an external one selectable via SW1 (labelled UARS external Hot Target). Adding views towards any of these targets would have involved a trivial software change, but was not found to be necessary. The UARS external Hot Target was the one used as the temperature-varying scene during linearity measurements discussed earlier in this document. Note that no hardware reconfiguration is required to switch between the high resolution sweeps discussed here and the linearity measurements described earlier – the only change required is to the software in the controller unit operating SW1. A good example of the flexibility of the calibration setup shown in Figure 3.2 is that in order to perform near-field FOV calibrations it was merely necessary to command the GHz Switching Mirror (not visible in Figure 3.2) to direct the receiver FOVs towards the Limb port – no changes were needed to the other two calibration setups shown in the figure in order to support NFR activities.

The lens and absorbing iris in Figure 3.2 serve two main purposes:

(1) The lens was positioned (differently for each radiometer being swept) to approximately match the source and receiver beamwidths.

(2) The absorbing iris was positioned as required to limit source intensity to the required level. In practise we maintained an interchangeable family of irises (with different aperture diameters) that were used as needed.

For some measurements it was found to be necessary to have 2 irises in series to reduce the incident source power to an appropriate level. A waveguide vane attenuator between source and horn was also used for coarse-tuning of the source amplitude. Instrument IF Attenuator levels were typically set for about 3 dB more attenuation than 'nominal' during these measurements as a compromise between resolution and dynamic range. Source power was kept constant for each sweep, and signal levels verified (and adjusted if necessary) as part of the 'quick look' sweep performed prior to the sweep of each band. In many cases the quick look data indicated correct signal levels, and the sweep was allowed to continue to cover the entire band without further adjustments or interruption.

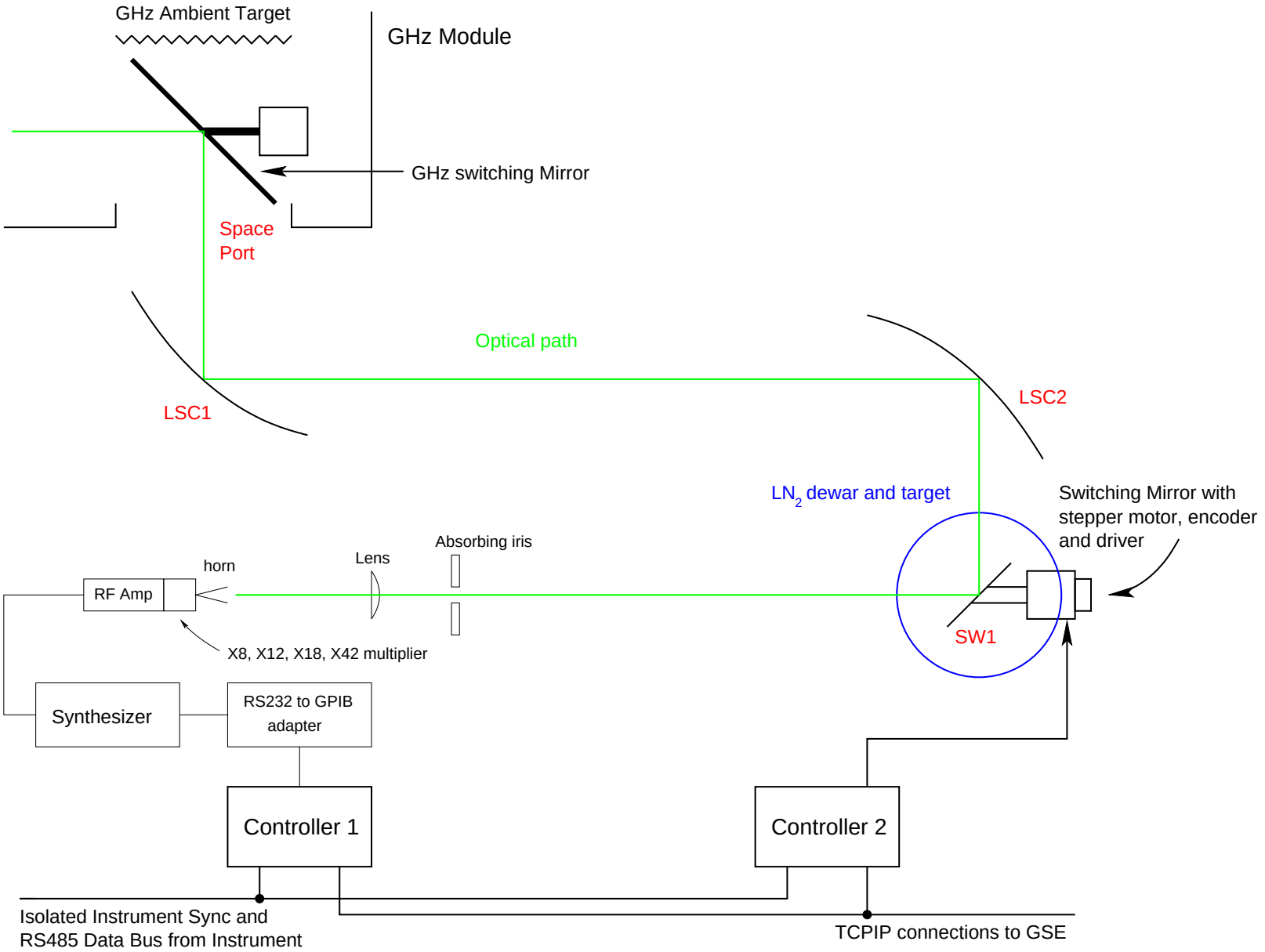

Figure 3.1: Schematic of the high-resolution fundamental sweeper system used for end-to-end measurements of channel shape for all GHz filter channels. See text for additional details.

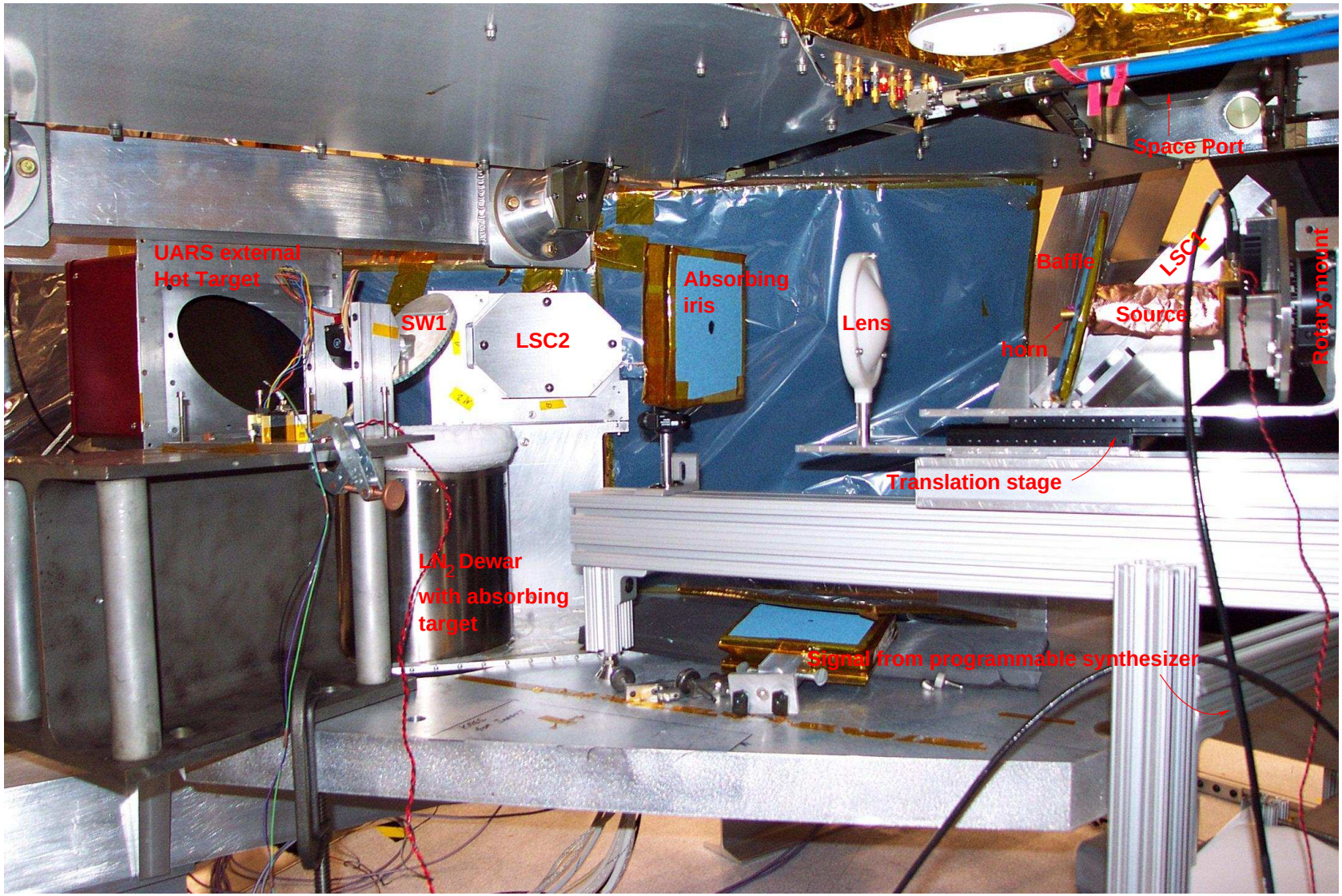

Figure 3.2: Front-end sweep calibration apparatus in the NFR configuration. See text for additional details.

The two controllers shown in Figure 3.1 are the same ones described in further detail in Appendix F, and are not discussed further here.

3.3 Similarities with UARS

The measurement system described here has several similarities to the one used for the equivalent UARS MLS calibrations:

- ❏ The measurement sequence was computer controlled,
- ❏ both sidebands of all GHz bands were swept (except for the single-sideband 118 GHz radiometers),
- ❏ all Filterbank Switch settings (signal paths) were swept,
- ❏ an internal calibration target and an external LN_2–cooled target provided periodic radiometric gain references, and
- ❏ the fundamental frequency source was phase locked to a precision reference so as to eliminate any errors in the frequency domain for these measurements.

3.4 Differences from UARS

Of more importance than the similarities to the UARS setup are the differences:

- ❏ Control in the UARS setup was provided by the GSE computer, whereas in this setup the controllers were custom-built for the task.
  - ⇨ The UARS setup exhibited large latencies between commands being sent to the calibration equipment (to move the switching mirror and step the synthesizer) and the results of these commands being reflected in the returned instrument data.
  - ⇨ The controllers for these calibrations monitored internal instrument bus traffic via an isolated RS-485 data/sync port, allowing the calibration equipment timing to be precisely synchronized with instrument operation and data integration.
    - ➳ An additional consequence of the large latency in the UARS setup was that individual data integrations were substantially longer than dictated by S/N considerations, adding further to the overall measurement time. This resulted in less than 30% of 'wall clock' time contributing useful data, and sweep times of ∼8 hours for a single 15-channel filterbank in one sideband.
    - ➳ In contrast, ∼90% of 'wall clock' time contributed useful data for the EOS MLS sweeps, with complete 25-channel filterbank sweeps taking 1 hour, including validation of the data in real-time.
- ❏ The controller software used to operate the synthesizer provided a startup mode in which each spectral sweep was preceded by a 'signalling' MAF in which the synthesizer was commanded to inject a spectral signature into the center of the lowest frequency channel of the filterbank(s) being swept during MIFs 20 to 40 and 60 to 80, with an 'out-of-band' signature for the remainder of that MAF.

- ⇨ This startup signature provided a reliable timing marker which allowed both quick-look and definitive calibration software to precisely identify the content of each MIF for the remainder of the spectral sweep. With the ability to validate measurements in near real time it was often possible to start new sweeps of 25-channel filterbanks (with ∼2,900 individual sweep frequencies) just over an hour apart.

❏ The good coupling between receivers and sources led to inevitable standing waves for many of the measurements, particularly at the lower sweep frequencies. A translation stage provided a simple means of reliably shifting the source by $\frac{\lambda}{4}$ to determine the level of these artifacts.

- ⇨ For each receiver being swept, abbreviated sweeps of the first few channels of a band were performed with the source in nominal and $\frac{\lambda}{4}$-shifted positions to determine the level of the standing waves.
- ⇨ If noticeable standing waves were present, the entire sweep was then performed with both nominal and shifted source positions, and the data from the sweeps combined to reduce the effect of the standing waves to negligible proportions.

❏ The sources were mounted on a rotary stage to allow for simple adjustment of source polarization. Attempts to measure both polarizations of the 118 GHz receivers simultaneously by judicious selection of source polarization were not successful because of the difficulty of maintaining satisfactory signal levels in both radiometers throughout a complete sweep.

❏ No monitor was used to measure source power during the course of these sweeps after it was noted that measured source power appeared to vary by unreasonable amounts during the sweep of some filterbank channels. This artifact was later determined to be due to the rapid variations (versus frequency) in the levels of unwanted harmonics generated by the multiplier chains following the synthesizer. The level of the desired harmonic from the multiplier chain remained essentially constant over the frequency span of even the widest filter channel, but the *total* RF power level emitted by the source was sometimes seen to vary by up to a factor of ∼2 across the same frequency range. Comparison of sweeps of a given channel in both of its sidebands indicated negligible variation of desired signal power over the frequency range of an individual channel.

❏ It can be seen from Figure 3.2 that the source (amplifier and multiplier chain) are wrapped in copper foil. This was found to be necessary because of the unfortunate positioning of this active signal source close to the GHz Space Port, with signal leakage from the waveguide joints into the signal path. These leakage signals interfered with the signals from the intended signal path, with unacceptable results. Judicious application of copper tape was sufficient to completely eliminate this problem.

3.5 Alignment

In order to provide adequate and reliable signal levels in all bands, it was necessary to precisely align the optical signal paths. The alignment of LSC1, LSC2 and SW1 was achieved by

observing an LN_2–cooled target through an irised absorber positioned as shown in Figure 3.2. The iris diameter was chosen to be similar to the expected beamwaist size[1], and the iris was moved to the calculated position of the expected beamwaist. The LN_2–cooled target was viewed through a suitable 45° reflector, and was sufficiently oversized that neither its precise location, nor the alignment of the 45° reflector, were critical.

Mirrors LSC1 and LSC2 were accurately located and oriented by means of shims, using the tooling balls (visible on LSC2 in Figure 3.2) on both focussing mirrors and the periphery of the GHz Module Space Port in conjunction with metering rods to provide mechanical alignment data. Mirror SW1 was then positioned to intercept the beam from the receivers at its center, and to direct the beam towards the iris in the absorber. This involved translating and rotating the mirror mount, and also fine-tuning the mirror rotation using the microstepping ability of the motor controller. This task was greatly facilitated by the use of an ultra-low-noise power meter designed and built especially for this task, which provided a real-time measure of the IF power in any chosen Band. Signal input to this power meter was provided by including a coupler in the IF cable running between Radiometer and Spectrometer Modules. The power meter had sufficient resolution that the signal contribution of the LN_2-cooled target viewed through the absorber iris could be maximized (i.e., IF power minimized) easily by minor adjustments to the locations and orientation of the optical components. Once this portion of the alignment process had been completed, all that remained was to position the source horn in line with the center of the iris and SW1, and to rotate the source about the center of the horn aperture (if needed) to maximize signal (i.e., obtain the correct source polarization orientation). This entire process took about 1 hour when first performed, and then 5 to 20 minutes after each change of signal source.

3.6 Measurement Timing

Figure 3.3 details the measurement timing common to all high resolution spectral sweeps. The timing sequence closely resembles the nominal in-orbit sequence for MLS, with the Limb viewing portion of each MAF (the first 120 MIFs) devoted to source measurements, and the 'radiometric calibration' portion at the tail of each MAF used for radiometic gain and offset measurements. This afforded the possibility of using Level 1 software to process these data to take advantage of the ensuing gain and offset interpolation benefits. In practise we found the high S/N ratio and low drifts of these data (due to the fast measurement sequence) allowed processing of the Level 0 data to final form with straightforward IDL routines, and without the need for use of any Level 1 processing capabilities. This is in constrast to the relative sideband measurements discussed later in this chapter, where timing very similar to that described here was chosen, but the much longer measurement times and subsequent data processing benefited greatly from an initial Level 1 processing step.

As can be seen from Figure 3.3, the first 120 MIF (20 s) of each MAF are used for 20 measurements of the swept source, with the source being stepped to its next frequency in the first MIF of each 6 MIF (1 s) time period. This aggressive timing was made possible by:

(1) the use of very efficient (low latency, interrupt driven) code in the synthesizer

[1]The calibration optics were designed to produce a convenient beamwaist which moved laterally by only a few inches with radiometer selection. The variation in beamwaist size with radiometer was accomodated by having a small collection of irised absorbers on hand.

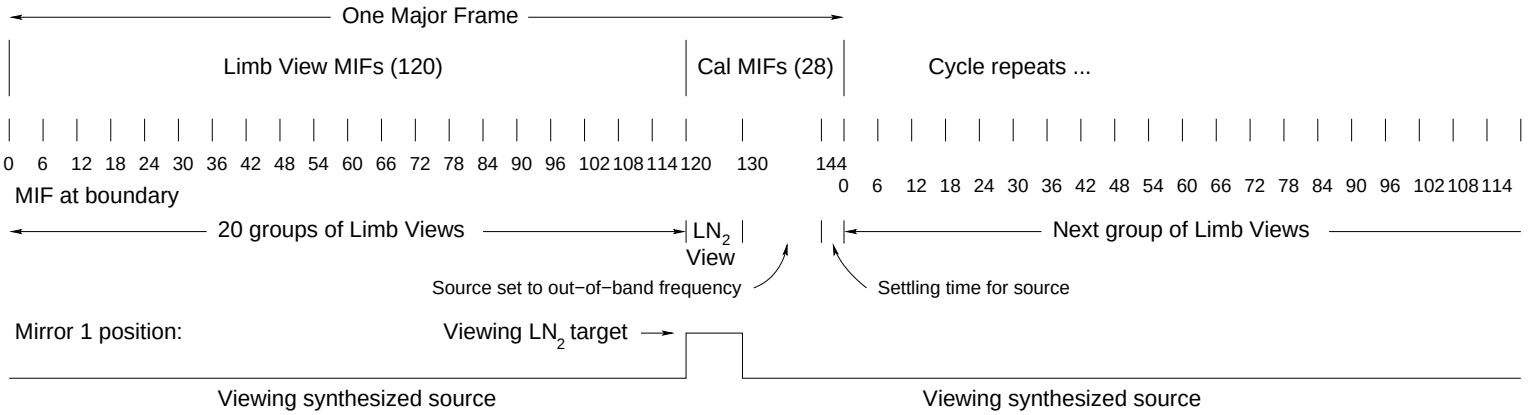

GSM: Always views Space Port

External Mirror 1: @MIF 120 move to LN2 view. @ MIF 130 return to view the synthesizer/multiplier output.

The following Level 1 overrides assume that Switching Mirror 1 completes its commanded motion in 1 MIF.

Level 1 overrides: (approximate)

T = MIFs 134..144. Use temperature of Internal Target in data processing.

S = MIFs 121..130. Assume 80 K temperature for LN2 view.

L = remaining MIFs, which are views to the synthesized source:

20 consecutive synthesized source views each of duration 6 MIFs starting at MIF 3, with the 1st. MIF of each set discarded (to allow the synthesizer/multiplier combination to step−and−settle).

Note: the raw data from these measurements were found to benefit only marginally from processing to Level 1, and the definitive calibration data were processed to final form directly from Level 0 'counts' using straightforward IDL procedures.

/users/jarnot/texinput/figures/FEsequence.fig

Figure 3.3: Front-end sweeper timing diagram. See text for additional details.

controller, which also

(2) maintained precise synchronization between instrument and controller operation, and by

(3) use of a synthesizer with appropriately fast step-and-settle time.

The source viewing sequence was followed by a view to an LN_2-cooled target, with just over 1 s of valid cold target views (limited by the ∼0.3 s taken for SW1 to step-and-settle). The measurement sequence for each MAF ended with a ∼1 s dwell viewing the source, but with the source frequency set out-of-band. This view served as a reference to be subtracted from each active source view, corresponding to the Space view during in-orbit operation. A 4 MIF ($\frac{2}{3}$ s) settling time was allowed for the synthesizer/amplifier/multiplier chain prior to the start of the next measurement sequence.

The choice of an out-of-band reference view was not arbitrary:

- ❏ A view to the source, but with the synthesizer output turned off, would have resulted in a substantial 'thermal tail' as the synthesizer and amplifier/multiplier chain settled after the drive signal was restored.

- ❏ Directing the receiver FOVs towards an ambient target via SW1 would have resulted in a reference view that was not at the same level as the signals to which it was being compared, due to differences in temperature and matching between the two loads.

  - ⇨ In addition, the RF source would still have had to be suppressed during the reference measurements to avoid low-level source leakage into the signal path, and this would have resulted in the potentially substantial, and undesirable, thermal settling times mentioned above.

- ❏ An out-of-band reference provides nominal signal power into the IF amplifiers at all times during the sweep. This is very important when one wishes to obtain the best possible data with measurements of this type, since changes in signal levels anywhere in the passband of an RF amplifier will have an effect on the signal levels at other frequencies within the amplifier passband.

3.7 Measurement Time

For convenience each filter channel was swept with 100 uniformly spaced frequencies across its nominal passband. In order to accomodate the wings of the outermost channels of each filterbank, 2 additional 'dummy' channels were assumed to be present at each filterbank edge, with the same characteristics as the outermost channels of each filterbank type. As a consequence of this, a 25-channel filterbank was swept as if it had 29 channels, requiring 2,900 measurement frequencies. Each 11-channel filterbank was assumed to have 15 channels, and required 1,500 measurements points for each sweep.

From Figure 3.3 it is apparent that a 25-channel filterbank sweep took 2,900/20=145 MAFs, with 1 additional MAF at the start of the sweep for timing synchronization. The instrument was operated at its nominal 6 Hz MIF rate for these calibrations, thus requiring 60 minutes to complete such a sweep. The corresponding calculation for an 11-channel

filterbank indicates a sweep time of 31 minutes. The 12 individual Wide Filter channels were swept assuming a single virtual channel of the same nominal width on either side of each channel, meaning that 300 points were swept during each calibration, taking 7 minutes for the sweep of each channel of this type. These times were of course doubled for all bands that were swept with nominal and $\frac{\lambda}{4}$–shifted source positions.

3.8 Additional Details

Several factors came into play which prevented these measurements from being completely turnkey, all of them attributable to less-than-perfect sources used to generate the fundamental frequency sweep signals.

3.8.1 Negative Filter Responses

One of the most disconcerting effects noted during these calibrations was that the upper sideband response of Channel 3 in Band 33 (a Wide Filter in R3) appeared to go negative at one side of the filter. This was clearly a problem in which the out-of-band signal was not completely out of band, and after a little discussion, calculation and data analysis it became clear that the 17th. harmonic of the synthesizer was passing through the lower sideband response of this channel as the 18th. harmonic was sweeping the upper sideband response. This led to the obvious solution of sweeping this channel in the upper sideband with the 17th. harmonic of the synthesizer, something that the controller software was flexible enough to accomodate readily with no code changes.

3.8.2 Source Level Shifts

A problem which affected several channels (Band 11, usb, channels 1 and 2; Band 12, lsb, channels 17, 20 and 23; Band 14, lsb, channels 4 and 19) was that of small, abrupt level changes part way through the sweep. The cause of this shifts was determined to be the sudden turn on (or off) of an unwanted mode in the the multiplier chain. This unwanted mode was always outside the passband of the filter being swept, and it was these modes that prevented the reliable use of an RF power monitor to measure source power during the sweeps. These level changes were handled relatively trivially in the analysis software by identifying the exact MIF at which the level jump occured, and simply scaling the measured signal on one side of the level shift to eliminate the discontinuity in the data.

3.8.3 Spurs

The spurs which generated the undesirable effects discussed above sometimes manifested in another way; when the sweep data for all channels of a spectrometer were plotted together, in some Bands an undesired harmonic response of the sweeper/multiplier could clearly be observed traveling through the opposite sideband. When this unwanted signal approached the desired signal in IF space, two competing signals swept a channel simultaneously. This affect was large enough to cause obvious and unacceptable distortion when sweeping channels 2 and 3 of the upper sideband of Band 11. Closer examination of the data revealed the 41st. harmonic of the synthesizer was sweeping these channels in the lower sideband while the 42nd. harmonic swept them in the upper sideband. Instead of sweeping the filterbank

with a 41st. harmonic (a solution corresponding to the one described earlier), an analysis solution was adopted. Since the filter shapes had been measured in the lower sideband, these responses were mirror imaged, scaled and shifted, then subtracted from the defective upper sideband sweep data. This resulted in good final data for the afflicted upper sideband channels.

3.9 THz High Resolution Sweeps

Due to the absence of suitable fundamental sources for sweeping the THz bands, we chose to perform sweeps of all THz 25-channel filterbanks through the 1st. IFs. These sweeps were performed with the output of the synthesizer shown in Figure 3.1 fed directly to the THz IF inputs. The software in the controller operating the synthesizer was designed to handle sweeps in this configuration as well as the GHz ones just described. For convenience, the THz sweep data were processed in the same manner as the corresponding GHz data, and channel shape plots and data files produced for both sidebands, as described in the following section.

3.10 Description of High Resolution Sweep Data

All high resolution sweep data are in a common format, and graphical data for all channels are presented in Volume 3 of this report. Below we present data for R1A in order to describe details of the data formats. Figure 3.4 is a quick-look plot of these data for all 25 channels of Band 1, each channel normalized to unity peak transmission. These data are plotted twice since they were taken with the source in its nominal and shifted position. The shifted source position was achieved using a micrometer driven translation stage, and the source was shifted by $\frac{\lambda}{4}$ (of the band center frequency) to reverse the phase of standing waves in the measurement path. The data from each channel was combined (to reduce standing wave artifacts) and filtered (to reduce noise), shown in Figure 3.5 for the first 4 channels of R1A Band 1. The bold blue line is the measured response on a linear scale after smoothing, and the green line is the same data plotted on a logarithmic scale. The blue line (smoothed data) is plotted over the unsmoothed data (black line), occasionally visible in the plots. The parameter fc is a smoothing parameter applied to the data as part of the data analysis, and was chosen for each channel to reduce noise without introducing any significant shape artifacts. All channels are plotted with 300 equally-spaced data points, centered at the nominal channel center position. For most channels the adjacent ones are of different nominal width, and for these channels the data are interpolated onto a frequency axis that provides data at the desired equally-spaced frequency points. Also included on these plots are the measured channel center frequency (cf, in IF space), and 3 dB width (width) in units of MHz. The numbers in parentheses after these parameters are their nominal values. Most bands can be analyzed by more than one filterbank spectrometer, so the plots of Volume 3 include all possible data paths through the instrument, and include sweep data for the 11-channel spectrometers and Wide Filter channels. DACS data are not included because they were not measured by this technique. THz data are included, but since front end sweeps were not possible for these channels, 1st IF sweeps were performed instead.

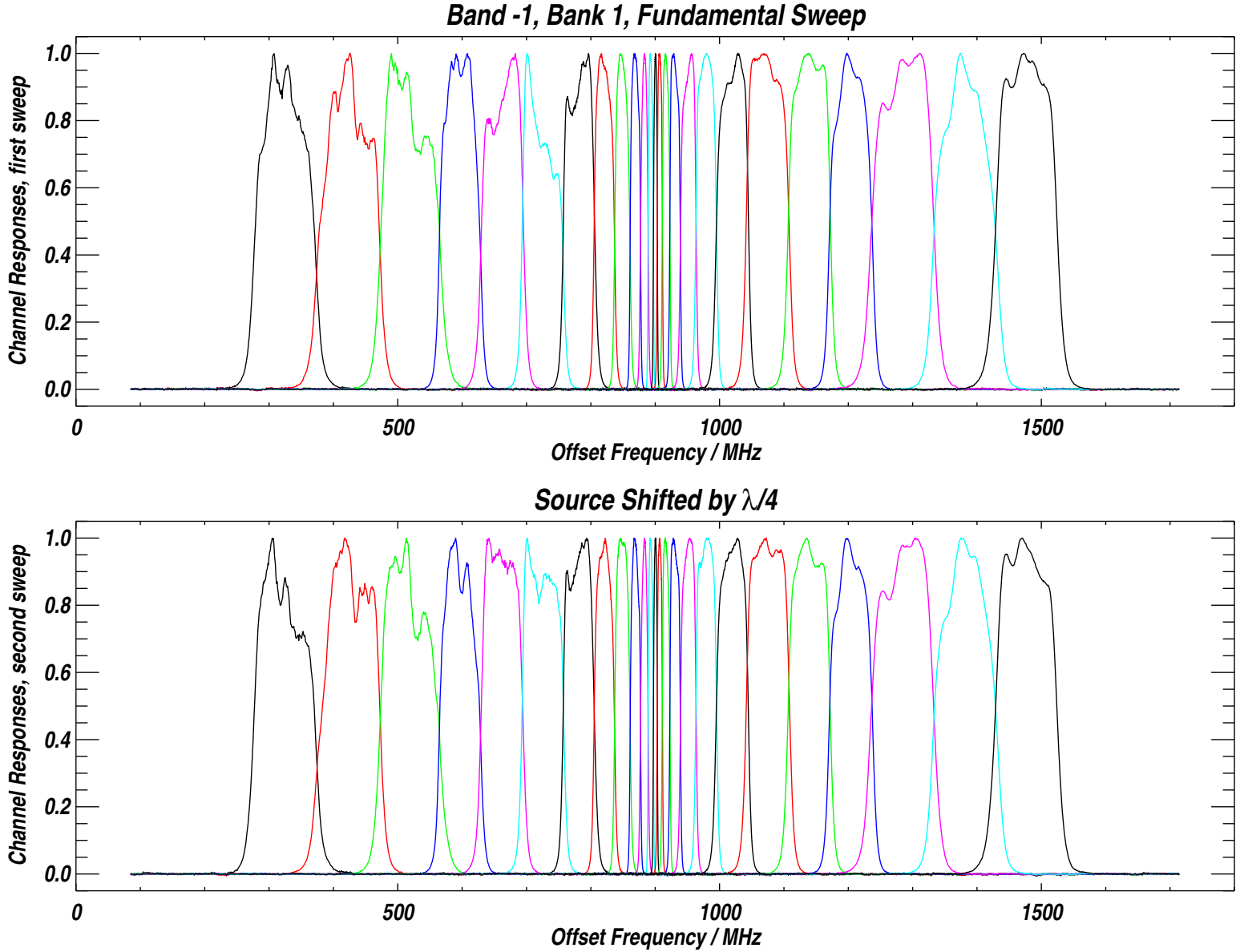

Figure 3.4: Front-end sweep data for Band 1 taken via Filterbank 1. For this measurement the sweep was performed twice, with the source moved towards the instrument by $\frac{\lambda}{4}$ (of the band center frequency). See text for additional details.

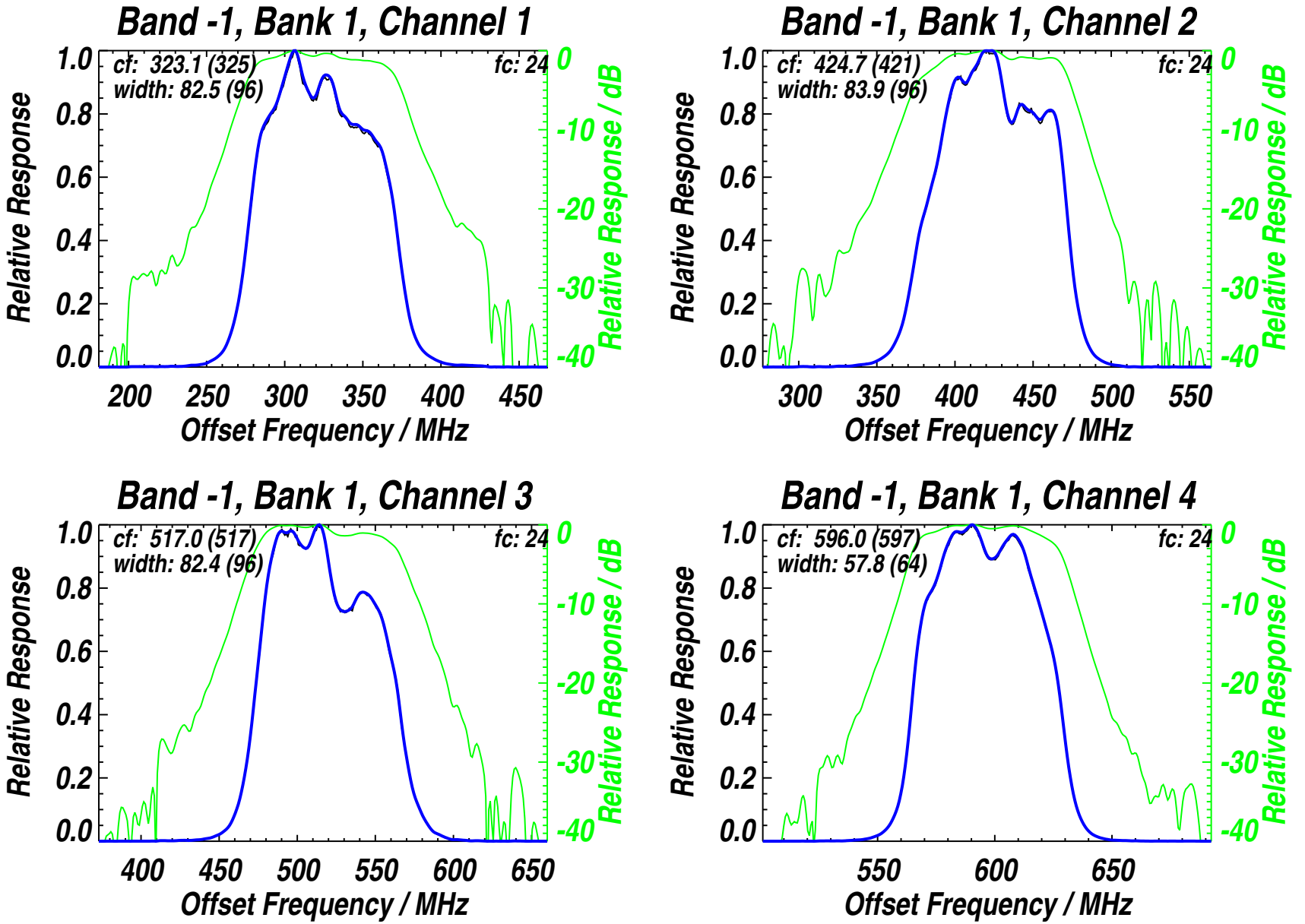

Figure 3.5: Front-end sweep data for Band 1 taken via Filterbank 1. For this measurement the sweep was performed twice, with the source moved towards the instrument by $\frac{\lambda}{4}$ (of the band center frequency). See text for additional details.

All sweeps were performed from low to high frequency, implying that the 'zero IF frequency' listed in the data files is only at the 'zero' frequency of the spectrometer input for about one half of the bands swept. For the remaining bands the 'zero IF frequency' corresponds to a frequency translated by 1,800 MHz from the true 'zero IF frequency.' Bands with no visible standing waves (as determined by performing a quick-look sweep with the source in its nominal and $\frac{\lambda}{4}$-shifted position) were swept once in each sideband. For double sideband radiometers, $\frac{\lambda}{4}$ was determined separately for each sideband (based on the band center frequency).

In addition to the graphical presentation of the high resolution sweep data, these data were generated in text form suitable for reading directly by the Forward Model software [5]. An example of such a data file is presented below. Its header indicates the Band and sideband, the name of the data file, the filterbank used in the measurement, and the channel being presented. The name of the data file indicates the Band, filterbank, sideband and channel. A letter m before the band number indicates lower sideband data. The smoothing parameter, fc, is presented next, and then some derived parameters: the signal and noise bandwidths; the center position of the channel in IF space; the channel's -3, -10 and -20 dB points and widths; the frequency in RF space that represents 'zero' IF frequency; the offset from 'zero' IF frequency of the first data point of the file, and the frequency spacing of each data point. The 300 data points that follow are the normalized channel transmission (linear).

The units of all parameters are given in each data file, except for fc, which is normalized to nominal channel width, and selected so as not to distort the filter shape. Smoothing was performed with a 2nd order low-pass Butterworth amplitude response (but perfect phase response) filter applied to the fourier transform of the measured amplitude response. The -3 dB point of the smoothing filter is at a frequency $\frac{fc}{F}$ where F is three times the nominal filter -3 dB width.

The data file corresponding to Band 1, channel 1, filterbank 1, lower sideband, follows:

---

1 ; Band (lsb) – /nas/gse/data/FESweep/Band1/Bandm1Bank1Chan1.dat
1 ; Bank
1 ; Channel
24 ; fc, smoothing parameter
82.5189 ; Signal bandwidth / MHz
108.431 ; Noise bandwidth / MHz
323.057 (325 nominal) ; Center frequency / MHz
277.987 369.945 91.9578 ; -3 dB points and width / MHz
265.028 383.140 118.112 ; -10 dB points and width / MHz
248.470 404.109 155.639 ; -20 dB points and width / MHz
117.853333328 ; Zero_IF_frequency / GHz
181.000 ; offset frequency of first data point / MHz
960000 ; frequency increment / Hz
0.0000000E+00 1.7808839E-05 2.8244805E-05 3.0900101E-05 3.9520131E-05 6.1056489E-05
8.7842775E-05 1.1146389E-04 1.3341014E-04 1.5714085E-04 1.7831627E-04 1.7409831E-04
1.2647764E-04 4.5810179E-05 4.6294055E-05 1.3679211E-04 1.9878829E-04 1.8263889E-04
3.3010368E-05 2.6669732E-04 6.6809065E-04 1.0499441E-03 1.3043691E-03 1.3962338E-03
1.3600069E-03 1.2928202E-03 1.2858604E-03 1.3520581E-03 1.4291975E-03 1.4950546E-03

1.5163118E-03 1.4713050E-03 1.4183157E-03 1.4481875E-03 1.5619047E-03 1.6350832E-03
1.5319078E-03 1.2617701E-03 1.0590776E-03 1.1354755E-03 1.4169234E-03 1.6226093E-03
1.6775610E-03 1.6089807E-03 1.5117852E-03 1.5279144E-03 1.7499159E-03 2.1204082E-03
2.4698188E-03 2.5836250E-03 2.3979070E-03 2.0886764E-03 1.9044284E-03 1.9152710E-03
2.0340523E-03 2.1846488E-03 2.3781217E-03 2.6986571E-03 3.2288425E-03 3.9785001E-03
4.8063709E-03 5.4673324E-03 5.7986910E-03 5.8570174E-03 5.8975774E-03 6.1610807E-03
6.6992729E-03 7.4141608E-03 8.1395358E-03 8.8278577E-03 9.6625751E-03 1.0862950E-02
1.2582210E-02 1.4829019E-02 1.7354982E-02 1.9884789E-02 2.2386631E-02 2.5052819E-02
2.8119568E-02 3.1713050E-02 3.5814356E-02 4.0388886E-02 4.5640238E-02 5.1978894E-02
5.9778064E-02 6.9213778E-02 8.0255002E-02 9.2709906E-02 1.0648239E-01 1.2174036E-01
1.3886473E-01 1.5825684E-01 1.8018559E-01 2.0479198E-01 2.3220301E-01 2.6268184E-01
2.9644474E-01 3.3344343E-01 3.7313843E-01 4.1458982E-01 4.5674703E-01 4.9881127E-01
5.4039860E-01 5.8119100E-01 6.2046748E-01 6.5701866E-01 6.8925136E-01 7.1581030E-01
7.3626381E-01 7.5136149E-01 7.6276451E-01 7.7219510E-01 7.8068048E-01 7.8869915E-01
7.9629958E-01 8.0332440E-01 8.1014925E-01 8.1785077E-01 8.2754689E-01 8.3978754E-01
8.5415220E-01 8.6970788E-01 8.8570613E-01 9.0195656E-01 9.1845524E-01 9.3491381E-01
9.5110327E-01 9.6682203E-01 9.8127419E-01 9.9291486E-01 9.9983954E-01 1.0000000E+00
9.9239159E-01 9.7786099E-01 9.5869517E-01 9.3796706E-01 9.1879421E-01 9.0289825E-01
8.8989741E-01 8.7858713E-01 8.6823517E-01 8.5905635E-01 8.5236704E-01 8.4989572E-01
8.5266250E-01 8.6073667E-01 8.7332404E-01 8.8811189E-01 9.0208292E-01 9.1300941E-01
9.1990811E-01 9.2296439E-01 9.2310929E-01 9.2111701E-01 9.1663992E-01 9.0854782E-01
8.9604712E-01 8.7923747E-01 8.5953504E-01 8.3958948E-01 8.2224649E-01 8.0942053E-01
8.0130553E-01 7.9633600E-01 7.9209197E-01 7.8682190E-01 7.8035307E-01 7.7392000E-01
7.6917881E-01 7.6685923E-01 7.6640218E-01 7.6657861E-01 7.6604128E-01 7.6383787E-01
7.5986165E-01 7.5509006E-01 7.5105768E-01 7.4873358E-01 7.4780786E-01 7.4687517E-01
7.4451172E-01 7.4019861E-01 7.3408991E-01 7.2688222E-01 7.1967256E-01 7.1323937E-01
7.0752734E-01 7.0145124E-01 6.9307011E-01 6.8076545E-01 6.6435611E-01 6.4487350E-01
6.2375653E-01 6.0197699E-01 5.7940507E-01 5.5478662E-01 5.2657551E-01 4.9408710E-01
4.5775375E-01 4.1917282E-01 3.8048035E-01 3.4328842E-01 3.0814239E-01 2.7484089E-01
2.4305822E-01 2.1288277E-01 1.8502951E-01 1.6039331E-01 1.3940984E-01 1.2185682E-01
1.0710733E-01 9.4474263E-02 8.3491519E-02 7.3946901E-02 6.5697394E-02 5.8623634E-02
5.2587781E-02 4.7384638E-02 4.2844836E-02 3.8925894E-02 3.5549268E-02 3.2536190E-02
2.9720634E-02 2.7004279E-02 2.4378665E-02 2.1923296E-02 1.9711103E-02 1.7720969E-02
1.5906157E-02 1.4224607E-02 1.2686661E-02 1.1361247E-02 1.0321927E-02 9.5269298E-03
8.8205989E-03 8.0767730E-03 7.2671194E-03 6.5253209E-03 6.0315900E-03 5.9032249E-03
6.1216820E-03 6.4472677E-03 6.5922169E-03 6.4386125E-03 6.1001871E-03 5.7721231E-03
5.5443798E-03 5.3933575E-03 5.2406038E-03 5.0016344E-03 4.6988050E-03 4.4138362E-03
4.2086304E-03 4.0937508E-03 3.9998721E-03 3.7978853E-03 3.4284522E-03 2.9173025E-03
2.3237439E-03 1.6758981E-03 9.7060768E-04 3.1999176E-04 1.9937361E-04 5.0882535E-04
6.0669781E-04 5.7397893E-04 4.9485988E-04 4.1191975E-04 3.1896634E-04 1.5829300E-04
1.0271115E-04 4.1071614E-04 6.4806489E-04 7.0965156E-04 5.7424832E-04 3.3048916E-04
9.9319797E-05 3.3919212E-05 5.9288821E-05 2.5444080E-05 1.1773230E-06 2.2940635E-06
6.1382725E-06 2.6350132E-05 3.9189661E-05 8.2636609E-07 1.0658882E-04 2.3702644E-04
3.2775317E-04 3.4545682E-04 2.9997472E-04 2.2133012E-04 1.4590102E-04 1.0103512E-04
8.1393417E-05 6.5801272E-05 4.3702476E-05 1.6888755E-05 1.4353394E-06 0.0000000E+00

Due to the extremely large number of calibration data files of this type (over 2,000), we have chosen not to reproduce the rest of them in this report. They are all available on the EOS MLS central computer system starting at /gse/data/FEsweep/, with subdirectories for each Band. The naming convention of the files allows the data to be readily identified by filename alone.

3.11 Master Oscillator

Figure 3.6 shows Master Oscillator (MO) frequency trend data. A highly accurate timebase[2] was used by the frequency counter to eliminate errors in the measurement. The lower sequence of data points shows data for the A-side MO, and the straight line is a linear fit to the data. The upper data and fit are for the B-side MO. The A-side MO is planned to be the unit used nominally in flight, the other unit providing redundancy for this key signal source. The requirement on long-term stability for these frequency sources is for a deviation of less than 7×10^{-8} of the nominal 5 MHz starting frequency at the end of mission, approximately 6 years from the time these data were taken. Extrapolating the linear fits to these data indicates that the A-side MO will drift by 1.7×10^{-8} of the nominal start frequency after 6 years, and the B-side MO by a factor of 2.8×10^{-8}, thus meeting requirements with substantial margin. Qualification tests were run on both MOs to ensure that power cycling and temperature cycling effects will add sufficiently small additional errors that remaining margin will not be fully consumed.

We will be able to monitor MO drifts in orbit with the high spectral resolution DACS, and this is planned as part of the in-orbit performance monitoring and calibration activities.

3.12 Precision and Accuracy

The precision of the channel shape measurements can be estimated by reviewing the data presented in this document, and it is clear that precision is not a concern. Accuracy requirements for end-to-end channel shapes are in terms of percentage accuracy of measured radiance. The accuracy obtained from a particular channel thus depends upon the *shape* of the radiance profile across the channel bandpass, and is not a simply-derived quantity. A suitable method for estimating the accuracy for a given radiance profile is given in [3]. The method described there is to assume a 'worst case' radiance profile across a channel (i.e., one with large high order derivatives), and to determine the error in calibrated radiance as the filter shape is perturbed systematically from 'truth.' The most harmful error in filter profile is one in which the frequency axis is incorrect. This source of error is essentially nonexistent in both the instrument and calibration setup, since both are phase-locked to precise references. Should there be a drift in channel center frequency in the instrument, the on-board calibration synthesizer will be used to measure the shift, eliminating this a source of error. We do not anticipate any significant changes in filter shapes over the lifetime of the instrument due to the manner in which the LC filters were fabricated. The filterbank vendor (REMEC Inc.) has considerable experience building similar filters for hostile environments, and an important part of the filter tuning process involves annealing of the inductors to remove stresses

[2] A GPS-derived reference was used at JPL, and a rubidium standard during instrument integration at NGST.

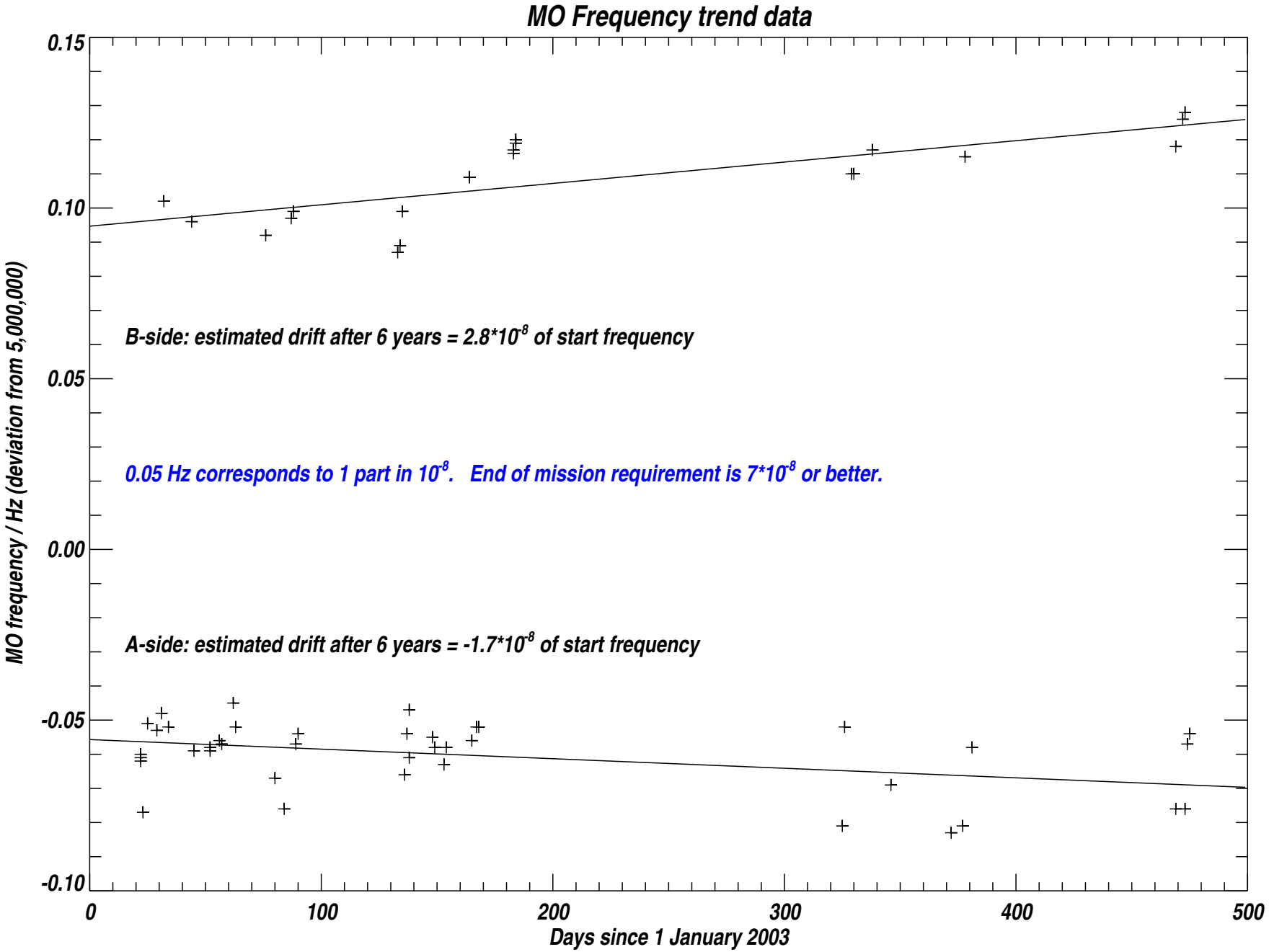

Figure 3.6: Trend data for the A- and B-side Master Oscillators. Data start in 2003, and proceeds into 2004. See text for additional details.

which might lead to future changes in characteristics. The temperature dependence of the filters has been measured by the vendor and verified at JPL, and is insignificant over the anticipated operating temperature range.

We are thus in the position that any known deficiencies in these measurements are sufficiently small that it is not possible to quantify the actual level of error in calibrated radiance, merely to be confident that the requirements are comfortably met.

3.13 Suggestions for future work

The measurements described above were carried out efficiently, and with few surprises, largely because the operation of all of the amplifier/multiplier chains, and the controller and quick-look software, had all been exhaustively verified before final calibrations were performed. An obvious area in which the setup could have been 'improved' would have been to replace the manual translation stage with a remotely controllable one (as used in the Relative Sideband apparatus). This would have alleviated the need for many of the trips into the High Bay[3] to manipulate the source position for those measurements which were done with nominal and translated source positions. For high measurement efficiency the front-end sweep measurements were performed with a two person team[4] so that setup could be performed simultaneously at the source (i.e., in the High Bay) and in the control room. Remote control of the source position would have reduced many of the measurements into a 1-person operation, and should be strongly considered for any future implementation of a calibration setup similar to this one.

3.14 GHz Relative Sideband Sweeps

Relative sideband calibrations of the UARS and EOS MLS GHz radiometers were both performed by observing external ambient and LN_2-cooled targets through a scanning linear Fabry-Pérot via the Space Port of the radiometer chassis. There are many significant differences in the implementation of the calibration hardware and software, as well as the software used to analyze the resulting signals, the intent being to apply 'lessons learned' from UARS to improve measurement efficiency as well as the end quality of the calibration product. These goals were achieved, and important details of the EOS implementation are discussed below. We also provide further details of the THz sideband calibrations, which of necessity differ quite considerably in detail from those performed on the GHz radiometers.

3.15 Differences from UARS

Significant differences between the UARS and EOS implementations of the GHz sideband calibrations, and the reasons for those differences, are:

- ❑ A compact mechanical setup was used for EOS GHz sideband calibration:

[3]High Bay ingress/egress required the tedious donning and doffing of clean room garments.

[4]I wish to thank Karen Lee for her valuable support during these measurements.

- ⇨ Reason: the large UARS MLS LSC[5] had no provisions for accurately orienting/positioning it with respect to the radiometer module. This gave rise to two main issues:
  - ➳ 1: Alignment of the LSC to the instrument was a relatively painful process, and
  - ➳ 2: the loose relative alignment between LSC and instrument meant that care had to be taken not to disturb the setup in any way during calibration measurements. In particular, the entire measurement setup was sensitive to floor vibrations, limiting the locations in which the calibration setup could be used without compromise.
- ⇨ The compact and more robust configuration of the EOS sideband calibrator, combined with its tight physical coupling to the GHz Radiometer Module, allowed it to be readily used in 2 convenient measurement configurations without undue concern for the operating environment. The cart configuration proved to be very useful prior to availability of the NFR configuration (Figure 3.8, used for definitive calibrations). In both configurations it was necessary to perform an optical alignment prior to the start of measurements, but the small size and weight of the calibrator (compared to the LSC) allowed this to be done with relative ease. In addition, tooling balls on sideband calibrator focusing mirrors (visible on the periphery of SW1 and LSC2 in Figure 3.8) allowed a precise initial setup of key components of the calibration system.

❑ Switching mirrors were used to direct the radiometer FOVs between external ambient and LN_2 targets:

- ⇨ Reason: Large rotating polarizers were used instead of switching mirrors (pre- and post-Fabry-Pérot) in the LSC to support system linearity measurements. These took about 1 minute to rotate by 90°, whereas the switching mirrors in the EOS calibrator completed their 90° movements in less than 3 MIFs ($\frac{1}{2}$ s), with Fabry-Pérot step-and-settle times of only 1 MIF ($\frac{1}{6}$ s).
  - ➳ 1: The slower switching of the UARS polarizers translated directly into increased drifts (inferior measurement precision and accuracy) as well as long measurement times.
  - ➳ 2: The improved efficiency of the EOS setup allowed sweeping of many more Fabry-Pérot orders with the EOS setup than was possible for the corresponding UARS measurements.
  - ➳ 3: In addition to increased measurement quality and efficiency, the precise timing control of the external switching mirrors and Fabry-Pérot allowed use of a measurement sequence compatible with Level 1 data processing software. This provided a valuable test of Level 1 processing software, in addition to the benefit of improved data quality.

❑ Calibration equipment operation was controlled by a bus-snooping interface:

[5] A combined Linearity-Sideband Calibrator (*aka* LSC) was used for UARS linearity and sideband calibrations.

- ⇨ Reason: The GSE computer was used on UARS to both record instrument data and to control the external calibration equipment. The large latency in data reception by the GSE (mainly introduced by the Spacecraft Simulator used to interface the Flight hardware to the GSE) meant that the GSE could not issue commands to the calibration equipment (e.g., 'move the Fabry-Pérot to its next spacing') until several seconds after the instrument had taken data at a given grid spacing.
  - ⋙ 1: The real-time bus sniffers monitor internal instrument RS-485 data traffic to determine 'time' in instrument coordinates (MIF number), and
  - ⋙ 2: use an interrupt generated by the instrument 'Sync' signal (end-of-data-integration timing marker) to trigger issuing of commands to the attached calibration equipment.
  - ⋙ 3: The efficient timing resulted in EOS sideband sweeps being performed in about an order of magnitude less time than it would have taken using the UARS equipment and timing methods.

- ❑ Level 1 software was used to process the instrument data prior to retrieval of sideband information:
  - ⇨ Reason: UARS sideband data processing was done in the filterbank 'count' domain. For EOS, the wider relative separation of sidebands meant that such details as variation of the Planck function between sidebands had to be taken into account. By using Level 1 software for initial processing of the sideband radiance data, details such as this were automatically taken into account, as well as compensation for gain and offset drifts.
  - ⇨ Note that the precise synchronization of the external calibration equipment to internal instrument operation was essential for this processing step to be possible.

- ❑ Data analyses for UARS treated the LN_2 view through the Fabry-Pérot as the signal of interest, whereas the corresponding EOS MLS analyses treated the *difference* between the ambient target and LN_2 views through the Fabry-Pérot as the signal of interest:
  - ⇨ Reason: To obtain the best possible sideband data signal quality it is necessary to provide excellent optical alignment between the instrument and calibration gear.
    - ⋙ 1: To minimize Fabry-Pérot walk-off losses, and to maximize signal amplitudes, it is necessary for the Fabry-Pérot grids to be both parallel to one another and orthogonal to the optical beam they are filtering.
    - ⋙ 2: This means that the receivers are 'seeing' themselves in reflection from the front of the Fabry-Pérot, with a reflection coefficient that varies with grid spacing, resulting in standing waves that add to the signals observed through the Fabry-Pérot, and which vary with grid spacing.
    - ⋙ 3: Since the radiance difference of interest for this measurement is that between the views to the ambient and LN_2 target seen through the Fabry-Pérot (for the same grid spacing, and hence with the same standing wave signature), this radiance difference has the standing wave artifacts removed.

- ➳ 4: UARS sideband calibration analyses were performed by fitting to just the LN_2 views through the Fabry-Pérot, with no subtraction of the ambient view data. Effort was made to reduce the magnitude of the standing waves in the data by tilting of grids, and the strategic application of absorbing irises at places in the optical path where unwanted reflections could arise. Even with such measures, the UARS sideband data were contaminated with residual standing wave artifacts.

❑ A least-squares fit between measurements and model were performed simultaneously for all channels in a 25-channel filterbank:

⇨ Reason: Atmospheric retrievals will be sensitive to channel-to-channel discontinuities in such calibration parameters as relative sideband response.

- ➳ 1: There is no reason to believe that relative sideband response will not vary smoothly across each EOS MLS measurement band, and
- ➳ 2: this should be reflected in the calibration data analysis method.
- ➳ 3: For UARS MLS, the sideband calibration data quality was such that only the outer 3 channels of each filterbank were analyzed, and a smooth function was fit to these results. Any information potentially provided by the remaining filterbank channels was discarded, primarily because of their larger standing waves, a problem eliminated with the EOS MLS measurement and analysis scheme.

3.16 Measurement System

A schematic of the relative sideband calibration system is given in Figure 3.7. This drawing is not to scale, and the view from the GHz Space Port to mirror LSC1 is vertically downwards in the NFR configuration used for definitive calibrations. The same schematic applies to the 'cart' configuration when the Space Port view is horizontal, but in this case LSC1 is replaced by a mirror with a different prescription. All other details remain unchanged.

The internal GHz switching mirror provides a view to an internal ambient calibration target, and external switching mirror SW1 provides a companion view to an LN_2-cooled target for periodic radiometric gain calibration. External focussing mirrors LSC1 and LSC2 produce a convenient beamwaist approximately 20 cm from SW1, and the view through the Fabry-Pérot continues to external switching mirror SW2, which switches between ambient and LN_2 views.

Important components of this calibration setup (also shared with the front-end spectral sweep calibrations), are the units labelled Controller 1 and Controller 2. Each of these units contains 2 microprocessors:

(1) An Atmel AVR device which snoops an optically-isolated connection to the internal instrument RS-485 bus which provides communications to all RIUs. This device decodes the internal instrument data traffic and uses the Sync signal from this bus to provide precise timing information to:

(2) a Rabbit Semiconductor TCP/IP-enabled system which generates and issues (via RS-232 ports) the control signals to the switching mirror and Fabry-Pérot controllers.

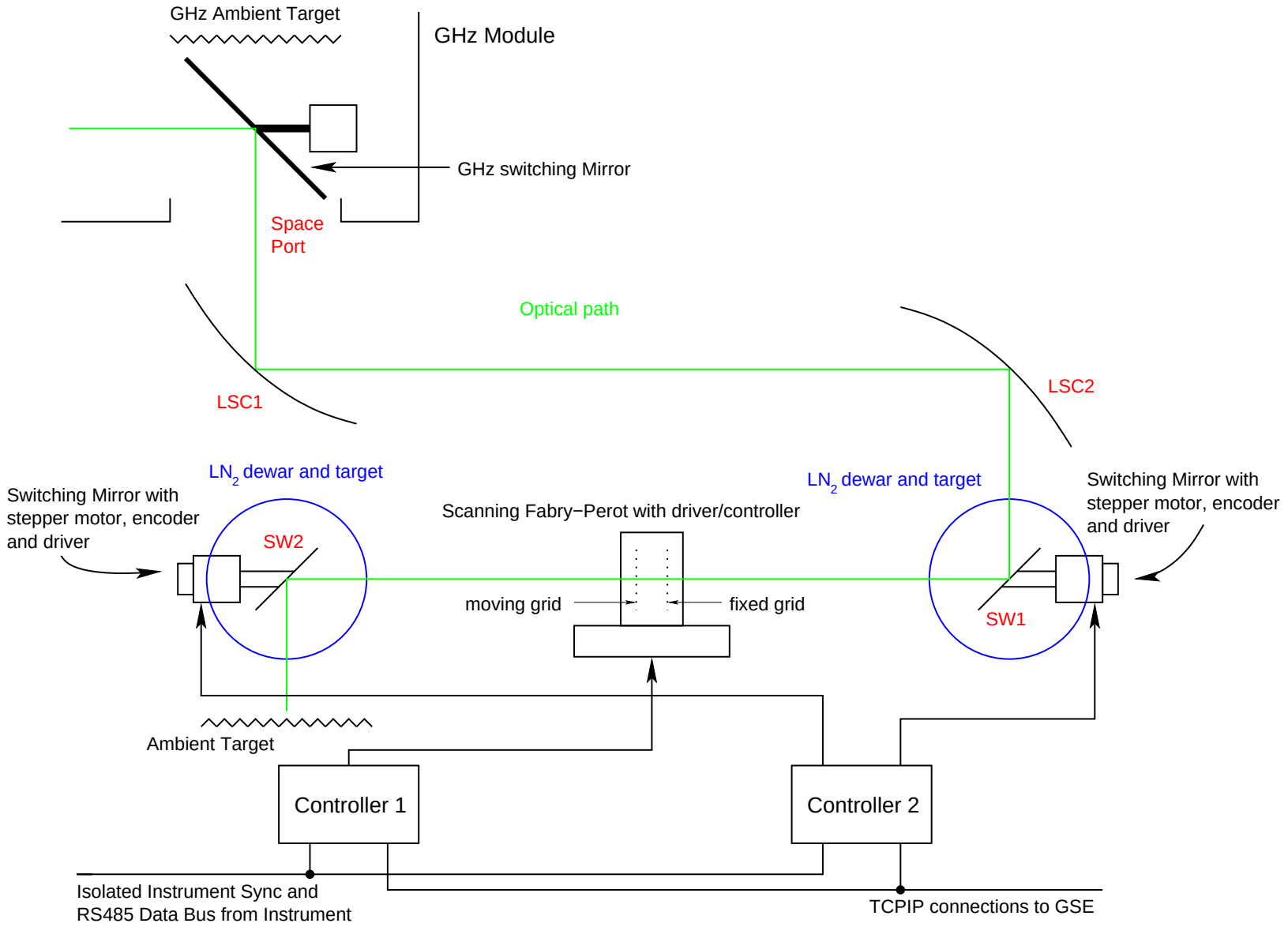

Figure 3.7: Schematic of relative sideband measurement system. The Fabry-Pérot grid closest to the space port (along the optical path) is fixed. See text for additional details.

Figure 3.8: Relative Sideband calibration apparatus in the NFR configuration. See text for additional details.

These Controllers were instrumental in achieving high efficiency in all linearity and spectral calibrations, and are described in more detail in Appendix F.

A photograph of the calibration setup in the NFR configuration is shown in Figure 3.8. This picture was taken during Engineering Model testing of the calibration apparatus, and no changes were required for definitive Flight Model measurements.

3.17 Measurement Timing

The nominal timing for this system is shown in Figure 3.9 for measurements in Bands 2 through 9. For the 640 GHz radiometer (Bands 10 through 14), the same switching sequence was used, but the Fabry-Pérot spacing was advanced only twice per MAF to partially compensate for the decreased signal-to-noise of the measurements from this radiometer. The switching rate between LN_2 and ambient targets behind the Fabry-Pérot was not reduced when the Fabry-Pérot stepping rate was halved, since this would have unnecessarily made the measurement system more susceptible to the effects of low frequency noise and gain variations.

Note that the Fabry-Pérot measurements are performed during the time alloted for limb views in the nominal GHz scan, and the radiometric gain calibration views take place in the interval alloted for in-orbit reference measurements. This ensured that the relative sideband data could be processed readily using standard Level 1 software. The only portion of the timing in which the instrument plays an active rôle is the GHz Switching Mirror view to the internal calibration target, once per MAF.

Figure 3.10 shows the raw data from a single MAF for Band 2, Channel 1. The data are plotted by MIF, and a small latency can be seen between the raw data and the nominal timing diagram in the previous figure. This arises because the calibration controllers trigger their actions based on the MIF number in the data packets being transferred within the instrument from each slave RIU to the master, and the Level 0 data of Figure 3.10 is labelled according to MIF number as generated by the C&DH when it assembles the data packets for transfer to the spacecraft. This latency was common to all calibration measurements which used the external controllers, and was entirely predictable, allowing it to be taken into account when implementing the controller and data analysis software.

Clearly visible in Figure 3.10 are the 4 views to LN_2 through the Fabry-Pérot during MIFs 4:16, 34:46, 64:76 and 94:106, with views through the Fabry-Pérot to an ambient target during MIFs 18:32, 48:62, 78:92 and 108:119. Ambient and LN_2 views to targets ahead of the Fabry-Pérot, used by Level 1 processing software for radiometric gain determination, occur during MIFs 135:147 and 123:133 respectively. Of note is the relatively rapid switching between the 2 targets behind the Fabry-Pérot, with only 1 MIF of data ($\frac{1}{6}$ s) overhead. The 4 views to the LN_2 target through the Fabry-Pérot can be seen to change (decrease) in count level as the grid spacing increases by 0.01 mm per measurement group, while the count level for views to the ambient target remain steady.

The entire data set taken with coarse (90 lines per inch) grids and processed to radiances (ambient minus LN_2 radiance viewed through the Fabry-Pérot) by Level 1 software for Bands 2 and 9, Channel 1 is shown in Figure 3.11. Channel 1 of Band 2 has the lowest center frequency, and narrowest sideband separation, of the bands swept with the coarse grids. Channel 1 of Band 9 has the highest center frequency, and widest sideband separation, of the bands swept with the coarse grids. The initial grid separation is $\sim$3.74 mm, and the entire

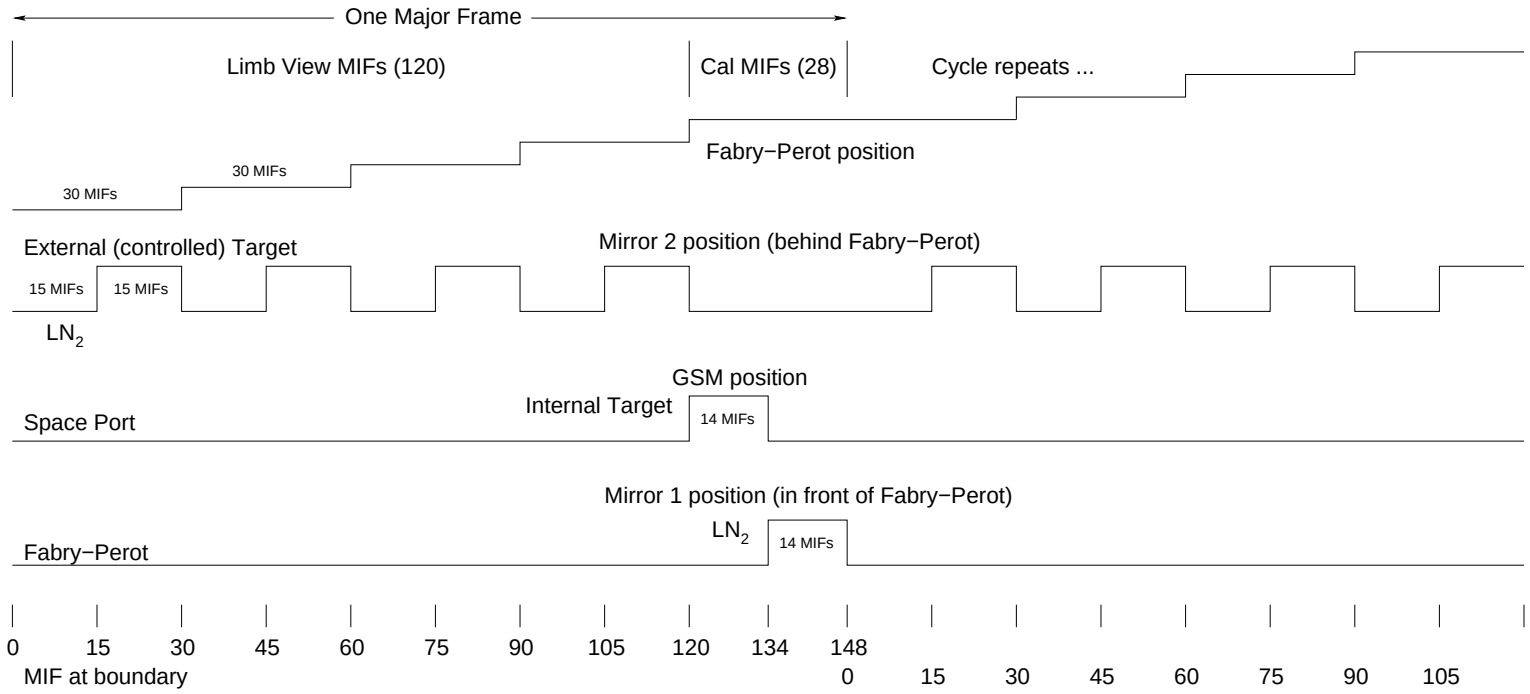

GSM: @MIF 120 move to Internal Target. @MIF 134 move to Space Port.

External Mirror 1: @MIF 0 (148) move to Fabry−Perot view. @ MIF 134 move to LN2 view

External Mirror 2: @MIFs 30, 60, 90 and 120 move to LN2 view. @MIFs 15, 45, 75 and 105 move to External (controlled) Target view.

Fabry−Perot movements are steps taking place starting at MIFS 30, 60, 90 and 120.

The following Level 1 overrides assume that the GSM and external switching mirrors perform their sequences exactly as indicated above, and that motions take 3 MIFs (or less) to complete (for all mirrors and Fabry−Perot).

Level 1 overrides: T = MIFs 123..133. Use actual temperature of Internal Target in data processing.

S = MIFs 137..147. Assume 80 K temperature for LN2 view.

L = remaining MIFs, which should be views through the Fabry−Perot as follows:

To LN2: MIFs 3..14, 33..44, 63..74 and 93..104. Assume T is stable (80 K).

To external target. MIFs 18..29, 48..59, 78..89 and 108..119. Assume temperature is stable (30 C).

The remaining MIFs should all be Discards (due to mirror/FP movement).

/users/jarnot/texinput/figures/FPsequence.fig

Figure 3.9: Relative sideband calibration timing. See text for additional details.

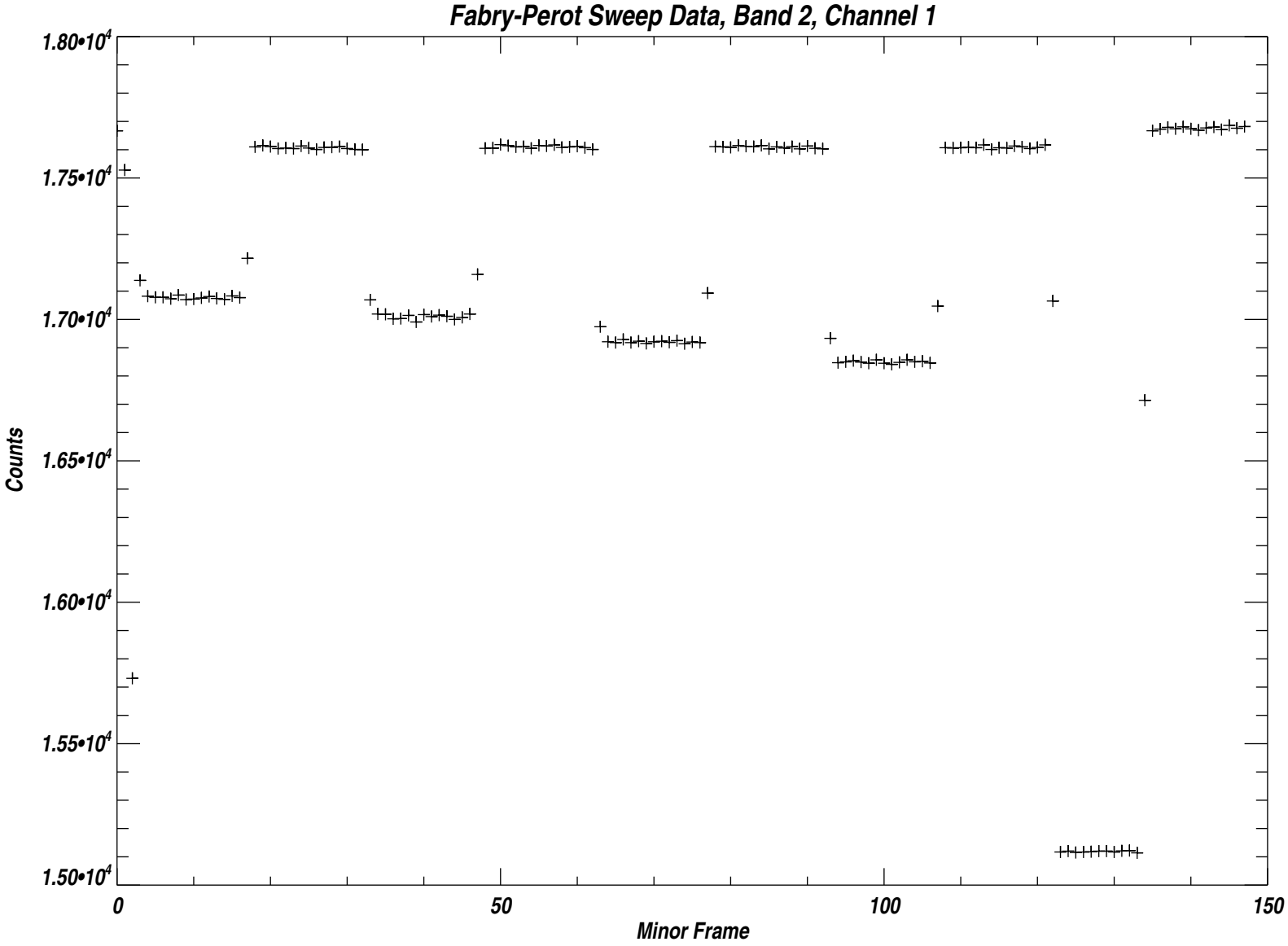

Figure 3.10: Relative sideband calibration raw data for a single MAF. These data are for Band 2, Channel 1. The minor differences in timing between the data shown here and Figure 3.9 arise from latency in the C&DH data processing and labelling. See text for additional details.

sweep increases this separation by ∼9.93 mm in steps of 0.01 mm.

Bands 10 through 14 were swept using grids with ∼200 lines per inch spacing, and the entire sweep for Channel 1 of Bands 10 and 14 is shown in Figure 3.12. Step size was 0.005 mm for this sweep, which started with a grid separation of ∼3.08 mm. The sweep is seen to be broken into 3 regions, the first corresponding to ∼0.6 mm of grid movement (ending at step ∼300). The x-axis thus defines Fabry-Pérot grid relative separation only for those regions of the plot in which the grids are moving. The grid separation was then reduced by ∼0.06 mm, and the sweep continued for ∼500 Fabry-Pérot steps (∼1.02 mm), corresponding approximately to relative spacings 440 to 960 in the figure. The grid spacing was then increased by manually[6] by 2.5 mm, and the sweep continued for another 0.9 mm. The grids were thus increased in separation from ∼3.08 to ∼8.04 mm (with one overlap region and one gap) during the data run. With these sets of grids spacings it was possible to obtain data with good sideband separation in all Channels of Bands 10 through 14.

During the sweeps, 'quick-look' software was used in realtime to verify that all targeted channels had provided data with good quality and clear sideband separation. All Fabry-Pérot sweeps were performed with the grid separation increasing to eliminate the possibility of inadvertently driving the grids into one another. The external LN_2 dewars were both capable of supporting even the longest continuous sweep of this type without the need to be topped up, eliminating this activity as a potential source of data disruption.

3.18 Alignment and Measurement Time

Accurate alignment of the sideband calibration apparatus was necessary for best results. With proper alignment relative sideband sweeps could be performed in the NFR and cart configurations with indistinguishably different results.

The first step in the alignment process was to put in place all of the equipment as shown in Figure 3.8, but with Fabry-Pérot grids and SW2 removed. A visible diode laser was then shone through the center of the Fabry-Pérot grid holders onto the polished spot visible at the center of the SW1. SW1 was rotated by hand about an axis passing vertically through the spot at its center, and rotated about the motor axis (by command through its controller), until the laser spot was reflected to the approximate center of LSC2. A piece of aluminized mylar was then held in good contact with the mirror surface under the laser spot on LSC2, and minor adjustment made (if necessary) until the laser beam traversed this entire path as intended. This was the most difficult part of the alignment process, mainly due to the relative inaccessibility of the calibration apparatus between the flight hardware and the optical bench supporting the calibration equipment.

The next step was to verify RF alignment of the system. This required placing SW2 in position with the mirror deflecting the instrument FOV toward the adjacent LN_2-cooled target. The low-noise power meter (described earlier in this chapter) was used to monitor RF power from IF Band 2. The power meter used a $4\frac{1}{2}$ digit panel meter for display, and had internal noise less than radiometric in the 1.3 GHz bandwidth of the IF signal. Its design combined chopper and low-noise amplifiers to essentially eliminate drift, providing a very sensitive measure of signal level changes. A piece of hand-held absorber with a hole ∼1 cm

[6]The Newport Research motorized micrometer used to move the translation stage had a convenient manual adjustment knob and position readout to facilitate such adjustments.

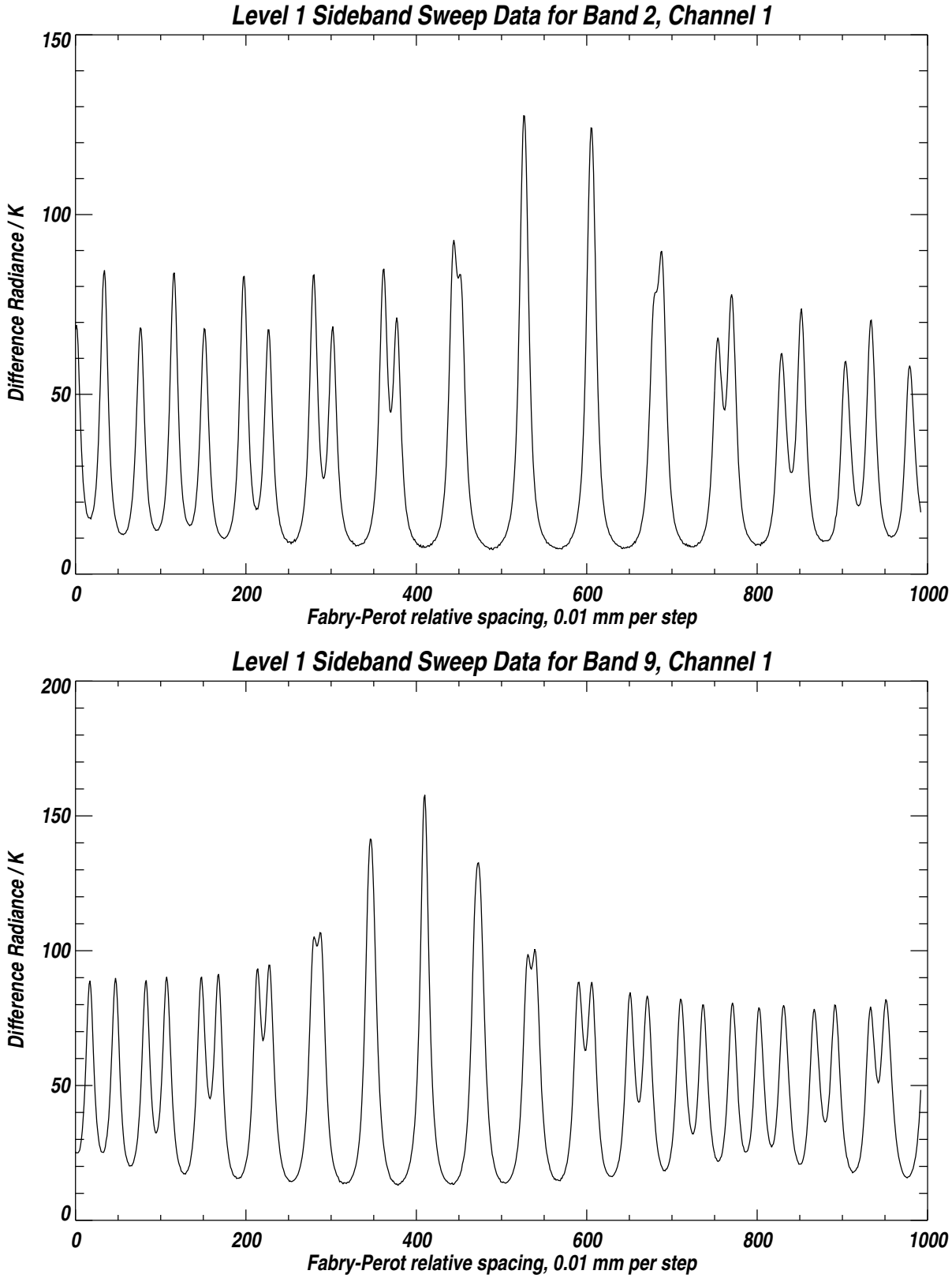

Figure 3.11: Relative sideband sweep data taken with 90 lpi grids and processed to radiances by Level 1 software. Data for Bands 2 through 9 were taken concurrently. These measurements were taken on 23 October 2002 (DOY 296). See text for additional details.

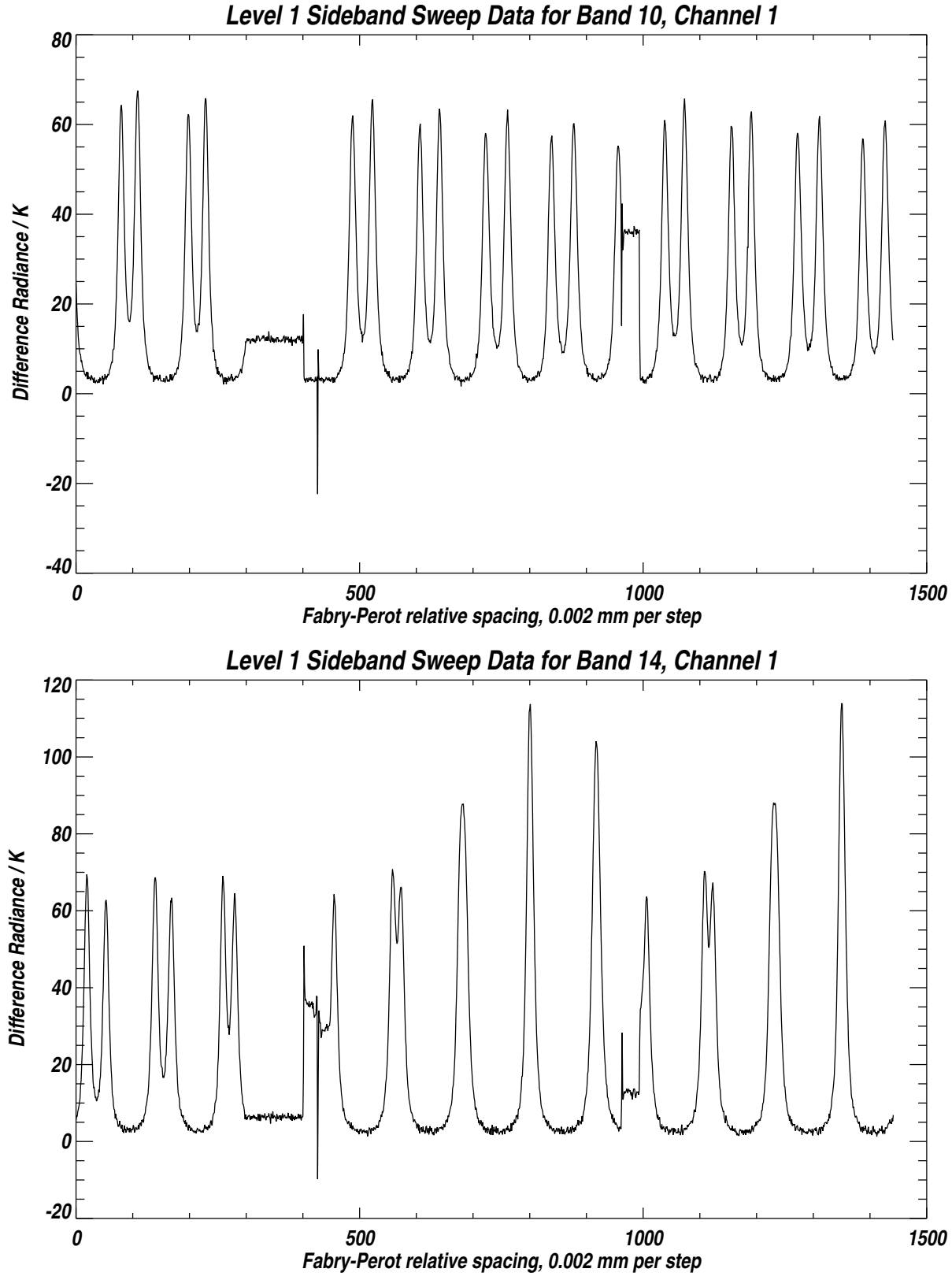

Figure 3.12: Relative sideband sweep data taken with 200 lpi grids and processed to radiances by Level 1 software. Data for Bands 10 through 14 were taken concurrently. These measurements were taken on 24 October 2002 (DOY 297). See text for additional details.

in diameter was then used as an aperture to trace the RF beam path. The first step was to verify that the RF beam passed through the center of the Fabry-Pérot grid holders, and it was occasionally found to be necessary to fine-tune the rotational position of the motor holding SW1 during this portion of the alignment process. The aperture was then moved to the fronts of SW1 and SW2 to confirm correct positioning of the RF beam at each of these elements.

The grids were then placed in position. This was a simple task since the grids were mounted in aluminum holders which fitted snugly and repeatably into the lens holders mounted on the motorized Fabry-Pérot translation stage. The grids were adjusted to be normal to the optical beam, and approximately parallel to one another. The low-noise power meter reading was then observed as the grid spacing and orientations were manually adjusted to minimize the RF power level observed in the Band 2 IF signal. This was a relatively easy task, typically taking about 5 minutes of the ∼1 hour needed for a full setup and alignment from scratch.

After this alignment procedure had been completed, the supports for SW1, SW2 and the Fabry-Pérot were clamped in place to avoid the possibility of accidental missalignment between measurement runs. The positions of the mounts for these components were also marked onto the aluminum support baseplate with a felt-tip pen to allow for a rapid future deployment of this calibration setup should the need have arisen at a later point in time.

3.18.1 Measurement Time

A full set of measurements took approximately 2 hours for Bands 2 to 9, and approximately 5 hours for Bands 10 to 14. The longer measurement time for the bands in R4 were required because of the slower stepping of the Fabry-Pérot chosen to partially compensate for the decreased S/N of these measurements compared to those in the lower frequency radiometers. It was thus possible to warm up (i.e., stabilize) the instrument fully, install and align the sideband calibration equipment, and perform a full set of measurements with one set of grids in an 8 hour shift. The R4 measurements (with the fine grids) benefited from the pre-alignment of the optical path from the prior run made with the coarse grids. Grid parallelism was checked each time the grids were installed in the Fabry-Pérot, but in practise it was found that no adjustment was needed after initial alignment. Had time been at a premium, all relative sideband measurements for EOS MLS could have been completed in a single 2 shift day (they were actually completed during a slightly extended one shift day during a dummy run on the Engineering Model which started with a fully warmed-up and stable instrument).

3.19 Fabry-Pérot Signals

Before discussing the analyses of these data, and the results obtained from these measurements, it is instructive to describe the actual Fabry-Pérot signals being analyzed. Figures 3.13 to 3.15 show calculated Fabry-Pérot signals in each of the double sideband GHz radiometers for grid spacings representative of those selected for detailed analysis. The dashed black curve shows the change in signal when the grid separation is increased by the increment used in each calibration run (the solid black curve is the unperturbed signal to which the dashed one is to be compared). The extent of each 25-channel filterbank band is shown (in both

sidebands), and it can be seen that a single Fabry-Pérot transmission maximum is present in the full IF passband for the range of grid separations presented here. For these simulations the grid reflectivities in each sideband are static, and representative of the values determined from the sideband retrievals. The plots show the expected 'ambient minus LN_2' radiance differences measured through the Fabry-Pérot assuming lossless grids and calibration optics. Note the substantial width of the Fabry-Pérot transmission orders compared to the width of an individual band, and enormous width compared to a typical MLS channel.

These plots are to be compared to the measured radiance differences of Figures 3.11 and 3.12. In those plots we chose to invert the spectral features so that they more closely resembled atmospheric emission spectra. Since the MLS GHz radiometers (except for R1A and R1B) are double sideband by nature, and have approximately equal responses in each sideband (shown below), we expect the well-differentiated Fabry-Pérot signals in these figures to be just under one half of the amplitude of the modelled signals, and that is the case.

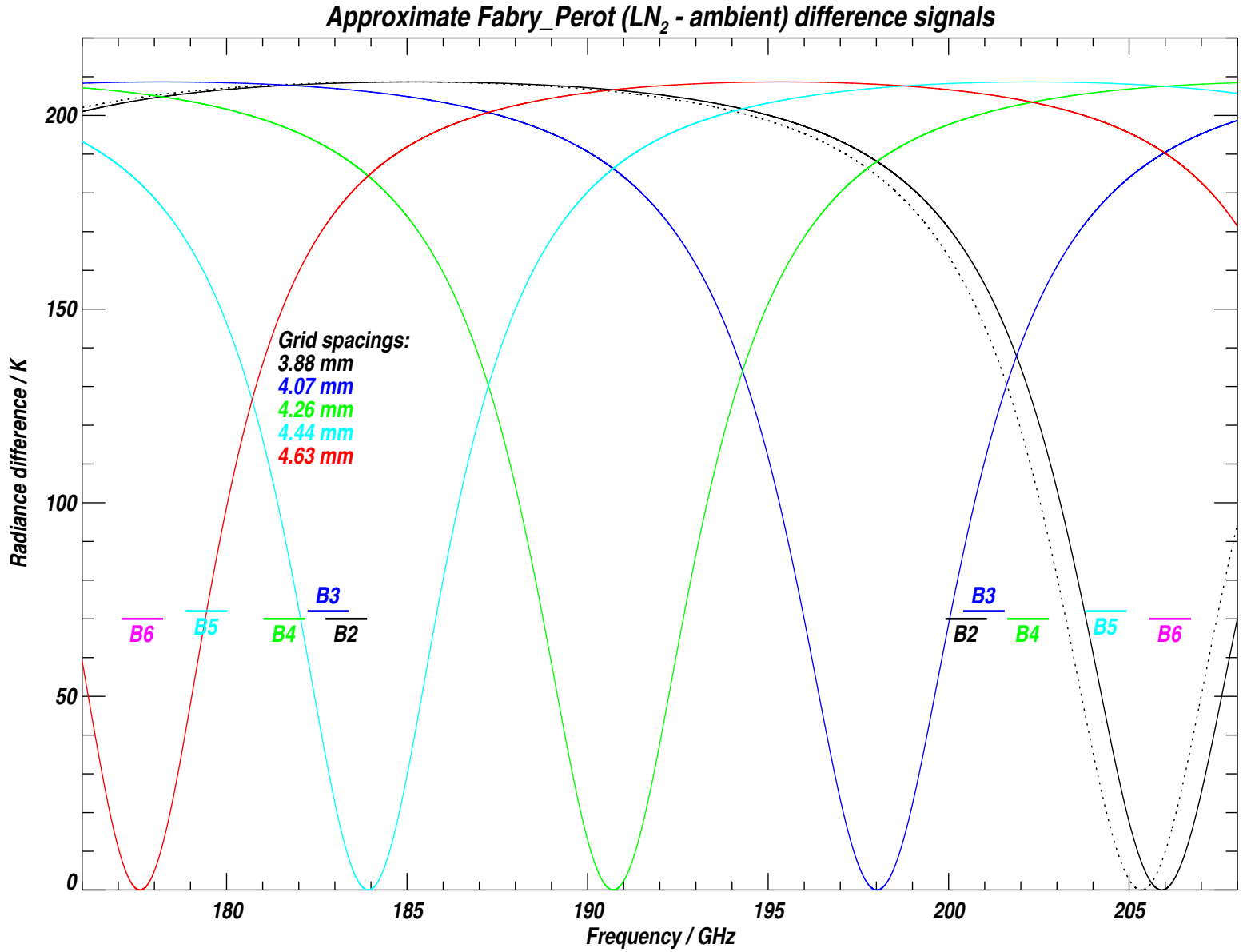

Figure 3.13: Computed radiance signature generated by the Fabry-Pérot for the 190 GHz radiometer bands. The dashed line shows the spectral shift corresponding to a 0.01 mm increase in grid spacing from the initial spacing. Band positions in both sidebands are indicated for convenience. See text for additional details.

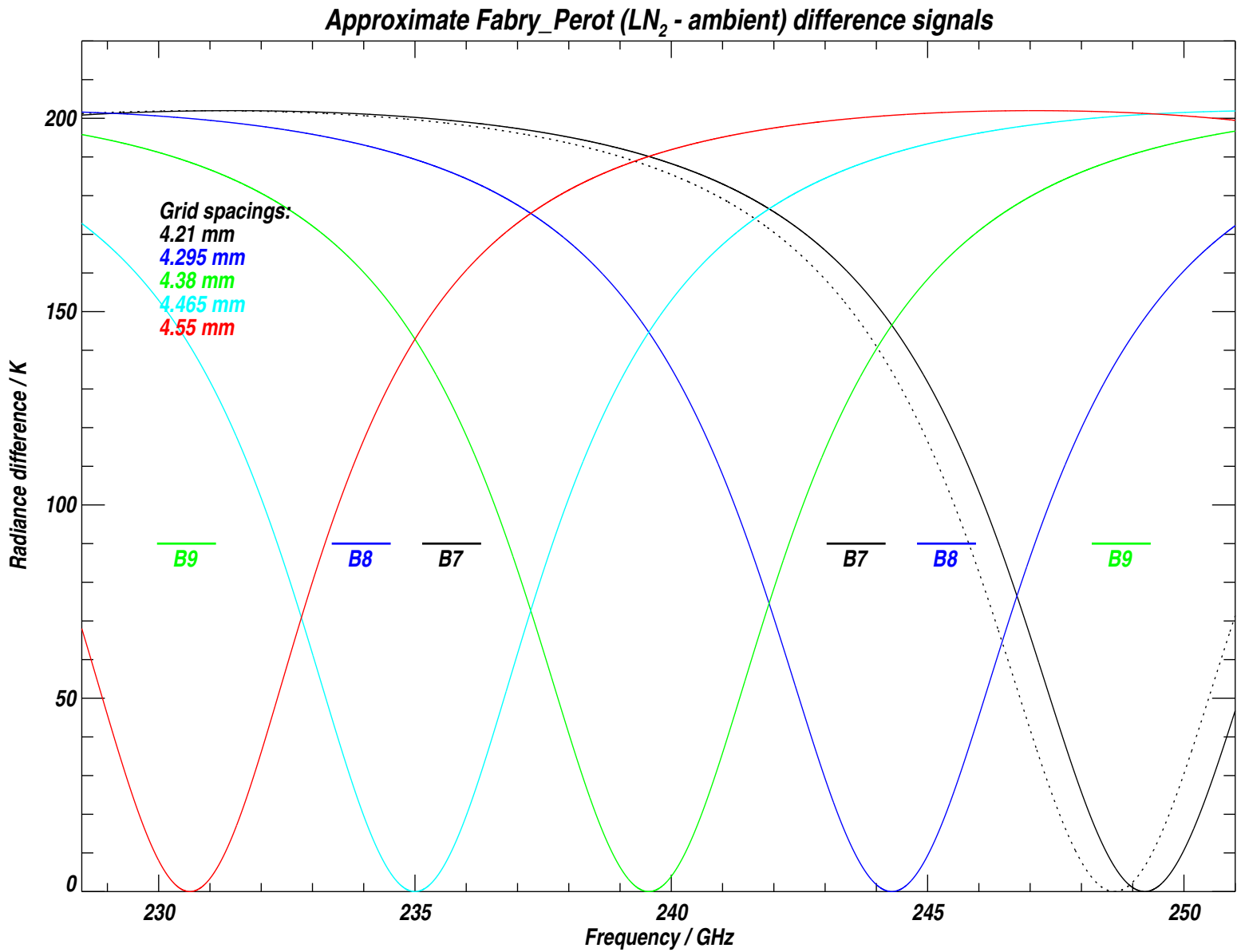

Figure 3.14: Computed radiance signature generated by the Fabry-Pérot when calibrating the 240 GHz radiometer bands. The dashed line shows the spectral shift corresponding to a 0.01 mm increase in grid spacing from the initial spacing. Band positions in both sidebands are indicated for convenience. See text for additional details.

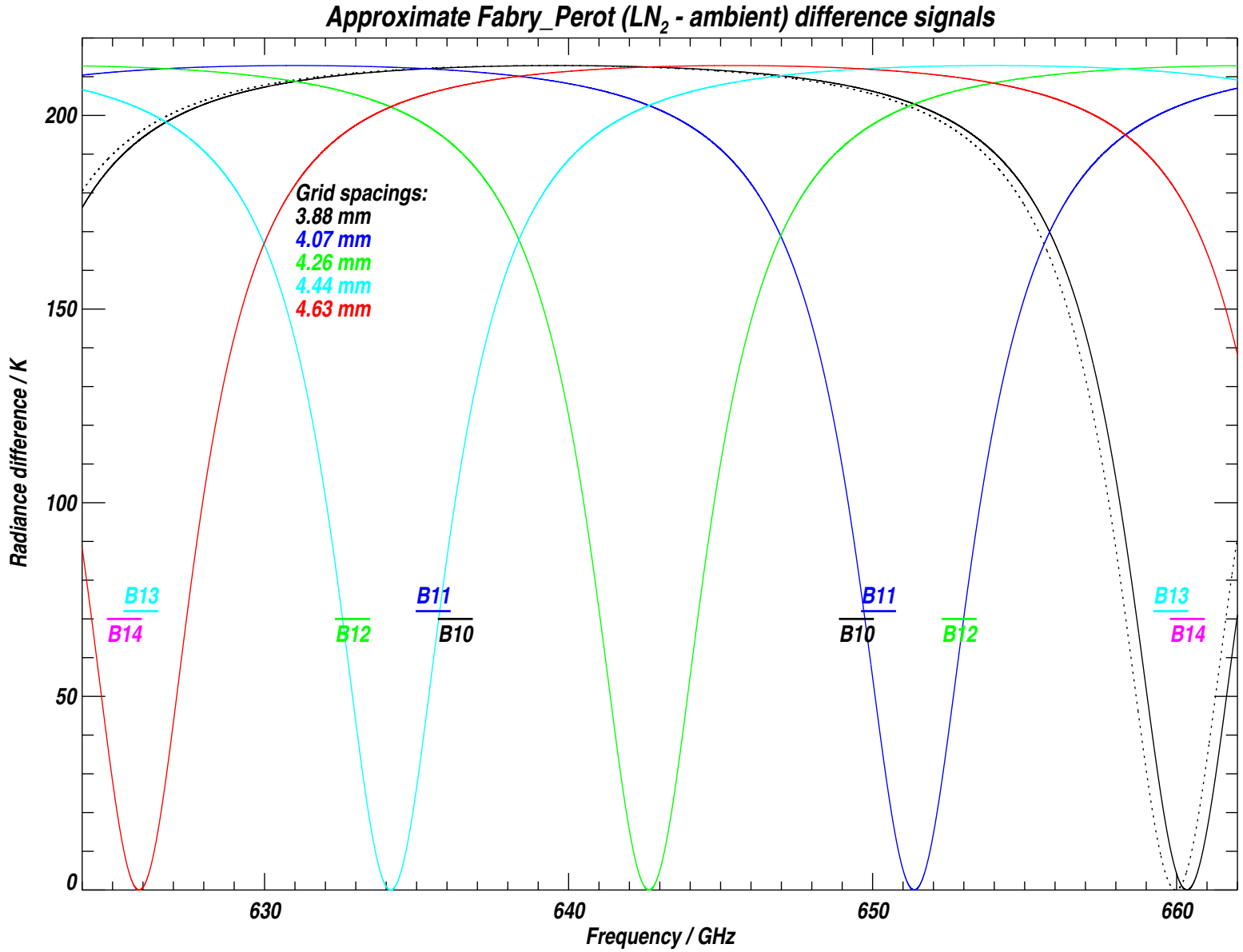

Figure 3.15: Computed radiance signature generated by the Fabry-Pérot when calibrating the 640 GHz radiometer bands. The dashed line shows the spectral shift corresponding to a 0.002 mm increase in grid spacing from the initial spacing. Band positions in both sidebands are indicated for convenience. See text for additional details.

3.20 Data Analysis

From this point forward we will discuss the Fabry-Pérot sweep data only in the form of calibrated radiance differences as shown in Figures 3.11 and 3.12. In order to understand how the sideband data were analyzed it is first necessary to describe the measurement model, and to discuss the simplifying assumptions included in the data analyses. Relative sideband response retrieval was performed on a band-by-band basis in each of the GHz FB25 bands. Data from the MB11 bands were not included in these analyses since they merely provide redundant information due to their overlap with the FB25 data, and also because all of their channels are narrow compared with the underlying FB25 channels that they overlap. No sideband response retrieval was performed for any of the R1 bands since both 118 GHz radiometers are single sideband. The 4 Wide Filters in R3 were analyzed using the same tools used for the FB25 analyses, with each FB25 'channel' containing duplicates of the measured data from a single Wide Filter channel. This was done purely as a method of saving time, since it allowed existing software to be used without further modification.

The following details apply to all relative sideband response retrievals:

(1) Each instrument filter response is approximated by a delta function at the nominal center frequency of that channel (in each sideband). This assumption was validated during analysis of the corresponding UARS MLS data for which the broadest filterbank channels were even wider (∼128 MHz) than the corresponding EOS MLS channels (∼96 MHz).

- For the Wide Filters in R3 we represented the filter response as four delta functions uniformly separated in frequency. This was because the spectral width of these channels (up to ∼450 MHz) began to approach the width of the Fabry-Pérot transmission order (∼1 GHz). Since most of the relative sideband information in the well-separated transmission peaks, the difference in retrieved relative sideband response due to this refinement is very small.

(2) We allow for (and retrieve) the phase shift *difference* in the Fabry-Pérot grid reflections in lower and upper sidebands, but assume the same difference in phase shift for all channels in a given sideband.

(3) Grid reflectivities are assumed to be the same for both grids at a given frequency, but allowed to be different in the lower and upper sidebands. Furthermore, we assume the same reflectivities for all channels of a given band in each sideband (a reasonable assumption given the relatively small fractional bandwidth of a band in one sideband compared to the fractional separation of the two sidebands).

(4) Relative sideband response across a given sideband is allowed to vary as a cubic (in IF frequency), except for the Wide Filter retrievals in which a single value of sideband response is individually determined for each channel.

These assumptions have all been tested to verify that they introduce negligible errors.

3.20.1 Details of the Measurement Model

We evaluate the transmission,τ, of a Fabry-Pérot using the expression:

$$\tau(s,\nu,r) = \left(\frac{1}{1 + 4 * \sin^2(s * 4.19169 * 10^{-2} * \nu/2) * r/(1-r)^2} \right) \tag{3.1}$$

where:

s	= grid spacing, mm
ν	= signal frequency, GHz
r	= grid reflectivity (assumed to be the same for both grids), and
$4.19169 * 10^{-2}$	$= 4 * \pi/c$ in appropriate units.

The estimated double-sideband difference radiance measured in the target channel, T, is then given by:

$$T = 220 * (R_l * \tau(s, \nu_l, r_l) + R_u * \tau(s + \delta s, \nu_u, r_u) * P)/2 \tag{3.2}$$

where:

220	= the approximate temperature difference between the 2 external targets, Kelvin,
ν_x	= the lower ($x = l$) and upper ($x = u$) sideband frequencies, GHz
s	= the grid spacing, mm
δs	= a correction applied to the upper sideband grid spacing to allow for the change in phase of the grid reflections as a function of signal frequency, mm
R_l	= sideband response (lower sideband)
R_u	= sideband response (upper sideband)
P	= a Planck correction – see text below, and
r_l, r_u	= lower and upper sideband grid reflectivities.

In Equation 3.2 above we assume that the ambient and LN_2-cooled targets observed through the Fabry-Pérot are stable and at temperatures of 300 K and 80 K for the duration of the measurements used in an individual fit to the data used to determine relative sideband response. In practice we use approximately 60 measurements (Fabry-Pérot spacings) in each fit, which takes approximately 12 minutes (and about double this time for R4), making the assumption of stability valid. The temperature difference between these targets is thus assumed to be 300 K minus 80 K, and hence the 220 K in the equation. This is clearly an approximation that does not model the actual temperatures of the targets exactly. The retrieval process fits to the estimated radiance in each sideband, outputting the coefficients of a pair of cubics which represent the estimated radiometric responses in each sideband. Since both sideband responses will be in error by the same (small) multiplicative factor, the error is eliminated when the responses in each sideband are divided (to obtain the relative sideband response of each channel).

Although this approach takes care of the minor issue of not knowing the precise target temperatures, it does not account for the difference in Planck function between the two sidebands. This is accomplished by means of parameter P in Equation 3.2, where:

$$P = \frac{B(\nu_u, 300) - B(\nu_u, 80)}{B(\nu_l, 300) - B(\nu_l, 80)} \tag{3.3}$$

and $B(\nu, T)$ is the Planck function at frequency ν and temperature T. This correction is extremely close to unity in all bands, and could have been ignored with no significant loss in accuracy.

The parameter δs in Equation 3.2 allows for the change in phase of the grid reflections between lower and upper sidebands, but does not account for the actual phase shift in the lower sideband. This is accounted for by fitting both parameters s and δs during sideband retrievals, the actual values of the phase shifts being unimportant to the end result.

3.20.2 Details of the Retrieval Model

The purpose of the sideband retrieval is simply to determine the values of s, δs, w, r_l, r_u and R which provide the best match (in the least-squares sense) between measurements and model. Since we wish to perform the sideband retrievals on a band by band basis (25 channel filterbank), and wish to allow R_l and R_u to vary smoothly across each sideband, we choose to represent R_l and R_u as cubics in IF frequency space with coefficients a_r^l, b_r^l, c_r^l and d_r^l:

$$R_l(f) = a_r^l + b_r^l \times f + c_r^l \times f^2 + d_r^l \times f^3 \tag{3.4}$$

with a corresponding expression for the upper sideband response. Parameter f is the nominal channel center frequency at the input to each spectrometer. The units of f are unimportant, and were chosen to be MHz in this code.

The final measurement model, T, thus has 12 parameters to be retrieved:

s	sp	initial grid spacing, mm
δs	tu	upper sideband phase correction, mm
r_l	rl	lower sideband grid reflectivity (0..1)
r_u	ru	upper sideband grid reflectivity (0..1)
a_r^l	al	constant coefficient of sideband polynomial, lower sideband
b_r^l	bl	*bl* linear coefficient
c_r^l	cl	*cl* quadratic coefficient
d_r^l	dl	*dl* cubic coefficient
a_r^u	au	*au* constant coefficient of sideband polynomial, upper sideband
b_r^u	bu	*bu* linear coefficient
c_r^u	cu	*cu* quadratic coefficient
d_r^u	du	*du* cubic coefficient

The column containing sp through du indicates the 2-letter variable names of these parameters in the retrieval code. For retrieval purposes s is the initial grid spacing of the measurement set. This is because all other grid spacings of the measurement set are accurately known by adding the appropriate grid relative movement to this initial spacing, and it is only necessary to retrieve the initial spacing. Note also that the phase difference between lower and upper sideband grid reflections is modelled as a small virtual grid separation offset, δs, in the upper sideband. This is purely for coding convenience, and is mathematically equivalent to modelling the phase shift difference as an angle.

The vector of measurements, dvec, is given by:

$$\mathsf{dvec} = \begin{bmatrix} d(0,s(0)) \\ d(1,s(0)) \\ d(2,s(0)) \\ \vdots \\ d(24,s(0)) \\ d(0,s(1)) \\ d(1,s(1)) \\ d(2,s(1)) \\ \vdots \\ d(24,s(1)) \\ \vdots \\ d(0,s(n)) \\ d(1,s(n)) \\ d(2,s(n)) \\ \vdots \\ d(24,s(n)) \end{bmatrix} \tag{3.5}$$

where $d(\text{channel}, \text{spacing})$ is the measured (ambient - LN_2) difference radiance through the Fabry-Pérot for the corresponding channel and grid spacing, $s(m)$. This linear vector sequences through all channels of an FB25, then steps to the next grid spacing and repeats until the last chosen spacing (n) has been selected.

The corresponding vector of expected (model) radiances, g, is given by:

$$\mathsf{g} = \begin{bmatrix} T(0,s(0),\delta s,r_l,r_u,a_r^l,b_r^l,c_r^l,d_r^l,a_r^u,b_r^u,c_r^u,d_r^u) \\ T(1,s(0),\delta s,r_l,r_u,a_r^l,b_r^l,c_r^l,d_r^l,a_r^u,b_r^u,c_r^u,d_r^u) \\ T(2,s(0),\delta s,r_l,r_u,a_r^l,b_r^l,c_r^l,d_r^l,a_r^u,b_r^u,c_r^u,d_r^u) \\ \vdots \\ T(24,s(0),\delta s,r_l,r_u,a_r^l,b_r^l,c_r^l,d_r^l,a_r^u,b_r^u,c_r^u,d_r^u) \\ T(0,s(1),\delta s,r_l,r_u,a_r^l,b_r^l,c_r^l,d_r^l,a_r^u,b_r^u,c_r^u,d_r^u) \\ T(1,s(1),\delta s,r_l,r_u,a_r^l,b_r^l,c_r^l,d_r^l,a_r^u,b_r^u,c_r^u,d_r^u) \\ T(2,s(1),\delta s,r_l,r_u,a_r^l,b_r^l,c_r^l,d_r^l,a_r^u,b_r^u,c_r^u,d_r^u) \\ \vdots \\ T(24,s(1),\delta s,r_l,r_u,a_r^l,b_r^l,c_r^l,d_r^l,a_r^u,b_r^u,c_r^u,d_r^u) \\ \vdots \\ T(0,s(n),\delta s,r_l,r_u,a_r^l,b_r^l,c_r^l,d_r^l,a_r^u,b_r^u,c_r^u,d_r^u) \\ T(1,s(n),\delta s,r_l,r_u,a_r^l,b_r^l,c_r^l,d_r^l,a_r^u,b_r^u,c_r^u,d_r^u) \\ T(2,s(n),\delta s,r_l,r_u,a_r^l,b_r^l,c_r^l,d_r^l,a_r^u,b_r^u,c_r^u,d_r^u) \\ \vdots \\ T(24,s(n),\delta s,r_l,r_u,a_r^l,b_r^l,c_r^l,d_r^l,a_r^u,b_r^u,c_r^u,d_r^u) \end{bmatrix} \tag{3.6}$$

where the first two parameters of function T are the filterbank channel number and grid spacing. We choose to relate the measurements and model by the standard expression:

$$\mathsf{gvec} \times \mathsf{mvec} = \mathsf{dvec} \tag{3.7}$$

where:

$$\begin{bmatrix} T(0,s(0)) & \frac{\partial T}{\partial s} & \frac{\partial T}{\partial \delta s} & \frac{\partial T}{\partial r_l} & \frac{\partial T}{\partial r_u} & \frac{\partial T}{\partial a_r^l} & \frac{\partial T}{\partial b_r^l} & \cdots & \frac{\partial T}{\partial c_r^u} & \frac{\partial T}{\partial d_r^u} \\ T(1,s(0)) & \frac{\partial T}{\partial s} & \frac{\partial T}{\partial \delta s} & \frac{\partial T}{\partial r_l} & \frac{\partial T}{\partial r_u} & \frac{\partial T}{\partial a_r^l} & \frac{\partial T}{\partial b_r^l} & \cdots & \frac{\partial T}{\partial c_r^u} & \frac{\partial T}{\partial d_r^u} \\ T(2,s(0)) & \frac{\partial T}{\partial s} & \frac{\partial T}{\partial \delta s} & \frac{\partial T}{\partial r_l} & \frac{\partial T}{\partial r_u} & \frac{\partial T}{\partial a_r^l} & \frac{\partial T}{\partial b_r^l} & \cdots & \frac{\partial T}{\partial c_r^u} & \frac{\partial T}{\partial d_r^u} \\ \vdots & \vdots & \vdots & \vdots & \vdots & \vdots & \vdots & \vdots & \vdots & \vdots \\ T(24,s(0)) & \frac{\partial T}{\partial s} & \frac{\partial T}{\partial \delta s} & \frac{\partial T}{\partial r_l} & \frac{\partial T}{\partial r_u} & \frac{\partial T}{\partial a_r^l} & \frac{\partial T}{\partial b_r^l} & \cdots & \frac{\partial T}{\partial c_r^u} & \frac{\partial T}{\partial d_r^u} \\ T(0,s(1)) & \frac{\partial T}{\partial s} & \frac{\partial T}{\partial \delta s} & \frac{\partial T}{\partial r_l} & \frac{\partial T}{\partial r_u} & \frac{\partial T}{\partial a_r^l} & \frac{\partial T}{\partial b_r^l} & \cdots & \frac{\partial T}{\partial c_r^u} & \frac{\partial T}{\partial d_r^u} \\ T(1,s(1)) & \frac{\partial T}{\partial s} & \frac{\partial T}{\partial \delta s} & \frac{\partial T}{\partial r_l} & \frac{\partial T}{\partial r_u} & \frac{\partial T}{\partial a_r^l} & \frac{\partial T}{\partial b_r^l} & \cdots & \frac{\partial T}{\partial c_r^u} & \frac{\partial T}{\partial d_r^u} \\ \vdots & \vdots & \vdots & \vdots & \vdots & \vdots & \vdots & \vdots & \vdots & \vdots \\ T(24,s(1)) & \frac{\partial T}{\partial s} & \frac{\partial T}{\partial \delta s} & \frac{\partial T}{\partial r_l} & \frac{\partial T}{\partial r_u} & \frac{\partial T}{\partial a_r^l} & \frac{\partial T}{\partial b_r^l} & \cdots & \frac{\partial T}{\partial c_r^u} & \frac{\partial T}{\partial d_r^u} \\ T(0,s(n)) & \frac{\partial T}{\partial s} & \frac{\partial T}{\partial \delta s} & \frac{\partial T}{\partial r_l} & \frac{\partial T}{\partial r_u} & \frac{\partial T}{\partial a_r^l} & \frac{\partial T}{\partial b_r^l} & \cdots & \frac{\partial T}{\partial c_r^u} & \frac{\partial T}{\partial d_r^u} \\ T(1,s(n)) & \frac{\partial T}{\partial s} & \frac{\partial T}{\partial \delta s} & \frac{\partial T}{\partial r_l} & \frac{\partial T}{\partial r_u} & \frac{\partial T}{\partial a_r^l} & \frac{\partial T}{\partial b_r^l} & \cdots & \frac{\partial T}{\partial c_r^u} & \frac{\partial T}{\partial d_r^u} \\ T(2,s(n)) & \frac{\partial T}{\partial s} & \frac{\partial T}{\partial \delta s} & \frac{\partial T}{\partial r_l} & \frac{\partial T}{\partial r_u} & \frac{\partial T}{\partial a_r^l} & \frac{\partial T}{\partial b_r^l} & \cdots & \frac{\partial T}{\partial c_r^u} & \frac{\partial T}{\partial d_r^u} \\ \vdots & \vdots & \vdots & \vdots & \vdots & \vdots & \vdots & \vdots & \vdots & \vdots \\ T(24,s(n)) & \frac{\partial T}{\partial s} & \frac{\partial T}{\partial \delta s} & \frac{\partial T}{\partial r_l} & \frac{\partial T}{\partial r_u} & \frac{\partial T}{\partial a_r^l} & \frac{\partial T}{\partial b_r^l} & \cdots & \frac{\partial T}{\partial c_r^u} & \frac{\partial T}{\partial d_r^u} \end{bmatrix} \times \begin{bmatrix} 1 \\ ds \\ d\delta s \\ dr_l \\ dr_u \\ da_r^l \\ db_r^l \\ dc_r^l \\ dd_r^l \\ da_r^u \\ db_r^u \\ dc_r^u \\ dd_r^u \end{bmatrix} = \begin{bmatrix} d(0,s(0)) \\ d(1,s(0)) \\ d(2,s(0)) \\ \vdots \\ d(24,s(0)) \\ d(0,s(1)) \\ d(1,s(1)) \\ d(2,s(1)) \\ \vdots \\ d(24,s(1)) \\ \vdots \\ d(0,s(n)) \\ d(1,s(n)) \\ d(2,s(n)) \\ \vdots \\ d(24,s(n)) \end{bmatrix}$$

In the representation of gvec we have chosen to indicate only the first 2 parameters of T in the left hand column, and to omit all of the parameters in the partial derivative elements. In each row, the model partial derivatives are computed for the parameters of T corresponding to those in the left hand element of that row. The goal of the sideband retrieval is to determine the values of the variables in mvec which minimize the least squares difference between measured and modelled signals. For a linear system this is a standard problem having the solution:

$$\mathsf{mvec}^{est} = [\mathsf{gvec}^{\mathsf{T}}\,\mathsf{gvec}]^{-1}\mathsf{gvec}^{\mathsf{T}}\mathsf{dvec} \tag{3.8}$$

In this formulation mvec^{est} returns the *changes* to parameters s through d_r which reduce (and ideally minimize) the least squares difference between model and measurements.

3.20.3 Refinements to the Basic Retrieval

Not all channels contribute the same information, so we choose to weight the information contribution from each channel by its measurement precision W, giving the modified solution:

$$\mathsf{mvec}^{est} = [\mathsf{gvec}^{\mathsf{T}}\,\mathsf{W}\,\mathsf{gvec}]^{-1}\mathsf{gvec}^{\mathsf{T}}\,\mathsf{W}\,\mathsf{dvec} \tag{3.9}$$

where W is a square matrix with its diagonal elements containing the nominal noise bandwidths of the corresponding filterbank channels. All of its other elements are zero.

During development of this retrieval model there were occasions when the results would suddenly diverge after several cycles of steady convergence. This led to the following enhancements:

(1) Introduction of a Marquard-Levenberg constraint parameter provided a simple global mechanism for aiding convergence.

(2) The updates provided in mvec^{est} were scaled individually by a user-input vector pdvec which instructed the software as to what fraction of the update for each parameter in mvec^{est} to apply. This scheme had the additional advantage that parameters such as the grid spacing, upper sideband phase correction, and grid reflectivities could be easily 'frozen' after their values had converged, and the retrieval allowed to concentrate on fitting the remaining parameters. This mechanism was also used to allow a single value of relative sideband response to be retrieved for each Wide Filter channel with no need for additional changes to the software.

After final debugging and 'tuning' of the retrieval code the convergence of sideband retrievals was found to be robust *except* when the 'threshold' parameter (see below) was set too loosely, thus including in the fitting process some sweep data from the regions where the Fabry-Pérot transmission was less than approximately 40% of its peak in either sideband. Under such conditions the receivers 'see themselves' partially in reflection, causing a change in bias conditions and mixer conversion loss. This manifests most clearly as an inability to precisely model the measured radiance differences in the regions of low Fabry-Pérot transmission. Since this region of the measurements contains the least information about relative sideband response, we merely omit this data from the retrieval.

With these changes, the updates to parameters s through d_r^u after each iteration are contained in the 12 elements of mvec^{est} where:

$$\mathsf{mvec}^{est} = \mathsf{pdvec}[\mathsf{gvec}^{\mathsf{T}}\,\mathsf{W}\,\mathsf{gvec} + \lambda \mathrm{I}]^{-1}\mathsf{gvec}^{\mathsf{T}}\,\mathsf{W}\,\mathsf{dvec} \tag{3.10}$$

The value of λ (by which the identity matrix I is multiplied) is set to zero for no Marquardt-Levenberg constraints, and to positive values of order unity when necessary to avoid unwanted divergence. pdvec is shown here as a diagonal matrix, but in the code is a 12-element array the elements of which are used to individually scale the updates to parameters s through d_r^u. With appropriate choice of the threshold parameter is was found that neither λ nor pdvec needed to be set to provide any constraints, and convergence to stable values of all 12 retrieved parameters was achieved in no more than 20 iterations, taking just a few seconds of processing time for each band (including 'real-time' graphical presentation of the fit during each iteration).

Computation of Partial Derivatives

The method chosen to determine partial derivatives was simply to perturb the selected parameter by an appropriate (small) amount and recompute the expected signal. No benefit was seen in generating these derivatives analytically given the very short time needed to process each band.

Additional implementation details

The retrieval software was written to operate as described above, but implements an additional refinement:

- ❑ One channel can be selected for exclusion from the fitting process. This was useful during Engineering Model evaluation of the calibration system when some channels

were producing erroneous data (later discovered to be a minor GSE software issue). This was accomplished by setting the noise bandwidth of the selected channel to zero in matrix W. The same mechanism could readily have been extended to strike out data from multiple channels, or even individual data points, but this was not found to be necessary.

3.21 Data Size and Computation Time

The sideband retrieval software is designed to allow selection of the start and end records of the data to be included in the fit. Definitive calibration data used one transmission order from each sideband, with the order selected on a band-by-band basis to provide data with good separation of the sidebands. No benefit was found from including multiple orders. Memory requirements increase approximately quadratically with data vector size. With the software written in IDL, running under Linux on a 1.3 GHz Athlon PC with 1.5 GB of RAM, 4 to 6 orders in each sideband could be included in a retrieval, but not the entire data sets shown in Figures 3.11 or 3.12.

For the standard retrieval data chunk size, the software looped through each iteration in about 1 s, with most of this time spent created high resolution plots of the measured and computed radiances, the radiance residuals, and the estimated relative sideband response, for all 25 channels of the selected band. Thus even the longest retrievals, with up to ∼20 iterations took well below one minute. Much more time was taken in homing in on good starting parameters for one band in each radiometer (quite easy in practise). Once a good retrieval had been performed, the retrieved parameter values for that band were used as the starting point for the next band in the same radiometer. Since a different grid initial spacing was typically selected for each band, a new estimate of the initial grid separation had to be determined for each band. Since the incremental grid separation was an extremely accurate quantity in this measurement setup, once s had been determined for any grid spacing for either of the grid types in any band, it was known for all other grid spacings for that particular set of grids. The controller units (Figure 3.7 and Appendix F) were programmed to return the micrometer to its initial separation at the end of every measurement sequence, even those that were manually terminated.

3.22 Precision and Accuracy

The covariance matrix for mvec^{est} can be readily computed from

$$\mathsf{E}[\mathsf{mvec}^{est}] = [\mathsf{gvec}^{\mathsf{T}}\,\mathsf{W}\,\mathsf{gvec}]^{-1}\mathsf{gvec}^{\mathsf{T}}\,\mathsf{W}\,\mathsf{R}\,\mathsf{W}\mathsf{gvec}[\mathsf{gvec}^{\mathsf{T}}\,\mathsf{W}\,\mathsf{gvec}]^{-1} \tag{3.11}$$

where $\mathsf{R} = \sigma^2\mathrm{I}$, and this computation was included in the retrieval code.

Examination of the radiance residuals shown in Volume 2 indicates that errors are dominated by systematics, not by measurement precision, greatly reducing the value of the contents of the error covariance matrix. As an additional check on the validity of the retrieval model, the relative sideband responses of all GHz filter channels (except those in R1A/B) were retrieved individually, and compared to the results of the band-level retrievals. Comparisons of the results of these two sets of retrievals indicate no apparent problems with the

chosen retrieval method. We thus have to estimate the accuracy of the retrieved relative sideband data based on assessment of the structure and magnitude of the radiance derivatives, and intuition.

3.23 Suggestions for future work

It appears that (with the possible exception of R4) limitations on sideband measurement accuracy arise mostly from the standing waves between mixer and Fabry-Pérot. This is evident from fact that the *rms* deviations between measurement and model for the widest FB25 channels are not reduced compared to narrow channel data in accordance with the noise on the measurements. This implies that systematics, not noise, dominate the error budget for R2 and R3 relative sideband calibrations.

The likely source of these low-level systematics is the receivers 'seeing themselves' in partial reflection from the Fabry-Pérot, retuning the mixers slightly as the reflection coefficient changes. An often-used method for reducing these reflections is to merely tilt the grids sufficiently (keeping them parallel) that the receivers no longer see themselves in reflection. The reflected path should of course be captured in a suitably located piece of microwave absorber. The drawback to this approach is that much of the advantages gained from having an excellent optical system are diluted, with degradation of signal-to-noise and the probable need to model Fabry-Pérot walk-off losses in order to obtain good fits between measurement and theory.

A potential method for reducing these systematics is to scramble the phase of reflections appropriately during the course of a data integration. Many methods exist for doing this, one being to simply mount the Fabry-Pérot translation stage on another translation stage which dithers the interferometer by $\frac{\lambda}{4}$ an even number of times during each data integration. Such a scheme could be readily implemented using the existing calibration controllers. The only obvious drawback of implementing such a scheme is that the significant variation in λ between the various radiometers would necessitate repeating Fabry-Pérot scans with modified dither amplitudes, increasing the overall measurement time for these calibrations. Since the actual measurement time for the entire GHz sideband calibration was only 2 days, we anticipate that the overall time for calibrations with the 'dithered' scheme would increase to 3 or 4 days for this particular instrument.

3.24 Results

Figure 3.16 shows the measured relative sideband responses (lower sideband response divided by upper sideband response for all double sideband GHz bands. The black lines covering the spectral regions analyzed by each 25-channel filterbank indicate the retrieved sideband responses for those bands. The individual small crosses indicate the results of retrieving the relative sideband response of each *channel* individually, and are included for comparison. The four individual larger black crosses in the panel for R3 indicate the measured relative sideband responses for the individual Wide Filter channels.

Since we wish to provide relative sideband data that has no discontinuities between overlapping channels, we chose to fit all of the measured 25-channel filterbank relative sideband data for a given radiometer to a high order polynomial (7th order for R2, 8th order for R3 and

R4). The relative sideband data used by the Forward Model are those given by these polynomial fits. The Wide Filter data for R3 was used directly (i.e., with no fitting). The green lines on the plot indicate results of these fits. The large red, green and blue crosses at the positions of the 11-channel filterbank channels indicate the relative sideband responses assigned to these channels. The 11-channel filterbanks and 128-channel autocorrelators provide redundant data since they analyze frequencies already measured by the 25-channel filterbanks, and so no information from these spectrometers was included in the sideband retrieval process.

Appendix C shows the detailed results of the relative sideband measurements in each GHz band. The relative sideband fractions shown in the plots of that appendix come directly from the retrievals, and indicate the individual sideband responses compared to those expected from a 'perfect' sideband measurement system switching between room temperature and ∼80 K scenes. If there were no losses at all in the Fabry-Pérot, we would expect the relative sideband fractions to add up to close to unity. Examination of the data presented in Appendix C indicates that the sum of the measured sideband responses ranges between ∼0.6 and ∼0.8, with highest losses in the highest frequency bands. The EOS MLS Forward Model and Retrieval software [5, 6] require normalized relative sideband fractions, and so for delivery to Level 2 data processing, the measured data were renormalized appropriately. The GHz relative sideband response data file delivered to Level 2 is reproduced in two column format directly following Figure 3.16.

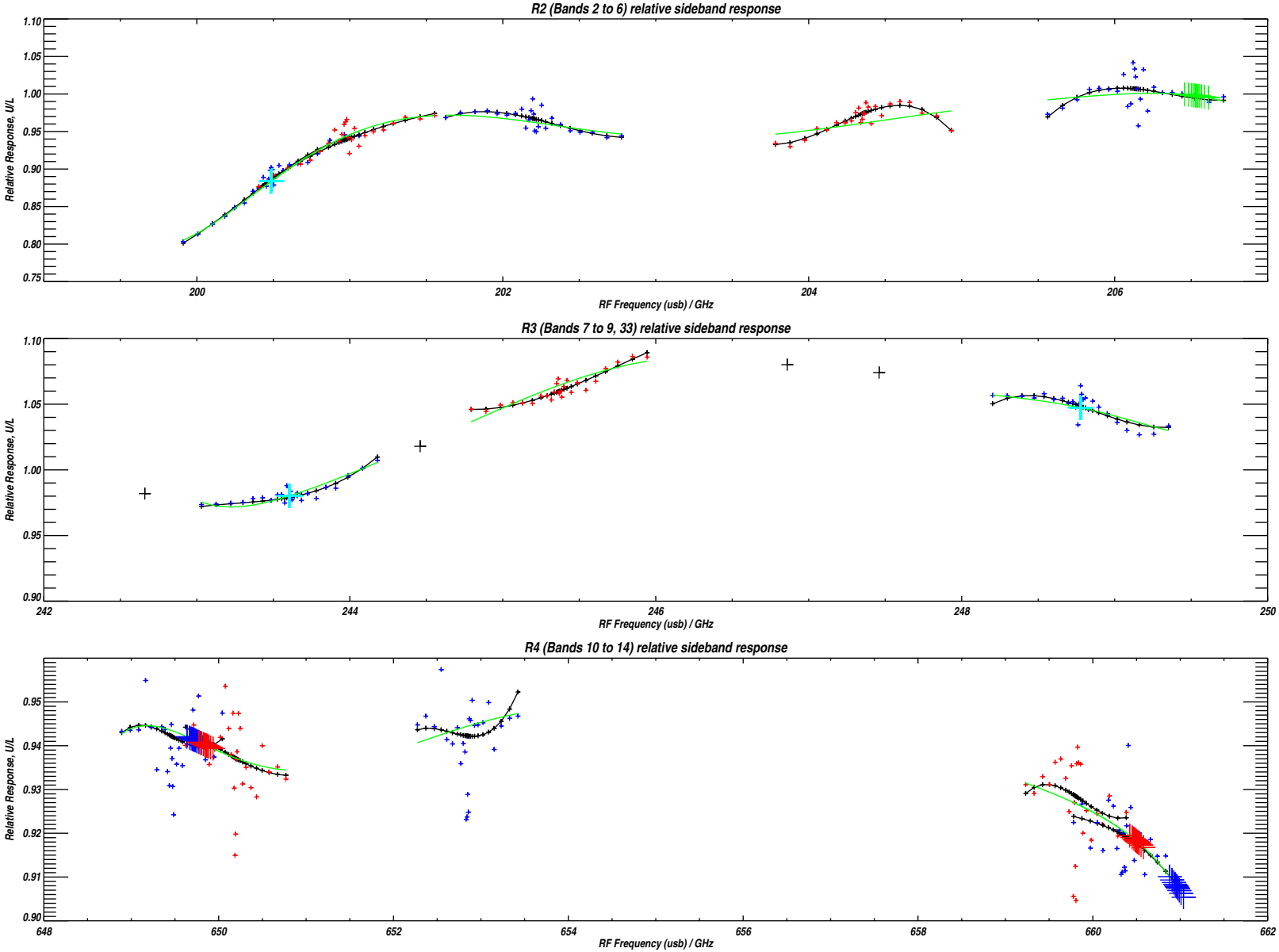

Figure 3.16: Relative sideband response for all double sideband channels of the GHz radiometers. See text for further details.

This is /nas/gse/data/FESweep/Sideband.dat, created by Plot_rsr_GHz.pro. Responses for lower and upper sidebands are listed separately for each band in Bill Read's desired format. For R2, R3 and R4 FB25s, the sideband ratios are derived from a single fit to the data from all bands in each radiometer.

Band 1 LSB:
1.00000 1.00000 1.00000 1.00000 1.00000
1.00000 1.00000 1.00000 1.00000 1.00000
1.00000 1.00000 1.00000 1.00000 1.00000
1.00000 1.00000 1.00000 1.00000 1.00000
1.00000 1.00000 1.00000 1.00000 1.00000
Band 1 USB:
0.00000 0.00000 0.00000 0.00000 0.00000
0.00000 0.00000 0.00000 0.00000 0.00000
0.00000 0.00000 0.00000 0.00000 0.00000
0.00000 0.00000 0.00000 0.00000 0.00000
0.00000 0.00000 0.00000 0.00000 0.00000
Band 2 LSB:
0.55401 0.55108 0.54746 0.54411 0.54132
0.53848 0.53601 0.53425 0.53304 0.53218
0.53159 0.53117 0.53087 0.53058 0.53016
0.52958 0.52877 0.52764 0.52608 0.52398
0.52172 0.51962 0.51724 0.51473 0.51261
Band 2 USB:
0.44599 0.44892 0.45254 0.45589 0.45868
0.46152 0.46399 0.46575 0.46696 0.46782
0.46841 0.46883 0.46913 0.46942 0.46984
0.47042 0.47123 0.47236 0.47392 0.47602
0.47828 0.48038 0.48276 0.48527 0.48739
Band 3 LSB:
0.53433 0.53023 0.52637 0.52339 0.52117
0.51912 0.51746 0.51635 0.51562 0.51511
0.51477 0.51453 0.51437 0.51420 0.51397
0.51366 0.51322 0.51264 0.51187 0.51089
0.50993 0.50913 0.50833 0.50766 0.50727
Band 3 USB:
0.46567 0.46977 0.47363 0.47661 0.47883
0.48088 0.48254 0.48365 0.48438 0.48489
0.48523 0.48547 0.48563 0.48580 0.48603
0.48634 0.48678 0.48736 0.48813 0.48911
0.49007 0.49087 0.49167 0.49234 0.49273
Band 4 LSB:
0.51375 0.51318 0.51254 0.51196 0.51148
0.51099 0.51055 0.51025 0.51003 0.50988
0.50977 0.50970 0.50965 0.50959 0.50952
0.50942 0.50927 0.50907 0.50880 0.50844
0.50806 0.50774 0.50742 0.50719 0.50715
Band 4 USB:
0.48625 0.48682 0.48746 0.48804 0.48852
0.48901 0.48945 0.48975 0.48997 0.49012
0.49023 0.49030 0.49035 0.49041 0.49048
0.49058 0.49073 0.49093 0.49120 0.49156
0.49194 0.49226 0.49258 0.49281 0.49285
Band 5 LSB:
0.50568 0.50634 0.50703 0.50762 0.50810
0.50858 0.50900 0.50931 0.50952 0.50967
0.50978 0.50985 0.50991 0.50996 0.51003
0.51014 0.51029 0.51050 0.51080 0.51121
0.51166 0.51211 0.51263 0.51322 0.51375
Band 5 USB:
0.49432 0.49366 0.49297 0.49238 0.49190
0.49142 0.49100 0.49069 0.49048 0.49033
0.49022 0.49015 0.49009 0.49004 0.48997
0.48986 0.48971 0.48950 0.48920 0.48879
0.48834 0.48789 0.48737 0.48678 0.48625
Band 6 LSB:
0.50195 0.50149 0.50106 0.50073 0.50049
0.50027 0.50011 0.50000 0.49994 0.49990
0.49988 0.49986 0.49985 0.49984 0.49982
0.49980 0.49978 0.49976 0.49975 0.49978
0.49989 0.50009 0.50049 0.50127 0.50243
Band 6 USB:
0.49805 0.49851 0.49894 0.49927 0.49951
0.49973 0.49989 0.50000 0.50006 0.50010
0.50012 0.50014 0.50015 0.50016 0.50018
0.50020 0.50022 0.50024 0.50025 0.50022
0.50011 0.49991 0.49951 0.49873 0.49757
Band 7 LSB:
0.49860 0.49976 0.50089 0.50181 0.50253
0.50323 0.50383 0.50424 0.50452 0.50471
0.50485 0.50494 0.50501 0.50507 0.50517
0.50529 0.50547 0.50571 0.50603 0.50642
0.50680 0.50706 0.50719 0.50698 0.50625
Band 7 USB:
0.50140 0.50024 0.49911 0.49819 0.49747
0.49677 0.49617 0.49576 0.49548 0.49529
0.49515 0.49506 0.49499 0.49493 0.49483
0.49471 0.49453 0.49429 0.49397 0.49358
0.49320 0.49294 0.49281 0.49302 0.49375
Band 8 LSB:
0.49100 0.48981 0.48865 0.48770 0.48696
0.48624 0.48563 0.48520 0.48491 0.48471
0.48456 0.48446 0.48439 0.48432 0.48423
0.48409 0.48389 0.48363 0.48326 0.48277
0.48224 0.48175 0.48119 0.48061 0.48013
Band 8 USB:
0.50900 0.51019 0.51135 0.51230 0.51304
0.51376 0.51437 0.51480 0.51509 0.51529
0.51544 0.51554 0.51561 0.51568 0.51577
0.51591 0.51611 0.51637 0.51674 0.51723
0.51776 0.51825 0.51881 0.51939 0.51987
Band 9 LSB:

0.49263 0.49195 0.49119 0.49055 0.49006
0.48958 0.48919 0.48893 0.48875 0.48863
0.48855 0.48849 0.48845 0.48841 0.48835
0.48827 0.48816 0.48801 0.48781 0.48755
0.48728 0.48703 0.48674 0.48643 0.48613
Band 9 USB:
0.50737 0.50805 0.50881 0.50945 0.50994
0.51042 0.51081 0.51107 0.51125 0.51137
0.51145 0.51151 0.51155 0.51159 0.51165
0.51173 0.51184 0.51199 0.51219 0.51245
0.51272 0.51297 0.51326 0.51357 0.51387
Band 10 LSB:
0.51472 0.51444 0.51429 0.51425 0.51426
0.51430 0.51437 0.51442 0.51446 0.51450
0.51452 0.51454 0.51455 0.51457 0.51458
0.51461 0.51465 0.51471 0.51480 0.51492
0.51508 0.51523 0.51543 0.51567 0.51589
Band 10 USB:
0.48528 0.48556 0.48571 0.48575 0.48574
0.48570 0.48563 0.48558 0.48554 0.48550
0.48548 0.48546 0.48545 0.48543 0.48542
0.48539 0.48535 0.48529 0.48520 0.48508
0.48492 0.48477 0.48457 0.48433 0.48411
Band 11 LSB:
0.51694 0.51688 0.51680 0.51671 0.51663
0.51654 0.51644 0.51637 0.51632 0.51628
0.51625 0.51623 0.51622 0.51621 0.51619
0.51616 0.51612 0.51606 0.51597 0.51584
0.51569 0.51553 0.51534 0.51510 0.51487
Band 11 USB:
0.48306 0.48312 0.48320 0.48329 0.48337
0.48346 0.48356 0.48363 0.48368 0.48372
0.48375 0.48377 0.48378 0.48379 0.48381
0.48384 0.48388 0.48394 0.48403 0.48416
0.48431 0.48447 0.48466 0.48490 0.48513
Band 12 LSB:
0.51352 0.51363 0.51374 0.51384 0.51393
0.51401 0.51410 0.51416 0.51420 0.51423
0.51425 0.51427 0.51428 0.51429 0.51431
0.51433 0.51436 0.51441 0.51447 0.51457
0.51468 0.51479 0.51493 0.51511 0.51529
Band 12 USB:
0.48648 0.48637 0.48626 0.48616 0.48607
0.48599 0.48590 0.48584 0.48580 0.48577
0.48575 0.48573 0.48572 0.48571 0.48569
0.48567 0.48564 0.48559 0.48553 0.48543
0.48532 0.48521 0.48507 0.48489 0.48471
Band 13 LSB:
0.51774 0.51793 0.51813 0.51830 0.51844
0.51859 0.51872 0.51881 0.51888 0.51893
0.51896 0.51899 0.51901 0.51902 0.51905
0.51908 0.51914 0.51921 0.51932 0.51947
0.51966 0.51985 0.52011 0.52045 0.52082
Band 13 USB:
0.48226 0.48207 0.48187 0.48170 0.48156
0.48141 0.48128 0.48119 0.48112 0.48107
0.48104 0.48101 0.48099 0.48098 0.48095
0.48092 0.48086 0.48079 0.48068 0.48053
0.48034 0.48015 0.47989 0.47955 0.47918
Band 14 LSB:
0.52392 0.52321 0.52258 0.52212 0.52178
0.52146 0.52120 0.52103 0.52091 0.52083
0.52077 0.52073 0.52070 0.52068 0.52064
0.52058 0.52051 0.52041 0.52026 0.52007
0.51987 0.51967 0.51944 0.51918 0.51894
Band 14 USB:
0.47608 0.47679 0.47742 0.47788 0.47822
0.47854 0.47880 0.47897 0.47909 0.47917
0.47923 0.47927 0.47930 0.47932 0.47936
0.47942 0.47949 0.47959 0.47974 0.47993
0.48013 0.48033 0.48056 0.48082 0.48106
Band 15 LSB:
0.95750 0.95800 0.95850 0.95890 0.95920
0.95960 0.95990 0.96010 0.96020 0.96030
0.96040 0.96040 0.96050 0.96050 0.96060
0.96060 0.96070 0.96090 0.96110 0.96140
0.96170 0.96210 0.96250 0.96300 0.96350
Band 15 USB:
0.04250 0.04200 0.04150 0.04110 0.04080
0.04040 0.04010 0.03990 0.03980 0.03970
0.03960 0.03960 0.03950 0.03950 0.03940
0.03940 0.03930 0.03910 0.03890 0.03860
0.03830 0.03790 0.03750 0.03700 0.03650
Band 16 LSB:
0.80400 0.80870 0.81290 0.81670 0.81960
0.82270 0.82520 0.82710 0.82840 0.82940
0.83000 0.83050 0.83080 0.83110 0.83160
0.83220 0.83310 0.83440 0.83630 0.83890
0.84170 0.84490 0.84840 0.85320 0.85720
Band 16 USB:
0.19600 0.19130 0.18710 0.18330 0.18040
0.17730 0.17480 0.17290 0.17160 0.17060
0.17000 0.16950 0.16920 0.16890 0.16840
0.16780 0.16690 0.16560 0.16370 0.16110
0.15830 0.15510 0.15160 0.14680 0.14280
Band 17 LSB:
0.42500 0.41920 0.41350 0.40850 0.40450
0.40030 0.39680 0.39440 0.39270 0.39150
0.39060 0.39000 0.38950 0.38910 0.38850
0.38760 0.38640 0.38460 0.38220 0.37860
0.37490 0.37090 0.36590 0.36010 0.35400
Band 17 USB:
0.57500 0.58080 0.58650 0.59150 0.59550
0.59970 0.60320 0.60560 0.60730 0.60850

0.60940 0.61000 0.61050 0.61090 0.61150
0.61240 0.61360 0.61540 0.61780 0.62140
0.62510 0.62910 0.63410 0.63990 0.64600
Band 18 LSB:
0.94650 0.94680 0.94700 0.94730 0.94740
0.94760 0.94780 0.94790 0.94800 0.94800
0.94800 0.94810 0.94810 0.94810 0.94810
0.94820 0.94820 0.94830 0.94840 0.94860
0.94870 0.94890 0.94910 0.94940 0.94970
Band 18 USB:
0.05350 0.05320 0.05300 0.05270 0.05260
0.05240 0.05220 0.05210 0.05200 0.05200
0.05200 0.05190 0.05190 0.05190 0.05190
0.05180 0.05180 0.05170 0.05160 0.05140
0.05130 0.05110 0.05090 0.05060 0.05030
Band 19 LSB:
0.78500 0.78980 0.79410 0.79800 0.80110
0.80400 0.80670 0.80860 0.80990 0.81090
0.81160 0.81200 0.81240 0.81270 0.81320
0.81380 0.81470 0.81600 0.81810 0.82060
0.82370 0.82670 0.83040 0.83510 0.83960
Band 19 USB:
0.21500 0.21020 0.20590 0.20200 0.19890
0.19600 0.19330 0.19140 0.19010 0.18910
0.18840 0.18800 0.18760 0.18730 0.18680
0.18620 0.18530 0.18400 0.18190 0.17940
0.17630 0.17330 0.16960 0.16490 0.16040
Band 20 LSB:
0.41870 0.41310 0.40650 0.40200 0.39800
0.39370 0.39040 0.38790 0.38620 0.38500
0.38410 0.38350 0.38300 0.38260 0.38200
0.38120 0.37990 0.37810 0.37570 0.37200
0.36850 0.36450 0.35930 0.35380 0.34760
Band 20 USB:
0.58130 0.58690 0.59350 0.59800 0.60200
0.60630 0.60960 0.61210 0.61380 0.61500
0.61590 0.61650 0.61700 0.61740 0.61800
0.61880 0.62010 0.62190 0.62430 0.62800
0.63150 0.63550 0.64070 0.64620 0.65240
Band 21 LSB:
1.00000 1.00000 1.00000 1.00000 1.00000
1.00000 1.00000 1.00000 1.00000 1.00000
1.00000 1.00000 1.00000 1.00000 1.00000
1.00000 1.00000 1.00000 1.00000 1.00000
1.00000 1.00000 1.00000 1.00000 1.00000
Band 21 USB:
0.00000 0.00000 0.00000 0.00000 0.00000
0.00000 0.00000 0.00000 0.00000 0.00000
0.00000 0.00000 0.00000 0.00000 0.00000
0.00000 0.00000 0.00000 0.00000 0.00000
0.00000 0.00000 0.00000 0.00000 0.00000
Band 22 LSB:
1.00000 1.00000 1.00000 1.00000 1.00000
1.00000 1.00000 1.00000 1.00000 1.00000
1.00000 1.00000 1.00000 1.00000 1.00000
1.00000 1.00000 1.00000 1.00000 1.00000
1.00000 1.00000 1.00000 1.00000 1.00000
1.00000 1.00000 1.00000 1.00000 1.00000
1.00000 1.00000 1.00000 1.00000 1.00000
1.00000 1.00000 1.00000 1.00000 1.00000
1.00000 1.00000 1.00000 1.00000 1.00000
1.00000 1.00000 1.00000 1.00000 1.00000
1.00000 1.00000 1.00000 1.00000 1.00000
1.00000 1.00000 1.00000 1.00000 1.00000
1.00000 1.00000 1.00000 1.00000 1.00000
1.00000 1.00000 1.00000 1.00000 1.00000
1.00000 1.00000 1.00000 1.00000 1.00000
1.00000 1.00000 1.00000 1.00000 1.00000
1.00000 1.00000 1.00000 1.00000 1.00000
1.00000 1.00000 1.00000 1.00000 1.00000
1.00000 1.00000 1.00000 1.00000 1.00000
1.00000 1.00000 1.00000 1.00000 1.00000
1.00000 1.00000 1.00000 1.00000 1.00000
1.00000 1.00000 1.00000 1.00000 1.00000
1.00000 1.00000 1.00000 1.00000 1.00000
1.00000 1.00000 1.00000 1.00000 1.00000
1.00000 1.00000 1.00000 1.00000 1.00000
1.00000 1.00000 1.00000 1.00000
Band 22 USB:
0.00000 0.00000 0.00000 0.00000 0.00000
0.00000 0.00000 0.00000 0.00000 0.00000
0.00000 0.00000 0.00000 0.00000 0.00000
0.00000 0.00000 0.00000 0.00000 0.00000
0.00000 0.00000 0.00000 0.00000 0.00000
0.00000 0.00000 0.00000 0.00000 0.00000
0.00000 0.00000 0.00000 0.00000 0.00000
0.00000 0.00000 0.00000 0.00000 0.00000
0.00000 0.00000 0.00000 0.00000 0.00000
0.00000 0.00000 0.00000 0.00000 0.00000
0.00000 0.00000 0.00000 0.00000 0.00000
0.00000 0.00000 0.00000 0.00000 0.00000
0.00000 0.00000 0.00000 0.00000 0.00000
0.00000 0.00000 0.00000 0.00000 0.00000
0.00000 0.00000 0.00000 0.00000 0.00000
0.00000 0.00000 0.00000 0.00000 0.00000
0.00000 0.00000 0.00000 0.00000 0.00000
0.00000 0.00000 0.00000 0.00000 0.00000
0.00000 0.00000 0.00000 0.00000 0.00000
0.00000 0.00000 0.00000 0.00000 0.00000
0.00000 0.00000 0.00000 0.00000 0.00000
0.00000 0.00000 0.00000 0.00000 0.00000
0.00000 0.00000 0.00000 0.00000 0.00000
0.00000 0.00000 0.00000 0.00000 0.00000
0.00000 0.00000 0.00000 0.00000 0.00000

0.00000 0.00000 0.00000 0.00000
Band 23 LSB:
0.53061 0.53062 0.53062 0.53062 0.53063
0.53063 0.53063 0.53064 0.53064 0.53064
0.53065 0.53065 0.53065 0.53066 0.53066
0.53066 0.53067 0.53067 0.53067 0.53068
0.53068 0.53068 0.53069 0.53069 0.53069
0.53070 0.53070 0.53070 0.53071 0.53071
0.53071 0.53072 0.53072 0.53072 0.53073
0.53073 0.53073 0.53074 0.53074 0.53074
0.53075 0.53075 0.53075 0.53076 0.53076
0.53076 0.53077 0.53077 0.53077 0.53078
0.53078 0.53078 0.53079 0.53079 0.53079
0.53080 0.53080 0.53080 0.53081 0.53081
0.53081 0.53082 0.53082 0.53082 0.53083
0.53083 0.53083 0.53084 0.53084 0.53084
0.53085 0.53085 0.53085 0.53086 0.53086
0.53086 0.53087 0.53087 0.53087 0.53088
0.53088 0.53088 0.53089 0.53089 0.53089
0.53090 0.53090 0.53090 0.53091 0.53091
0.53091 0.53092 0.53092 0.53092 0.53093
0.53093 0.53093 0.53094 0.53094 0.53094
0.53095 0.53095 0.53096 0.53096 0.53096
0.53097 0.53097 0.53097 0.53098 0.53098
0.53098 0.53099 0.53099 0.53099 0.53100
0.53100 0.53100 0.53101 0.53101 0.53101
0.53102 0.53102 0.53102 0.53103 0.53103
0.53103 0.53104 0.53104 0.53104
Band 23 USB:
0.46939 0.46938 0.46938 0.46938 0.46937
0.46937 0.46937 0.46936 0.46936 0.46936
0.46935 0.46935 0.46935 0.46934 0.46934
0.46934 0.46933 0.46933 0.46933 0.46932
0.46932 0.46932 0.46931 0.46931 0.46931
0.46930 0.46930 0.46930 0.46929 0.46929
0.46929 0.46928 0.46928 0.46928 0.46927
0.46927 0.46927 0.46926 0.46926 0.46926
0.46925 0.46925 0.46925 0.46924 0.46924
0.46924 0.46923 0.46923 0.46923 0.46922
0.46922 0.46922 0.46921 0.46921 0.46921
0.46920 0.46920 0.46920 0.46919 0.46919
0.46919 0.46918 0.46918 0.46918 0.46917
0.46917 0.46917 0.46916 0.46916 0.46916
0.46915 0.46915 0.46915 0.46914 0.46914
0.46914 0.46913 0.46913 0.46913 0.46912
0.46912 0.46912 0.46911 0.46911 0.46911
0.46910 0.46910 0.46910 0.46909 0.46909
0.46909 0.46908 0.46908 0.46908 0.46907
0.46907 0.46907 0.46906 0.46906 0.46906
0.46905 0.46905 0.46904 0.46904 0.46904
0.46903 0.46903 0.46903 0.46902 0.46902
0.46902 0.46901 0.46901 0.46901 0.46900
0.46900 0.46900 0.46899 0.46899 0.46899
0.46898 0.46898 0.46898 0.46897 0.46897
0.46897 0.46896 0.46896 0.46896
Band 24 LSB:
0.50504 0.50504 0.50504 0.50504 0.50504
0.50504 0.50504 0.50504 0.50504 0.50504
0.50504 0.50504 0.50504 0.50504 0.50504
0.50504 0.50504 0.50503 0.50503 0.50503
0.50503 0.50503 0.50503 0.50503 0.50503
0.50503 0.50503 0.50503 0.50503 0.50503
0.50503 0.50503 0.50503 0.50503 0.50503
0.50503 0.50503 0.50503 0.50503 0.50503
0.50502 0.50502 0.50502 0.50502 0.50502
0.50502 0.50502 0.50502 0.50502 0.50502
0.50502 0.50502 0.50502 0.50502 0.50502
0.50502 0.50502 0.50502 0.50502 0.50502
0.50502 0.50502 0.50502 0.50501 0.50501
0.50501 0.50501 0.50501 0.50501 0.50501
0.50501 0.50501 0.50501 0.50501 0.50501
0.50501 0.50501 0.50501 0.50501 0.50501
0.50501 0.50501 0.50501 0.50501 0.50501
0.50501 0.50500 0.50500 0.50500 0.50500
0.50500 0.50500 0.50500 0.50500 0.50500
0.50500 0.50500 0.50500 0.50500 0.50500
0.50500 0.50500 0.50500 0.50500 0.50500
0.50500 0.50500 0.50500 0.50500 0.50499
0.50499 0.50499 0.50499 0.50499 0.50499
0.50499 0.50499 0.50499 0.50499 0.50499
0.50499 0.50499 0.50499 0.50499 0.50499
0.50499 0.50499 0.50499 0.50499
Band 24 USB:
0.49496 0.49496 0.49496 0.49496 0.49496
0.49496 0.49496 0.49496 0.49496 0.49496
0.49496 0.49496 0.49496 0.49496 0.49496
0.49496 0.49496 0.49497 0.49497 0.49497
0.49497 0.49497 0.49497 0.49497 0.49497
0.49497 0.49497 0.49497 0.49497 0.49497
0.49497 0.49497 0.49497 0.49497 0.49497
0.49497 0.49497 0.49497 0.49497 0.49497
0.49498 0.49498 0.49498 0.49498 0.49498
0.49498 0.49498 0.49498 0.49498 0.49498
0.49498 0.49498 0.49498 0.49498 0.49498
0.49498 0.49498 0.49498 0.49498 0.49498
0.49498 0.49498 0.49498 0.49499 0.49499
0.49499 0.49499 0.49499 0.49499 0.49499
0.49499 0.49499 0.49499 0.49499 0.49499
0.49499 0.49499 0.49499 0.49499 0.49499
0.49499 0.49499 0.49499 0.49499 0.49499
0.49499 0.49500 0.49500 0.49500 0.49500
0.49500 0.49500 0.49500 0.49500 0.49500
0.49500 0.49500 0.49500 0.49500 0.49500
0.49500 0.49500 0.49500 0.49500 0.49500

0.49500 0.49500 0.49500 0.49500 0.49501
0.49501 0.49501 0.49501 0.49501 0.49501
0.49501 0.49501 0.49501 0.49501 0.49501
0.49501 0.49501 0.49501 0.49501 0.49501
0.49501 0.49501 0.49501 0.49501

Band 25 LSB:

0.48839 0.48839 0.48839 0.48839 0.48839
0.48839 0.48839 0.48839 0.48839 0.48839
0.48840 0.48840 0.48840 0.48840 0.48840
0.48840 0.48840 0.48840 0.48840 0.48840
0.48840 0.48840 0.48840 0.48840 0.48841
0.48841 0.48841 0.48841 0.48841 0.48841
0.48841 0.48841 0.48841 0.48841 0.48841
0.48841 0.48841 0.48842 0.48842 0.48842
0.48842 0.48842 0.48842 0.48842 0.48842
0.48842 0.48842 0.48842 0.48842 0.48842
0.48843 0.48843 0.48843 0.48843 0.48843
0.48843 0.48843 0.48843 0.48843 0.48843
0.48843 0.48843 0.48843 0.48844 0.48844
0.48844 0.48844 0.48844 0.48844 0.48844
0.48844 0.48844 0.48844 0.48844 0.48844
0.48844 0.48845 0.48845 0.48845 0.48845
0.48845 0.48845 0.48845 0.48845 0.48845
0.48845 0.48845 0.48845 0.48845 0.48846
0.48846 0.48846 0.48846 0.48846 0.48846
0.48846 0.48846 0.48846 0.48846 0.48846
0.48846 0.48846 0.48846 0.48847 0.48847
0.48847 0.48847 0.48847 0.48847 0.48847
0.48847 0.48847 0.48847 0.48847 0.48847
0.48847 0.48848 0.48848 0.48848 0.48848
0.48848 0.48848 0.48848 0.48848 0.48848
0.48848 0.48848 0.48848 0.48848

Band 25 USB:

0.51161 0.51161 0.51161 0.51161 0.51161
0.51161 0.51161 0.51161 0.51161 0.51161
0.51160 0.51160 0.51160 0.51160 0.51160
0.51160 0.51160 0.51160 0.51160 0.51160 0
0.51160 0.51160 0.51160 0.51160 0.51159
0.51159 0.51159 0.51159 0.51159 0.51159
0.51159 0.51159 0.51159 0.51159 0.51159
0.51159 0.51159 0.51158 0.51158 0.51158
0.51158 0.51158 0.51158 0.51158 0.51158
0.51158 0.51158 0.51158 0.51158 0.51158
0.51157 0.51157 0.51157 0.51157 0.51157
0.51157 0.51157 0.51157 0.51157 0.51157
0.51157 0.51157 0.51157 0.51156 0.51156
0.51156 0.51156 0.51156 0.51156 0.51156
0.51156 0.51156 0.51156 0.51156 0.51156
0.51156 0.51155 0.51155 0.51155 0.51155
0.51155 0.51155 0.51155 0.51155 0.51155
0.51155 0.51155 0.51155 0.51155 0.51154
0.51154 0.51154 0.51154 0.51154 0.51154
0.51154 0.51154 0.51154 0.51154 0.51154
0.51154 0.51154 0.51154 0.51153 0.51153
0.51153 0.51153 0.51153 0.51153 0.51153
0.51153 0.51153 0.51153 0.51153 0.51153
0.51153 0.51152 0.51152 0.51152 0.51152
0.51152 0.51152 0.51152 0.51152 0.51152
0.51152 0.51152 0.51152 0.51152

Band 26 LSB:

1.00000 1.00000 1.00000 1.00000 1.00000
1.00000 1.00000 1.00000 1.00000 1.00000
1.00000 1.00000 1.00000 1.00000 1.00000
1.00000 1.00000 1.00000 1.00000 1.00000
1.00000 1.00000 1.00000 1.00000 1.00000
1.00000 1.00000 1.00000 1.00000 1.00000
1.00000 1.00000 1.00000 1.00000 1.00000
1.00000 1.00000 1.00000 1.00000 1.00000
1.00000 1.00000 1.00000 1.00000 1.00000
1.00000 1.00000 1.00000 1.00000 1.00000
1.00000 1.00000 1.00000 1.00000 1.00000
1.00000 1.00000 1.00000 1.00000 1.00000
1.00000 1.00000 1.00000 1.00000 1.00000
1.00000 1.00000 1.00000 1.00000 1.00000
1.00000 1.00000 1.00000 1.00000 1.00000
1.00000 1.00000 1.00000 1.00000 1.00000
1.00000 1.00000 1.00000 1.00000 1.00000
1.00000 1.00000 1.00000 1.00000 1.00000
1.00000 1.00000 1.00000 1.00000 1.00000
1.00000 1.00000 1.00000 1.00000 1.00000
1.00000 1.00000 1.00000 1.00000 1.00000
1.00000 1.00000 1.00000 1.00000 1.00000
1.00000 1.00000 1.00000 1.00000 1.00000
1.00000 1.00000 1.00000 1.00000 1.00000
1.00000 1.00000 1.00000 1.00000 1.00000
1.00000 1.00000 1.00000 1.00000

Band 26 USB:

0.00000 0.00000 0.00000 0.00000 0.00000
0.00000 0.00000 0.00000 0.00000 0.00000
0.00000 0.00000 0.00000 0.00000 0.00000
0.00000 0.00000 0.00000 0.00000 0.00000
0.00000 0.00000 0.00000 0.00000 0.00000
0.00000 0.00000 0.00000 0.00000 0.00000
0.00000 0.00000 0.00000 0.00000 0.00000
0.00000 0.00000 0.00000 0.00000 0.00000
0.00000 0.00000 0.00000 0.00000 0.00000
0.00000 0.00000 0.00000 0.00000 0.00000
0.00000 0.00000 0.00000 0.00000 0.00000
0.00000 0.00000 0.00000 0.00000 0.00000
0.00000 0.00000 0.00000 0.00000 0.00000
0.00000 0.00000 0.00000 0.00000 0.00000
0.00000 0.00000 0.00000 0.00000 0.00000
0.00000 0.00000 0.00000 0.00000 0.00000
0.00000 0.00000 0.00000 0.00000 0.00000

0.00000 0.00000 0.00000 0.00000 0.00000
0.00000 0.00000 0.00000 0.00000 0.00000
0.00000 0.00000 0.00000 0.00000 0.00000
0.00000 0.00000 0.00000 0.00000 0.00000
0.00000 0.00000 0.00000 0.00000 0.00000
0.00000 0.00000 0.00000 0.00000 0.00000
0.00000 0.00000 0.00000 0.00000 0.00000
0.00000 0.00000 0.00000 0.00000 0.00000
0.00000 0.00000 0.00000 0.00000
Band 27 LSB:
0.50016 0.50029 0.50040 0.50048 0.50055
0.50059 0.50064 0.50072 0.50082 0.50099
0.50125
Band 27 USB:
0.49984 0.49971 0.49960 0.49952 0.49945
0.49941 0.49936 0.49928 0.49918 0.49901
0.49875
Band 28 LSB:
0.51530 0.51523 0.51518 0.51515 0.51512
0.51510 0.51509 0.51506 0.51503 0.51498
0.51492
Band 28 USB:
0.48470 0.48477 0.48482 0.48485 0.48488
0.48490 0.48491 0.48494 0.48497 0.48502
0.48508
Band 29 LSB:
0.51525 0.51532 0.51537 0.51541 0.51543
0.51545 0.51546 0.51549 0.51552 0.51557
0.51564
Band 29 USB:
0.48475 0.48468 0.48463 0.48459 0.48457
0.48455 0.48454 0.48451 0.48448 0.48443
0.48436
Band 30 LSB:
0.52171 0.52157 0.52147 0.52141 0.52136
0.52133 0.52130 0.52125 0.52119 0.52110
0.52098
Band 30 USB:
0.47829 0.47843 0.47853 0.47859 0.47864
0.47867 0.47870 0.47875 0.47881 0.47890
0.47902
Band 31 LSB:
0.52483 0.52458 0.52441 0.52429 0.52421
0.52415 0.52409 0.52401 0.52390 0.52375
0.52354
Band 31 USB:
0.47517 0.47542 0.47559 0.47571 0.47579
0.47585 0.47591 0.47599 0.47610 0.47625
0.47646
Band 32 LSB:
1.00000 1.00000 1.00000 1.00000
Band 32 USB:
0.00000 0.00000 0.00000 0.00000
Band 33 LSB:
0.50456 0.49555 0.48075 0.48215
Band 33 USB:
0.49544 0.50445 0.51925 0.51785
Band 34 LSB:
1.00000 1.00000 1.00000 1.00000
Band 34 USB:
0.00000 0.00000 0.00000 0.00000

3.25 Accuracy

In the case where calibration measurements are noise-limited it is relatively easy to estimate the resulting uncertainty in calibrated radiance. In the case of EOS MLS spectral calibrations, the measurement precision is typically so good that the dominant sources of errors are systematic, and the these are much harder to estimate. There is also the important issue of calibration resilience – i.e., how stable are the pre-launch calibration parameters, and how do we account for post-launch drifts in instrument characteristics? We discuss these topics below.

3.25.1 Filterbank Spectrometers

The EOS MLS filterbank spectrometers were fabricated by REMEC Inc. using the same techniques as the filters used in their airborne electronics designs. These are designed for extremely harsh thermal and mechanical environments compared to those that will be experienced in this application. The inductive elements of these filters are hand wound and thermally annealed prior to being soldered to the circuit substrate, and all but the end turns glued in place. After final tuning (by small deformations of the unglued turns), a further annealing and gluing step is performed. This fabrication technique, coupled with the appropriate choice of substrate materials and surface mount capacitors, results in bandpass filters with extremely good long-term stability, and significant temperature sensitivity only when operated at temperatures significantly below those anticipated operationally.

Even though these factors give us high confidence in the long-term stability of the filter channels, the instrument incorporates a programmable IF synthesizer capable of simultaneously sweeping all 11- and 25-channel filterbanks from their inputs. If radiance residuals raise questions about the integrity of the calibration data for any of these channels, an in-flight sweep of all filterbank spectrometers will performed.

Other sources of channel placement error (such as drifts in downconversion local oscillators) are eliminated by the design choice to phase lock all of these elements to the extremely stable instrument Master Oscillator (MO). Should an MO malfunction take place that allows significant drift to occur, it will be relatively easy to retrieve MO frequency from in-orbit data, and correct for this in ground data processing.

3.25.2 Wide Filters and Digital Autocorrelators

The 12 Wide Filter channels in this instrument are fabricated as stripline devices, and we anticipate no significant drift in these components. The frequency response of each Digital Autocorrelator Spectrometer (DACS) channel is dominated by the frequency of the sampling clock for this device. Each autocorrelator pair uses an independent 25 MHz quartz crystal oscillator for this clock, and these oscillators are not phase locked to the 5 MHz MO. Since these oscillators are used to sample an IF bandpass near baseband, even drifts in these devices at the maximum expected levels raise no calibration issues.

3.25.3 High Resolution Sweeps

The previous subsections have discussed the anticipated stability of the final bandpass defining elements in the IF signal chains, but not the preceding bandpass elements in the IF

multiplexers, or the frequency responses of the front-end mixers themselves. All of these elements have bandpasses considerably wider than the individual channel filters, and wide enough that even if drifts occured in their edges, it would not have significant impact on the overall frequency response of any given channel. In addition, these elements are all designed to present a relatively flat response throughout the bandpass of each spectral band. As a consequence, we have no concerns about minor changes in the characteristics of these elements affecting overall calibration accuracy.

The high resolution sweeps were performed using a multiplied synthesizer output as the fundamental source. To eliminate errors in the source frequency we always used the instrument MO as the frequency reference for the synthesizer. The MO itself was periodically monitored during instrument integration and test using a frequency counter phase-locked to a reference provided by a GPS receiver, guaranteeing the accuracy of these measurements.

The most serious error by far in knowledge of channel response is that of placement. Fortunately this source of is essentially eliminated for the reasons discussed above, and can even be measured in orbit using the built-in synthesizer.

The effects of errors in measured filter shape (as opposed to placement) are readily modelled using techniques discussed in [3] in which the effects of distorted filter shapes on representative brightness kernels are numerically modelled. For the earlier UARS measurements there was a clear understanding of the level of random and systematic error in these measurements, but the improvements to the technique applied to the EOS MLS measurements have made the situation somewhat murkier. Measurement precision for the EOS measurements was high enough that noise can typically be ignored as a source of error, leaving just systematic errors to consider. Standing waves present the most obvious source of error in this regard, and were either absent (as verified by sweeping several channels with source in two positions displaced by $\frac{\lambda}{4}$), or compensated by performing the sweeps with both nominal and translated sources. This leaves power variations in the source across the passband of a filter as the dominant source of error in these calibration data. Comparison of measured channel shape data in both sidebands of the double sideband radiometers, combined with the fact that the fractional bandwidth encompassed by the sweep of any one channel is minute, leads us to believe that this is not a significant source of error in these measurements.

We are thus in the position of not being able to identify any significant sources of error in these calibrations. Rather than assuming this to be the true case we have chosen to assign 0.5% in calibrated radiance as the peak magnitude of the error in these calibrations, but we are confident that the true magnitude of these calibration errors is *much* smaller for most, if not all channels.

3.25.4 Relative Sideband Calibrations

For the GHz relative sideband measurements, shown in Figure 3.16, the situation is somewhat simpler. The precision of the measurements is clearly shown by the scatter of the individual channel data, and the level of systematic error may be estimated by observing the difference between the fits 'by band' (black curves), and global radiometer fits to these data (green curves). The discontinuities between data in overlapping regions (where the data should be the same for IF frequencies common to the overlapping bands) provide an additional, and consistent, indicator of the error levels on these measurements.

For the 118 GHz radiometers there are no errors in sideband data. These radiometers are

single sideband implementations, confirmed by measurements with the front-end fundamental sweep apparatus, and by inspection of the Fabry-Pérot sweep data for Bands 1 and 21. For R2 the largest deviations between the band and whole IF fit data are ∼0.02 in relative sideband response, corresponding to 1% error in single sideband radiance[7]. For R3 the errors are approximately halved, and for R4 halved again, indicating peak relative sideband uncertainties of ∼0.01 and ∼0.005, corresponding to radiometric errors of 0.5% and 0.25% in these radiometers.

There is no measure in flight of parameters such as 1st LO drive which can affect relative sideband response. We are thus reliant upon the long-term stability of the 1st LO and mixer assemblies in this regard. Subsystem-level measurements were made in which changes in relative sideband response as a function of LO drive, and of mixer temperature, were made for all double sideband receivers. These tests showed that for the maximum expected levels of LO degradation and subsystem operating temperature range we should not have noticeable changes in relative sideband response. We will be able to verify this in flight to some degree by retrieving relative sideband response as a diagnostic from the Level 2 software.

3.26 GHz Spectral Calibration Uncertainty

Directly adding the uncertainties due to channel shape and relative sideband uncertainties (rather than a more optimistic *rss* combination) leads to peak errors due to spectral calibration errors of 0.5% in the bands of R1/R21, 1.5% in the R2 bands, 1% in the bands of R3, and 0.75% for the bands in R4. Note that these are estimates of *peak* radiance uncertainty, to be compared to the 1% *rms* uncertainties specified in the instrument requirements. We thus believe that spectral calibration requirements are met with comfortable margins, and are confident that this will be verified by analyses of in-orbit data. Note that significant changes took place to R4 relative sideband characteristics between the time that the calibrations described here took place, and launch. These changes came about because of a late decision to change the 1st LO tripler from a whisker-contacted to a planar implementation in the interests of reliability. The effects of this changeout, and the impact on R4 relative sideband response, are discussed in Volume 4 of this report.

Table 3.1: Systematic error budget for limb port radiances arising from uncertainties in spectral calibration, expressed as a percentage of reported limb radiance.

Channel shape uncertainty	0.5%	Worst-case estimate
R1 Sideband uncertainty	0.0%	Single-sideband radiometer
R2 Sideband uncertainty	1.0%	
R3 Sideband uncertainty	0.4%	
R4 Sideband uncertainty	0.25%	See text

[7]For a double sideband radiometer with approximately balanced sideband response a small error in sideband response is split evenly, half to each sideband.

3.27 THz Relative Sideband Sweeps

The requirements for the THz spectral calibration are essentially the same as those for the GHz channels. Because of water vapor attenuation, all measurements had to be made in vacuum. The approach for both sideband and spectral response calibrations was to use a high-resolution Fabry-Pérot resonator illuminated by parabola-fed medium-pressure Mercury arc source. The Mercury arc provides a stable continuum source with an equivalent brightness of 1000–1200 K, and can be operated in vacuum. A solenoid-actuated shutter located near the Mercury arc source allowed differencing of signals with the source on and the source blocked. The Fabry-Pérot resonator was the same unit that has been use for many years in the FILOS balloon experiment for measuring OH. The distance between resonances (free spectral range or FSR) is 1.5 GHz, and the width of the resonance is 50 MHz. The resonator can scan 140 μm and is vacuum compatible. The filterbank response was observed as a function of Fabry-Pérot length, providing both sideband response and spectral response down to a resolution of 50 MHz. Since no appropriate spectrally-narrow swept sources exist in the THz region, swept spectra of the IF's were used for the narrow-band (<20 MHz) characterization of spectral response.

Special Equipment Needed

1. Six foot THz vacuum chamber
2. Medium-pressure water-cooled Mercury arc in an elliptical cavity. The arc is at one focus of the ellipse, and a 1.6 mm aperture is at the other focus. This aperture is at the focus of a 600 mm focal-length 267 mm diameter off-axis parabola.
3. Test parabola
4. FILOS Fabry-Pérot resonator
5. Mercury arc power supply and igniter
6. Scan electronics for Fabry-Pérot resonator
7. ±5V voltage source and shutter driver controlled by GSE
8. THz and Spectrometer Modules

Sensitivity and Accuracy

The Fabry-Pérot filter is step-scanned with 4 s observation with the shutter open, and 4 s with the shutter closed per step for a total of 385 steps. The time for a sweep is 80 minutes after allowance is made for laser re-optimization dead time. The FILOS Fabry-Pérot has 40% throughput at resonance. Combined with the expected brightness of the source, the predicted contrast at resonance is (1200 K − 300 K) × 0.4 = 360 C. For the 6 MHz filterbank channels, ΔT_{rms} = 3.0 K for 4 s data integration, or 1.2% after allowance for differencing. For the 96 MHz filterbank channels, the signal averaged over the filter is 230 C, while $\Delta T_{\rm rms} = 0.76$ K, for 0.45% precision under the same conditions. Actual performance is degraded because of standing wave interactions between the LLO and the Fabry-Pérot. Radiometric zero comes from the shutter differencing, while radiometric gain will come from assuming that the source

Table 3.2: THz Relative Sideband Results.

Band	lsb fraction	*rms* error	slope * GHz	*rms* error
Band 15 (OHa-H)	0.960	0.0010	-0.0053	0.0038
Band 18 (OHa-V)	0.948	0.0017	-0.0027	0.0066
Band 16 (OHb-H)	0.831	0.0019	-0.0463	0.0067
Band 19 (OHb-V)	0.812	0.0032	-0.0473	0.0113
Band 17 (O_2-H)	0.390	0.0031	-0.0620	0.0123
Band 20 (O_2-V)	0.383	0.0016	-0.0619	0.0064

output and Fabry-Pérot throughput are both independent of frequency. Fabry-Pérot length calibration comes automatically from measuring the repeat length for the scan (equal to half the wavelength). We took measurements for 4 scans for a total measurement time of 320 minutes.

Measurement and Analysis

Analysis is simple in principle, but somewhat more complicated in practice. Essentially the response from each channel is the integral of the Fabry-Pérot response multiplied by the filter response:

$$R(V)_i = Z_i + \sum_{k=0}^{1} \int \frac{A_{i,k} F(\nu)_{i,k} d\nu}{1 + |Q \sin[\pi\nu(1 + V/FSR_L)/FSR_\nu + \pi\phi]|^2} \tag{3.12}$$

where V is the etalon tuning voltage, $A_{i,k}$ is an amplitude for channel i and sideband k, Z_i is a zero, $F(\nu)_{i,k}$ is the known filter response, Q is related to the width of the Fabry-Pérot resonance, FSR_L is the free spectral range in voltage units, FSR_ν is the free spectral range in frequency units, and ϕ is a phase shift. The values of Q, FSR_L, and FSR_ν are fit for all scans and all bands. The values of ϕ, Z_i, and $A_{i,k}$ are fit for each scan and each band. The quantity of interest is the lower sideband fraction: $A_{i,0}/(A_{i,0} + A_{i,1})$.

Note that, for a few channels, the upper and lower sideband resonances occur at the same etalon length. For such channels the sideband fraction cannot be determined. We found it expedient to fit the resulting sideband fractions that were determinable to a straight line *vs* the average second IF frequency of the filter (less 900 MHz).

We fit the sideband ratio with a graphic interface that allows user intervention before starting the least square fit for a given scan and band. An example of a fit is shown in Figure 3.17. Final sideband calibration was performed on 7 December 2002, and the results are given in Table 3.2. A graphical depiction of the sideband results (before the straight line fit) are shown in Figure 3.18. The expected sideband performance for the diplexer is shown as the solid line assuming a diplexer FSR = 36.57 GHz and an offset of 6.52 GHz. Note that the sideband fraction and slope for each band are consistent with a model in which all the sideband performance is explained by the diplexer throughput.

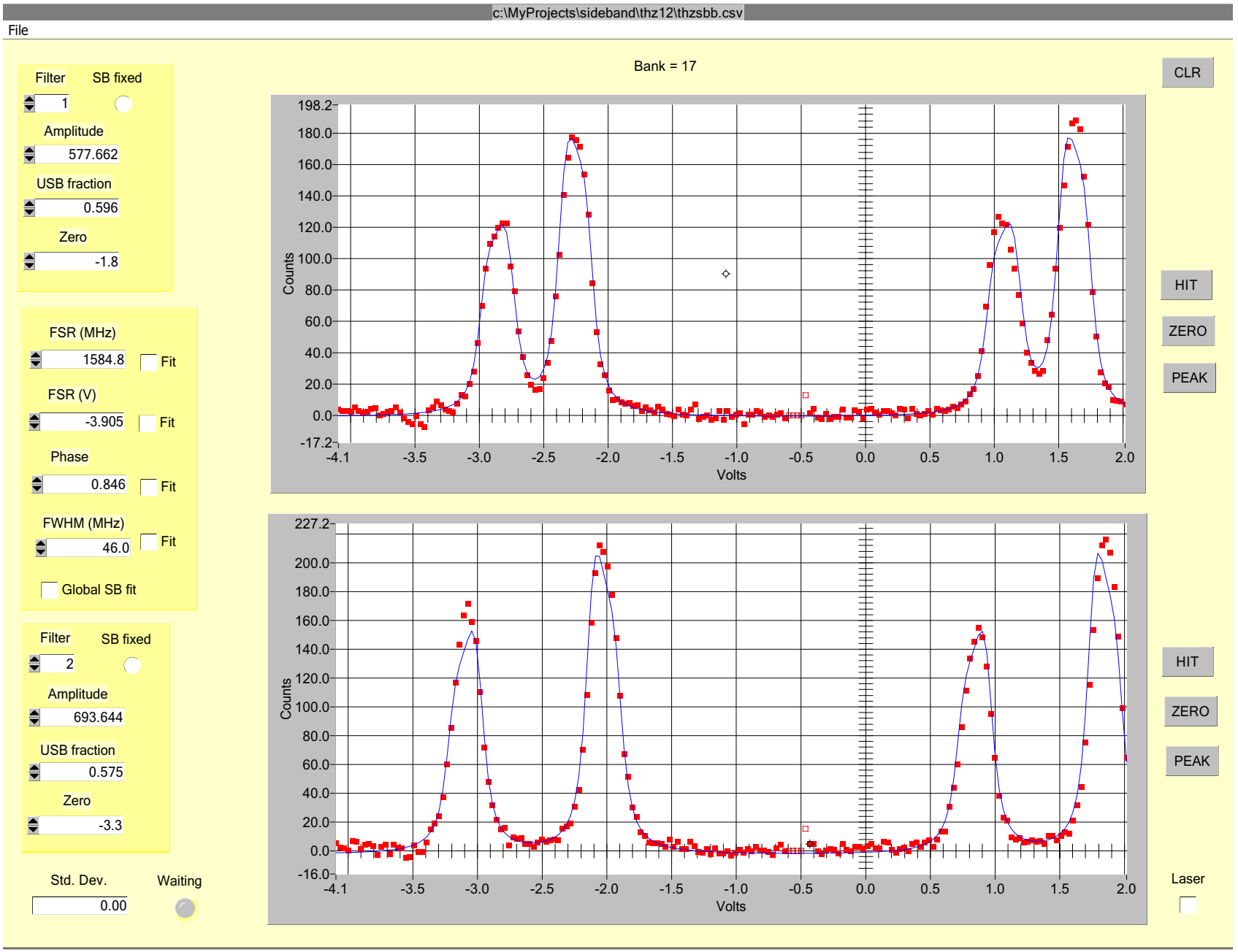

Figure 3.17: Fits to relative sideband data for channels 1 and 2 of THz Band 17. See text for further details.

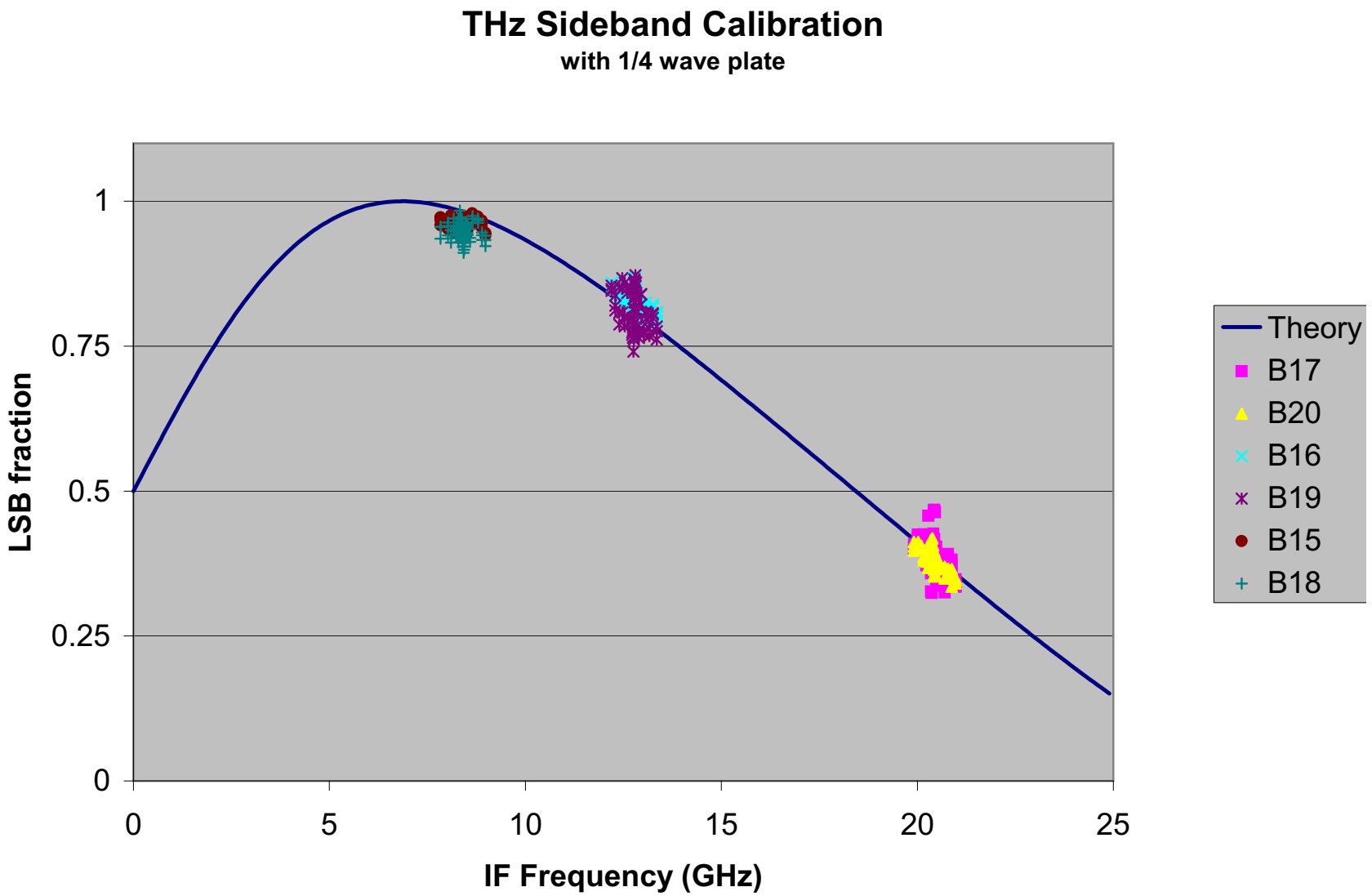

Figure 3.18: Relative sideband data for all THz bands expressed as an *lsb* fraction. See text for further details.

3.28 THz Band Spectral Calibration Uncertainty

For the THz bands, filter shape/position data were provided by IF sweeps with similar uncertainties to the front-end GHz sweeps. In addition, the Fabry-Pérot relative sideband sweeps provided end-to-end filter shape measurements with ∼50 MHz resolution, useful for the outer filterbank channels. In orbit we anticipate significant LLO drifts (up to ∼2 MHz), which will be handled in flight by retrieving its frequency from the science data.

We need to beef up this section in the future. There should be some useful end-to-end channel shape data from the FP sweeps to compare with the IF sweep data. After that we may be able to modify the IF sweep data according to diplexer response in order to obtain better estimates of true end-to-end channel shapes. We then need to quantify the uncertainties.

Chapter 4

FIELD OF VIEW (FOV) CALIBRATION

4.1 Performance Verification

The following FOV-related requirements, quoted from the Science Requirements document [**?**], cover performance verification as well as calibration, but are included here because data were taken to verify adequate instrument performance as part of the definitive calibration measurements.

4.1.1 FOV beamwidths and beam efficiency

Science Requirement 3.5.1 'FOV beamwidth' is defined as the angle between the half-power points of the antenna response as a function of angle. Beam efficiency is defined as that fraction of power from an isotropic source which is collected within a specified angular range centered at the antenna boresight.

Requirements on the MLS FOV beamwidths and beam efficiency are set by the vertical resolution needed for the measurements. The requirements given here are an acceptable compromise between the scientific desire for better vertical resolution, and the engineering/accommodation difficulties associated with the increase in antenna size required for better resolution. These requirements correspond to an antenna for the GHz channels which is the same size as that used for the MLS experiment on the Upper Atmosphere Research Satellite (UARS).

EOS MLS FOV beamwidths shall meet the requirements stated in Table 4.1. The beam efficiency within a solid angle range range of 2.5 times the beamwidth shall be 0.95 or greater.

4.1.2 FOV boresight coincidence

Science Requirement 3.5.2 'FOV boresight' is defined as the direction given by the peak value of the Gaussian function which best fits the antenna response down to the -10 dB power points. Requirements on FOV boresight coincidence ensure that different radiometers observe the same region of the atmosphere to within acceptable limits.

Table 4.1: Requirements on the EOS MLS Field-Of-View beamwidths

Radiometer	FOV beamwidth at 20 km tangent height			
	in vertical plane		in horizontal plane	
	/ km	/°	/ km	/°
118 GHz	≤6.5 km	≤*0.123*	≤15 km	≤*0.285*
190 GHz	≤4.5 km	≤*0.085*	≤10 km	≤*0.190*
240 GHz	≤3.5 km	≤*0.066*	≤10 km	≤*0.190*
640 GHz	≤1.5 km	≤*0.028*	≤10 km	≤*0.190*
2.5 THz	≤2.5 km	≤*0.047*	≤10 km	≤*0.190*

*FOV boresights of the 190, 240 and 640 GHz radiometers shall coincide with the B8LF:PT FOV boresight (EMLS pointing reference) to within one-fifth of the 118 GHz beamwidth. Engineering considerations make it desirable for the 2.5 THz radiometer to have separate optics, which is acceptable provided: (1) the 2.5 THz FOV boresight relative to the pointing reference shall be known to within one-fifth of the 118,GHz beamwidth, (2) the scan plane of the 2.5 THz boresight shall be within 10 km of that of the pointing reference at the atmospheric limb tangent point, over the tangent height range of 10 to 60 km, and (3) that the THz and GHz scans shall be synchronized as described in section 3.5.3 of [**?**].*

4.1.3 FOV scan

Science Requirement 3.5.4 *The FOV boresights shall be programmably scanned in the vertical through the atmospheric limb. The scan plane shall be within 1° of the orbit plane.*

4.1.4 Placement and knowledge of the FOV boresight directions

Science Requirement 3.5.4 *Tolerance in placement and knowledge of the tangent height of the FOV boresights, after in-orbit adjustments, is ±0.6 km at the start of each limb scan and degrading to ±1 km at the end of the limb scan. The tangent heights are with respect to a geoid model of the Earth and the scan must account for Earth s oblateness.* This requirement ensures efficient coverage of the vertical region of interest.

The change in elevation of the FOV boresights with respect to nadir during each limb scan shall be known to an accuracy of 2 arcsecond (3σ), and the rate of change shall be known to an accuracy of 1 arcsecond per second (3σ), at time scales between 0.17 and 25 seconds. MLS instrument data on the FOV boresight elevation shall be recorded at least twice per individual radiometric integration period. Spacecraft data relevant to the MLS FOV boresight elevation shall be recorded at least once per individual radiometric integration period. Jitter in the FOV boresights at time scales shorter than 0.17 second shall not exceed 2 arcsecond (3σ). These requirements ensure that tangent height uncertainties due to boresight elevation uncertainties are comparable or less than the equivalent height uncertainties in MLS measurements of tangent pressure.

4.1.5 FOV Calibration

Science Requirement 3.7.2 *Spectral and FOV calibration shall be performed and provide the instrument relative response as a function of frequency and angle for each spectral channel.*

The spectral and FOV responses of the instrument shall be characterized sufficiently that their separate uncertainties in the MLS 'forward model' calculations of the atmospheric/Earth radiances of more than (at the 90% confidence level):

(1) 3 K in the absolute value of the atmospheric/Earth radiances measured through each spectral channel, and

(2) 1% or $\Delta I_{min}/3$, where ΔI_{min} for each spectral channel is given in Table 3.2-2, in the spectrally-varying component of the atmospheric/Earth radiances measured from one channel or filter to another throughout a given radiometer.

4.1.6 Interpretation of FOV Requirements

Taper level for Gaussian fits

Calculation of FOV direction from measured patterns included points down to -10 dB from the measured peak, not -3 dB as implied by "half-power" in §4.1.4. Likewise, HPBW in §4.1.1 was calculated as the full width at half power of the Gaussian fit including points down to -10 dB.

EOS MLS pointing reference

Simulated retrievals of atmospheric constituents, done in studies performed after the flow-down of science requirements to instrument requirements, revealed that pointing retrieved from line shapes in band B8LF:PT would be superior to that from the 118 GHz channels, mostly because of the small FOV beamwidth at 234 GHz. Therefore the current flight software uses B8LF:PT as the MLS pointing reference instead of the 118 GHz FOV direction, even though the instrument requirements are still levied (and have been met) with respect to 118 GHz dFOV. Thus in the remainder of this report, dFOV coincidence, for calibration and for forward-model inputs, is referred to B8LF:PT.

Brightness Temperature Kernels to Test Compliance with Calibration Requirement

The *antenna temperature* T_A of the received atmospheric signal can be written

$$T_A = \frac{1}{4\pi} \iint_{4\pi} T_B(\Omega) G(\Omega) d\Omega$$

where $G(\Omega)$ describes the FOV in direction $\Omega(\theta, \phi)$ and is normalized such that

$$\oint G(\Omega) d\Omega = 4\pi.$$

$T_B(\Omega)$ is the brightness temperature of the radiation field in direction Ω, and the integral is over all directions. $G(\Omega)$ must be determined with sufficient accuracy and resolution for T_A

to meet the FOV calibration requirement of §4.1.5. A set of brightness temperature kernels which varies only in the vertical direction was computed by NJL according to[5], and is shown in Figure 4.1.

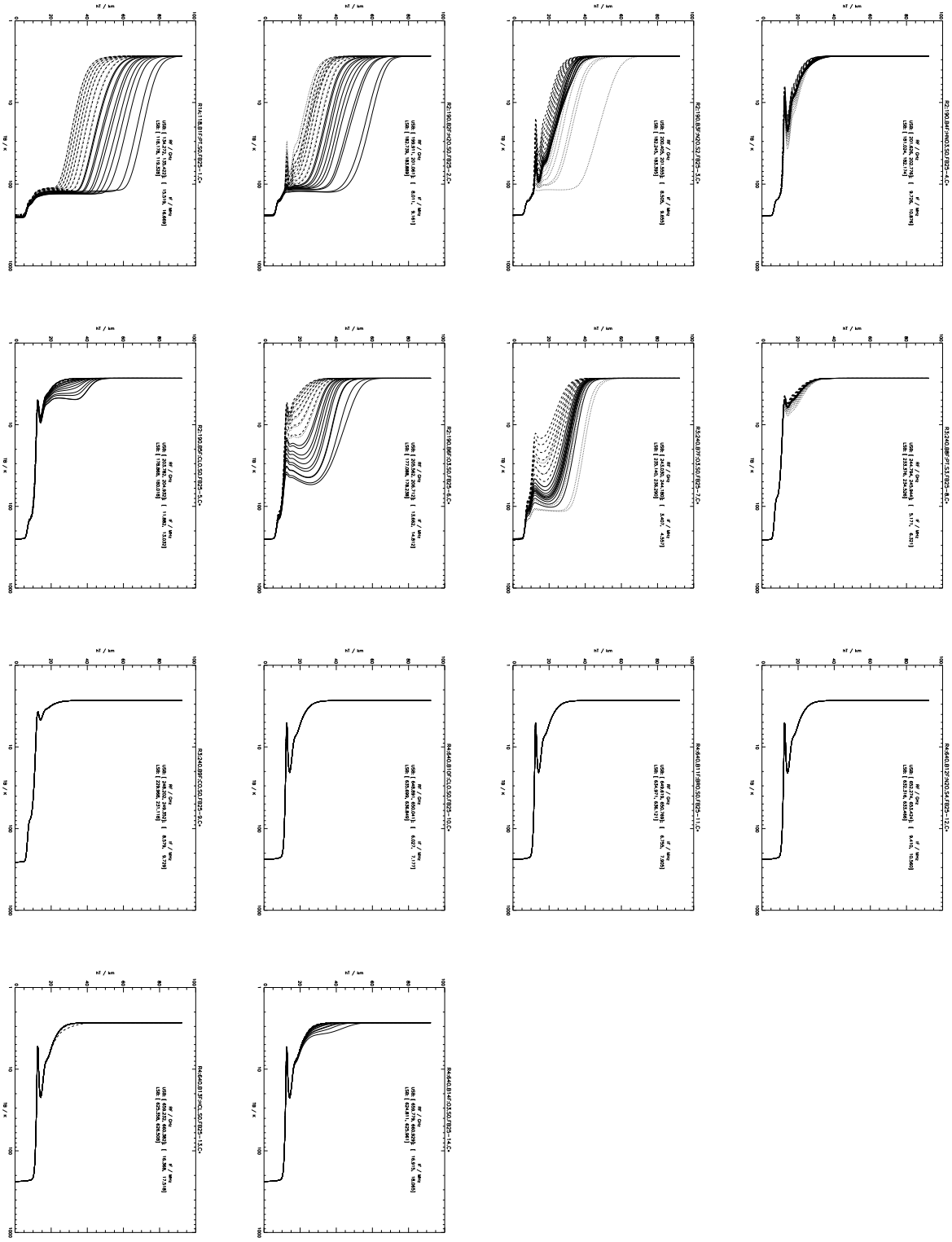

Figure 4.1: Models of Atmospheric Brightness Temperature for GHz Standard Filter Banks

4.2 FOV direction (dFOV)

4.2.1 Encoder/dFOV/alignment cube calibration

The definitive determination of dFOV was made by a theodolite survey of the alignment cube and the transmitter immediately following or before a pattern measurement in the GHz pointing reference, `B8LF:PT`. This *fiducial* pattern was abbreviated to concentrate on main beam pointing rather than sidelobes. In the analysis phase, a time series of fiducial pointing information was constructed to permit interpolation of reference pointing angles onto the patterns of the other radiometers.

In the definitive FOV calibration following environmental tests at JPL, dFOV was measured, along with the scan encoder reading, at 4 angles within the full scan range, to produce the the encoder–to–cube calibration data.

Appendix **??** describes a regression model which fits heuristic misalignment parameters to dFOVs measured for each GHz radiometer, along with dFOV coincidence measurements described below. The results are tabulated in Chapter 5 and input to the Level 1 and forward model software.

Knowledge of alignment to Aura is summarized in [**?**] as elements of the rotation matrix from nominal MLS pointing frame (tangent height $h_T = 30$ km) to the Instrument Alignment Cube (IAC) and to the observatory. A placeholder is left for the transformation from observatory (Spacecraft Body-fixed Frame, or SBF) to Attitude Control System (ACS), to allow for modeling of deformations (both static and dynamic) between SBF and ACS frames; this is currently an identity matrix which may be modified as we further understand the chain of alignment transformations from MLS FOV to Earth-Centered Inertial (ECI) frames.

4.2.2 dFOV coincidence between radiometers

The repetition of fiducial patterns between those of other radiometers allowed the dFOV coincidence between radiometer FOVs to be evaluated quickly and without inflation of uncertainties which would result from going through the optical alignment data path. Table 4.2 and Figure 4.2 show the compliance of dFOV coincidence with requirements. The grouping of boresight directions reflects the tolerances on elements of the optical multiplexer.

4.3 Half-Power Beamwidth (HPBW) and Beam Efficiency

Table 4.3 lists HPBW for the MLS bands. Knowledge values assume no information about the frequency or scan dependence of this beam statistic; Appendix **??** shows these dependences and argues that HPBW is independent of them. This appendix also outlines the algorithm for calculating a best-fit Gaussian function to the beam peak, and discusses errors, plus a rationale for truncating the fit at 10 dB below the empirical peak.

The table also lists beam efficiency within the measured solid angle Ω_A ($\pm 6°$). This does not include the fraction scattered outside the measurement region, which is included in γ_r^A below.

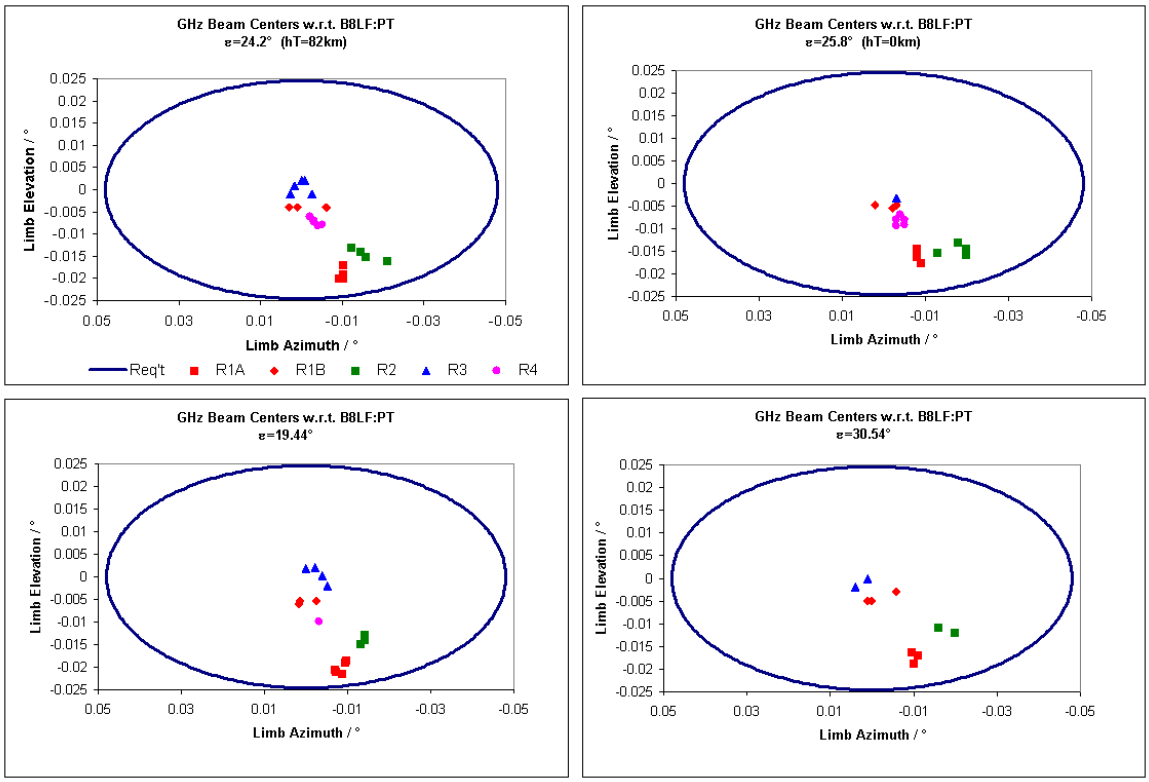

Figure 4.2: Boresight coincidence of EOS MLS GHz radiometers

Table 4.2: Requirements and measured dFOV coincidence of the GHz FOVs.

Limb Vertical	R3	R1A	R1B	R2	R4	R5
	B8LF:PT	Requirement: coincident within 0.025°				
measured dθ / °	≡0	-0.019	-0.006	-0.014	-0.008	≡0
3σ* / °	-	0.006	0.004	0.003	0.003	-
Limb Horizontal	R3	R1A	R1B	R2	R4	R5
	B8LF:PT	Requirement: coincident within 0.05°				within 1°
measured dϕ / °	≡0	-0.010	-0.002	-0.017	-0.003	0.039
3σ* / °	-	0.004	0.010	0.006	0.004	0.008

θ, ϕ are spherical polar angles in GHz cube frame:
$\theta = -\epsilon$ increases towards sky, decreases towards Earth
$\phi = +\alpha$ increases towards radiometer, decreases towards encoder
*σ includes IF and scan angle dependences of GHz dFOV

Table 4.3: Requirements and measured performance of the GHz FOVs: beamwidth and beam efficiency.

GHz Band	HPBW Vertical / °		HPBW Horizontal / °		Beam Efficiency / %	
	Required	Measured	Required	Measured	Required	Measured
118 R1A	0.123	[0.107,0.118]	0.283	[0.227,0.245]	≥0.95	[0.978,0.987]
R1B	0.123	[0.111,0.119]	0.283	[0.220,0.236]	≥0.95	[0.980,0.982]
190 R2	0.085	[0.074,0.084]	0.189	[0.147,0.168]	≥0.95	[0.959,0.980]
240 R3	0.066	[0.058,0.064]	0.189	[0.116,0.126]	≥0.95	[0.962,0.973]
640 R4	0.028	[0.0252,0.0271]	0.189	[0.0528,0.0572]	≥0.95	[0.962,0.967]

4.3.1 FOV Polarization angle

Knowledge of the polarization direction of the MLS FOV, although not addressed in the Science Requirements, is needed when the effect of Earth's magnetic field is included, in the polarized forward model and for `B22LD:PT` and `B26LD:PT` retrievals. Figure 4.3 represents the electric field vector of the FOV, when looking into the antenna. Ignoring effects due to reflector curvature, the antenna scan rotates the FOV field direction ξ about the boresight; *i.e.* $\xi = \xi_0 + (\epsilon - 25.2°)$, where ϵ is one of the angles relating Instrument Reference Frame to FOV Boresight Frame (Section 4.2.1). *A priori* values of the reference directions ξ_0 can be obtained from the design geometries of antenna and radiometers.

During FOV tests, we attempted to measure ξ_0 in the determination of cross-polarization directions, but were unable to obtain the absolute polarization with respect to the alignment cube to better than 0.7°. Fabrication tolerances allowed for 0.5° total error in alignment of **E** or **H** to the scan axis, so in Table 4.4 we report the design values of polarization angle at the scan angle $\epsilon = 25.2°$.

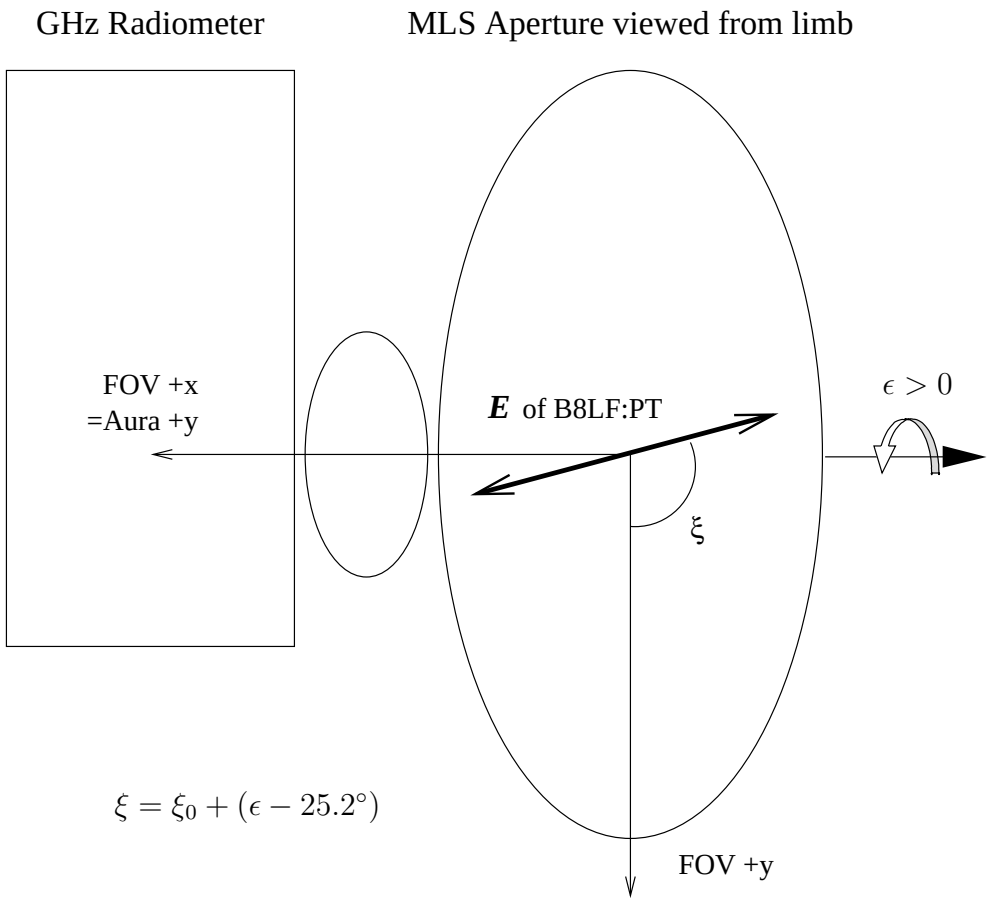

Figure 4.3: FOV Electric Field Vector projected onto MLS Aperture from limb.

Table 4.4: FOV polarization angles, from optics fabrication tolerances

	R1A	R1B	R2	R3	R4
$\xi_0/^\circ \pm 0.5$	0.0	90.0	0.0	90.0	90.0

4.4 FOV Calibration

4.4.1 Primary Considerations

Sources of error in convolving T_B with pattern gain to the required accuracy include

- random noise and systematic errors in the FOV test set-up,
- its noise floor, and
- pointing uncertainty.

The sensitivity of the T_A calculation to these sources depends on the fact that the T_B function is nearly one-dimensional. Appendix **??** transforms measurement noise to the T_A domain in which the calibration requirement applies.

4.4.2 Definitive FOV functions for Level 2 Processing Coefficients

Beyond the functional verification of HPBW, pointing and beam efficiency listed above, the gain functions are delivered to the forward model program to provide linearization points for calculation of partial derivatives.

The $G_r^M(\theta, \phi)$ are reduced to one-dimensional functions $G_r^M(\epsilon)$ for delivery to the forward model and for verification of the calibration requirement by convolution with horizontally-invariant radiance profiles, as described in Appendix **??**. Figures 4.4–4.8 show the functions $G_r^M(\epsilon)$.

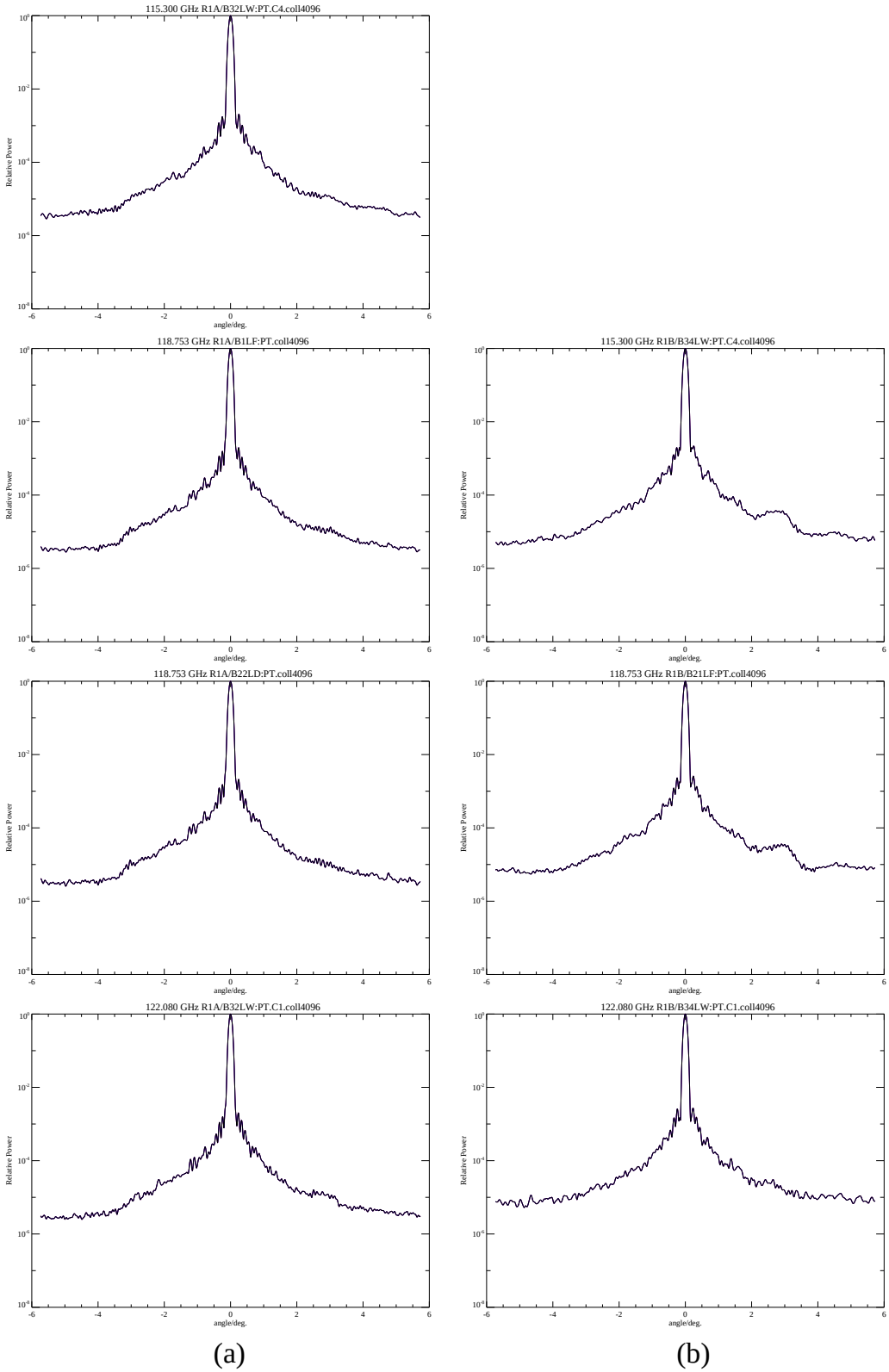

Figure 4.4: Definitive R1 FOV functions for Level 2 Processing Coefficients: (a) R1A, (b) R1B.

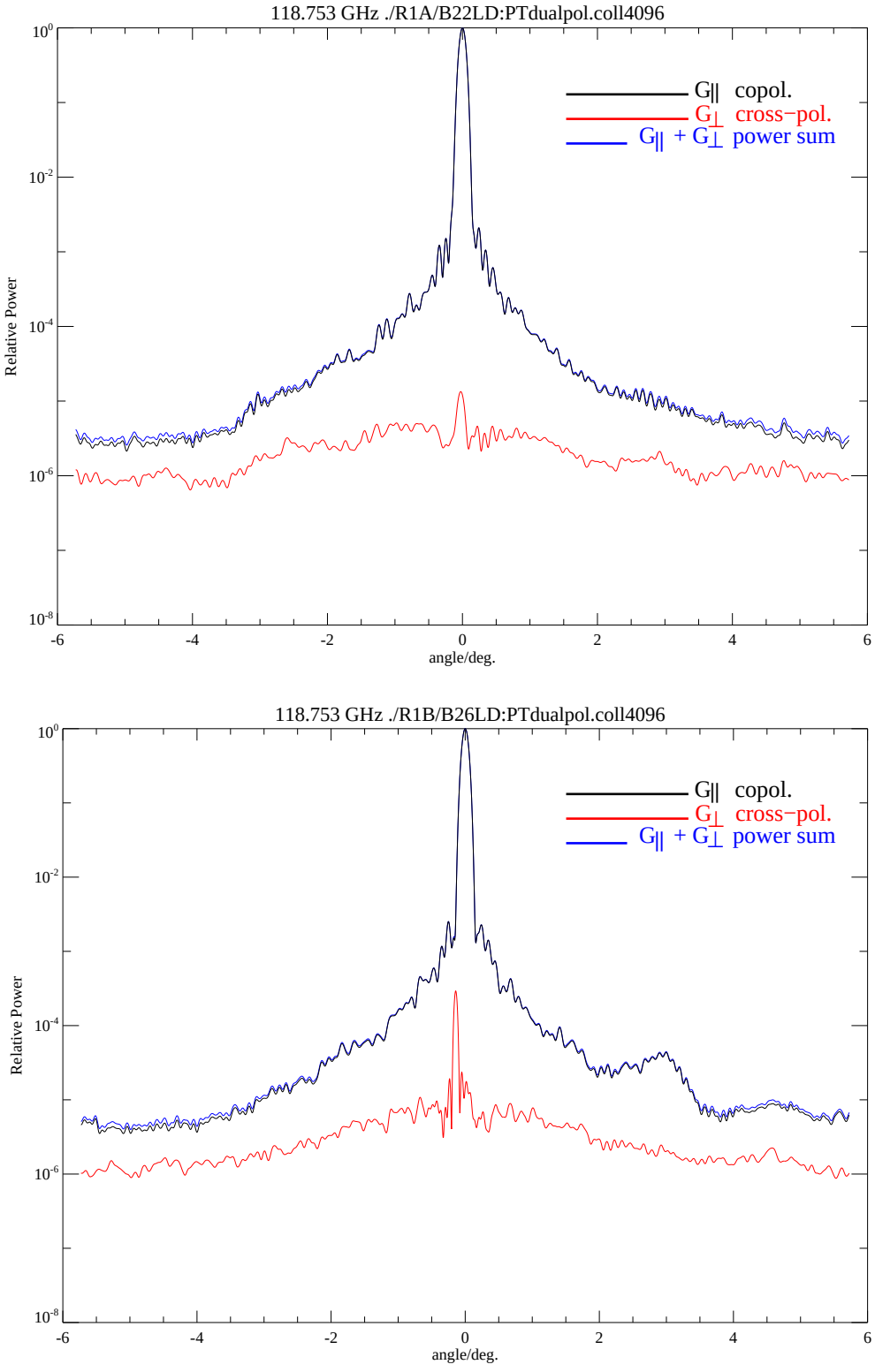

Figure 4.5: Definitive R1 dual-polarized FOV functions for Level 2 Processing Coefficients. R1B X-pol boresight shift also in 4-up plots; check.

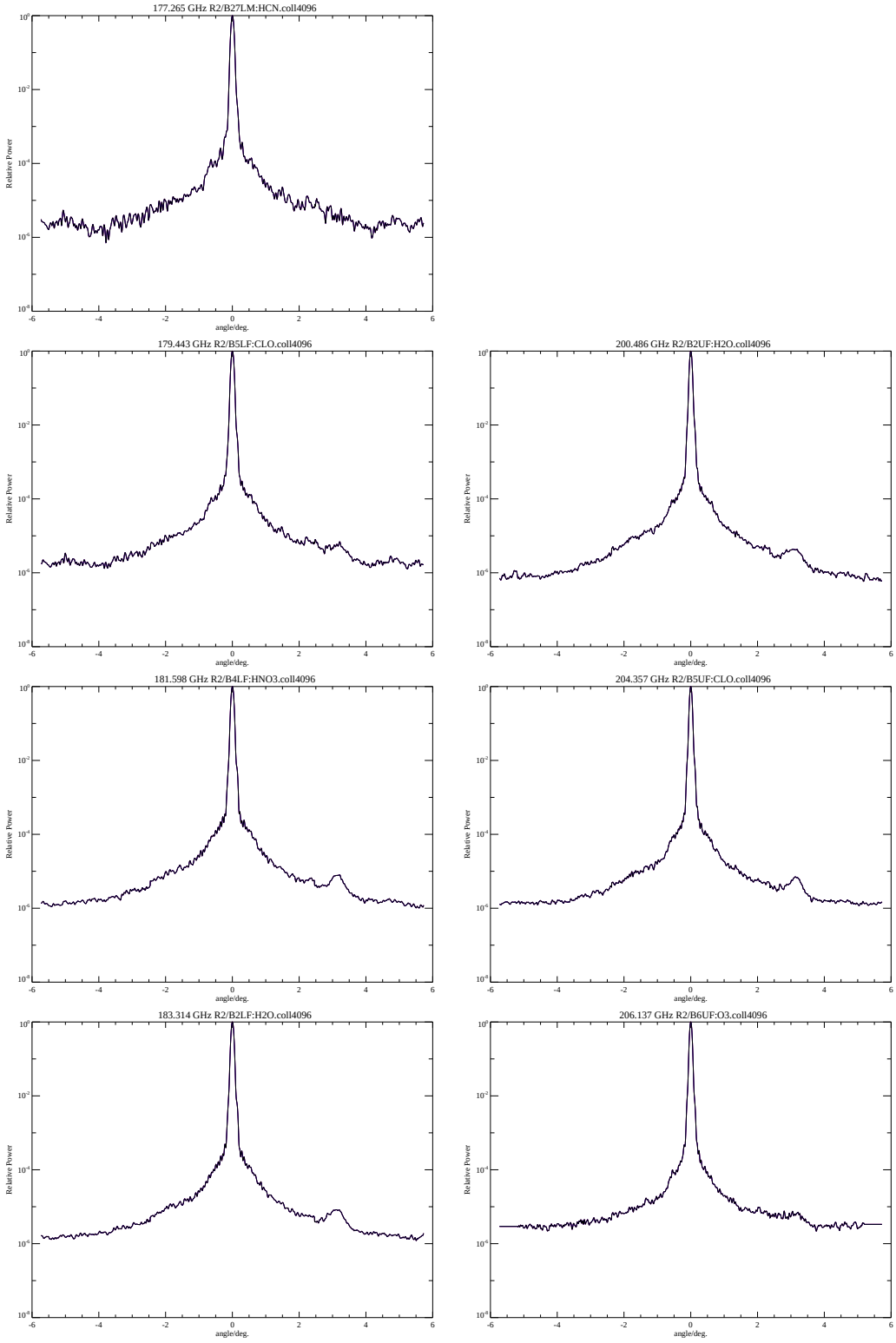

Figure 4.6: Definitive R2 FOV functions for Level 2 Processing Coefficients.

4.4.3 Effect of Measurement Errors on FOV Calibration

Appendix **??** describes the sources of error in FOV determination due to both equipment limitations and the analysis algorithms.

4.5 Radiometer FOV patterns and Internal Spillover

Allocations flowed down from the science FOV requirements for each Radiometer Front End (RFE) included some FOV pattern statistics. This section summarizes evaluations of beamwidth, pointing and beam efficiency made when the RFEs were delivered for integration. Details of calculations and datasets are in Appendix **??**.

4.5.1 HPBW and FOV direction

The interface requirement, $< 5\%$ deviation from nominal beamwaist size (hence, from nominal HPBW), was met by all three radiometers. The requirement on alignment of the RF beam with mechanical features reached the limit of mechanical alignment capability in the radiometer multiplexer design. Thus, for each RFE, at least 1 iteration of shimming, at the three feed mirror mounts, was required to align the RFE boresight and phase center with features on the receiver/multiplexer interface.

4.5.2 Beam efficiency

Integrations over radiometer ports

These were performed on the principal plane patterns of each radiometer, using design values for the port edges. Limb, Space and Target ports were all designed for identical (and symmetric) beam truncation. The ports are in the near field for 118 GHz, so the integration limit was obtained by propagating the cut-off point (x, y, z) along the nominal Gaussian beam to the far field to get an angle. This is valid even for an illumination expanded in higher-order modes, since only the phase slippage, not power taper level, varies as each mode is brought from near to far-field.

Integrated relative power values are summarized in Table 4.5 from the material in Appendix **??**. Values at the port edges are provided for Radiometric Calibration. The Level 1 radiance analysis deals with an antenna feed FOV normalized to unity at the radiometer limb port, hence beam integrals over the projected outlines of the antenna reflectors are divided by the limb port integral to produce spillover efficiencies, also in the table.

Spillover past Primary Reflector

This spillover is of concern since the Primary is the limiting aperture of the system, at -20 dB nominal edge taper for the R1 radiometers. Testing of the engineering model UARS MLS revealed a spectral baseline which appeared to be proportional to scan angle, suggesting a frequency-dependent spillover. To mitigate this, the apodization was increased for the EMLS instrument, and the "blue-sky" test described elsewhere in this report was devised. It appeared to rule out scan-dependent FOVs in all radiometers but R4 , where other instrument problems prevented any useful spectral contrast for this test. Nonetheless, the configuration of MLS on Aura is similar enough to that on UARS that we shall look for small stray radiance

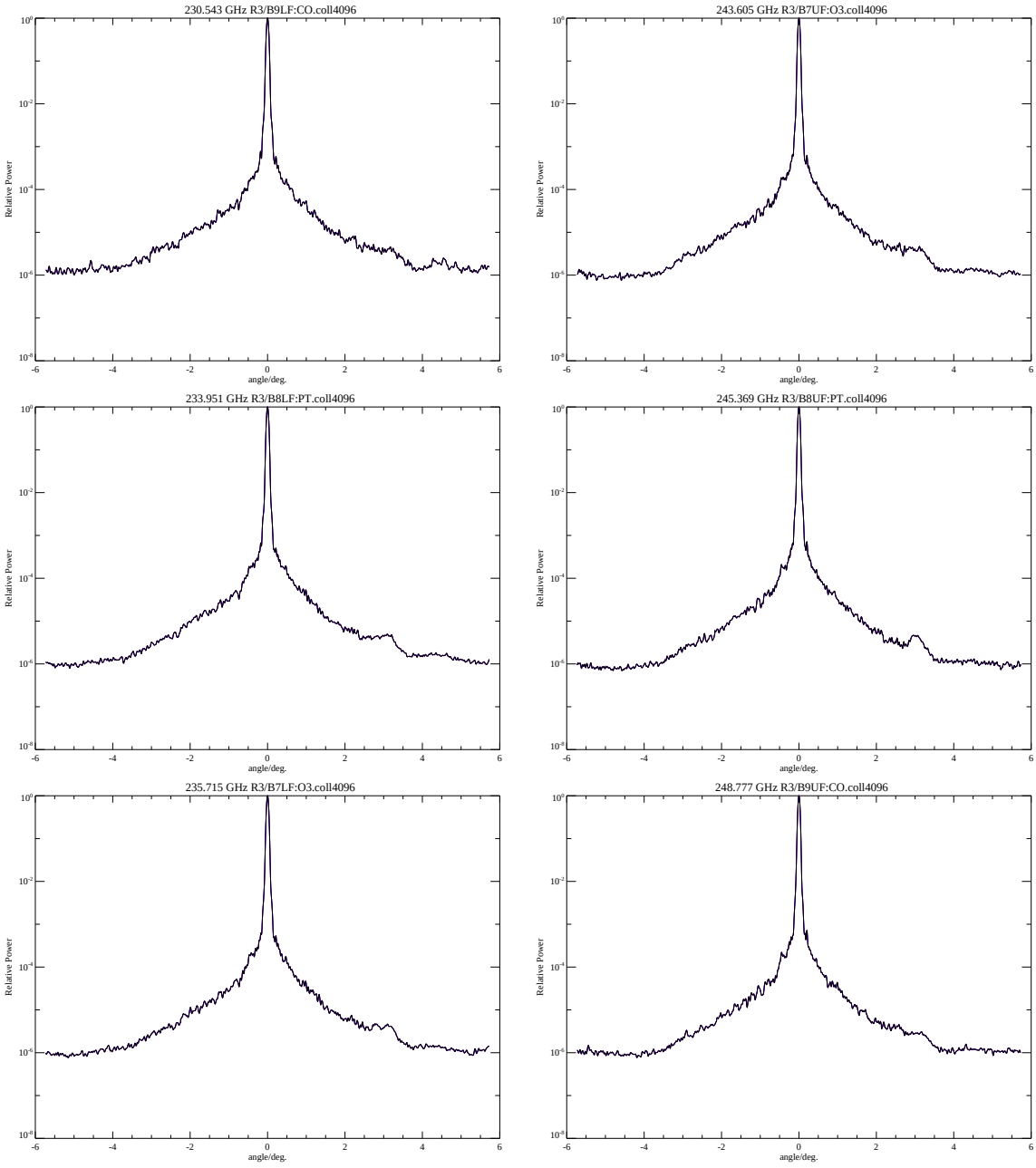

Figure 4.7: Definitive R3 FOV functions for Level 2 Processing Coefficients.

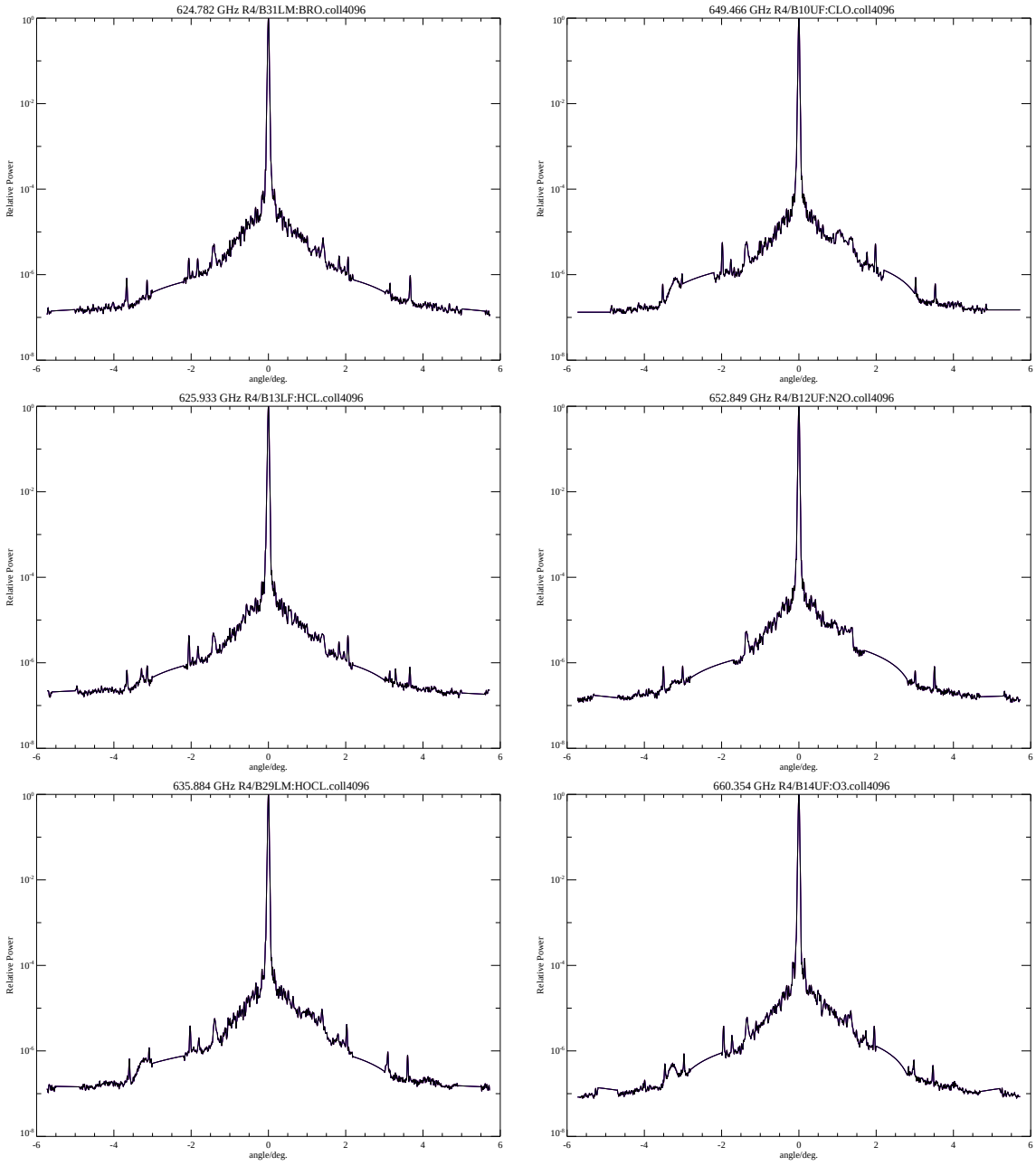

Figure 4.8: Definitive R4 FOV functions for Level 2 Processing Coefficients.

contamination due to *e.g.* solar array motion in the primary reflector's spillover during the first few months of operation on Aura.

4.6 Antenna Effects on Radiometric Response

4.6.1 Detailed Antenna Radiance Budget

The Level 1 Theoretical Basis document contains equations[2, eq. 4.14–5] which give the radiance emerging from the antenna and incident on the radiometer limb port, for channel i. Quantities in these equations which are supplied from FOV calibration include coefficients

ρ_r^k = reflectivity of reflector $k = 1, 2, 3$ (primary, secondary, tertiary) (= 1−ohmic loss),

$\eta_{i,s}^{AA}$ = optical transmission of the antenna system: the product of scattering ($\eta_{i,s}^{AS}$) and diffraction ($\eta_{i,s}^{AD}$) from the primary plane,

$\eta_{i,s}^k$ = optical transmission of reflector k,

and estimates of stray radiance:

$\dot{P}_{i,s}^{SA}$ = radiance power in the limb hemisphere but outside FOV measurement angle Ω_A,

$\dot{P}_{i,s}^{Sk}$ = radiance power illuminating the spillover solid angle for reflector k, and

$\dot{P}_{i,s}^{Ok}$ = power thermally emitted by reflector k.

where i,s indicates channel i, sideband s (l or u), and r indicates radiometer r. We supply the coefficients from ohmic loss measurements, integration of receiver feed patterns, and analytical models of scattering far from the antenna's main lobe. Stray radiances are given by simple models of MLS measurement geometry and scene radiance in orbit, plus reflector temperatures in the engineering telemetry.

4.6.2 Antenna Transmission

Ohmic loss

Ohmic loss within the antenna reflectors was inferred from reflectivity measurements in all GHz bands, using a radiometric insertion loss technique with the RFE FOVs switched between an external LN_2 cooled target and the internal ambient target. Two witness specimens had been delivered with the Primary Reflector, having undergone the same thermal cycling and bead-blasting. The insertion loss measurement and analyses are described in Appendix **??**. In a similar measurement on UARS MLS[**?**], analyses of variance showed the reflectivities to be statistically indistinguishable between samples of the same reflector, although significantly different from Primary to Secondary. However, witness samples from the Tertiary and Secondary were too small to cover the space-view beam where it was reflected into the LN_2 load, so for this calculation the Primary reflectivity was substituted.

Reflectivity was found to decrease with frequency, as expected if the loss mechanism is surface micro-structure. Using calculated reflectivities of the silver plate standard, the worst-case reflectivity (640 GHz) was $\rho_{R4}^1 = 0.9882$ with standard deviation of 0.00066. This does

not meet the engineering requirement $\mathcal{R}_{i,r} > 0.99$[**?**], which in retrospect is too stringent for the sub-millimeter bands. The resulting loss of sensitivity is expected to be acceptably small and will be investigated in the Level 2 retrievals during the first few months of operation in orbit.

The total reflectivities for the 3-reflector antenna system, $\rho_r^A = \prod_{k=1,3} \rho_r^k$, appear in Table 4.5 for all radiometers.

Diffraction and scattering outside measured solid angle

The antenna gain $G_r^M(\theta, \phi)$ is measured only over directions included in a solid angle Ω_A (in the limb vertical direction, about $\pm 6°$ around the boresights of scan extrema, tabulated in 4.2.1). The fractional power scattered into directions $\overline{\Omega}_A$ outside of Ω_A is

$$\gamma_r^A = 1 - \eta_r^A = \frac{1}{4\pi} \int_{\overline{\Omega}_A} G_r^A(\theta, \phi)\, d\Omega$$

The response for directions in $\overline{\Omega}_A$ is calculated assuming two mechanisms for large-angle scattering:

- Edge diffraction on the outlines of Primary Reflector, and (less significant) Secondary and Tertiary Reflectors. When analyzed using the Geometrical Theory of Diffraction (GTD), this mechanism also covers spillover losses.
- Scattered radiation from small-scale and small-amplitude irregularities in the reflector surfaces.

Both these contributions to scattering are frequency dependent at the radiometer level, but assumed constant over each IF band. Values appear in Table 4.5, from derivations in Appendix **??**.

4.6.3 Predicted Stray Radiances

Radiances illuminating the limb hemisphere and reflector spillover regions are partitioned using fish-eye views provided by the spacecraft provider, and assuming bulk radiances of 350 K for Aura and the UARS value of 150 K for the limb hemisphere. Reflector temperature predictions are from the MLS thermal model as of July 2003, and are to be converted to Planck radiances before incorporation into the forward model.

4.7 Conclusions

1. FOV direction (dFOV) in the reference pointing band of the MLS GHz module is known with respect to the Instrument Reference Frame (fixed in the sensor alignment cube) to 48 arcsec (3σ) absolute accuracy, at the reference environment in which the patterns were measured. A thermal/mechanical/optical model of the MLS predicted pointing changes of 82 arcsec (horizontal) and 21 arcsec (vertical), using maximum expected antenna temperature excursions over all orbits. The scan encoder tracks the vertical change to within 2 arcsec/minute over the orbits modeled; longer-term residuals are: 0.7 arcsec over a "cold" orbit (solar β angle of 36°), 1.9 arcsec over a "hot" orbit

Table 4.5: Antenna and radiometer baffle transmissions, and predicted stray radiances, for each MLS radiometer.

Contributor	R1A	R1B	R2	R3	R4
$\prod_{k=1}^{3} \rho_r^k$ (reflectivity)	0.995		0.9921	0.9835	0.9646
scattering	0.9997		0.9993	0.9988	0.9916
edge diffraction	0.9990	0.9967	0.99986	0.99986	0.99997
η_r^{AA}	0.9987	0.9964	0.9992	0.9987	0.9916
$\eta_{i,s}^k$	see Table 5.1				
Primary spillover	0.9813	0.9788	0.9953	0.9966	0.9972
η_r^A TBR	0.9800	0.9753	0.9945	0.9953	0.9888
η_r^A (total spillover)	.9734	.9656	.9926	.9939	.9873
η_r^{MX} (port baffle transmission)					
$X = L$ Limb	0.99598	0.99344	0.99889	0.99929	0.99907
$X = S$ Space	0.99587	0.99317	0.99890	0.99928	0.99907
$X = T$ Target	0.99575	0.99274	0.99889	0.99929	0.99907

$\dot{P}_{i,s}^{SA}$	$\dot{P}_{\nu}^{BB}(150°\mathrm{K})$
$\dot{P}_{i,s}^{S1}$	$\dot{P}_{\nu}^{BB}(100°\mathrm{K})$
$\dot{P}_{i,s}^{S2}$	$\dot{P}_{\nu}^{BB}(140°\mathrm{K})$
$\dot{P}_{i,s}^{S3}$	$\dot{P}_{\nu}^{BB}(120°\mathrm{K})$
$\dot{P}_{i,s}^{O1}$	$\dot{P}_{\nu}^{BB}([-11,+83]°\mathrm{C})$
$\dot{P}_{i,s}^{O2}$	$\dot{P}_{\nu}^{BB}([+18,+62]°\mathrm{C})$
$\dot{P}_{i,s}^{O3}$	$\dot{P}_{\nu}^{BB}([+10,+41]°\mathrm{C})$

($\beta = 16°$), and 5.6 arcsec between hot and cold orbits. These angles correspond to 10, 27 and 81 m at the limb tangent point. A linear model of horizontal pointing error, as a function of reflector temperature field, is being developed for Level 1, with details to be finalized after the first few months of in-orbit operation.

The coincidence of dFOV between radiometers meets the placement requirement; error in knowledge of dFOV coincidence make negligible contributions to the FOV calibration requirement.

2. HPBW met the "placement" requirements, and its standard deviation over all cases measured during FOV tests (*i.e.*, varying scan angle and IF) was less than the knowledge requirement. Polar beam efficiency was calculated by surface integrations of the two-dimensional FOV functions, and met the requirements in the same sense.

3. Antenna transmissions and scene radiances were calculated for each radiometer using measured ohmic loss and feed spillover, scattering loss from reflector surface data, and theoretical diffraction for the far sidelobes.

4. Compliance with the FOV calibration requirement has been demonstrated with examples of pattern repeatability, and for certain cases of scan and IF interpolation across areas of missing data, but has not been rigorously proven from models which combine multiple error sources. We will continue analysis of the total FOV calibration uncertainty through launch and activation of MLS, and publish conclusions in an update to this report after the first few months of operation in orbit.

4.8 THz Field-of-View Measurements

The requirements for the THz FOV calibrations are the same as those for the GHz channels.

The approach to measurement of the vertical field-of-view is to use a compact range that is scanned only in the vertical. The compact range consists of a medium-pressure mercury arc in an elliptical cavity and a test parabola. The arc is at one focus of the ellipse, and a slit aperture is at the other focus. This aperture is at the focus of a 600 mm focal-length 267 mm diameter off-axis parabola that was machined at the same time as the MLS THz primary. The faces of the slit in the direction of the test parabola are wedged at 15° over an angular extent of ±1.5° to reduce standing waves with the instrument. The surface figures of both mirrors were interferometrically tested at 3 μm wavelength. The slit used for the FOV calibration is 0.216 mm wide. In effect, the slit source and parabola appear to be a synthetic atmosphere with a very hot layer in comparison with the surroundings. The one-dimensional integrated field of view is then determined directly by scanning the instrument using the flight scan mechanism. These patterns are absolute, because the FOV scans will be referenced by imaging the visible light from the mercury source onto the focal aperture of the MLS THz primary. The focal aperture is then referenced through alignment cubes to the spacecraft.

The horizontal FOV is less critical than the vertical, but it can be inferred by three lines of reasoning. First, the MLS optics has a limiting aperture at the primary focus, a 1.6 mm pinhole, that limits the possible deviations of the horizontal boresight to ±0.075°. Second, the optical system is designed to have circular beam cross-section, which means that the horizontally polarized channel should have a horizontal pattern which matches the vertical pattern of the vertically polarized channel. A reciprocal inference can be made about the horizontal pattern of the vertically polarized channel. Finally, the calculated patterns from the x-y patterns can be used to infer the full 2-dimensional pattern.

Boresight is measured in much the same way as the vertical FOV, except that the measurements are made in air over the central part of the pattern. The THz boresight is referenced to a visible image of the source slit projected onto the instrument primary focus pinhole. This image is observed with a closed-circuit TV so that the instrument platform is not distorted by human observers, as well as to protect users from the intense visible and UV light form the Mercury arc source. In a separate measurement, the horizontal and vertical position of the pinhole is referenced to the spacecraft mounting points of the THz module using theodolite measurements.

4.8.1 Special Equipment Needed

1. Six foot THz vacuum chamber
2. Medium-pressure water-cooled mercury arc in an elliptical cavity with a 0.2 mm slit.
3. Test parabola
4. Mercury arc power supply and igniter
5. Closed-circuit TV
6. THz and Spectrometer Modules

4.8.2 Sensitivity and Accuracy

The FOV will be continuously scanned in 1° segments with 0.01° steps per MIF (0.167 s). These segments will overlap by 0.1° and will be combined together to produce a ±1.3° FOV pattern. This angular extent was set by the angular extent of the wedged slit assembly at the focus of the test parabola. The effect of the 0.216 mm slit (0.0206° angular size) is to convolve the true FOV with an rectangular filter. The effect of the continuous scan is to convolve the FOV with a second smaller rectangular filter. The true FOV can be obtained by deconvolving the effects of the finite slit width and the continuous scan. Equivalently, the true FOV can be obtained by Fourier transforming the measured pattern, by dividing the resulting aperture autocorrelation function by the two *sinc* functions out to the telescope diameter (and setting larger distance to zero), and then by back transforming the corrected autocorrelation function to the angular domain. The size of the slit is chosen so that its Fourier transform produces a *sinc* function that has a value of 0.45 at a distance equal to the diameter of the MLS THz parabola. The size of the sample spacing is chosen so that its Fourier transform produces a *sinc* function that has a value of 0.82 at a distance equal to the diameter of the MLS THz parabola. The noise amplification of the deconvolution is partially offset by the oversampling of the FOV relative to the slit size.

For FOV measurements we will combine filterbank channels for an effective bandwidth of 1200 MHz. Unfortunately, the nature of the source means that the measurements will be double sideband patterns. Any linear trend with frequency will be masked by the necessity of averaging the upper and lower sideband FOV patterns. However, second order trends can be observed as well as differences in sidelobe levels that are dependent on IF. The small ratio of IF frequency to sky frequency (0.008) implies that there should be little dependence of FOV on sky frequency.

Given that radiometric noise for the full 1200 MHz bandwidth is likely to be dominated by drift effects, we estimate $\Delta T_{rms} = 4$ K (DSB) for 0.167 s of integration and 1200 MHz bandwidth. For the 0.216 mm slit, limb-equivalent angular width is 1.1 km and the boresight radiance contrast is 900 K. We made 1 hour of measurements (146 scans) for each scan type for a total of 3 hours of measuring time. The estimated rms noise level is -36 dB.

The accuracy of the FOV patterns is actually limited by the need to establish a zero. The measured patterns were differenced with a view of the ambient calibration load, but the wedged reflecting surfaces near the slit 'see' a slightly different temperature than the temperature of the ambient target. A first estimate of the zero is to average the pattern outside the main lobe. This estimate is refined by noting that an in appropriate zero appears in the aperture autocorrelation function as a narrow *sinc* near zero displacement. The zero can be refined by making the autocorrelation function smooth near zero. The estimated uncertainty of this zero is -24 dB.

A second effect that must be recognized is that the standing waves of the test system with the THz instrument are different at the exact center of the pattern when the radiation from the instrument enters the source compared with other angles where the radiation is reflected off of the wedged slit assembly. This effect shows up in the corrected autocorrelation function as a constant offset. We correct the measured and sinc-corrected correlation function by an offset that makes the correlation function zero at a displacement equal to the diameter of the primary. The effect in the pattern is that the center of the antenna pattern is slightly bigger or smaller than it would be without the correction.

Table 4.6: THz Vacuum FOV Results for THz Radiometers. See text for additional information.

Band	Center	FWHM	Beam Efficiency
15 (OHa-H)	359.2723	0.0463	1.0139
16 (OHb-H)	359.2721	0.0452	1.0110
17 (O_2-H)	359.2717	0.0448	1.0116
18 (OHa-V)	359.2708	0.0387	0.9957
19 (OHb-V)	359.2699	0.0384	0.9576
20 (O_2-V)	359.2694	0.0387	1.0271

4.8.3 Measurements

The FOV measurements were made in three consecutive scan averages of 60 minutes each on 12 October 2002. Each scan had a linear portion, a view of the ambient target, and a view of the center of the pattern. The linear portion of the scans covered 359.94 – 358.85°, 358.90 – 357.869°, and 359.84 – 0.905°, respectively. The center of the pattern was 359.27°. The ambient and center view showed that the source and instrument were stable over the measurement time. The three scans were 'stitched' together by determining the average difference of two scans in the overlapping region. This difference was subtracted from the outlying scan. The overlapping region was averaged with a weight that changed linearly from 0 to 1 over the overlap region. The maximum point in the scan was then shifted to zero, and the Fourier transform was taken with no apodization. After decorrelating the slit and the time averaging, the corrections described in the previous section were applied, and the correlation function was set to zero beyond ± one diameter of the primary. The results are shown in Figure 4.9. These autocorrelation functions are then back Fourier transformed to give the FOV patterns, as shown in Figure 4.10. An offset of -21.25 dB has been added to the data in this figure to avoid taking the logarithm of a negative number. Note that the sidelobes are much larger for the V bands than the H bands, and that there are also small differences in the width and position. Nonetheless, the patterns for bands within the same mixer are remarkably similar. The pattern used for the MLS retrievals for bands 15–17 are the average of the patterns shown here for these bands, while the pattern used for bands 18–20 are the average of patterns for bands 18 and 19. The center of these patterns was fitted to a Gaussian down to -5 dB. The results of the fit for center and full width at half maximum (FWHM) are shown in Table 4.6.

Measurements in air of the vertical boresight showed that the visible center was located at 358.95°, while the THz center was located at 358.9324° ± 0.002 and 358.9329° ± 0.0006 for the H and V mixers, respectively. Offsets from the vacuum measurements are due to distortion of the alignment of the measurement equipment under vacuum and is not significant to the calibration.

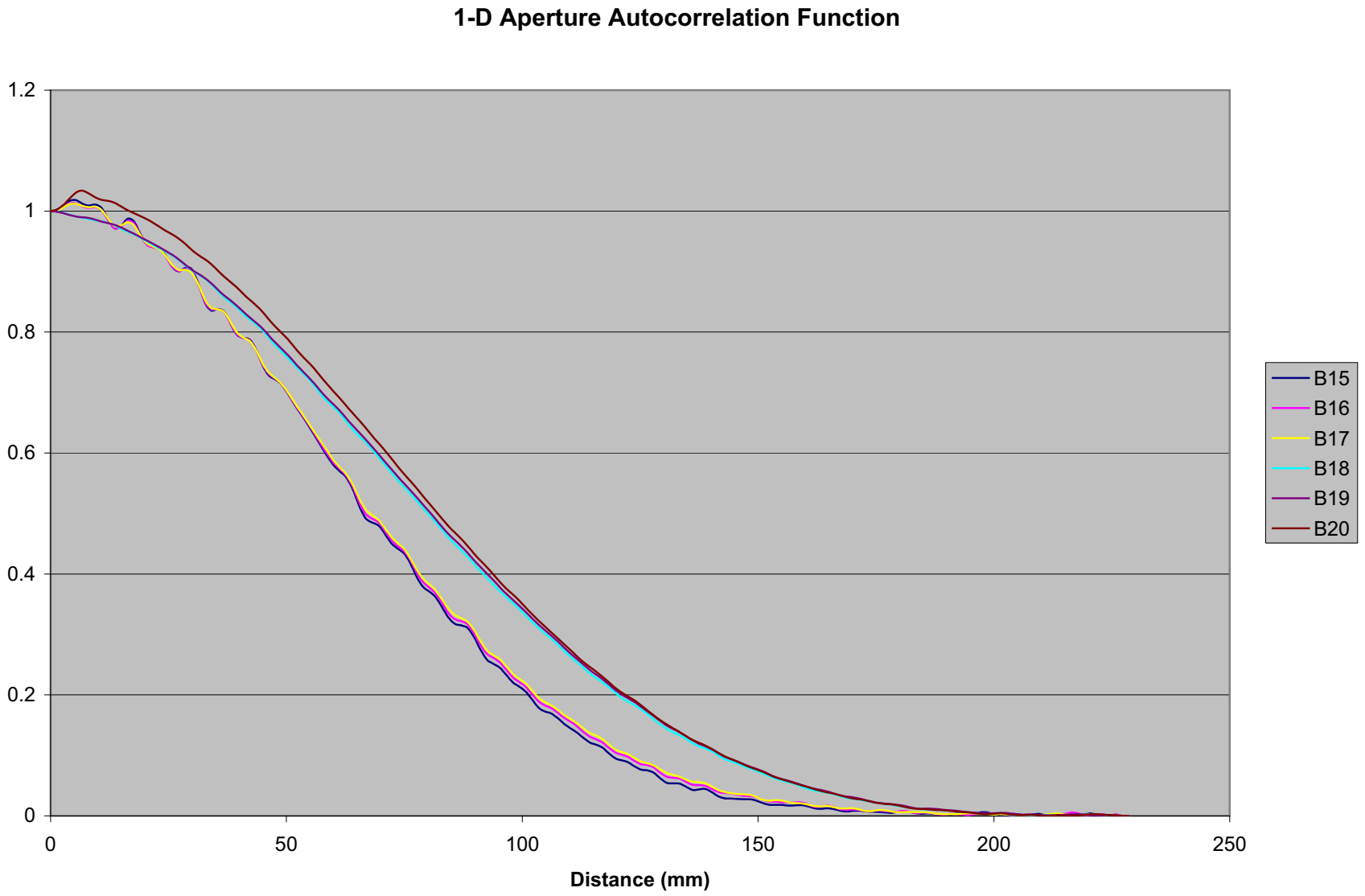

Figure 4.9: THz FOV autocorrelation functions. See text for further details.

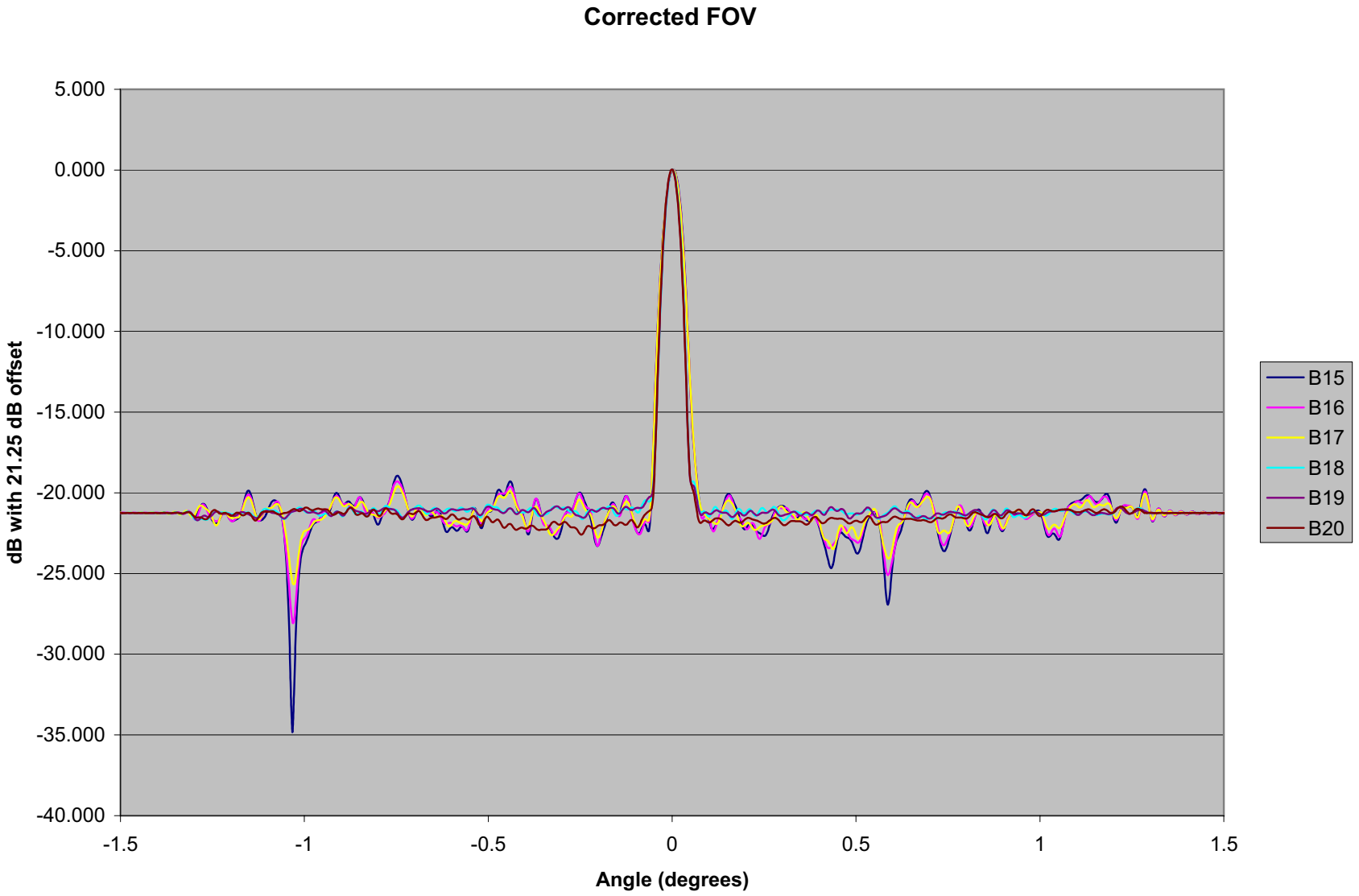

Figure 4.10: THz FOV patterns. See text for further details.

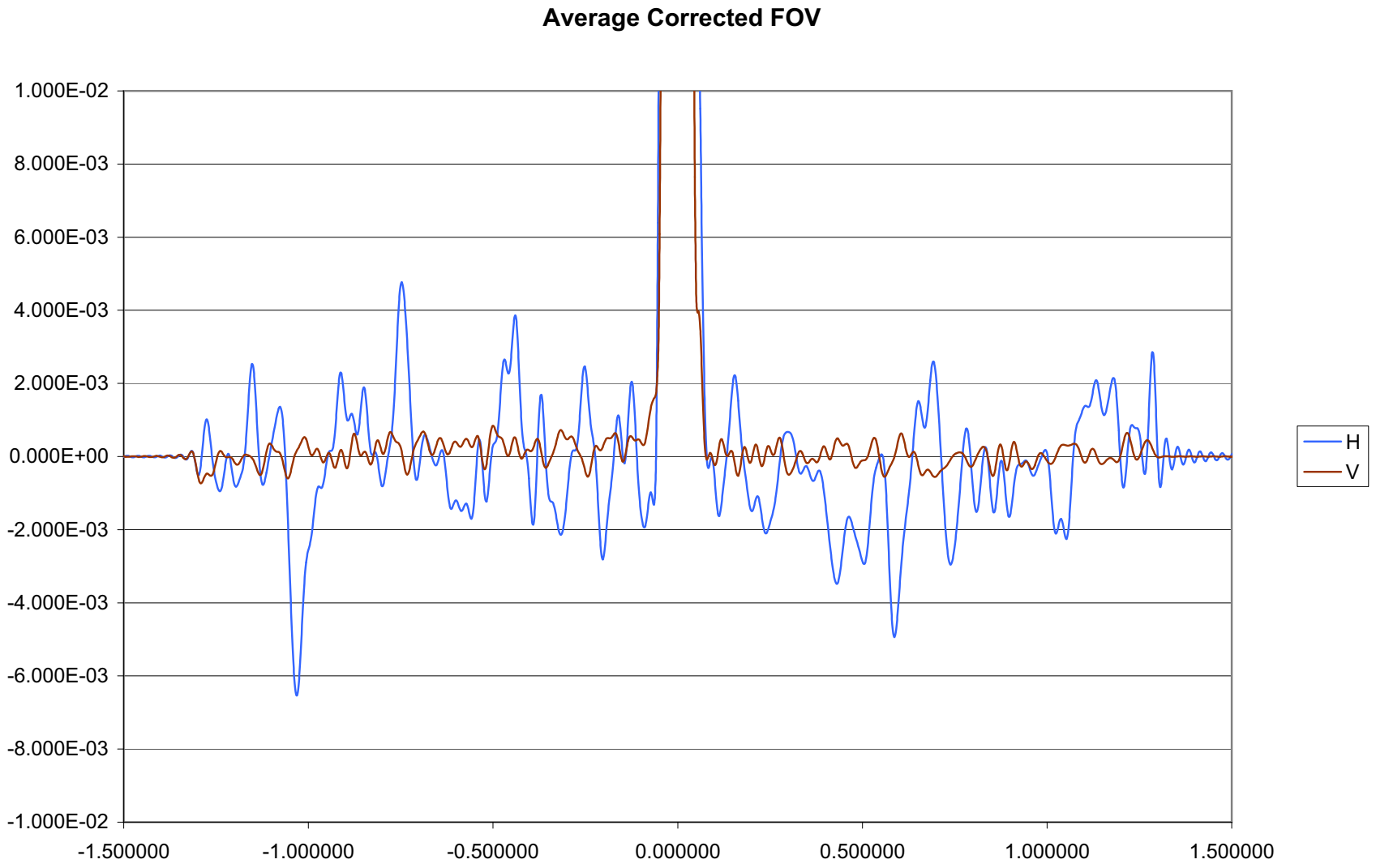

Figure 4.11: Expanded view of THz FOV patterns on a linear vertical scale. See text for further details.

Chapter 5

Parameters Required for Data Processing

Level 1 processing converts the limb view data "counts" from each Filter Bank channel into calibrated radiances according to the model described in the Level 1 Theoretical Basis Document[2]

This chapter provides a cross-reference to the Data Dictionary[1] entries, and to the other quantities used as parameters[2] in the data processing software.

The following sections group the inputs according to the processing software (Level 1, Level 2 and Level 2PC) using the data.

The nature of much of these data is such that they cannot be reproduced completely in this report, and directions on retrieving all machine readable calibration data is provided in Appendix **??**.

5.1 Level 1 Processing Software.

5.1.1 FOV Direction Data.

Table 5.2 gives the FOV-related inputs required for determination of FOV elevation and azimuth of each GHz band RF boresight relative to `B8LF:PT`, while Table 5.3 gives the rotation matrices to transform pointing from the FOV%TBDaka IPF? frames of both GHz and THz pointing reference channels to respective alignment cube frames and to spacecraft reference frames.

[1] The Level 1 and Level 2 Data Dictionaries are part of the MLS File Description Document, Version 3, C.C. Voge, 31 January, 1991.**TBR for EMLS**

[2] "Parameters" are numerical quantities coded directly into the Fortran sources.

Table 5.1: GHz FOV Data for Level 1 Processing.

Band.channel	U/LSB	f / GHz	η_1(Primary)	η_2(Secondary)	η_3(Tertiary)
32.4	L	115.300	0.9815	0.9931	0.9931
32.3	L	117.000	0.9823	0.9936	0.9936
1,22	L	118.753	0.9807	0.9930	0.9930
32.2	L	120.500	0.9809	0.9931	0.9931
32.1	L	122.000	0.9811	0.9932	0.9932
34.4	L	115.300	0.9796	0.9906	0.9906
34.3	L	117.000	0.9785	0.9901	0.9901
21,26	L	118.753	0.9786	0.9900	0.9900
34.2	L	120.500	0.9782	0.9897	0.9897
34.1	L	122.000	0.9792	0.9901	0.9901
27	L	177.265	0.9945	0.9976	0.9976
6	L	177.663	0.9945	0.9976	0.9976
5	L	179.443	0.9947	0.9977	0.9977
4	L	181.598	0.9949	0.9978	0.9978
3	L	182.820	0.9949	0.9979	0.9979
2,23	L	183.314	0.9949	0.9979	0.9979
2,23	U	200.486	0.9959	0.9984	0.9984
3	U	200.980	0.9959	0.9984	0.9984
4	U	202.202	0.9959	0.9984	0.9984
5	U	204.357	0.9958	0.9983	0.9983
6	U	206.137	0.9958	0.9983	0.9983
27	U	206.535	0.9957	0.9983	0.9983
9,25	L	230.543	0.9965	0.9986	0.9986
33.4	L	231.860	0.9964	0.9985	0.9986
33.3	L	232.460	0.9964	0.9985	0.9985
8	L	233.951	0.9963	0.9985	0.9985
33.2	L	234.860	0.9964	0.9985	0.9986
7,24	L	235.715	0.9966	0.9986	0.9986
33.1	L	236.660	0.9966	0.9986	0.9986
33.1	U	242.660	0.9967	0.9987	0.9987
7,24	U	243.605	0.9967	0.9987	0.9987
33.2	U	244.460	0.9968	0.9987	0.9987
8	U	245.369	0.9968	0.9987	0.9987
33.3	U	246.860	0.9968	0.9987	0.9987
33.4	U	247.460	0.9968	0.9987	0.9987
9,25	U	248.777	0.9969	0.9987	0.9987
31	L	624.782	0.9972	0.9984	0.9984
30	L	625.240	0.9972	0.9984	0.9985
14	L	625.386	0.9972	0.9984	0.9985
13	L	625.933	0.9972	0.9984	0.9985
12	L	632.891	0.9972	0.9985	0.9985
11	L	635.546	0.9972	0.9984	0.9985
29	L	635.884	0.9972	0.9984	0.9985
28	L	636.024	0.9972	0.9984	0.9985
10	L	636.274	0.9972	0.9984	0.9985
10	U	649.466	0.9973	0.9985	0.9985
28	U	649.717	0.9973	0.9985	0.9985
29	U	649.856	0.9973	0.9985	0.9985
11	U	650.194	0.9973	0.9985	0.9985
12	U	652.849	0.9972	0.9984	0.9984
13	U	659.807	0.9972	0.9983	0.9984
14	U	660.354	0.9972	0.9983	0.9984
30	U	660.501	0.9972	0.9983	0.9984
31	U	660.958	0.9972	0.9983	0.9984

Table 5.2: FOV Direction Coincidence Data: dFOV relative to B8LF:PT. $\theta = -\epsilon$ increases towards sky, decreases towards Earth; $\phi = +\alpha$ increases towards radiometer, decreases towards encoder. THz coincidence (ϕ only) is based on NGST's final (*i.e.* post-Aura environmental test) measurement set.

Band.channel	U/LSB	f/GHz	$\Delta\theta/^\circ$	$\Delta\phi/^\circ$	$3\sigma_\theta/^\circ$	$3\sigma_\phi/^\circ$
32.4	L	115.300	-0.0172	-0.0106	0.0054	0.0032
32.3	L	117.000	-0.0186	-0.0125	0.0052	0.0034
1,22	L	118.753	-0.0187	-0.0096	0.0051	0.0036
32.2	L	120.500	-0.0215	-0.0110	0.0054	0.0046
32.1	L	122.080	-0.0200	-0.0103	0.0057	0.0055
34.4	L	115.300	-0.0063	0.0011	0.0060	0.0035
34.3	L	117.000	-0.0060	-0.0022	0.0048	0.0031
21,26	L	118.753	-0.0056	-0.0057	0.0036	0.0028
34.2	L	120.500	-0.0057	-0.0030	0.0044	0.0050
34.1	L	122.080	-0.0057	-0.0005	0.0051	0.0070
27	L	177.265	-0.0144	-0.0146	0.0058	0.0006
6	L	177.663	-0.0144	-0.0151	0.0053	0.0009
5	L	179.443	-0.0146	-0.0171	0.0030	0.0022
4	L	181.598	-0.0148	-0.0195	0.0003	0.0037
3	L	182.820	-0.0150	-0.0187	0.0036	0.0026
2,23	L	183.314	-0.0151	-0.0184	0.0050	0.0021
2,23	U	200.486	-0.0141	-0.0174	0.0035	0.0039
3	U	200.980	-0.0140	-0.0173	0.0032	0.0041
4	U	202.202	-0.0138	-0.0170	0.0025	0.0044
5	U	204.357	-0.0133	-0.0165	0.0012	0.0050
6	U	206.137	-0.0130	-0.0126	0.0012	0.0050
27	U	206.535	-0.0130	-0.0117	0.0012	0.0050
9,25	L	230.543	0.0004	0.0002	0.0071	0.0080
33.4	L	231.860	-0.0001	0.0004	0.0069	0.0075
33.3	L	232.460	-0.0003	0.0004	0.0068	0.0072
8	L	233.951	0	0	0.0067	0.0067
33.2	L	234.860	-0.0003	-0.0005	0.0045	0.0077
7,24	L	235.715	0.0002	-0.0015	0.0024	0.0088
33.1	L	236.660	0.0002	-0.0015	0.0027	0.0089
33.1	U	242.660	-0.0001	-0.0018	0.0050	0.0097
7,24	U	243.605	-0.0001	-0.0018	0.0053	0.0098
33.2	U	244.460	-0.0002	-0.0018	0.0042	0.0064
8	U	245.369	-0.0003	-0.0019	0.0030	0.0029
33.3	U	246.860	0.0000	-0.0016	0.0030	0.0037
33.4	U	247.460	0.0001	-0.0014	0.0030	0.0041
9,25	U	248.777	0.0003	-0.0012	0.0030	0.0049
31	L	624.782	-0.0076	-0.0016	0.0038	0.0022
30	L	625.240	-0.0076	-0.0018	0.0038	0.0024
14	L	625.386	-0.0076	-0.0018	0.0038	0.0025
13	L	625.933	-0.0076	-0.0019	0.0038	0.0027
12	L	632.891	-0.0077	-0.0036	0.0035	0.0058
11	L	635.546	-0.0077	-0.0042	0.0035	0.0070
29	L	635.884	-0.0077	-0.0043	0.0035	0.0072
28	L	636.024	-0.0077	-0.0043	0.0035	0.0071
10	L	636.274	-0.0077	-0.0043	0.0034	0.0070
10	U	649.466	-0.0078	-0.0031	0.0030	0.0021
28	U	649.717	-0.0079	-0.0030	0.0029	0.0023
29	U	649.856	-0.0080	-0.0030	0.0029	0.0024
11	U	650.194	-0.0081	-0.0029	0.0028	0.0028
12	U	652.849	-0.0089	-0.0021	0.0022	0.0050
13	U	659.807	-0.0079	-0.0022	0.0004	0.0016
14	U	660.354	-0.0078	-0.0022	0.0003	0.0014
30	U	660.501	-0.0078	-0.0022	0.0002	0.0013
31	U	660.958	-0.0078	-0.0022	0.0001	0.0011
15—17	both	2500	0	0.040	—	0.008

Table 5.3: FOV Direction Data for Level 1 Processing.

Data Dictionary Item	*symbol*	*value*	*Description*
TRANS_FOV2INST(3,3)	**F**	GHz: APE = -2.5192°(side A) $\begin{pmatrix} -0.0003346 & -0.4266207 & 0.9044306 \\ 0.9999944 & 0.0028561 & 0.0017172 \\ -0.0033157 & 0.9044261 & 0.4266174 \end{pmatrix}$ THz: TSSE = -1.0841° $\begin{pmatrix} -0.0051267 & -0.4302693 & 0.9026860 \\ 0.9999851 & -0.0005219 & 0.0054306 \\ -0.0018655 & 0.9027004 & 0.4302656 \end{pmatrix}$ [**?**, Tables 3.5.5-1a,b]	Rotation matrix from FOV to Instrument Alignment Cube (IAC). Encoder values APE for GHz and TSSE for THz were chosen to point both modules' FOVs at 30 km tangent height assuming no spacecraft mounting error and nominal orbit (spherical Earth radius 6371.1 km and Aura altitude 705 km)
TRANS_INST2OBS(3,3)	**E**	GHz: $\begin{pmatrix} 0.9999994 & -0.0000184 & 0.0010691 \\ 0.0000213 & 0.9999962 & -0.0027430 \\ -0.0010690 & 0.0027430 & 0.9999959 \end{pmatrix}$ THz: $\begin{pmatrix} 0.9999817 & 0.0039359 & 0.0045878 \\ -0.0039286 & 0.9999910 & -0.0015930 \\ -0.0045940 & 0.0015750 & 0.9999882 \end{pmatrix}$ NGST EOS.04.3.210-002 TBR for S/C distortions	Rotation matrix from IAC to Observatory Frame
TRANS_OBS2MACS(3,3)	**D**	$\begin{pmatrix} 1 & 0 & 0 \\ 0 & 1 & 0 \\ 0 & 0 & 1 \end{pmatrix}$ Placeholder (MACS aka IRU,STA?), TBR	Rotation matrix from Observatory (SBF) to MACS Frame Bob/Dennis, Do we need this placeholder? Is there a (GSFC) document describing coordinate transformation(s) from Spacecraft Body Frame to Earth-Centered Inertial Frame?

Chapter 6

Engineering Data

Although the main focus of this report is to document the calibration and performance of the instrument science data paths, it is important to remember that the accuracy of the engineering data used in science data processing is of relevance. Such parameters include the telemetry reporting the temperatures of the calibration targets and GHz external optical surfaces.

Three techniques are used in EOS MLS to acquire analog engineering telemetry:

(1) GHz, THz and Spectrometer module engineering data are processed in 'Engineering Data Hybrids,' one of which is included in each RIU. The exception to this method is:

(2) THz LLO telemetry, which is acquired with a relatively fast successive approximation A/D converter since some of it is used by the LLO microprocessor in the operation and real-time control of that subsystem.

(3) Survival telemetry, which is acquired directly by the Spacecraft, and not used in routine instrument data processing.

Below we discuss the implementation, timing and some important characteristics of the Engineering Data Hybrids (EDH) used to acquire the majority of the instrument analog engineering data. EDH units are included on all RIUs.

6.1 Engineering Data Hybrid operation

Engineering data are acquired in a manner similar to that for the spectrometers filter channels. The low and high reference views (cold Space and ambient target views) are replaced with low and high calibration point measurements to references within each of the EDH modules. Six reference sources are included within each EDH:

(1) Low and high voltages,

(2) Low and high thermistor calibration reference resistances, and

(3) Low and high PRD calibration reference resistances.

Each of the PRD calibration references can be measured with the signal conditioning electronics in both standard and high-resolution (narrow range) modes. The narrow range mode is implemented to support internal calibration target temperature monitoring with higher resolution and greater accuracy than the standard PRD mode.

A simplified block diagram of the EDH analog signal processing electronics is shown in Figure 6.1. A control word from the RIU FPGA selects an input source and the mode of the Signal Conditioning Block. The Calibration Multiplexer conditions (if necessary) and samples the selected calibration input. Although the Calibration Multiplexer is shown as having eight inputs, only seven are implemented – the six reference sources listed above, and an additional input generated by a temperature-dependent voltage output from the AD537 VFC (and used as a relatively low-resolution indicator of hybrid electronics temperature). Note that the 'user' inputs are shown with four connections. This is because all of the sixteen user input channels can be independently configured for any measurement type or polarity, and the highest-accuracy PRD measurements utilize a 4-wire measurement scheme.

The selectable modes of the Signal Conditioning Block ensure that all valid inputs limit the VFC output to the range ∼40 to ∼80 kHz, shown in Figure 6.2. The conditioning block also allows the polarity of incoming signals to be reversed. This is of particular relevance for the Calibration Target PRD measurements which are made in pairs with opposite excitation current polarities so that thermocouple EMFs generated in the wiring can be compensated by merely averaging the two values of measured resistance.

The overall measurement scheme for a single user input signal is illustrated in generic form in Figure 6.2. The VFC operating range is restricted to provide good linearity, and the user signal is estimated by linear interpolation of the VFC frequency between the two calibration measurement points. This system does not rely on long-term stability of the majority of the electronic components used in the EDH, and conveys the usual S/N advantages inherent in integrating A/D conversion systems.

EDH units which do not perform a given type of measurement (e.g., only a small number of EDH units are used to monitor reduced-range PRDs in the internal radiometric calibration reference targets) are programmed not to include the associated calibration measurements as part of their routine measurement cycle. The entire measurement sequence is directed by the Control Word from the RIU FPGA, which is updated under software control by each RIU microprocessor. Each EDH is cycled through all of its internal calibration and external user measurements once every MAF.

6.1.1 VFC frequency measurement

UARS MLS employed an analog engineering data measurement scheme very similar to the one just described, and the relatively long MIF duration for that instrument (2.048 s) meant that a simple counter could be used to determine VFC frequency with 16 bit resolution. The substantially shorter MIF duration of EOS MLS dictated a more sophisticated measurement scheme to retain this level of resolution. UARS experience indicated the usefulness of high-resolution engineering telemetry for in-orbit troubleshooting, a good example being our ability to monitor 'glitches' in temperature trends of only ∼0.01 K when the antenna actuator briefly stalled against a piece of internal debris.

Referring to Figure 6.3, the nominal period for recording VFC output is the same ∼161 ms period used to integrate all science data. For the EDH units, the beginning and end of the

nominal science data integration period are used as start and end of integration flags, and the true integration time is set by the rising edge of the VFC output following the setting of these flags. This means that the true integration period is delayed in time (by up to 1 VFC clock cycle) compared to that of the science data, and is slightly variable in length since it consists of an integer number of VFC cycles, accumulated by a 16 bit counter. The start and end of VFC counting also signal the start and end of counting the output from a 2 MHz timebase derived from the 12 MHz RIU processor clock. In the ∼161 ms duration of the period used to count the timebase, this results in a count of almost 2×10^6, and a 22-bit counter is used to accumulate these data, sufficient to support a MIF duration of $\frac{1}{3}$ s. The large number of timebase counts means that no exceptional steps needed to be taken in the electronics design to account for the asynchronous relationship between the VFC and timebase signals – even an error of 2 counts in the 22 bit counter only represents a 1 ppm error.

An estimate of VFC frequency can be obtained by appropriately scaling the ratio of the contents of the 16 and 22 bit counters (which we will call cnt16 and cnt22 from this point forward). Since we chose to format engineering DN as 16 bit integers, it is also necessary to offset and rescale the scaled ratio of these two counters to make efficient use of the full range

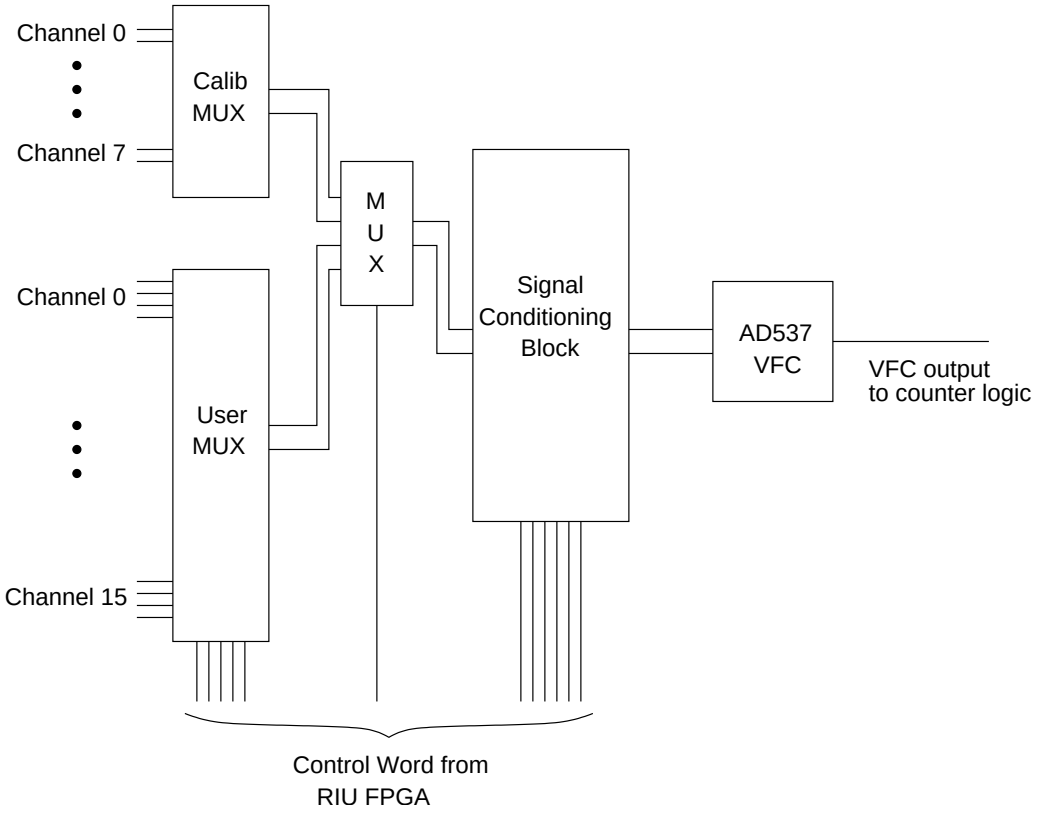

Figure 6.1: Simplified block diagram illustrating the analog blocks within the EDH. See text for additional details.

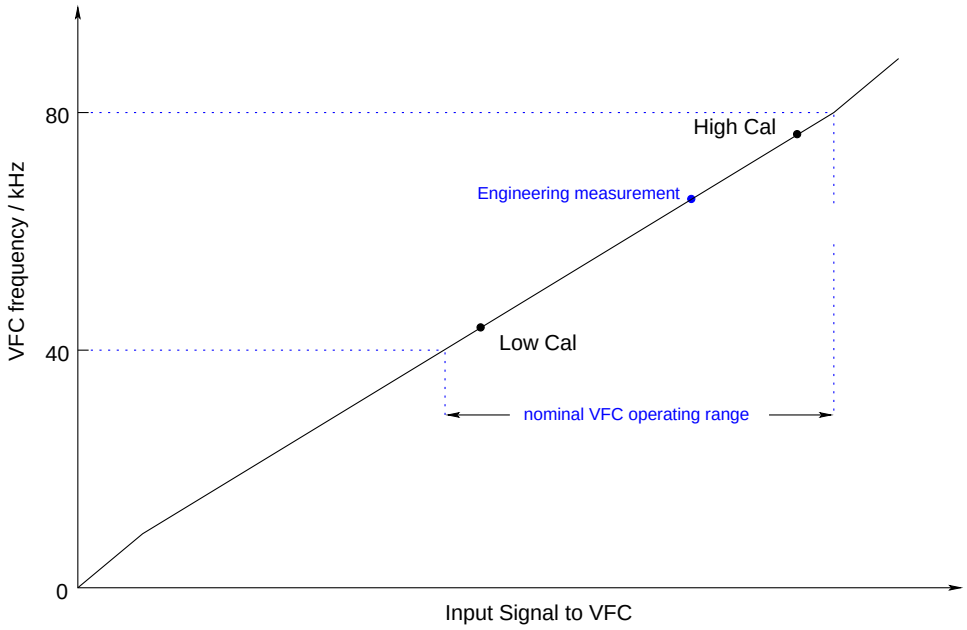

Figure 6.2: Simplified representation of the 3-point measurement scheme implemented in each EDH. The nonlinearity of the VFC transfer function has been exaggerated in this illustration. See text for additional details.

of the 16 bit format. The C&DH computes the telemetry DN via the equation:

$$\mathrm{DN} = \left(12 \times 10^6 \times \frac{(\mathrm{cnt16}/2)}{\mathrm{cnt22}} - 36,000\right) \times 1.35 \tag{6.1}$$

where cnt16 and cnt22 are treated as unsigned integers, and the arithmetic is performed after conversion to single precision floating point format. DN is then converted back to an unsigned 16 bit integer for placement into the telemetry stream. The divisor of 2 associated with cnt16 arises because of the implementation of the logic which causes this counter to increment on each edge of the VFC output.

A useful advantage of this measurement scheme is that engineering DN are insensitive to MIF duration, allowing some limit checking (for health and safety) to be performed by the C&DH based on DN values alone.

6.1.2 EDH calibration details and measured performance

All non-temperature analog engineering data are externally conditioned to levels between 0 V and +5 V or –5 V and 0 V for measurement by the EDH. The useful input range of the EDH is about 1 V beyond these levels to allow for unexpectedly large aging effects or drifts. Input polarity is software selectable for each measurement channel. The calibration points for voltage measurements are 0 V and +5 V. The 0 V signal is provided by a simply grounding the multiplexer input pair, and the +5 V reference is generated by an RH1021-5 radiation-hardened reference IC. Long-term accuracy of voltage measurements is designed to be better than 0.1% of full-scale based upon predicted component performance in the expected radiation environment.

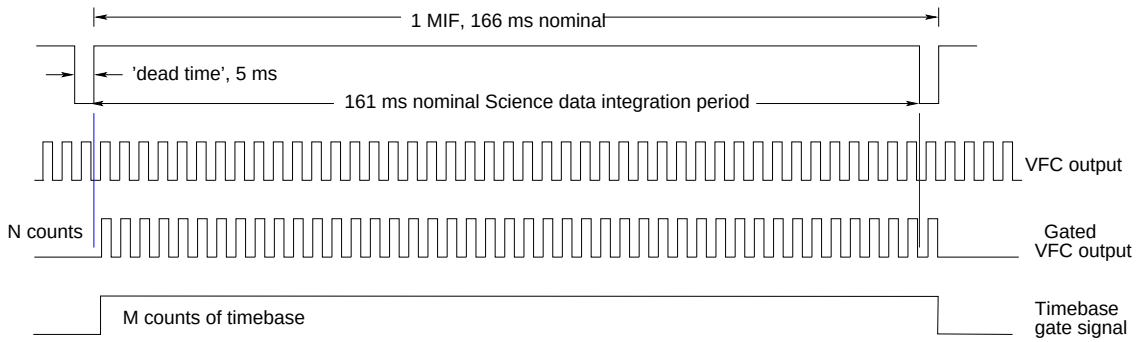

Figure 6.3: Simplified timing diagram illustrating the dual-counter digitization scheme implemented for the EDH units. See text for additional details.

Thermistor telemetry calibration is provided by measurements to 996 Ω and 4,525 Ω precision Vishay reference resistors. Analyses indicate a worst-case end-of-life error of 0.2 C for measurements in the range 0 C to +100 C due to EDH electronics, including reference resistors. Thermistor tolerance for the YSI 44004 devices adds another ∼0.2 C uncertainty at room temperature. Excitation current for all thermistor measurements is 1 mA, introducing only small additional error through device self-heating.

PRD measurements are referenced to calibrations against 480 Ω and 620 Ω precision Vishay reference resistors. Excitation current is limited to 0.1 mA to limit self-heating errors to negligible levels, and the calibration target PRDs in both the GHz and THz modules are measured twice in succession with reversed bias current polarity. The two measured resistances are then averaged to remove the effects of thermocouple-generated EMFs in the 4-wire connections between sensor and EDH. An example of such thermocouple-generated EMFs is presented later in this chapter. The signals from the calibration target PRDs are conditioned to provide enhanced resolution over the restricted range –20 C to +70 C. The remainder of the PRDs are used to monitor such points as the external structure and reflector temperatures, and hence are set up to cover the range –100 C to +100 C. Analyses indicate that long term accuracy of the calibration target measurements is better than ±0.2 C, with ±0.3 C accuracy for the wide range PRD measurements.

As-built accuracy of the hybrids was verified by measurement of externally applied standards, and long-term accuracy was determined by analysis. Individual calibration parameters (Voltages, resistances) were supplied for each individual EDH, and each PRD was supplied with its own calibration data sheet from the vendor (Rosemount Engineering Company). These parameters are included in Level 1 processing software.

Verification of EDH performance included measurements of noise on each measurement channel, with observed levels of 0.013 to 0.023 bits rms on each 16-bit DN, dependent upon measurement type. Drift of calibration measurements over the 24.7 s period between such measurements was typically 1 part in 10^6 when the EDHs were subject to thermal variation similar to those predicted in orbit. These measurements were made with the EDH units in a special test fixture prior to delivery from the vendor (Teledyne), not in an RIU.

6.1.3 Additional details

Most RIUs operate in the manner just described, but the RIU FPGAs in selected subassemblies were modified prior to instrument delivery to provide operating modes for the hybrids that eliminated some of the problems with Wide Filter science data observed during radiometric calibration. In native mode, the 16 and 22-bit counters are run every second MIF, and read out every 4th MIF. This scheme was chosen because the hybrid analog multiplexer addresses are generated by firmware in each RIU 8051 processor, and at least one MIF of settling time is required to guarantee that the input to the VFC has settled to the 16 bit level. This restricts the analog data multiplexers to select new inputs on alternate MIFs, or slower. Since the maximum number of analog signals to be digitized by a hybrid is 25 (16 externally selectable signals and 9 internal calibration[1] and housekeeping signals), the RIU firmware was implemented so as to be able to accept only every second valid set of results from the VFC counters. With this restriction all high-level functional requirements were met, since even with a 4 MIF cycle time for each engineering datum, the maximum possible number of analog sources (25) could readily be sampled in a single MAF (which is restricted to have no fewer than 128 MIFs).

As a side-effect of these implementation decisions, the 16 and 22-bit counters are only enabled on alternate MIFs. This results in an FPGA power consumption that systematically alternates between odd and even MIFs, and is the source of the odd-even MIF offset problem described in Chapter 2. This problem manifested in all filter channels, and was corrected in the Spectrometer Module by increasing the output voltages from the central power supply, and applying local regulation on each spectrometer shearplate. This solution also conveniently dealt with the additional spectrometer interaction (and other) problems caused by voltage drops in the wiring harnesses which changed with signal levels.

For the Wide Filters implemented in the second IF multiplexers of R1A, R1B and R3, the power supply implementation precluded the regulator solution implemented for the Spectrometer Module. The dominant source of the odd/even artifacts is the gating of the 22-bit VFC counter, due to its high clock rate (2 MHz) compared to the 16 bit counter (40 to 80 kHz). The chosen solution was to create modified, but pin-compatible FPGAs, for the afflicted shearplates. The modifications consisted of providing additional options for the operation of the 16 and 22-bit counters, with the default behavior of the FPGA/counter combination being identical to that of the standard product. The modifications to the FPGA design added the following two modes to the operation of the counters:

(1) Inhibit operation of 22-bit counter, and

(2) allow both 16 and 22-bit counters to operate continuously, with the count data being latched at the end of every MAF.

For nominal instrument operation we selected the second of these two modes, reducing the effects of varying FPGA power consumption to levels at which the odd/even artifacts were no longer visible in analyses of multi-hour duration data sets.

[1] There are only 7 calibration inputs within each EDH, but the ones for the PRDs are measured in restricted and full range mode, increasing the number of internal calibration measurements to 9.

6.2 Observed performance

An example of instrument engineering telemetry is shown in Figure 6.4. The upper panel shows GHz Switching Mirror temperature telemetry (thermistor) over a 24 hour period during Spacecraft thermal vacuum testing. The lower panel show the corresponding DN computed as described earlier.

The systematic structure visible on the data arises from temperature variations generated by the test system thermal control system. When these data are examined on an expanded vertical scale, measurement noise and resolution is seem to be below the 0.01 C level, as expected.

Data from the same sensor is plotted in Figure 6.5 during instrument warm-up in the NGST High Bay, with the instrument mounted on the Spacecraft. Note that at a superficial level the telemetry consists of a sequence of 'flat spots' connected by 'line segments.' This behavior is typical of all analog telemetry monitored by the RIU/EDH combinations. Since the end of one flat spot is connected to the start of the next one by a line segment[2], the line segments clearly have the incorrect slope to represent the true signal behavior. Analysis of data from several RIUs indicates that rather than the 18 bit 'data quality' predicted from stand-alone EDH testing, the worst-case system level performance is closer to 8 bits, a degradation by a factor of 1,000.

6.3 Systematic noise and VFC-based A/D converters

Integrating A/D converters, of which VFCs are a subset, all operate by measuring the time taken for an integrated signal to traverse between two levels. In the case of the VFC-based A/D converter we typically choose to count *how many times* the integrated signal traverses the chosen levels in a data integration period. For this particular implementation we go one step further, as described earlier in this chapter, and measure the average frequency of the VFC during the data integration period.

The VFC chosen for EOS MLS (Analog Devices AD537) is a little unusual compared to more conventional devices of this type in that it consists of a bipolar emitter-coupled multivibrator, the emitter currents of the long-tailed-pair being proportional to input signal. Additional circuitry is included in this device to alleviate nonlinearity at low signal levels that would otherwise arise from the finite β of the transistors, and the degradation in β at very small collector currents. Since we chose to operate the VFCs over a restricted frequency range well away from the nonlinear region close to zero frequency, this additional linearizing circuitry does not come into play for our application.

Since the AD537 implements the VFC as an emitter-coupled multivibrator, its output is close to a square wave. This allowed the counter that recorded VFC cycles (cnt16) to be implemented is such a way that it incremented on both edges of the VFC output signal, effectively doubling measurement resolution. The same dual-edge counting scheme is implemented in the Spectrometer Daughter Board FPGAs which record the science data outputs from the AD537s in the REMEC filterbanks. In the case of the Daughter Board FPGAs, all filter channel outputs are recorded using 16 bit (cnt16) counters, and a single 22 bit (cnt22) counter can be programmed in flight to provide higher resolution ('dual counter') monitoring of any single, selectable, filterbank channel.

[2]We assume for simplicity that the data are varying linearly with time for this discussion.

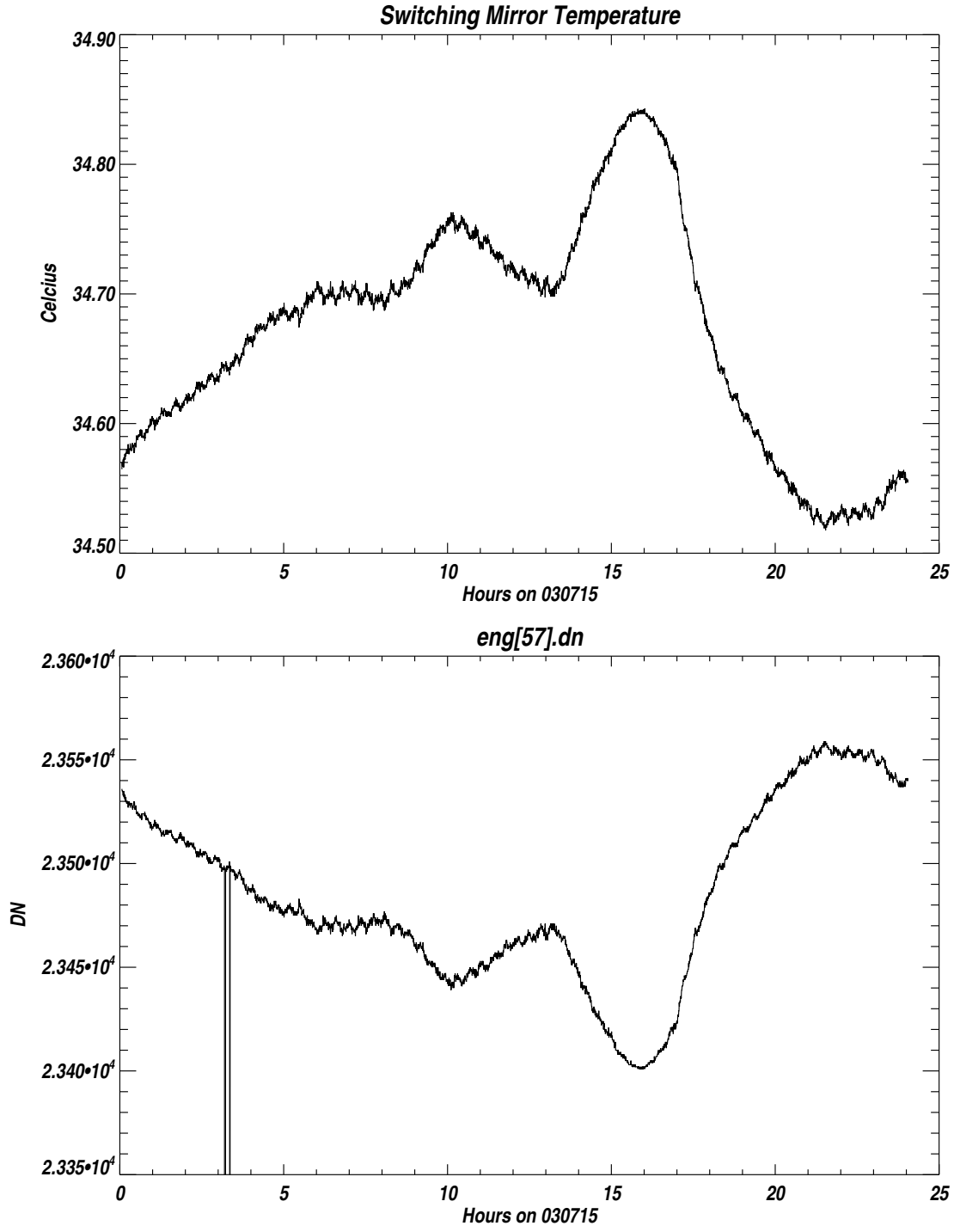

Figure 6.4: GHz Switching Mirror temperature for a 24 hours period during Spacecraft thermal vacuum testing. Lower panel shows the corresponding DN. The 'glitches' in DN around 03:20 hours correspond to loss of engineering telemetry due to spacecraft configuration activities.

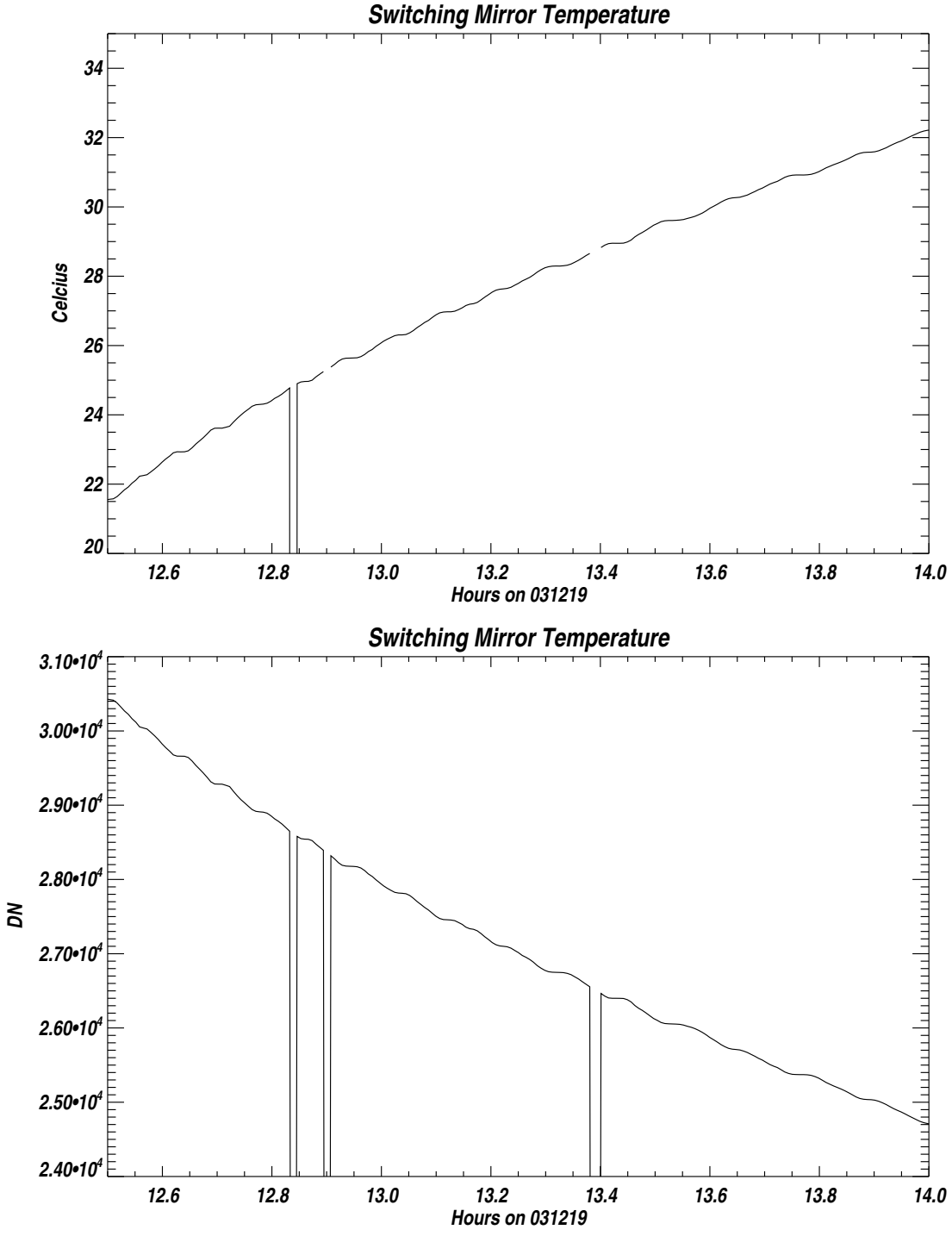

Figure 6.5: GHz Switching Mirror temperature for a 1.5 hour period during instrument warm-up in the High Bay at NGST. Lower panel shows the corresponding DN. Note the presence of multiple 'flat spots.' The 'glitches' in both temperature and DN plots correspond to loss of engineering telemetry due to instrument and spacecraft configuration activities.

A 'weak point' common to the operation of all integrating A/D converters is that the integrator output is required to generate a trigger signal of some kind when it reaches/crosses one or more thresholds. The integrator output exhibits noise from both the input signal and the integrator electronics, and the comparators used to generate the triggers are activated by a combination of the signal and noise. A repetitive noise source like a logic clock can put 'grass' on the integrator output (or comparator input), and since such interference sources tend be at a much higher frequency than the VFC output frequency, the effect is one of prematurely triggering the VFC on every cycle. The most obvious manifestation of this unwanted pre-triggering is that the VFC frequency increases in the presence of an interfering signal. This effect was observed in the RIU/EDH combination under laboratory test conditions using a high resolution frequency counter on the VFC output. As the RIU transitioned from ROM to RAM-load to execute from RAM states, the VFC output was seen to increase in noise (jitter), and change in level by ∼20 Hz.

The more striking, and troublesome, aspect of the data in Figure 6.5 is the presence of substantial flat spots, and consequent incorrect behavior in the VFC output between the flat spots. It is a simple matter to determine VFC frequency from telemetered DN by solving Equation 6.1 for cnt16 with the knowledge that cnt22 always has the same approximate count under nominal operating conditions (∼1,940,000). We then find that the frequencies of the flat spots are simply integer sub-multiples of 12 MHz, the RIU processor clock frequency. That is to say, the flat spots consist of a set of VFC frequencies where each VFC cycle is an integer number of 12 MHz clock cycles.

During laboratory testing, effort was made to reduce the coupling between logic and VFC by changing ground configuration, adding decoupling, and filtering some of the key signals at the EDH hybrid pins. The only method found to provide substantial improvement to the flat spots was to place a small capacitor (nominally 600 pF) between the input pins of the op-amp feeding the VFC. These signal nodes were available at two of the hybrid pins, and all flight RIU/EDH combinations have this retrofit. A disadvantage of this noise reduction scheme is that it places an undesirable zero in the transfer function of the op-amp, potentially leading to instability. As a result, all RIU/EDH combinations were tested for stability by observing the output of the op-amp with a square wave input stimulus, and the value of the capacitor individually selected for each unit to provide adequate stability margin. All engineering data plots presented in this report are from RIU/EDH units which have this noise/flat spot reduction capacitor in place. The typical improvement from this 'fix' was a factor of ∼2 reduction in the width of the flat spots.

The DN, f, which represent flat spot are given approximately by:

$$f = (12.0 \times 10^6/i - 36000.0) * 1.35 \tag{6.2}$$

where i ranges from 142 to 333, thus indicating 192 flat spots over the nominal input signal range of the EDH. For i in the range 333 down to 142 we obtain for f:

48.6475	195.180	342.599	490.910	640.122	790.246
941.282	1093.25	1246.16	1400.00	1554.80	1710.56
1867.29	2025.00	2183.70	2343.39	2504.10	2665.82
2828.57	2992.35	3157.19	3323.08	3490.03	3658.06

3827.19	3997.40	4168.73	4341.18	4514.75	4689.47
4865.35	5042.38	5220.60	5400.00	5580.60	5762.42
5945.45	6129.73	6315.25	6502.04	6690.10	6879.45
7070.10	7262.07	7455.36	7650.00	7845.99	8043.36
8242.10	8442.25	8643.82	8846.81	9051.24	9257.15
9464.52	9673.38	9883.76	10095.7	10309.1	10524.1
10740.7	10958.8	11178.6	11400.0	11623.0	11847.8
12074.2	12302.3	12532.1	12763.6	12997.0	13232.1
13469.0	13707.7	13948.3	14190.7	14435.0	14681.2
14929.4	15179.5	15431.6	15685.7	15941.8	16200.0
16460.2	16722.6	16987.0	17253.7	17522.5	17793.4
18066.7	18342.2	18619.9	18900.0	19182.4	19467.2
19754.4	20044.1	20336.2	20630.8	20927.9	21227.6
21529.9	21834.8	22142.4	22452.6	22765.6	23081.4
23400.0	23721.4	24045.7	24373.0	24703.2	25036.4
25372.6	25711.9	26054.4	26400.0	26748.8	27100.9
27456.3	27815.1	28177.3	28542.9	28912.0	29284.6
29660.9	30040.8	30424.4	30811.8	31203.0	31598.0
31997.0	32400.0	32807.0	33218.2	33633.5	34053.1
34476.9	34905.2	35337.8	35775.0	36216.8	36663.2
37114.3	37570.2	38031.0	38496.8	38967.6	39443.5
39924.6	40411.0	40902.8	41400.0	41902.8	42411.2
42925.4	43445.5	43971.4	44503.4	45041.6	45586.1
46136.8	46694.1	47258.0	47828.6	48406.0	48990.4
49581.8	50180.5	50786.5	51400.0	52021.1	52650.0
53286.8	53931.6	54584.7	55246.2	55916.1	56594.8
57282.4	57978.9	58684.8	59400.0	60124.8	60859.5
61604.1	62358.9	63124.1	63900.0	64686.7	65484.5

The upper panel of Figure 6.6 plots the temperature of PRD1 on the GHz Controlled Calibration Target during instrument taken with the instrument cold during thermal vacuum testing at NGST on 18 October 2003. The black and blue curves in the upper panel are the inferred temperature of the sensor using forward and reversed excitation currents. The lower panel plots the same data, but as DN. On the lower panel we also indicate the expected DN flat spots predicted from Equation 6.2, and the agreement between theory and measurement is seen to be excellent. Investigations of similar telemetry with the instrument hot (i.e., near the other extreme of the DN range) also indicate excellent agreement between predicted and observed flat spots. The data presented in Figure 6.6 show an odd/even behavior[3] in the flat spots at the lowest temperatures. This behavior is present on all EDH data from the RIU monitoring this PRD. Other RIUs have their own odd/even characteristics, varying from the type of behavior shown here, down to no difference in the magnitudes of adjacent flat spots. The reasons for the differing behavior between RIUs is not understood at this time.

[3]By odd/even behavior we mean that the flat spots alternate in width.

6.4 Thermocouple EMFs

Just as striking as the flat spots in Figure 6.6 are the *differences* between measurements of the same sensor taken less than 1 second apart, but with reversed excitation currents. As

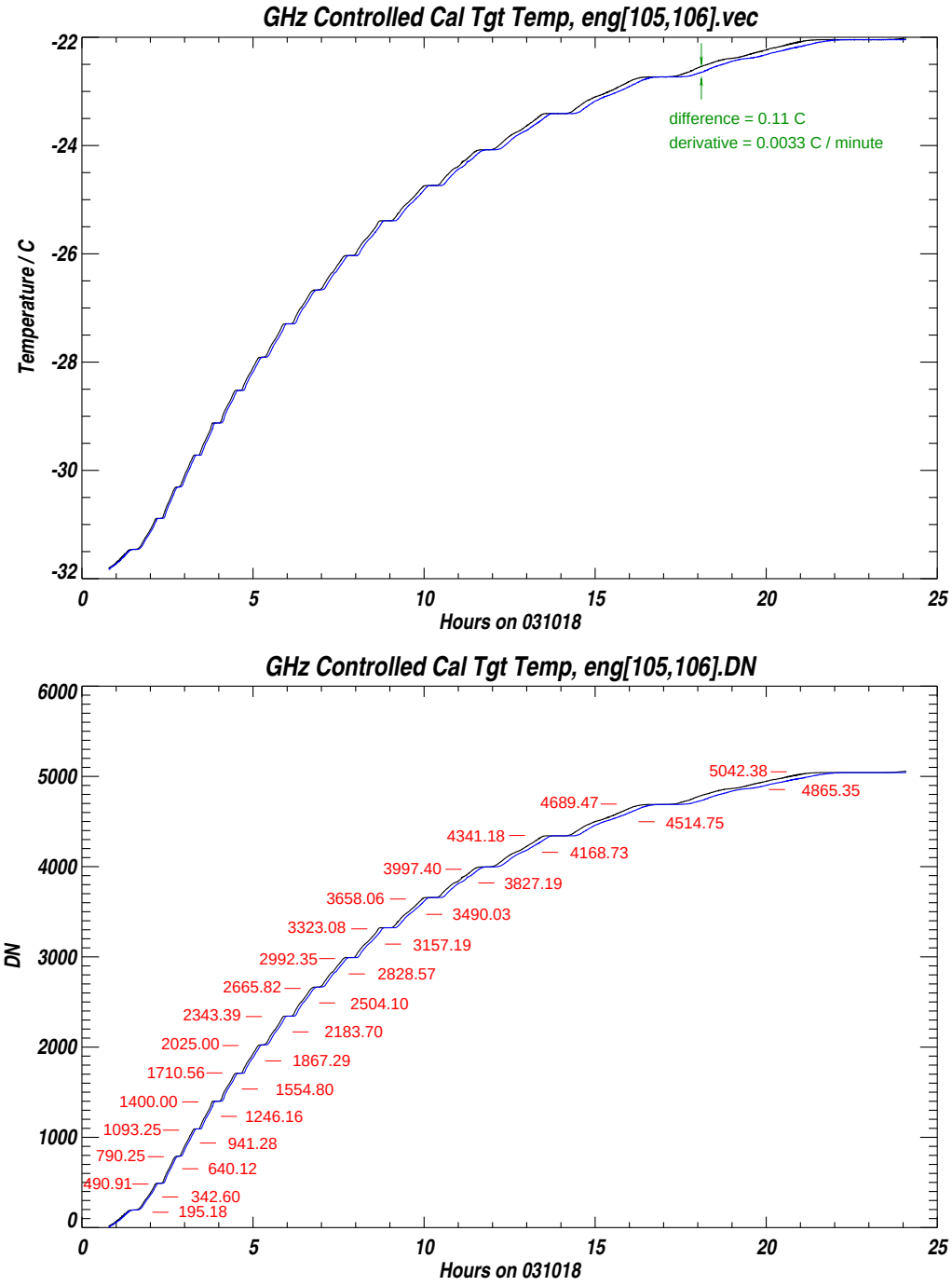

Figure 6.6: Temperature telemetry from sensor 1 on the GHz Controlled Calibration Target during thermal vacuum testing at NGST. The upper panel indicates temperature, the lower panel shows DN. The black and blue curves correspond to data taken with forward and reversed excitation currents. See text for further details.

indicated on the upper panel, the difference in inferred temperature is 0.11 C when temperatures are varying at a rate of 0.2 C per hour (0.0033 C per minute). These differences are sufficiently large that the forward and reversed current flat spots do not even occur at the same times, most clearly visible in the DN plot.

The 500 Ω PRD sensors used in the Calibration Targets have a nominal temperature dependence of $2\,\Omega\,\mathrm{C}^{-1}$ at room temperature. A temperature difference of 0.11 C thus corresponds to an equivalent resistance error of 0.22 Ω. Since the PRD excitation current is 0.1 mA, we infer a thermal EMF of 22 μV in this example. During thermal vacuum testing transitions between plateaus, thermal EMFs of several hundred μV have been observed, sufficient to remove any overlap between the flat spots on forward and reverse excitation currents measurements on a given sensor.

This 22 μV is removed by combining the forward and reversed excitation current data. Examination of many data sets obtained from the instrument during ground testing and operation indicates that significant thermocouple effects only appear in Calibration Target temperature telemetry when the instrument is not at thermal equilibrium. Under the thermal conditions predicted for in-flight operation we do not anticipate any difficulties from thermal EMFs.

6.5 A proposed method for reducing the impact of telemetry flat spots in calibration Target telemetry

Several problems with Calibration Target temperature telemetry have been described:

(1) The telemetry transfer function exhibits significant flat spots,

(2) the 'slope' of the transfer function between flat spots is not correct, and

(3) significant thermocouple effects are evident in these data except when the instrument is very stable thermally (as expected in orbit).

Note that these issues are not unique to Calibration Target telemetry. For the Calibration Targets we have the advantage that there are multiple PRD sensors (10), there is significant variation in R_0 (the resistance at 0 C) between devices, and we anticipate only small thermal gradients across the Targets once in orbit. The significant variation in device R_0 serves to scatter the flat spots in temperature, thus ensuring most sensors are not in a flat spot region at any given time. This has been verified by examination of engineering telemetry. The low anticipated thermal gradients in orbit serves to create far more overlap between forward and reverse readings than shown in the data of Figure 6.6.

We can thus envisage a scheme in which the telemetry from each temperature sensor is given a weighting according the proximity of its DN to a predicted flat spot. Since we must combine forward and reversed excitation current data, the lower of the weightings from either measurements is applied to both. The entire ensemble of data from all Target sensors are then combined to provide an estimate of average Target temperature. Such a scheme has been prototyped in IDL, and verified to work. Such a scheme should not be employed under conditions of thermal instability since the resulting lack of overlap between forward and reversed readings causes sensor to drop in and out of the ensemble. The large variation between forward and reversed inferred temperatures, as well as individual sensors, under

such dynamic conditions, adds significant high frequency structure to the inferred Target temperature.

The weakest point in this scheme is that although it produces an estimate of Target temperature that is free of flat spots, we do not currently know how to correct for the incorrect slope between flat spots in data of the type shown in Figure 6.6. To answer this question would require significant laboratory work, and is not proposed here because the ensemble estimate of Calibration Target temperature meets accuracy requirements, even with the most pessimistic interpretation of the effects of the flat spots. Note that all of the calibration point measurements made within the EDH are also subject to flat spots.

6.6 Precision and accuracy

The measurement range, accuracy and precision (resolution) of the EDH units is given in Table 6.1. These data are taken from the documentation provided with these units, and are based on worst-case analyses and measurements taken under laboratory conditions. The quoted accuracy and precision for the thermistor measurements are for temperatures between -20 C to +70 C, with degraded performance outside of this range. The stated thermistor measurement accuracy is for errors introduced by EDH electronics, not unit-to-unit variations in the thermistors. The thermistor type, a space-qualified verion of the Yellow Spring Industries (YSI) 44007, are interchangeable with unit-to-unit variations in resistance at 25 C corresponding to better than ± 0.2 C. Additional (small) errors arise from variations in the 4.990 kΩ resistors in parallel with each thermistor, from unaccounted resistance in the wiring to the thermistors from the EDH, and approximations in the algorithms used to convert from measured resistance to inferred temperature. All of these additional sources of error are small, combining to an estimated total error of less than 0.4 C for measurements near room temperature for all sources combined. No thermistor data are used in calibration algorithms.

The PRD sensors (Rosemount 118 series) are connected in a 4-wire configuration for calibration target sensing, and a 3-wire configuration for the less important monitoring of structure and reflector temperatures. Each sensor is individually calibrated by the vendor, and the data processing software uses these data to eliminate the otherwise significant (greater than ± 4 C) unit-to-unit variations at 0 C. The estimated maximum temperature error in each PRD is dominated by the 'flat spots' in EDH telemetry, discussed earlier. For each calibration target this effect is considerably mitigated by the large number of PRDs being averaged, and the additional data arising from the forward and reverse excitation current measurement pairs. We estimate the maximum error in ensemble-averaged calibration target telemetry to be less than ± 0.3 C.

Table 6.1: Range, accuracy and precision of engineering data acquired by the Engineering Data Hybrid (EDH) units. These performance numbers do not account for the 'flat spots' evident in EDH telemetry. See text for additional information.

Measurement type	nominal range	accuracy	precision	
Voltage	0 V to +6 V	0.5%	0.05%	-1 V to +7 V before overrange
Voltage (inv)	-6 V to 0 V	0.5%	0.05%	-7 V to +1 V before overrange
PRD	-100 C to +100 C	0.3 C	0.01 C	
PRD (high res)	-20 C to +70 C	0.15 C	0.01 C	
Thermistor	-80 C to +100 C	0.5 C	0.01 C	

Bibliography

[1] Waters, J.W., An Overview of the EOS MLS Experiment, JPL D-15745, Version 1.0, 15 Jan. 1999.

[2] Jarnot, R.F., EOS MLS Level 1 Data Processing Algorithm Theoretical Basis, JPL D–15210.

[3] Jarnot, R.F. and Cofield, R.E., Microwave Limb Sounder (MLS) Instrument Calibration Report, JPL Document D–9394, August 1991.

[4] Waters, J.W. and Jarnot, R.F., Science Requirements on the EOS MLS Instrument and Data Processing Software, JPL–D14421, Revision 3.0.

[5] Read, W.G. and Shippony S., Microwave Limb Sounder (MLS) Forward Model Algorithm Theoretical Basis Document, JPL-D-18130

[6] Livesey, N.J. and Wu. D.L., EOS MLS Retrieval Processes Algorithm Theoretical Basis, JPL-D-16159.

[7] MTPE EOS Reference Handbook 1995, available from the EOS Project Science Office, code 900, NASA Goddard Space Flight Center, Greenbelt, MD 20771.

[8] Jarnot, R.F., Cofield, R.E., Waters, J.W. and Flower, D.E., Calibration of the Microwave Limb Sounder on the Upper Atmosphere Research Satellite, *J. Geophys Res.*, 101, April 1996, No. D6, 9957–9982.

[9] Erickson, N., Tolls, V., Near-Field Measurements of the SWAS Antenna, *20th ESTEC Antenna Workshop on Millimetre Wave Antenna Technology and Antenna Measurements*, 18–20 June 1997, Noordwijk, The Netherlands.

[10] Slater,D., Near Field Antenna Measurements, 1991 Artech House, Inc. ISBN 0-89006-361-3.

[11] Slater,D., *et.al.*, A Large Aperture 650 GHz Near-Field Measurement System for the Earth Observing System Microwave Limb Sounder, *Antenna Measurement Techniques Association Conference*, October 2001.

[12] www.nearfield.com